Hybrid discretization methods for Signorini contact and Bingham flow problems.

Karol Cascavita

UNIVERSITÉ PARIS-EST

Thèse

présentée pour obtenir le grade de

Docteur de l'université Paris-Est

École doctorale MSTIC, mention Mathématiques Appliquées

par Karol Cascavita

Hybrid discretization methods for Signorini contact and Bingham flow problems

Méthodes de discrétisation hybrides pour les problèmes de contact de Signorini et les écoulements de Bingham

---

Soutenue publiquement le 18 décembre 2018 devant le jury composé de

Rapporteurs	Patrick Hild	Université Paul Sabatier, Toulouse
	Pierre Saramito	ENSIMAG, Grenoble
Examinateurs	Jérémy Bleyer	Université Paris-Est
	Erik Burman	University College London
	Miguel Fernández	Inria-Paris
	Raphaèle Herbin	Université d'Aix-Marseille
Directeur de thèse	Alexandre Ern	Université Paris-Est & Inria
Co-directeur de thèse	Xavier Chateau	Université Paris-Est

Acknowledgment

I owe my gratitude to all the people who contribute in a way or another to the achievement of this thesis.

I feel very honored to have been supervised by Alexandre Ern, due to his knowledge and expertise. I owe him my gratitude for his mathematical guidence, accurate contribution to my research, and for providing me continuous support for my PhD studies throughout these years at Paris. I am also grateful to the rest of my thesis committee, Xavier Chateau and Jérémy Bleyer, that provided me links with engineering and interesting exchanges with a more physical point of view. I would like to thank especially Jérémy for the numerical results aimed to compare our own results and for his assistance. My sincere thanks also goes to Franz Chouly for the fruitful interactions to the second chapter of this thesis. His valuable comments are very appreciated.

I am grateful with Pierre Saramito and Patrick Hild for accepting to review this document and for their scientific comments. I also owe my gratitude to the experts who were involved in the examination of this manuscript: Erik Burman, Miguel Angel Fernandez and Raphael Herbin, for being the chair of the jury.

A very special gratitude goes out to SERENA project-team at Inria for their warm welcome Geraldine, Martin and specially my fellow labmates for the special atmosphere: Amina, Ani, Jad, Nicolas, Mohammad and Patrik. Finally, thanks to the old Cermics members: François, Atmane et Yannick.

I am indebted to all the people who opened their homes to me, who provided me their priceless company and their care during my time at Paris: Dominique & Olivier, Jérôme, Jihad & Shamima, Cristian and Jonathan. Thanks to my closest friends Matteo, Tania and Yushun for their love, this is my most precious treasure in my parisian life. I would like to mention also my old friends for their emotional support: Alejandra, Ana Maria, Carolina, David, Felipe, Juan Camilo, Laura, Nayan and Oscar.

Finally, I must express my very profound gratitude to my Mum and Dad, Martha, my sisters Lorena, Luisa and Sara, and Andrea. Thanks for being the strength when distance and research challenges were enough to weaken the spirit. I am grateful also to Matteo for his invaluable friendship that bloomed all these years around diskpp and in the middle of my own Macondo. I am very thankful for his unfailing moral and emotional support and continuous encouragement, especially the last months when writing this document. This accomplishment would not have been possible without them.

This Thesis has been supported by a PhD fellowship from the French government managed by ANR within the framework of the National Program Investments for the Future ANR-11-LABX-0022-01. This support is gratefully acknowledged.

Contents

Chapter 1

Introduction

Contents

This thesis is concerned with the devising and analysis of hybrid discretization methods for nonlinear variational inequalities arising in computational mechanics. The main example of hybrid discretization methods considered in this thesis is the Hybrid High-Order (HHO) method recently introduced in 2014 by Di Pietro et al. [60, 59]. Hybrid discretization methods are based on discrete unknowns attached to the mesh faces. Discrete unknowns attached to the mesh cells are also introduced, but they are eliminated locally by means of a Schur complement technique known as static condensation, thereby increasing computational efficiency. Salient advantages of hybrid discretization methods are local conservation at the cell level, robustness in various regimes and the possibility to use polygonal/polyhedral meshes with hanging nodes, which is very attractive in the framework of mesh adaptation. Two main applications are addressed in this thesis. The first one is the treatment of Signorini's unilateral contact problem (in the scalar-valued case) with a nonlinearity in the boundary conditions. The second main application is viscoplastic Bingham flows which are governed by a nonlinear relation between the stress tensor and the strain rate tensor.

This Chapter is organized as follows. In Section 1.1 we briefly review the state-of-the-art and the mathematical setting for Signorini's unilateral contact problem. We do the same in Section 1.2 for viscoplastic Bingham flows. We present an introduction to HHO methods in Section 1.3. Finally, we outline the contents of the following chapters in Section 1.4 and we highlight our main contributions.

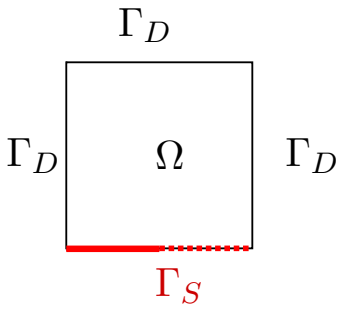

Figure 1.1: Boundary setting for Signorini's unilateral contact problem. The contact boundary is represented by a straight red line where contact is happening ($u = 0, \sigma_n(u) \leq 0$) and by a dashed red line otherwise ($u < 0, \sigma_n(u) = 0$).

1.1 Signorini's unilateral contact problem

Signorini conditions were introduced by Signorini [122] in 1933. They are the constitutive building block to model unilateral contact between a deformable body and a rigid support, or between deformable bodies. Moreover, these conditions appear naturally as the Karush–Kuhn–Tucker conditions in the context of variational inequalities whenever some convex functional is minimized under some inequality constraint at the boundary. Signorini conditions also represent the first step toward more comprehensive models in computational mechanics including friction. Contact and friction problems are relevant to a broad range of applications (see e.g. Kikuchi & Oden [94], Glowinski & Le Tallec [77], Haslinger et al. [86], Han & Sofonea [82], Laursen [101], Wriggers [130], Wohlmuth [129] and Section 1.1.4). In this section, we briefly present the mathematical setting for Signorini's unilateral contact problem, its discretization by conforming finite elements, and the treatment of the nonlinear boundary conditions by means of Nitsche's method.

1.1.1 Mathematical model

Let $\Omega \subset \mathbb{R}^d$, $d \geq 2$, denote an open, bounded, connected subset of $\mathbb{R}^d$ with a Lipschitz boundary $\partial\Omega$, and unit outward normal vector $\boldsymbol{n}$. Let $f : \Omega \to \mathbb{R}$ be a source term. Let

$$\partial\Omega = \overline{\Gamma_D} \cup \overline{\Gamma_N} \cup \overline{\Gamma_S} \tag{1.1}$$

be a partition of the boundary $\partial\Omega$ into three mutually disjoint subsets, where the boundary condition is respectively a Dirichlet, a Neumann, and Signorini's unilateral contact condition, see Figure 1.1. We assume that Γ_D has nonempty relative interior. We consider the following model problem:

$$\Delta u + f = 0 \quad \text{in } \Omega, \tag{1.2a}$$
$$u = 0 \quad \text{on } \Gamma_D, \tag{1.2b}$$
$$\sigma_n(u) = 0 \quad \text{on } \Gamma_N, \tag{1.2c}$$

and the unilateral contact boundary conditions on Γ_S as follows:

$$u \leq 0 \quad \text{on } \Gamma_S, \tag{1.3a}$$
$$\sigma_n(u) \leq 0 \quad \text{on } \Gamma_S, \tag{1.3b}$$
$$u\sigma_n(u) = 0 \quad \text{on } \Gamma_S, \tag{1.3c}$$

with the shorthand notation $\sigma_n(w) = \boldsymbol{n} \cdot \nabla w$ for a smooth enough function $w : \Omega \to \mathbb{R}$.

Remark 1.1 (Mechanical interpretation)**.** *When $d = 2$, the primal unknown can be viewed as the vertical displacement of a membrane (along the transverse direction z). The reference configuration of the membrane is Ω. The membrane has unit tension, is subjected to a surface load f (along the direction z); it is clamped on Γ_D and is free on Γ_N. On Γ_S, the first condition* (1.3a) *enforces that the admissible displacements must accomplish the condition of non-penetration into the rigid support located at $\{z = 0\}$. The second condition* (1.3b) *enforces that the normal reaction of the rigid support must be oriented toward the membrane. The last condition* (1.3c) *means that either the membrane and the support are in contact ($u = 0$), or the membrane is still unconstrained so that the rigid support does not exert any reaction ($\sigma_n(u) = 0$).*

Let $L^2(\Omega)$ denote the space of square-integrable functions over Ω and let us set $\boldsymbol{L}^2(\Omega) := L^2(\Omega;\mathbb{R}^d)$. The inner product in both spaces is denoted $(\cdot,\cdot)_\Omega$ and the associated norm $\|\cdot\|_\Omega$. Let $\gamma_{\partial\Omega} : H^1(\Omega;\mathbb{R}) \to H^{\frac{1}{2}}(\partial\Omega;\mathbb{R})$ be the classical trace map. Let the following subspace specifying a zero-trace of the displacement on the Dirichlet boundary:

$$H^1_D(\Omega) := \{w \in H^1(\Omega) \mid \gamma_{\partial\Omega}(w)_{|\Gamma_D} = 0\}. \tag{1.4}$$

Let us enforce the non-penetration condition $u \le 0$ on Γ_S by considering the following closed convex cone:

$$K_D(\Omega) = \{w \in H^1_D(\Omega) \mid \gamma_{\partial\Omega}(w)_{|\Gamma_S} \le 0\}, \tag{1.5}$$

so that the closed convex cone $K_D(\Omega)$ specifies the admissible solutions. Assuming $f \in L^2(\Omega)$, the solution of (1.2)-(1.3) is the unique minimizer in $K_D(\Omega)$ of the following strongly convex energy functional:

$$u = \underset{v\in K_D(\Omega)}{\arg\min}\, \frac{1}{2}\|\nabla v\|^2_\Omega - (f,w)_\Omega. \tag{1.6}$$

The unique minimizer of (1.6) can be characterized as the unique solution of the following elliptic variational inequality:

$$\begin{cases} \text{Find } u \in K_D(\Omega) \text{ such that} \\ (\nabla u, \nabla(w-u))_\Omega \ge (f, w-u)_\Omega \qquad \forall w \in K_D(\Omega). \end{cases} \tag{1.7}$$

It is well-known that the problem (1.7) is well-posed (see, e.g., Lions & Stampacchia [104] or Glowinski [80]).

1.1.2 Finite element discretization

We focus now on the discretization of Signorini's unilateral contact problem by means of the well-known Finite Element (FE) method. This allows us to highlight the difficulties arising in the treatment of the nonlinear boundary conditions.

Let $(\mathcal{T}_h)_{h>0}$ be a mesh sequence. For simplicity, we assume that Ω is a polygon / polyhedron in $\mathbb{R}^d$, $d \in \{2,3\}$ and that the meshes cover Ω exactly. For all $h > 0$, the mesh $\mathcal{T}_h$ is composed of nonempty disjoint open cells such that $\overline{\Omega} = \bigcup_{T\in\mathcal{T}_h} \overline{T}$. We assume that the meshes are compatible with the boundary partition (1.1). We assume that the mesh cells are simplices in $\mathbb{R}^d$, that is, triangles if $d = 2$ and tetrahedrons if $d = 3$. The mesh sequence $(\mathcal{T}_h)_{h>0}$ is assumed to be shape-regular in the usual sense of Ciarlet [49]. The mesh-size is denoted $h = \max_{T\in\mathcal{T}_h} h_T$, with h_T the diameter of the cell T. We define the space of continuous, piecewise polynomials with degree $k \in \{1,2\}$ (higher values of k are not considered owing to the lack of regularity of the exact solution see Andersson [5], Kinderlehrer [95] and Moussaoui & Khodja [109]):

$$V_h := \{w_h \in C^0(\overline{\Omega};\mathbb{R}) \mid w_{h|T} \in \mathbb{P}^k(T;\mathbb{R}); \forall T \in \mathcal{T}_h\}, \tag{1.8}$$

together with the subspace satisfying the homogenuous Dirichlet boundary condition on Γ_D:

$$V_{h,D} := V_h \cap H^1_D(\Omega). \tag{1.9}$$

We also introduce the discrete convex cone $K_{h,D}$. For $k = 1$, this cone is defined as

$$K_{h,D} := K_D(\Omega) \cap V_{h,D} = \{w_h \in V_{h,D} \mid w_h(a_i) \leq 0, \forall a_i \in \Gamma_S\}, \tag{1.10}$$

where $a_i, 1 \leq i \leq I$, denote a generic vertex of the mesh $\mathcal{T}_h$. For $k = 2$, one possibility is to define

$$K_{h,D} := \{w_h \in V_{h,D} \mid v_h(a_i) \leq 0, \forall a_i \in \Gamma_S, w_h(m_j) \leq 0, \forall m_j \in \Gamma_S\}, \tag{1.11}$$

where m_j, $1 \leq j \leq J$, denotes a generic edge midpoint. Note that for $k = 2$, $K_{h,D} \nsubseteq K_D$, i.e., the approximation setting is nonconforming. Other possibilities exist for defining $K_{h,D}$ with $k \in \{1, 2\}$; for instance, one can only enforce the mean-value of v_h to be non-negative on the mesh faces located in Γ_S. The discrete solution u_h is the unique minimizer in $K_{h,D}$ of the same energy functional as in (1.6), i.e., the discrete problem is

$$u_h := \underset{u_h \in K_{h,D}}{\arg\min} \frac{1}{2}\|\nabla w_h\|_\Omega^2 - (f, w_h)_\Omega. \tag{1.12}$$

Note that we can use the same energy functional as in (1.6) since the FE method is a conforming method. The unique minimizer of (1.12) can be characterized as the unique solution of the following discrete variational inequality:

$$\begin{cases} \text{Find } u_h \in K_{h,D} \text{ such that} \\ (\nabla u_h, \nabla(w_h - u_h))_\Omega \geq (f, w_h - u_h)_\Omega. \qquad \forall v_h \in K_{h,D}. \end{cases} \tag{1.13}$$

For the above FE discretization as well as for many variants such as mixed/nonconforming methods (e.g., Hild [90], Ben Belgacem & Renard [13], Laborde & Renard [99]), stabilized mixed methods (e.g., Hild & Renard [91]), penalty methods (e.g., Chouly & Hild [41]), it has been quite challenging to establish optimal convergence in the H^1-norm in the case the solution belongs to $H^{\frac{3}{2}+s}(\Omega)$ $(0 < s \leq 1/2)$. The first fully optimal result without extra assumptions for the standard FE discretization has been achieved only recently, in 2015, see Drouet & Hild [65]. The first analyses in the 1970s were actually sub-optimal with a convergence rate of order $O(h^{\frac{1}{2}+\frac{s}{2}})$, instead of $O(h^{\frac{1}{2}+s})$, see Scarpini & Vivaldi [120], Haslinger [85], Haslinger et al. [86], see also Hild & Renard [92]. Optimal error bounds were devised under additional assumptions on the contact set for the exact solution, see Belhachmi & Ben Belgacem [12] and Hüeber & Wohlmuth [93], whereas Drouet & Hild [65] have circumvented this assumption. We refer the reader, e.g., to Wohlmuth [93, 129] and Hild & Renard [92, 65] for more detailed reviews on the subject.

In what follows when stating error estimates, we often abbreviate as $a \lesssim b$ the inequality $a \leq Cb$ with positive real numbers a, b and a constant $C > 0$ whose value can change at each occurrence but is independent of the mesh size and the exact solution u (the value can depend on the mesh shape-regularity and the polynomial degree). Let us state for completeness the classical error estimate for the above FE discretization of the scalar Signorini problem.

Theorem 1.2 (Finite Element error estimate)**.** *Let $k \in \{1, 2\}$ and $d \in \{2, 3\}$. Suppose that the solution u of* (1.6) *belongs to $H^{\frac{3}{2}+s}(\Omega) \cap H^1_D(\Omega)$ with $0 < s < k - \frac{1}{2}$. The following error estimate for the discrete solution u_h solving* (1.12) *holds true:*

$$\|\nabla(u - u_h)\|_\Omega \lesssim h^{\frac{1}{2}+s}|u|_{H^{\frac{3}{2}+s}(\Omega)}. \tag{1.14}$$

Proof. See Drouet & Hild [65]. □

A drawback of the FE discretization is the difficulty to handle the discrete convex cone $K_{h,D}$. One possibility to circumvent this difficulty is to use Lagrange multipliers to enforce the non-penetration constraint, resulting in the need to solve a saddle-point problem. Another relatively recent approach, which is the focus of the next section, is to use Nitsche's method to enforce

weakly the nonlinear conditions. For a review of numerical approximations to Signorini's unilateral contact conditions, we refer the reader to [38], see also e.g Herbin & Marchand [88] for the Finite Volumes method, and more recently Alnashri & Droniou [4] for the Gradient schemes framework.

1.1.3 Nitsche's enforcement of Signorini's conditions

Nitsche's method has been introduced in 1971 to enforce weakly Dirichlet boundary conditions in linear elliptic problems [110]. This method has been extended to Signorini's problem discretized with Lagrange finite elements by Chouly & Hild [40, 45] (see also Chouly et al. [38] for an overview of recent results). For this Nitsche-based FE discretization, optimal convergence in the $H^1(\Omega)$-norm of order $O(h^{\frac{1}{2}+s})$ has been proved, provided the solution has a regularity $H^{\frac{3}{2}+s}(\Omega)$, $0 < s \leq k - 1/2$ ($k = 1, 2$ is the polynomial degree of the Lagrange finite elements). As for the FE analysis by Drouet & Hild [65], there is no need of any additional assumption on the contact/friction zone, such as an increased regularity of the contact stress or a finite number of transition points. Moreover, the proof applies in the two-dimensional and in the three-dimensional cases, and for continuous affine and quadratic finite elements.

The key idea to devise the Nitsche-FEM discretization of (2.7)-(2.8) is to reformulate Signorini conditions (2.8) as a single nonlinear equation on the normal flux $\sigma_n(u)$. Thus, let us first present a reformulation of the unilateral contact conditions, as introduced by Alart & Curnier [54].

Lemma 1.3 (Reformulation of Signorini's condition)**.** *Let $\gamma > 0$ be a positive real number. Signorini's unilateral contact condition* (1.3) *is equivalent to*

$$\sigma_n(u) = [\phi_\gamma(u)]_{\mathbb{R}^-}\,, \tag{1.15}$$

with $\phi_\gamma(w) := \sigma_n(w) - \gamma w = \boldsymbol{n}\cdot\nabla w - \gamma w$ for any smooth enough function $w : \Omega \to \mathbb{R}$, and where $[x]_{\mathbb{R}^-} := \min(x, 0)$ denotes the projection onto the convex subset $\mathbb{R}^- := (-\infty, 0]$ of any real number x.

Proof. See the work by Alart & Curnier [54] and the work by the Chouly & Hild [40, Proposition 2.1]. Let us briefly sketch the proof.
(i) (1.15) $\Longrightarrow$ (1.3). The second contact condition (1.3b) follows from $[x]_{\mathbb{R}^-} \leq 0$. If $\sigma_n(u) = 0$, then (1.15) implies $[-\gamma u]_{\mathbb{R}^-} = 0$. Otherwise, $\sigma_n(u) < 0$ and (1.3c) implies $\sigma_n(u) = \phi_\gamma(u) = \sigma_n(u) - \gamma u$, so that $u = 0$. This proves (1.3a) and (1.3c).
(ii) (1.3) $\Longrightarrow$ (1.15). Observe that (1.3) results in two possible scenarios: The first one is $u = 0$ and $\sigma_n(u) \leq 0$, which can be written as $\sigma_n(u) = [\sigma_n(u)]_{\mathbb{R}^-} = [\sigma_n(u) - \gamma u]_{\mathbb{R}^-}$. The second scenario is $\sigma_n(u) = 0$ and $u \leq 0$, which can be written as $\sigma_n(u) = 0 = [-\gamma u]_{\mathbb{R}^-} = [\sigma_n(u) - \gamma u]_{\mathbb{R}^-}$. Whence the equivalence. □

We are now in a position to formulate Nitsche's method for Signorini's unilateral contact conditions. Let us first define the energy functional $J_{\gamma,h} : V_{h,D} \to \mathbb{R}$ originally used for Dirichlet boundary conditions, and adapted here to treat Signorini's unilateral contact conditions (see, e.g, Chouly et al. [48] for a complete derivation):

$$J_{\gamma,h}(w_h) := \frac{1}{2}\|\nabla w_h\|_\Omega^2 - (f, w_h)_\Omega - \frac{1}{2}\int_{\Gamma_S}\frac{1}{\gamma}\sigma_n(w_h)^2 + \frac{1}{2}\int_{\Gamma_S}\frac{1}{\gamma}\left[\phi_\gamma(w_h)\right]_{\mathbb{R}^-}^2\,, \tag{1.16}$$

where $\gamma > 0$ is a penalty parameter specified in Theorem 1.6. The discrete solution is defined to be the unique minimizer of this convex functional over $V_{h,D}$, namely

$$u_h = \underset{w_h \in V_{h,D}}{\arg\min}\, J_{\gamma,h}(w_h). \tag{1.17}$$

The discrete problem in weak form follows from the Euler equations characterizing the unique minimizer in (1.17). Nitsche's formulation for the discrete Signorini problem thus reads:

$$\begin{cases} \text{Find } u_h \in V_{h,D} \text{ such that} \\ a_{\gamma,h}(u_h, w_h) = \ell_{\gamma,h}(w_h) \qquad \forall w_h \in V_{h,D}, \end{cases} \tag{1.18}$$

with the semi-linear form

$$\begin{aligned} a_{\gamma,h}(v_h, w_h) &= (\nabla v_h, \nabla w_h)_\Omega - \int_{\Gamma_S} \frac{1}{\gamma}\sigma_n(v_h)\sigma_n(w_h) + \int_{\Gamma_S} \frac{1}{\gamma}\left[\phi_\gamma(v_h)\right]_{\mathbb{R}^-} \phi_\gamma(w_h), \\ \ell_{\gamma,h}(w_h) &= (f, w_h)_\Omega. \end{aligned}$$

Remark 1.4 (Linear case)**.** *Consider the linear case where one wants to solve the PDE* (1.2a) *supplemented with the Dirichlet condition $u = g$ on Γ_D with $g \in H^{\frac{1}{2}}(\partial\Omega; \mathbb{R})$, and $\sigma_n(u) = 0$ on Γ_N, with $\partial\Omega = \overline{\Gamma}_D \cup \overline{\Gamma}_N$. Then, the usual Nitsche's formulation is recovered by considering the functional $\tilde{J}_{\gamma,h} : V_h \to \mathbb{R}$ such that*

$$\tilde{J}_{\gamma,h}(v_h) = \frac{1}{2}\|\nabla v_h\|_\Omega^2 - (f, v_h)_\Omega - \int_{\Gamma_D} (v_h - g)\sigma_n(v_h) + \frac{1}{2}\int_{\Gamma_D} \frac{1}{\gamma}(v_h - g)^2. \tag{1.19}$$

Considering the Euler equation leads to the following weak formulation for the unique minimizer of $\tilde{J}_{\gamma,h}$ over V_h:

$$\begin{cases} \textit{Find } u_h \in V_h \textit{ such that} \\ a_{\gamma,h}(u_h, v_h) = \ell_{\gamma,h}(v_h) \qquad \forall v_h \in V_h, \end{cases} \tag{1.20}$$

where

$$\begin{aligned} a_{\gamma,h}(u_h, v_h) &= (\nabla u_h, \nabla v_h)_\Omega - \int_{\Gamma_D} (\sigma_n(u_h)v_h + \sigma_n(v_h)u_h) + \int_{\Gamma_D} \frac{1}{\gamma} u_h v_h, \\ \ell_{\gamma,h}(v_h) &= (f, v_h)_\Omega - \int_{\Gamma_D} \left(g\sigma_n(v_h) + \frac{1}{\gamma} g v_h \right). \end{aligned}$$

Note that $a_{\gamma,h}$ is nonlinear in its first argument. Adding and subtracting the term $\frac{1}{2}\int_{\Gamma_D} \frac{1}{\gamma}\sigma_n(v_h)^2$ in (1.19)*, we obtain*

$$\tilde{J}_{\gamma,h}(v_h) = \frac{1}{2}\|\nabla v_h\|_\Omega^2 - (f, v_h)_\Omega - \frac{1}{2}\int_{\Gamma_S} \frac{1}{\gamma}\sigma_n(v_h)^2 + \frac{1}{2}\int_{\Gamma_S} \frac{1}{\gamma}(\sigma_n(v_h) - \gamma(v_h - g))^2.$$

Letting $g = 0$, this makes the link with the energy functional defined in (1.16) *more explicit.*

A key property of the discrete problem (1.18) is its strong consistency whenever the exact solution has enough regularity to be used as the first argument of the semi-linear form $a_{\gamma,h}$.

Lemma 1.5 (Strong consistency)**.** *Suppose that the solution u of* (1.6) *belongs to $H^{\frac{3}{2}+s}(\Omega)$, with $s > 0$. The following holds true:*

$$a_{\gamma,h}(u; v_h) = (f, v_h)_\Omega \qquad \forall v_h \in V_{h,D}. \tag{1.21}$$

Proof. Since $u \in H^{\frac{3}{2}+s}(\Omega)$, $s > 0$, we have

$$(\nabla u, \nabla v_h)_\Omega = (f, v_h)_\Omega - \int_{\Gamma_S} \sigma_n(u)v_h \quad \forall v_h \in V_{h,D}, \tag{1.22}$$

where we used that $v_{h|\Gamma_D} = 0$ and that $\sigma_n(u)_{|\Gamma_N} = 0$ (this localization of the Neumman boundary condition is possible since $u \in H^{\frac{3}{2}+s}(\Omega)$, and $s > 0$). Moreover, Lemma 1.3 implies that $\sigma_n(u) = [\phi_\gamma(u)]_{\mathbb{R}^-}$. Hence, we complete the proof as follows:

$$\begin{aligned} a_{\gamma,h}(u; v_h) &= (\nabla u_h, \nabla v_h)_\Omega - \frac{1}{\gamma}\int_{\Gamma_S} \sigma_n(u)\left(\phi_\gamma(v_h) - \sigma_n(v_h)\right) \\ &= (\nabla u_h, \nabla v_h)_\Omega + \int_{\Gamma_S} \sigma_n(u)v_h \\ &= (f, v_h)_\Omega. \end{aligned}$$

□

Theorem 1.6 (Error estimate for Nitsche's method)**.** *Suppose that the solution u of* (1.6) *belongs to $H^{\frac{3}{2}+s}(\Omega)$ with $s > 0$. Assume that $\gamma = \gamma_0 h^{-1}$ with γ_0 large enough (the minimum value depends on a discrete trace inequality and therefore on the shape-regularity of the mesh sequence and the polynomial degree k, see, e.g., [110, 123, 84]). Then the following error estimate for the discrete solution u_h of* (1.18) *holds true:*

$$\begin{aligned}\|\nabla(u-u_h)\|_\Omega + \gamma^{-\frac{1}{2}}\|\sigma_n(u) - [\phi_\gamma(u_h)]_{\mathbb{R}^-}\|_{L^2(\Gamma_S)} \\ \lesssim \inf_{v\in V_h}\left\{\|\nabla(u-v_h)\|_\Omega + \gamma^{\frac{1}{2}}\|u-v_h\|_{L^2(\Gamma_S)} + \gamma^{-\frac{1}{2}}\|\sigma_n(u-v_h)\|_{L^2(\Gamma_S)}\right\},\end{aligned} \tag{1.23}$$

and for $0 < s \leq k - \frac{1}{2}$, $k \in \{1, 2\}$, we have

$$\|\nabla(u-u_h)\|_\Omega + \gamma^{-\frac{1}{2}}\|\sigma_n(u) - [\phi_\gamma(u_h)]_{\mathbb{R}^-}\|_{L^2(\Gamma_S)} \lesssim h^{\frac{1}{2}+s}|u|_{H^{\frac{3}{2}+s}(\Omega)}. \tag{1.24}$$

Proof. See Chouly & Hild [40]. □

Taking for example the primal unknown with enough regularity, i.e., $u \in H^2(\Omega)$ so that $s = 1/2$, we obtain a convergence, as in Theorem 1.2 for FEM, of order $O(h)$ (optimal) from Theorem 1.6.

In this thesis we use the semi-smooth Newton method to obtain the numerical solution of the discrete Signorini problem. The steps of this method are listed in Algorithm 1.

Algorithm 1 Semi-smooth Newton method for the discrete Signorini problem

1: Choose $u_h^0 \in V_{h,D}$
2: Choose $\epsilon > 0$, set $R^0 = \infty$ and $n = 0$
3: **while** $R^n > \epsilon$ **do**
4: Seek $\delta_h \in V_{h,D}$ solving the linear problem

$$a_{\gamma,h}^{(N)}(\delta_h, v_h) - \int_{\Gamma_S} H(\phi_\gamma(u_h^n))\phi_\gamma(\delta_h)\phi_\gamma(v_h) = r_h(u_h^n; v_h) \qquad \forall v_h \in V_{h,D}, \tag{1.25}$$

where H denotes the Heaviside function ($H(s) = 1 if s \geq 0$ or $H(s) = 0$ otherwise), whereas the bilinear form and the nonlinear residual in (1.25) are defined as follows for all $w_h, v_h \in V_h$:

$$a_{\gamma,h}^{(N)}(w_h, v_h) := (\nabla w_h, \nabla v_h)_\Omega - \int_{\Gamma_S} \frac{1}{\gamma}\sigma_n(w_h)\sigma_n(v_h), \tag{1.26}$$

$$r_h(w_h; v_h) := a_{\gamma,h}^{(N)}(w_h, v_h) + \int_{\Gamma_S} [\phi_\gamma(w_h)]_{\mathbb{R}^-}\,\phi_\gamma(v_h) - (f, v_h)_\Omega \tag{1.27}$$

5: Compute $u_h^{n+1} := u_h^n + \delta_h$
6: Compute $R^{n+1} := \|\nabla\delta_h\|_\Omega$
7: $n = n + 1$
8: **end while**

1.1.4 Variants and extensions

The Nitsche-based FE discretization introduced by Chouly et al. [45] encompasses symmetric and nonsymmetric variants depending upon a parameter denoted $\theta \in \{-1, 0, 1\}$. The symmetric case presented in the previous section is recovered when $\theta = 1$. When $\theta \neq 1$, the advantage of having a variational formulation is lost. Nevertheless, some other advantages are recovered, mostly from the numerical viewpoint. Namely, one of the variants ($\theta = 0$) involves a reduced quantity of terms, which makes it easier to implement and to extend to contact problems in the

framework of nonlinear elasticity. In addition, numerical experiments reported by Renard [116] indicate that this nonsymmetric variant with $\theta = 0$ performs better in the sense that it requires less Newton iterations to converge for a wide range of values of the Nitsche parameter, than the symmetric variant with $\theta = 1$. Concerning the skew-symmetric variant $\theta = -1$, the main advantage is that the well-posedness of the discrete formulation and the optimal convergence are preserved irrespectively of the value of the Nitsche parameter γ_0, that can even be taken as 0 (penalty-free Nitsche's method, see, e.g., Boiveau & Burman [18, 23]). Note that in the linear case when enforcing a non-homogeneous Dirichlet boundary condition, the symmetric variant ($\theta = 1$) as originally proposed by Nitsche [110] is the most widespread, since on the one hand it preserves symmetry and therefore leads to optimal L^2-error estimates by means of duality arguments, and on the other hand it allows for efficient solvers for linear systems with a symmetric matrix. However, some nonsymmetric variants have been reconsidered recently, due to some remarkable robustness properties (see, e.g., Burman et al. [23], Boiveau & Burman [18]). In the context of discontinuous Galerkin methods, such nonsymmetric variants are well-known as well (see, e.g., Di Pietro & Ern [58, Section 5.3.1] and the references therein).

Recently, various extensions of the Nitsche-based FE method have been devised. The method has been adapted to Tresca friction by Chouly [37], to Coulomb's friction by Chouly et al. [42], Renard [116], to contact in elastodynamics by Chouly et al. [43, 44], Verlet et al. [47], and to contact between two elastic bodies by Fabre et al. [71], Chouly et al. [46], Mlika et al. [105]. In Fabre et al. [71], Nitsche's method is combined with a Cut-FEM / fictitious domain discretization in the small deformations framework. In Chouly et al. [46], Mlika et al. [105], an unbiased variant treats the contact between two elastic bodies without making any difference between master and slave contact surfaces, i.e., the contact condition is the same on each surface. This is an advantage for the treatment of self-contact and multi-body contact problems. Residual-based *a posteriori* error estimates are presented and analyzed by Chouly [39], with a saturation assumption, and by Gustafsson et al. [81], without a saturation assumption. The topic of small-sliding frictional contact in 3D has been studied by Annavarapu et al. [6], where a weighted Nitsche method is designed and tested numerically. In Hansbo et al. [83], a least-squares stabilized Augmented Lagrangian method, inspired by Nitsche's method, is introduced for unilateral contact. It shares some common features with Nitsche's method and allows for increased flexibility in the discretization of the contact pressure. This has been followed up recently by some papers by Burman et al. [29, 31, 27], that explore further the link between Nitsche's and the Augmented Lagrangian methods for unilateral contact, obstacle, and interface problems with adhesive contact. A penalty-free Nitsche's method has been designed and studied by Burman et al. [30] for the scalar Signorini's unilateral contact problem; this method is an extension of the one studied by Burman [23] for the Dirichlet problem. It is combined with a non-conforming discretization based on Crouzeix–Raviart finite elements. Stability and optimal convergence rates in the broken H^1-norm are established. Very recently, the idea of Chouly & Hild [40] has been transposed in the context of the transport equation to enforce the discrete maximun principle by Burman & Ern [40]. Other extensions include complex multi-physics problems such as finite deformation thermomechanical contact by Seitz et al. [121], fluid-structure-contact interaction by Burman et al. [26], and the Stefan–Signorini problems by Claus et al. [26]. Finally, an abstract framework to derive Nitsche-based formulations for different (linear and nonlinear) boundary and interface problems, combined with a numerical study in the context of isogeometric approximation (IGA) has been provided by Hu et al. [26].

1.2 Viscoplastic fluids

Viscoplastic fluids belong to the family of non-Newtonian fluids and describe materials which behave like a rigid solid for stresses below a critical yield stress and flow like a viscous fluid otherwise. They stand out from other materials since the change of regime is due to stress,

Figure 1.2: Examples of applications of viscoplastic fluids.

contrary to other phenomena due to temperature variations. Viscoplastic fluids are of interest in applications encountered in civil and material engineering and in the food, petroleum, and biological industries, see Figure 1.2 for some illustrations.

The notion of viscoplasticity can be traced back to Bingham [15] in 1922, where experimental and theoretical data were presented to study the complex behavior of some flowing materials. This seminal work opened the door to a new branch of physics, called rheology, to study the relationship between stress and strain rates in materials capable of flowing. The Bingham model specifies a constitutive relation with a von Mises criterion based on a threshold on the norm of the deviatoric part of the stress tensor, as introduced in this context by Oldroyd in 1947 [112]. Such a relatively simple model turns out to be sufficient to reproduce relevant behaviors in several practical situations. For recent reviews on yield stress fluids and their applications, we refer the reader to the work of Balmforth et al. [8] and Coussot [53].

1.2.1 Mathematical model

The mathematical formulation of Bingham flow models rests on variational inequalities, and their analysis has been developed by Mosolov & Miasnikov [106, 107, 108] for pipe flows and more generally by Duvaut & Lions [66]; see also the book of Fuchs & Seregin [74] and the references therein for the mathematical analysis and the book of Glowinski et al. [78] for the numerical analysis of variational inequalities. The expected regularity of the solution is still an open question, but it seems unreasonable to hope for a high regularity.

Let $\Omega \subset \mathbb{R}^d$, $d \geq 2$, denote an open, bounded, connected subset of $\mathbb{R}^d$ with a Lipschitz boundary. Given an external force field $\boldsymbol{f} : \Omega \to \mathbb{R}^d$ and considering, for simplicity, homogeneous Dirichlet boundary conditions, the Bingham flow model consists of looking for the total symmetric stress tensor field $\boldsymbol{\sigma}_{\mathrm{tot}} : \Omega \to \mathbb{R}^{d\times d}_{\mathrm{s}}$ and the velocity field $\boldsymbol{u} : \Omega \to \mathbb{R}^d$ such that

$$\begin{aligned} \nabla\cdot\boldsymbol{\sigma}_{\mathrm{tot}} + \boldsymbol{f} &= \boldsymbol{0} \qquad && \text{in } \Omega, \\ \nabla\cdot\boldsymbol{u} &= 0 && \text{in } \Omega, \\ \boldsymbol{u} &= \boldsymbol{0} && \text{on } \partial\Omega, \end{aligned} \tag{1.28}$$

and the constitutive relation

$$\begin{cases} \boldsymbol{\sigma} = 2\mu\nabla_{\mathrm{s}}\boldsymbol{u} + \sqrt{2}\sigma_0\dfrac{\nabla_{\mathrm{s}}\boldsymbol{u}}{|\nabla_{\mathrm{s}}\boldsymbol{u}|_{\ell^2}} & \text{for } |\boldsymbol{\sigma}|_{\ell^2} > \sqrt{2}\sigma_0, \\ \nabla_{\mathrm{s}}\boldsymbol{u} = \boldsymbol{0} & \text{for } |\boldsymbol{\sigma}|_{\ell^2} \leq \sqrt{2}\sigma_0, \end{cases} \tag{1.29}$$

where the deviatoric part $\boldsymbol{\sigma}$ of the total stress tensor $\boldsymbol{\sigma}_{\mathrm{tot}}$ and the symmetric velocity gradient $\nabla_{\mathrm{s}}\boldsymbol{u}$ are defined as follows:

$$\boldsymbol{\sigma} = \boldsymbol{\sigma}_{\mathrm{tot}} - \frac{1}{d}\mathtt{tr}(\boldsymbol{\sigma}_{\mathrm{tot}})\boldsymbol{I}_d, \qquad \nabla_{\mathrm{s}}\boldsymbol{u} = \frac{1}{2}(\nabla\boldsymbol{u} + \nabla\boldsymbol{u}^{\mathrm{T}}), \tag{1.30}$$

and $\boldsymbol{I}_d$ is the identity tensor of $\mathbb{R}^{d\times d}$. Moreover, $\mu > 0$ and $\sigma_0 > 0$ denote, respectively, the shear viscosity and the shear yield stress, and the Frobenius norm of a tensor is defined as follows:

$$|\boldsymbol{\tau}|_{\ell^2} := (\boldsymbol{\tau} : \boldsymbol{\tau})^{\frac{1}{2}} = \left(\sum_{i,j=1}^{d} \tau_{ij}^2 \right)^{\frac{1}{2}} \qquad \forall \boldsymbol{\tau} \in \mathbb{R}^{d\times d}. \tag{1.31}$$

The region where $|\boldsymbol{\sigma}|_{\ell^2} > \sqrt{2}\sigma_0$ is called the yielded zone and corresponds to liquid behavior, whereas the region where $|\boldsymbol{\sigma}|_{\ell^2} \leq \sqrt{2}\sigma_0$ is called the unyielded zone and corresponds to solid behavior. The yield surface where $|\boldsymbol{\sigma}|_{\ell^2} = \sqrt{2}\sigma_0$ separates the two regions. The yield surface is not known a priori, and its prediction is an important aspect of viscoplastic flow simulation.

Remark 1.7 (Yield stress)**.** *In the literature, the yield stress is sometimes defined as* $\tilde{\sigma}_0 := \sqrt{2}\sigma_0$*, and in certain cases, the Frobenius norm is defined as* $(\frac{1}{2}\boldsymbol{\tau} : \boldsymbol{\tau})^{\frac{1}{2}}$*. The present choice is just one possibility for the definition of* σ_0*.*

As in the previous section, let $L^2(\Omega)$ denote the space of square-integrable functions over Ω and let us set $\boldsymbol{L}^2(\Omega) := L^2(\Omega;\mathbb{R}^d)$. We also consider the space $L^2(\Omega;\mathbb{R}^{d\times d}_s)$ composed of square-integrable tensor-valued functions taking symmetric values. The inner product in all spaces is denoted $(\cdot,\cdot)_\Omega$ and the associated norm $\|\cdot\|_\Omega$. Let $\boldsymbol{H}^1(\Omega) := H^1(\Omega;\mathbb{R}^d)$, $\boldsymbol{H}^{\frac{1}{2}}(\partial\Omega) := H^{\frac{1}{2}}(\partial\Omega;\mathbb{R}^d)$ and let $\gamma_{\partial\Omega} : \boldsymbol{H}^1(\Omega) \to \boldsymbol{H}^{\frac{1}{2}}(\partial\Omega)$ be the classical trace map acting componentwise. Let us consider the following subspace where a zero-trace of the velocity on the boundary of the domain is specified:

$$\boldsymbol{H}^1_0(\Omega) := \{\boldsymbol{v} \in \boldsymbol{H}^1(\Omega) \mid \gamma_{\partial\Omega}(\boldsymbol{v}) = \boldsymbol{0}\}, \tag{1.32}$$

and the subspace of velocities with zero divergence

$$\boldsymbol{V}_0(\Omega) := \{\boldsymbol{v} \in \boldsymbol{H}^1_0(\Omega) \mid \nabla\cdot\boldsymbol{v} = 0\}. \tag{1.33}$$

Let us now introduce the dissipation potential $H : \mathbb{R}^{d\times d}_s \to \mathbb{R}$ such that

$$H(\boldsymbol{d}) = \mu|\boldsymbol{d}|^2_{\ell^2} + \sqrt{2}\sigma_0|\boldsymbol{d}|_{\ell^2} \qquad \forall \boldsymbol{d} \in \mathbb{R}^{d\times d}_s. \tag{1.34}$$

The first term on the right-hand side of (1.34) evaluated with $\boldsymbol{d} = \nabla_{\mathrm{s}}\boldsymbol{u}$ represents the viscous dissipation potential and the second term the plastic dissipation potential. Note that due to the latter term, the classical derivative of H is not well defined when $\boldsymbol{d} = \boldsymbol{0}$, and we need to consider a generalized concept of differentiation for convex functions, called the sub-differential (see Figure 1.3)

$$\partial H(\boldsymbol{d}) = \left\{ \boldsymbol{\tau} \in \mathbb{R}^{d\times d}_s \mid H(\boldsymbol{e}) - H(\boldsymbol{d}) \geq \boldsymbol{\tau} : (\boldsymbol{e} - \boldsymbol{d}) \quad \forall \boldsymbol{e} \in \mathbb{R}^{d\times d}_s \right\}. \tag{1.35}$$

Let us briefly prove that the constitutive relation (1.29) is equivalent to $\boldsymbol{\sigma} \in \partial H(\nabla_{\mathrm{s}}\boldsymbol{u})$. The identification of the sub-differential $\partial H(\boldsymbol{d})$ can be decomposed in two cases: when $\boldsymbol{d} \neq \boldsymbol{0}$, it reduces to a single element which is computed using the usual derivative. Instead, when $\boldsymbol{d} = \boldsymbol{0}$, we use the definition (1.35) to infer that $\boldsymbol{\sigma} \in \partial H(\boldsymbol{0})$ if and only if

$$H(\boldsymbol{e}) - H(\boldsymbol{0}) = \mu|\boldsymbol{e}|^2_{\ell^2} + \sqrt{2}\sigma_0|\boldsymbol{e}|_{\ell^2} \geq \boldsymbol{\sigma} : \boldsymbol{e} \qquad \forall \boldsymbol{e} \in \mathbb{R}^{d\times d}_s. \tag{1.36}$$

Applying the Cauchy-Schwarz inequality, we can see that a sufficient condition for $\boldsymbol{\sigma} \in \partial H(\boldsymbol{0})$ is $|\boldsymbol{\sigma}|_{\ell^2} \leq \sqrt{2}\sigma_0$. This is also a necessary condition. Indeed, let us take $\boldsymbol{e} = c\boldsymbol{\sigma}/|\boldsymbol{\sigma}|_{\ell^2}$, with $c > 0$ an arbitrary constant in (1.36), then we obtain $\mu c + \sqrt{2}\sigma_0 \geq |\boldsymbol{\sigma}|_{\ell^2}$, and the expected result follows by letting $c \to 0^+$. Hence, it follows that for all $\boldsymbol{d} \in \mathbb{R}^{d\times d}_s$,

$$\partial H(\boldsymbol{d}) = \begin{cases} \left\{ 2\mu\boldsymbol{d} + \sqrt{2}\sigma_0 \dfrac{\boldsymbol{d}}{|\boldsymbol{d}|_{\ell^2}} \right\} & \text{for } \boldsymbol{d} \neq \boldsymbol{0}, \\ \left\{ \boldsymbol{\tau} \mid |\boldsymbol{\tau}|_{\ell^2} \leq \sqrt{2}\sigma_0 \right\} & \text{for } \boldsymbol{d} = \boldsymbol{0}. \end{cases} \tag{1.37}$$

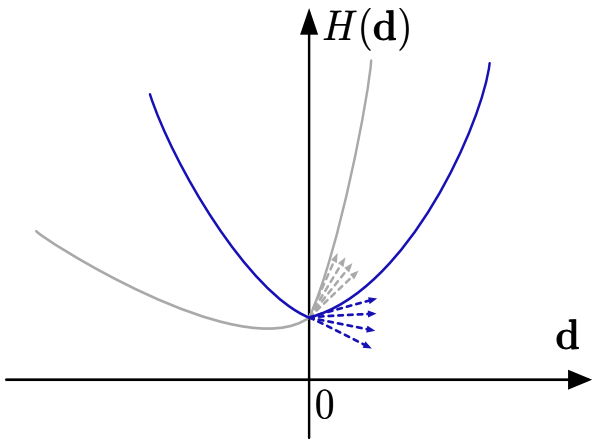

Figure 1.3: Schematic representation of the sub-differential for a functional with $\mathbf{0} \notin \partial H(\mathbf{0})$ (gray line) and a functional with $\mathbf{0} \in \partial H(\mathbf{0})$ (blue line). Arrows represent the elements in $\partial H(\mathbf{0})$.

Let us now consider the weak formulation of (1.28)-(1.29) and let us assume that $\boldsymbol{f} \in \boldsymbol{L}^2(\Omega)$. Since we have $(\mathtt{tr}(\boldsymbol{\sigma}_{\rm tot})\boldsymbol{I}_d, \nabla_{\rm s}\boldsymbol{v})_\Omega = 0$ for all $\boldsymbol{v} \in \boldsymbol{V}_0(\Omega)$ since $\nabla{\cdot}\boldsymbol{v} = 0$, we infer that $(\boldsymbol{\sigma}_{\rm tot}, \nabla_{\rm s}\boldsymbol{v})_\Omega = (\boldsymbol{\sigma}, \nabla_{\rm s}\boldsymbol{v})_\Omega$ for all $\boldsymbol{v} \in \boldsymbol{V}_0(\Omega)$. Hence, the weak formulation of (1.28)-(1.29) is:

$$\begin{cases} \text{Find } \boldsymbol{u} \in \boldsymbol{V}_0(\Omega) \text{ such that} \\ (\boldsymbol{\sigma}, \nabla_{\rm s}\boldsymbol{v})_\Omega = (\boldsymbol{f}, \boldsymbol{v})_\Omega \quad \forall \boldsymbol{v} \in \boldsymbol{V}_0(\Omega), \\ \boldsymbol{\sigma} \in \partial H(\nabla_{\rm s}\boldsymbol{u}). \end{cases} \tag{1.38}$$

Remark 1.8 (Mixed formulation)**.** *We can also look for $\boldsymbol{u} \in \boldsymbol{H}^1_0(\Omega)$, without the divergence constraint embedded in the trial and test spaces. Let*

$$L^2_0(\Omega) := \left\{ q \in L^2(\Omega) \mid \int_\Omega q = 0 \right\}$$

be the space composed of square-integrable functions with zero mean in the domain. Owing to de Rham's Theorem, the first equation in (1.38) *holds true if and only if there exists $p \in L^2_0(\Omega)$ such that $(\boldsymbol{\sigma}, \nabla_{\rm s}\boldsymbol{v})_\Omega - (p, \nabla{\cdot}\boldsymbol{v})_\Omega = (\boldsymbol{f}, \boldsymbol{v})_\Omega$ for all $\boldsymbol{v} \in \boldsymbol{H}^1_0(\Omega)$. Therefore,* (1.38) *is equivalent to: Find $(\boldsymbol{u}, p) \in \boldsymbol{H}^1_0(\Omega) \times L^2_0(\Omega)$ such that*

$$\begin{aligned} (\boldsymbol{\sigma}, \nabla_s\boldsymbol{v})_\Omega - (p, \nabla{\cdot}\boldsymbol{v})_\Omega = (\boldsymbol{f}, \boldsymbol{v})_\Omega \qquad & \forall \boldsymbol{v} \in \boldsymbol{H}^1_0(\Omega), \\ (q, \nabla{\cdot}\boldsymbol{u})_\Omega = 0 \qquad & \forall q \in L^2_0(\Omega), \end{aligned} \tag{1.39}$$

together with $\boldsymbol{\sigma} \in \partial H(\nabla_s\boldsymbol{u})$. The total stress tensor is then given by $\boldsymbol{\sigma}_{\rm tot} = \boldsymbol{\sigma} - p\boldsymbol{I}_d$, i.e., we have $p = -\frac{1}{d}\mathtt{tr}(\boldsymbol{\sigma}_{\rm tot})$. The system (1.39) *is called the mixed formulation, whereas the first equation in* (1.38) *is called the primal formulation.*

It is well-known that the velocity field solving (1.28)-(1.29) is the unique minimizer in $\boldsymbol{V}_0(\Omega)$ of the following energy functional:

$$\boldsymbol{u} = \underset{\boldsymbol{v} \in \boldsymbol{V}_0(\Omega)}{\arg\min} \{ (H(\nabla_{\rm s}\boldsymbol{v}), 1)_\Omega - (\boldsymbol{f}, \boldsymbol{v})_\Omega \}. \tag{1.40}$$

The existence and uniqueness of the velocity field satisfying (1.40) relies on standard results of convex analysis, see the book of Glowinski [76, Chapter 1, Theorem 4.1 and Lemma 4.1]. Note however that the stress tensor $\boldsymbol{\sigma}$ is not uniquely defined in the solid region where $\nabla_s\boldsymbol{u} = \mathbf{0}$.

Proposition 1.9 (Variational inequality)**.** *The minimizer of* (1.40) *is the unique solution in* $\boldsymbol{V}_0(\Omega)$ *of the variational inequality*

$$2\mu(\nabla_s \boldsymbol{u}, \nabla_s(\boldsymbol{v}-\boldsymbol{u}))_\Omega + (h_p(\nabla_s \boldsymbol{v}) - h_p(\nabla_s \boldsymbol{u}), 1)_\Omega \geq (\boldsymbol{f}, \boldsymbol{v}-\boldsymbol{u})_\Omega. \qquad \forall \boldsymbol{v} \in \boldsymbol{V}_0(\Omega), \tag{1.41}$$

with the plastic dissipation potential such that $h_p(\boldsymbol{d}) = \sqrt{2}\sigma_0 |\boldsymbol{d}|_{\ell^2}$ *for all* $\boldsymbol{d} \in \mathbb{R}^{d\times d}_s$.

Proof. See the book of Glowinski [76]. □

1.2.2 Augmented Lagrangian algorithm

The numerical simulation of viscoplastic fluids is extremely challenging because of the lack of smoothness in the constitutive relation between the stress and the strain rate tensors. Moreover, the yield surface, which separates the solid region (or unyielded region) from the flowing region (or yielded region), is not known a priori. In addition, the stress field is not unique in the solid region.

The numerical methods used for viscoplastic flow simulations over the past three decades can be classified into two groups. The first approach hinges on introducing a small artificial parameter in the constitutive relation, thereby replacing solid zones by flowing zones with a very high viscosity, as in the work by Bercovier & Engelman [14] or Papanastasiou [114]. The advantage is that the regularized equations become differentiable and are suitable for Newtonian fluid solvers. Nonetheless, this benefit comes at the expense of difficulties in accurately capturing the yield surface. The second approach is based on introducing an augmented Lagrangian and using a steepest descent method of Uzawa-type to solve the problem. Augmented Lagrangian methods have been introduced by Hestenes [89] and by Powell [115] for nonlinear constrained minimization problems and have been successfully used in the context of Bingham flow models and nonlinear mechanics by Fortin & Glowinski [72], and by Glowinski & Le Tallec [77]. The work by Saramito & Roquet [118, 117] demonstrated the effectivity of the approach, combined with adaptive finite element techniques, to accurately capture the yield surface in various settings, see also the works by Wang [128] and more recently Zhang [132]. Despite the need for introducing two additional tensor fields (a proxy for the strain rate tensor and the corresponding tensor-valued Lagrange multiplier), Augmented Lagrangian methods have progressively emerged over the last decade as the method of choice to simulate viscoplastic flows. For a recent review, we refer the reader to the paper of Saramito & Wachs [119]. We also mention the recent interior-point methods combined with second-order cone programming considered by Bleyer et al. [16, 17].

The minimization problem (1.40) can be tackled by decomposition-coordination methods so as to decouple the nonlinearity from the velocity field. To this purpose, an auxiliary field $\boldsymbol{\gamma} \in L^2(\Omega; \mathbb{R}^{d\times d}_s)$ is introduced and the equality $\boldsymbol{\gamma} = \nabla_s \boldsymbol{u}$ is enforced by means of the Lagrange multiplier $\boldsymbol{\sigma} \in L^2(\Omega; \mathbb{R}^{d\times d}_s)$ (which turns out to be indeed the deviatoric stress tensor) together with a least-squares penalty term. Let us set

$$X(\Omega) := \boldsymbol{V}_0(\Omega) \times L^2(\Omega; \mathbb{R}^{d\times d}_s) \times L^2(\Omega; \mathbb{R}^{d\times d}_s). \tag{1.42}$$

The augmented Lagrangian is defined as $\mathcal{L} : X(\Omega) \to \mathbb{R}$ such that

$$\mathcal{L}(\boldsymbol{u}, \boldsymbol{\gamma}, \boldsymbol{\sigma}) := (H(\boldsymbol{\gamma}), 1)_\Omega + (\boldsymbol{\sigma}, \nabla_s \boldsymbol{u} - \boldsymbol{\gamma})_\Omega + \alpha \|\nabla_s \boldsymbol{u} - \boldsymbol{\gamma}\|^2_\Omega - (\boldsymbol{f}, \boldsymbol{u})_\Omega, \tag{1.43}$$

where $\alpha > 0$ is the augmentation parameter. The triplet $(\boldsymbol{u}, \boldsymbol{\gamma}, \boldsymbol{\sigma}) \in X(\Omega)$ is a saddle-point of the Lagrangian $\mathcal{L}$, that is to say

$$\mathcal{L}(\boldsymbol{u}, \boldsymbol{\gamma}, \boldsymbol{\tau}) \leq \mathcal{L}(\boldsymbol{u}, \boldsymbol{\gamma}, \boldsymbol{\sigma}) \leq \mathcal{L}(\boldsymbol{v}, \boldsymbol{\delta}, \boldsymbol{\sigma}) \qquad \forall (\boldsymbol{v}, \boldsymbol{\delta}, \boldsymbol{\tau}) \in X(\Omega), \tag{1.44}$$

if and only if $\boldsymbol{\gamma} = \nabla_s \boldsymbol{u}$ and the pair $(\boldsymbol{u}, \boldsymbol{\sigma})$ solves (1.38).

In this thesis, we will resort to the Alternating Direction Method of Multipliers (ADMM), originally introduced by Glowinski & Marrocco [79] and Gabay & Mercier [75], to solve the

discrete variational inequalities of viscoplasticity. The convergence rate to be expected with the ADMM is of the order of $O(1/n)$, where n is the iteration number, see He & Yuan [87]. Recent advances leading to faster convergence rates include the accelerated ADMM from Treskatis et al. [125] and the ADMM with variable step sizes from Bartels & Milicevic [9]. For a review on the ADMM and other steepest-descent methods for Augmented Lagrangian methods, we refer the reader to the book of Glowinski [76]. The so-called ALG2 method from Fortin & Glowinski [72] and Glowinski & Le Tallec [77] is an Uzawa-type iterative method that, at each step, minimizes first the augmented Lagrangian $\mathcal{L}$ jointly with respect to the pair $(\boldsymbol{u}, \boldsymbol{\gamma})$ and then updates the Lagrange multiplier $\boldsymbol{\sigma}$. The idea in the ADMM is that the joint minimization is replaced by a successive minimization with respect to $\boldsymbol{\gamma}$ and then to $\boldsymbol{u}$. This method is presented in Algorithm 2.

Algorithm 2 Bingham vector flows: ADMM in continuous form

1: Choose $\boldsymbol{u}^0 \in \boldsymbol{V}_0(\Omega)$ and $\boldsymbol{\sigma}^0 \in L^2(\Omega; \mathbb{R}^{d\times d}_s)$
2: Choose $\epsilon > 0$, set $R^0 = \infty$ and $n = 0$
3: **while** $R^n > \epsilon$ **do**
4: ***Step 1:*** Given $(\boldsymbol{u}^n, \boldsymbol{\sigma}^n) \in \boldsymbol{V}_0(\Omega) \times L^2(\Omega; \mathbb{R}^{d\times d}_s)$, define $\boldsymbol{\gamma}^{n+1} \in L^2(\Omega; \mathbb{R}^{d\times d}_s)$ such that:

$$\boldsymbol{\gamma}^{n+1} := \begin{cases} \dfrac{1}{2(\alpha+\mu)} \left(|\boldsymbol{\theta}^n|_{\ell^2} - \sqrt{2}\sigma_0 \right) \dfrac{\boldsymbol{\theta}^n}{|\boldsymbol{\theta}^n|_{\ell^2}} & \text{if } |\boldsymbol{\theta}^n|_{\ell^2} > \sqrt{2}\sigma_0, \\ \boldsymbol{0} & \text{if } |\boldsymbol{\theta}^n|_{\ell^2} \leq \sqrt{2}\sigma_0. \end{cases} \tag{1.45}$$

where $\boldsymbol{\theta}^n := \boldsymbol{\sigma}^n + 2\alpha\nabla_{\mathrm{s}}\boldsymbol{u}^n$.
5: ***Step 2:*** Seek $\boldsymbol{u}^{n+1} \in \boldsymbol{V}_0(\Omega)$ solving

$$2\alpha(\nabla_s \boldsymbol{u}^{n+1}, \nabla_s \boldsymbol{v})_\Omega = (\boldsymbol{f}, \boldsymbol{v})_\Omega - (\boldsymbol{\sigma}^n - 2\alpha\boldsymbol{\gamma}^{n+1}, \nabla_{\mathrm{s}}\boldsymbol{v})_\Omega \qquad \forall \boldsymbol{v} \in \boldsymbol{V}_0(\Omega). \tag{1.46}$$

6: ***Step 3:*** Update the Lagrange multiplier $\boldsymbol{\sigma}^{n+1} \in L^2(\Omega; \mathbb{R}^{d\times d}_s)$:

$$\boldsymbol{\sigma}^{n+1} := \boldsymbol{\sigma}^n + 2\alpha(\nabla_{\mathrm{s}}\boldsymbol{u}^{n+1} - \boldsymbol{\gamma}^{n+1}). \tag{1.47}$$

7: Evaluate the residual:

$$R^{n+1} := \left(\|\boldsymbol{\sigma}^{n+1} - \boldsymbol{\sigma}^n\|^2_\Omega + \alpha^2 \|\nabla_s(\boldsymbol{u}^{n+1} - \boldsymbol{u}^n)\|^2_\Omega \right)^{\frac{1}{2}}. \tag{1.48}$$

8: $n = n + 1$
9: **end while**

Remark 1.10 (Variants for decomposition-coordination)**.** *It is possible to consider other decompositions for the nonlinear convex minimization problem* (1.28)-(1.29)*, e.g., one where the auxiliary variable is only used for the plastic dissipation potential. It is observed by Dean et al. [55] that both formulations lead to fairly comparable computational costs. Therefore, we only consider in what follows the method where the auxiliary variable is used for the whole dissipation potential.*

Remark 1.11 (Critical point)**.** *It is readily verified that Step 1 of Algorithm 2 amounts to*

$$\partial_{\boldsymbol{\gamma}} \mathcal{L}(\boldsymbol{u}^n, \boldsymbol{\gamma}^{n+1}, \boldsymbol{\sigma}^n) = 0,$$

that Step 2 amounts to

$$\partial_{\boldsymbol{u}} \mathcal{L}(\boldsymbol{u}^{n+1}, \boldsymbol{\gamma}^{n+1}, \boldsymbol{\sigma}^n) = 0,$$

and that Step 3 amounts to

$$(\boldsymbol{\sigma}^{n+1} - \boldsymbol{\sigma}^n, \boldsymbol{\tau})_\Omega = 2\alpha \partial_{\boldsymbol{\sigma}} \mathcal{L}(\boldsymbol{u}^{n+1}, \boldsymbol{\gamma}^{n+1}, \boldsymbol{\sigma}^{n+1})[\boldsymbol{\tau}] \qquad \forall \boldsymbol{\tau} \in L^2(\Omega, \mathbb{R}^{d\times d}_s).$$

Thus, if the ADMM convergences, it reaches a critical point of the Lagrangian.

Remark 1.12 (Mixed formulation)**.** *Note that, alternatively, in Step 2 of Algorithm 2, we can solve the following mixed formulation: Find* $(\boldsymbol{u}^{n+1}, p^{n+1}) \in \boldsymbol{H}^1_0(\Omega) \times L^2_0(\Omega)$ *s.t.* $\forall (\boldsymbol{v}, q) \in \boldsymbol{H}^1_0(\Omega) \times L^2_0(\Omega)$*:*

$$\begin{aligned} 2\alpha(\nabla_s \boldsymbol{u}^{n+1}, \nabla_s \boldsymbol{v})_\Omega - (p^{n+1}, \nabla\cdot\boldsymbol{v})_\Omega &= (\boldsymbol{f}, \boldsymbol{v})_\Omega - (\boldsymbol{\sigma}^n - 2\alpha\boldsymbol{\gamma}^{n+1}, \nabla_s \boldsymbol{v})_\Omega, \\ (q, \nabla\cdot\boldsymbol{u}^{n+1})_\Omega &= 0. \end{aligned}$$

Proposition 1.13 (Identification of the limit)**.** *The ADMM from Algorithm 2 converges and at convergence reaches a saddle-point of the Lagrangian* $\mathcal{L}$*.*

Proof. For the convergence proof, see the work by Fortin & Glowinski [72]. Let the triplet $(\boldsymbol{u}, \boldsymbol{\gamma}, \boldsymbol{\sigma})$ be the limit. One possibility to prove that $(\boldsymbol{u}, \boldsymbol{\gamma}, \boldsymbol{\sigma})$ is a saddle-point of the Lagrangian $\mathcal{L}$ is to observe that it is a critical point and invoke convexity arguments, as observed in Remark 1.11. One can also proceed directly as follows. Step 3 implies that the constraint $\boldsymbol{\gamma} = \nabla_{\mathrm{s}}\boldsymbol{u}$ introduced by the augmented Lagrangian method is accomplished, so that we replace $\boldsymbol{\gamma}$ by $\nabla_{\mathrm{s}}\boldsymbol{u}$. Next, it suffices to cancel out in (1.46) the terms having the augmentation parameter α to recover the momentum conservation equation

$$(\boldsymbol{\sigma}, \nabla_s \boldsymbol{v})_\Omega = (\boldsymbol{f}, \boldsymbol{v})_\Omega \qquad \forall \boldsymbol{v} \in \boldsymbol{V}_0(\Omega).$$

Finally, in Step 1, the constitutive equation is recovered as follows: *a)* Replace $\boldsymbol{\gamma} = \nabla_{\mathrm{s}}\boldsymbol{u}$ to obtain

$$\nabla_{\mathrm{s}}\boldsymbol{u} := \begin{cases} \dfrac{1}{2(\alpha+\mu)}\left(1 - \dfrac{\sqrt{2}\sigma_0}{|\boldsymbol{\theta}|_{\ell^2}}\right)\boldsymbol{\theta} & \text{if } |\boldsymbol{\theta}|_{\ell^2} > \sqrt{2}\sigma_0, \\ \mathbf{0} & \text{if } |\boldsymbol{\theta}|_{\ell^2} \le \sqrt{2}\sigma_0. \end{cases}$$

b) Apply $|\cdot|_{\ell^2}$ and rearrange terms to find $|\boldsymbol{\theta}|_{\ell^2} = 2(\alpha+\mu)|\nabla_{\mathrm{s}}\boldsymbol{u}|_{\ell^2} + \sqrt{2}\sigma_0$.
c) If $|\boldsymbol{\theta}|_{\ell^2} > \sqrt{2}\sigma_0$, use the proportionality between $\nabla_{\mathrm{s}}\boldsymbol{u}$ and $\boldsymbol{\theta}$ to obtain

$$\boldsymbol{\theta} = \frac{\nabla_{\mathrm{s}}\boldsymbol{u}}{|\nabla_{\mathrm{s}}\boldsymbol{u}|_{\ell^2}}|\boldsymbol{\theta}|_{\ell^2} = 2(\alpha+\mu)\nabla_{\mathrm{s}}\boldsymbol{u} + \frac{\sqrt{2}\sigma_0\nabla_{\mathrm{s}}\boldsymbol{u}}{|\nabla_{\mathrm{s}}\boldsymbol{u}|_{\ell^2}}.$$

d) Finally, use that $\boldsymbol{\theta} = \boldsymbol{\sigma} + 2\alpha\nabla_{\mathrm{s}}\boldsymbol{u}$, cancel out terms and rearrange terms. If $|\boldsymbol{\theta}|_{\ell^2} \ge \sqrt{2}\sigma_0$, $\nabla_{\mathrm{s}}\boldsymbol{u} = \mathbf{0}$, so that we have $|\boldsymbol{\sigma}|_{\ell^2} \le \sqrt{2}\sigma_0$. □

1.3 Introduction to Hybrid High-Order (HHO) methods

In this section, we briefly present the Hybrid High-Order (HHO) methods introduced for linear elasticity by Di Pietro & Ern [59] and for linear diffusion problems by Di Pietro et al. [60]. HHO methods have been extended to other linear PDEs, such as advection-diffusion by Di Pietro et al. [57] and Stokes by Di Pietro et al. [61], and to nonlinear PDEs, such as Leray–Lions by Di Pietro & Droniou [56], steady incompressible Navier–Stokes by Di Pietro & Krell [63], nonlinear elasticity by Botti et al. [20], elastoplasticity with small deformations by Abbas et al. [2], and hyperelasticity with finite deformations by Abbas et al. [1]. HHO methods are formulated in terms of face unknowns which are polynomials of arbitrary order $k \ge 0$ on each mesh face and in terms of cell unknowns which are polynomials of order $l \ge 0$, with $l \in \{k, k \pm 1\} \cap \mathbb{N}$, in each mesh cell. The cell unknowns can be eliminated locally by static condensation leading to a global transmission problem posed solely in terms of the face unknowns. HHO methods offer various assets:

- They support polyhedral meshes;
- They lead to a local conservation principle in each mesh cell;
- Their construction is independent of the space dimension;

- They offer robustness in various regimes (dominant advection, incompressible elasticity and flows);
- They offer attractive computational costs owing to the compactness of the face-based stencil (compared to FE methods) and to the fact that the number of local degrees of freedom scales to k^{d-1} (as opposed to k^d for discontinuous Galerkin methods).

Lowest-order HHO methods are closely related to the Hybrid Finite Volume method by Eymard et al. [69], the Compatible Discrete Operator framework by Bonelle & Ern [19], and the Mimetic Finite Difference methods by Kuznetsov et al. [98], Brezzi et al [22], see also the unifying viewpoint devised by Droniou et al. [64]. HHO methods have been bridged by Cockburn et al. [51] to the Hybridizable Discontinuous Galerkin (HDG) methods devised by Cockburn et al. [52] and to the nonconforming Virtual Element (ncVEM) methods devised by Ayuso de Dios et al. [7].

The goal of this section is to outline the main principles for devising a HHO discretization. For the sake of simplicity, we consider a diffusion model with homogeneous Dirichlet boundary conditions:

$$\begin{aligned} -\Delta u &= f \quad \text{in } \Omega, \\ u &= 0 \quad \text{on } \partial\Omega, \end{aligned} \tag{1.49}$$

where $u \in H^1_0(\Omega) = \{v \in H^1(\Omega) \mid \gamma_{\partial\Omega}(v) = 0\}$, $\gamma_{\partial\Omega} : H^1(\Omega) \to H^{\frac{1}{2}}(\partial\Omega)$ is the classical trace map, $f \in L^2(\Omega)$ is the forcing term, and Ω is for simplicity a polygon/polyhedron in $\mathbb{R}^d$, $d \in \{2, 3\}$. The weak formulation of the model problem (1.49) is as follows:

$$\begin{cases} \text{Find } u \in H^1_0(\Omega) \text{ such that} \\ a(u, w) = \ell(w), \qquad \forall w \in H^1_0(\Omega), \end{cases} \tag{1.50}$$

with the bilinear and linear forms

$$a(v, w) = (\nabla v, \nabla w)_\Omega, \qquad \ell(w) = (f, w)_\Omega. \tag{1.51}$$

1.3.1 Discrete setting

Let $(\mathcal{T}_h)_{h>0}$ be a mesh sequence where for all $h > 0$ the mesh $\mathcal{T}_h$ is composed of nonempty disjoint cells such that $\overline{\Omega} = \bigcup_{T\in\mathcal{T}_h} \overline{T}$. The mesh cells are conventionally open subsets in $\mathbb{R}^d$ which can have a polygonal/polyhedral shape with straight edges (if $d = 2$) and planar faces (if $d = 3$). The mesh sequence $(\mathcal{T}_h)_{h>0}$ is assumed to be shape-regular (in the sense of Di Pietro & Ern [59]). In a nutshell, each mesh $\mathcal{T}_h$ admits a matching simplicial submesh $\mathfrak{S}_h$ having locally equivalent length scales, and the mesh sequence $(\mathfrak{S}_h)_{h>0}$ is shape-regular in the sense of Ciarlet [49]. Examples of polygonal meshes supported by HHO methods are shown in Figure 1.4. The mesh-size is denoted $h = \max_{T\in\mathcal{T}_h} h_T$, with h_T the diameter of the cell T. A closed subset F of $\overline{\Omega}$ is called a mesh face if it is a subset with nonempty relative interior of some affine hyperplane H_F and if (i) either there are two distinct mesh cells $T_1(F), T_2(F) \in \mathcal{T}_h$ so that $F = \partial T_1(F) \cap \partial T_2(F) \cap H_F$ (and F is called an interface) (ii) or there is one mesh cell $T(F) \in \mathcal{T}_h$ so that $F = \partial T(F) \cap \Gamma \cap H_F$ (and F is called a boundary face). The mesh faces are collected in the set $\mathcal{F}_h$ which is further partitioned into the subset of interfaces $\mathcal{F}_h^i$ and the subset of boundary faces $\mathcal{F}_h^b$. For all $T \in \mathcal{T}_h$, $\mathcal{F}_{\partial T}$ is the collection of the mesh faces that are subsets of ∂T and $\boldsymbol{n}_T$ is the unit outward normal to T. Let S be a mesh cell or a mesh face, then $(\cdot, \cdot)_S$ denotes the $L^2(S)$-inner product and $\|\cdot\|_S$ the corresponding norm.

Let a polynomial degree $k \geq 0$ be fixed. For all $T \in \mathcal{T}_h$, the local space of degrees of freedom is defined as

$$\hat{U}_T^k := \mathbb{P}^k(T; \mathbb{R}) \times \mathbb{P}^k(\mathcal{F}_{\partial T}; \mathbb{R}), \tag{1.52}$$

where $\mathbb{P}^k(T; \mathbb{R})$ is the space of $d-$variate polynomials of total degree $\leq k$ on T, whereas $\mathbb{P}^k(\mathcal{F}_{\partial T}; \mathbb{R})$ is the space of piecewise $(d-1)-$variate polynomials of total degree $\leq k$ on the

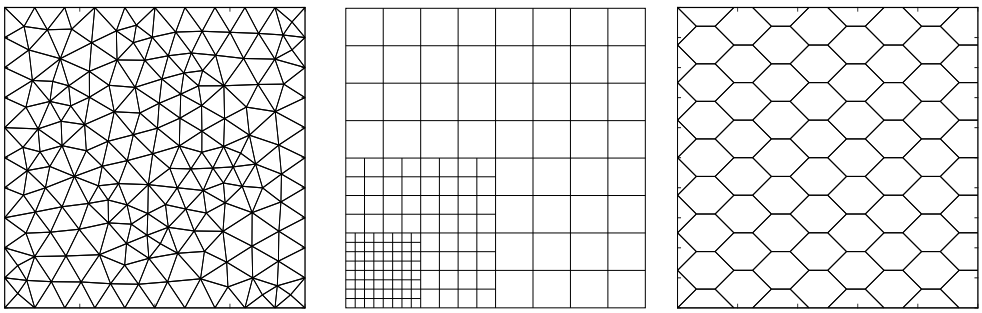

Figure 1.4: Examples of polygonal meshes: triangular, nonmatching (with local refinement producing hanging nodes) and hexagonal-dominant meshes.

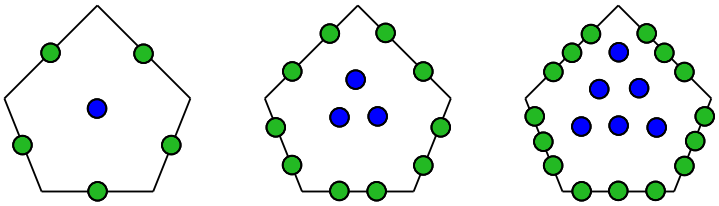

Figure 1.5: Schematical representation of the face (green) and cell (blue) degrees of freedom in a pentagonal mesh cell for $k = 0, 1, 2$. Note that the degrees of freedom are polynomial coefficients and do not have any "physical" positioning in the actual element.

faces of T, see Figure 1.5. Following (1.52), a generic element $\hat{v}_T \in \hat{U}_T^k$ is a pair $\hat{v}_T = (v_T, v_{\partial T})$ with $v_T \in \mathbb{P}^k(T;\mathbb{R})$ and $v_{\partial T} \in \mathbb{P}^k(\mathcal{F}_{\partial T};\mathbb{R})$.

Remark 1.14 (Cell unknowns)**.** *HHO methods allow for some variations in the degree ℓ of the polynomial associated with the cells, since we can take $\ell \in \{k-1, k, k+1\} \cap \mathbb{N}$, see Cockburn et al. [51] for more details.*

1.3.2 Local reconstruction and stabilization operators

We define a local reconstruction operator $R_T^{k+1} : \hat{U}_T^k \to \mathbb{P}^{k+1}(T;\mathbb{R})$ such that, for all $\hat{v}_T = (v_T, v_{\partial T}) \in \hat{U}_T^k$, $R_T^{k+1}(\hat{v}_T) \in \mathbb{P}^{k+1}(T;\mathbb{R})$ solves the following equation:

$$(\nabla R_T^{k+1}(\hat{v}_T), \nabla w)_T = (\nabla v_T, \nabla w)_T + (v_{\partial T} - v_T, \boldsymbol{n}_T \cdot \nabla w)_{\partial T} \quad \forall w \in \mathbb{P}^{k+1}(T;\mathbb{R}), \tag{1.53}$$

together with the condition $(R_T^{k+1}(\hat{v}_T), 1)_T = (v_T, 1)_T$. This corresponds to solving a local and well-posed Neumann problem, see Figure 1.6 for a schematic representation with constant polynomials on the faces and in the cell. The local reconstruction operator defined in (1.53) is not stable in the sense that $\nabla R_T^{k+1}(\hat{v}_T) = 0$ does not imply that $v_T = v_{\partial T} = cte$. In fact, we introduce an additional local stabilization operator $S_{\partial T}^k : \hat{U}_T^k \to \mathbb{P}^k(\mathcal{F}_{\partial T};\mathbb{R})$ to penalize the difference between $v_{\partial T}$ and $v_{T|\partial T}$ in a least-squares sense. The operator $S_{\partial T}^k$ is defined such that, for all $\hat{v}_T = (v_T, v_{\partial T}) \in \hat{U}_T^k$, we have

$$S_{\partial T}^k(\hat{v}_T) := \pi_{\partial T}^k(v_{\partial T} - R_T^{k+1}(\hat{v}_T)_{|\partial T}) - \pi_T^k(v_T - R_T^{k+1}(\hat{v}_T))_{|\partial T}, \tag{1.54}$$

where π_T^k and $\pi_{\partial T}^k$ denote the L^2-orthogonal projectors onto $\mathbb{P}^k(T;\mathbb{R})$ and $\mathbb{P}^k(\mathcal{F}_{\partial T};\mathbb{R})$, respectively.

We use the two above operators to formulate the local bilinear form $\hat{a}_T$ on $\hat{U}_T^k \times \hat{U}_T^k$, that mimics locally the exact local bilinear form $(\nabla v, \nabla w)_T$ from (1.51):

$$\hat{a}_T(\hat{v}_T, \hat{w}_T) := (\nabla R_T^{k+1}(\hat{v}_T), \nabla R_T^{k+1}(\hat{w}_T))_T + (\eta_{\partial T} S_{\partial T}^k(\hat{v}_T), S_{\partial T}^k(\hat{w}_T))_{\partial T}, \tag{1.55}$$

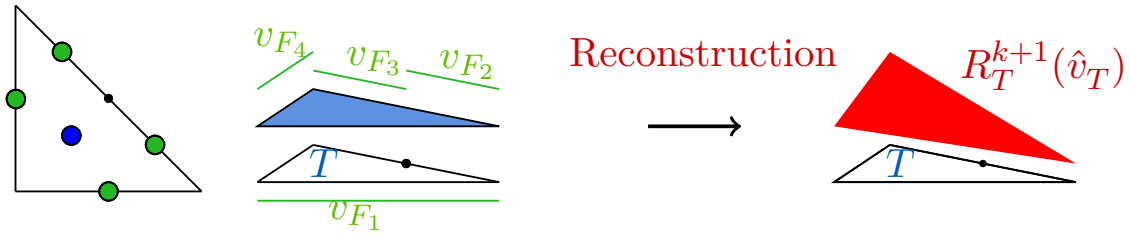

Figure 1.6: Schematic representation of the local reconstrunction from $\hat{v}_T$ in a quadrangular mesh cell (a triangle with a hanging node depicted in black) for constant polynomials.

where $\eta_{\partial T}$ is the piecewise constant function on ∂T such that $\eta_{\partial T}|_F = h_F^{-1}$ for all $F \in \mathcal{F}_{\partial T}$. Let us briefly outline the stability and boundedness properties associated with the bilinear form $\hat{a}_T$. We equip the discrete space $\hat{U}_T^k$ with the following H^1-like seminorm:

$$|\hat{v}_T|_{\hat{U}_T^k}^2 := \|\nabla v_T\|_T^2 + \|\eta_{\partial T}^{\frac{1}{2}}(v_{\partial T} - v_T)\|_{\partial T}^2 \qquad \forall \hat{v}_T = (v_T, v_{\partial T}) \in \hat{U}_T^k. \tag{1.56}$$

Lemma 1.15 (Stability and boundedness)**.** *There is a real number $\rho > 0$, independent of h, such that, for all $T \in \mathcal{T}_h$ and all $\hat{v}_T \in \hat{U}_T^k$,*

$$\rho^{-1}|\hat{v}_T|_{\hat{U}_T^k}^2 \le ||\nabla R_T^{k+1}(\hat{v}_T)||_T^2 + \|\eta_{\partial T}^{\frac{1}{2}} S_{\partial T}(\hat{v}_T)\|_{\partial T}^2 \le \rho |\hat{v}_T|_{\hat{U}_T^k}^2. \tag{1.57}$$

The parameter ρ only depends on the mesh regularity and the polynomial degree.

Proof. See the proof by Di Pietro et al. [60, Lemma 4]. □

The first inequality in (1.57) implies the coercivity of the bilinear form $\hat{a}_T$ on $\hat{U}_T^k$, up to constant arguments. In particular, $\hat{a}_T(\hat{v}_T, \hat{v}_T) = 0$ implies that both functions v_T and $v_{\partial T}$ are constant functions taking the same value.

The design of the two operators R_T^{k+1} and $S_{\partial T}^k$ is also motivated by the polynomial invariance in $\mathbb{P}^{k+1}(T;\mathbb{R})$ stated in the next lemma.

Lemma 1.16 (Polynomial invariance)**.** *Let $\hat{I}_T^k : H^1(T) \to \hat{U}_T^k$ be the local reduction operator such that $\hat{I}_T^k(v) = (\pi_T^k(v), \pi_{\partial T}^k(v_{|\partial T})) \in \hat{U}_T^k$, for all $v \in H^1(T)$ and all $T \in \mathcal{T}_h$. Then we have*

$$R_T^{k+1}(\hat{I}_T^k(v)) = E_T^{k+1}(v) \qquad \forall v \in H^1(T), \tag{1.58}$$

where $E_T^{k+1} : H^1(T) \to \mathbb{P}^{k+1}(T;\mathbb{R})$ is the standard local elliptic projector such that, for all $v \in H^1(T)$,

$$(\nabla E_T^{k+1}(v) - v, \nabla w)_T = 0, \qquad \forall w \in \mathbb{P}^{k+1}(T;\mathbb{R}), \qquad (E_T^{k+1}(v) - v, 1)_T = 0. \tag{1.59}$$

The second important result on polynomial invariance is

$$S_{\partial T}^k(\hat{I}_T^k(p)) = 0 \qquad \forall p \in \mathbb{P}^{k+1}(T;\mathbb{R}). \tag{1.60}$$

Proof. See the proof by Di Pietro et al. [60]. Let us briefly prove (1.58). Let $v \in H^1(T)$. Let us use the definition of the local reconstruction and reduction operators to infer that, for all $w \in \mathbb{P}^{k+1}(T;\mathbb{R})$,

$$\begin{aligned}(\nabla R_T^{k+1}(\hat{I}_T^k(v)), \nabla w)_T &= -(\pi_T^k(v), \nabla\cdot(\nabla w))_T + (\pi_{\partial T}^k(v), \boldsymbol{n}_T\cdot\nabla w)_{\partial T} \\ &= -(v, \nabla\cdot(\nabla w))_T + (v, \boldsymbol{n}_T\cdot\nabla w)_{\partial T} \\ &= (\nabla v, \nabla w)_T,\end{aligned}$$

where we integrated by parts and used that $\nabla\cdot(\nabla w) \in \mathbb{P}^{k-1}(T;\mathbb{R}) \subset \mathbb{P}^k(T;\mathbb{R})$ as well as $\boldsymbol{n}_T\cdot\nabla w \in \mathbb{P}^k(\mathcal{F}_{\partial T};\mathbb{R})$. Since $(R_T^{k+1}(\hat{I}_T^k(v)), 1)_T = (\pi_T^k(v), 1)_T = (v, 1)_T = (E_T^{k+1}(v), 1)_T$, we conclude the proof of (1.58). □

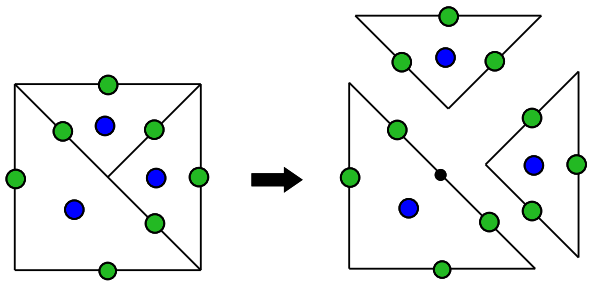

Figure 1.7: Example of global patching of the face unknowns (blue) with a nonmatching mesh (a hanging node is depicted in black).

Remark 1.17 (Link with HDG)**.** *The HDG-like stabilization operator is* $S_{\partial T}^k(\hat{v}_T) := \pi_{\partial T}^k(v_T - v_{\partial T})$*, instead of* (1.54)*. However, this operator does not lead to* (1.60) *on* $\mathbb{P}^{k+1}(T;\mathbb{R})$*, but only on* $\mathbb{P}^k(T;\mathbb{R})$*. However, this operator leads to optimmal convergence whenever the cell unknowns are of degree* $\ell = k+1$*, as shown in the HDG setting by Lehrenfeld & Schöberl [102] and by Oikawa [111].*

1.3.3 HHO discretization of a model elliptic problem

The global discrete space is obtained by assembling the local spaces $\hat{U}_T^k$ and forcing the interface DOFs to be single-valued (see Figure 1.7):

$$\hat{U}_h^k := U_{\mathcal{T}_h}^k \times U_{\mathcal{F}_h}^k, \tag{1.61}$$

where

$$U_{\mathcal{T}_h}^k := \left\{ v_{\mathcal{T}_h} \in L^2(\mathcal{T}_h) \mid v_{\mathcal{T}_h|T} \in \mathbb{P}^k(T;\mathbb{R}), \quad \forall T \in \mathcal{T}_h \right\}, \tag{1.62}$$

$$U_{\mathcal{F}_h}^k := \left\{ v_{\mathcal{F}_h} \in L^2(\mathcal{F}_h) \mid v_{\mathcal{F}_h|F} \in \mathbb{P}^k(\mathcal{F}_{\partial T};\mathbb{R}), \quad \forall F \in \mathcal{F}_h \right\}. \tag{1.63}$$

We enforce strongly the homogeneous Dirichlet boundary conditions by considering the subspace $\hat{U}_{h,0}^k := U_{\mathcal{T}_h}^k \times U_{\mathcal{F}_h,0}^k$, with

$$U_{\mathcal{F}_h,0}^k = \left\{ v_{\mathcal{F}_h} \in U_{\mathcal{F}_h}^k \mid v_F = 0 \quad \forall F \in \mathcal{F}_h^b \right\}. \tag{1.64}$$

The HHO discretization of the elliptic model problem (1.50) is as follows:

$$\begin{cases} \text{Find } \hat{u}_h \in \hat{U}_{h,0}^k \text{ such that} \\ a_h(\hat{u}_h, \hat{v}_h) = \hat{\ell}_h(\hat{v}_h) \qquad \forall \hat{v}_h \in \hat{U}_{h,0}^k, \end{cases} \tag{1.65}$$

where $\hat{a}_h$ is the global version of the local bilinear form $\hat{a}_T$. The bilinear form $\hat{a}_h$ and the source term contribution $\hat{\ell}_h$ are simply built by elementwise assembly as follows:

$$\begin{aligned} a_h(\hat{w}_h, \hat{v}_h) &= \sum_{T\in\mathcal{T}_h} \hat{a}_T(\hat{w}_T, \hat{v}_T) \quad \text{on } \hat{U}_{h,0}^k \times \hat{U}_{h,0}^k, \\ \hat{\ell}_h(v_h) &= \sum_{T\in\mathcal{T}_h} (f, v_T)_T \qquad \text{on } \hat{U}_{h,0}^k, \end{aligned} \tag{1.66}$$

Here, for a generic element $\hat{v}_h \in \hat{U}_{h,0}^k$, and a mesh cell $T \in \mathcal{T}_h$, we denote $\hat{v}_T = (v_T, v_{\partial T}) \in \hat{U}_T^k$ the local component of $\hat{v}_h$ associated with T. Let us now address the error estimate. Recall the notation $a \lesssim b$ defined above Theorem 1.2.

Theorem 1.18 (Energy error-estimate)**.** *Let $k \geq 0$. Let $u \in H_0^1(\Omega)$ be the solution to the model problem* (1.49) *and assume the additional regularity $u \in H^{k+2}(\Omega)$. Let $\hat{u}_h \in \hat{U}_{h,0}^k$ be the unique solution to the discrete problem* (1.65)*. Then, the following energy-norm error estimate holds true:*

$$\|\hat{I}_h^k(u) - \hat{u}_h\|_{\hat{U}_{h,0}^k} \lesssim h^{k+1}|u|_{H^{k+2}(\Omega)}. \tag{1.67}$$

with the global reduction map $\hat{I}_h^k : H_0^1(\Omega) \to \hat{U}_{h,0}^k$ such that $\hat{I}_h^k(u)_{|T} = \hat{I}_T^k(u) \in \hat{U}_T^k$, for all $T \in \mathcal{T}_h$, and the global norm on $\hat{U}_{h,0}^k$ such that

$$\|\hat{v}_h\|_{\hat{U}_{h,0}^k}^2 = \sum_{T\in\mathcal{T}_h} |\hat{v}_T|_{\hat{U}_T^k}^2, \tag{1.68}$$

with the local seminorm $|\cdot|_{\hat{U}_T^k}$ defined in (1.56)*.*

Proof. See the proof by Di Pietro et al. [60]. □

We say that elliptic regularity holds true if for all $g \in L^2(\Omega)$, the unique solution $z \in H_0^1(\Omega)$ of $(\nabla z, \nabla v)_\Omega = (g, v)_\Omega$ for all $v \in H_0^1(\Omega)$, satisfies $\|z\|_{H^2(\Omega)} \lesssim \|g\|_{L^2(\Omega)}$.

Theorem 1.19 (L^2-error estimate)**.** *Let the assumptions of Theorem 1.28 and elliptic regularity hold true. Then the following holds true: For all $k \geq 1$,*

$$\left(\sum_{T\in\mathcal{T}_h} \|\pi_T^k(u) - u_T\|_T^2\right)^{\frac{1}{2}} \lesssim h^{k+2}|u|_{H^{k+2}(\Omega)}, \tag{1.69}$$

and for $k = 0$, assuming that $f \in H^1(\Omega)$,

$$\left(\sum_{T\in\mathcal{T}_h} \|\pi_T^0(u) - u_T\|_T^2\right)^{\frac{1}{2}} \lesssim h^2\|f\|_{H^1(\Omega)}. \tag{1.70}$$

Proof. See the proof by Di Pietro et al. [60]. □

1.4 Outline of the thesis

This thesis is composed of 4 chapters. Chapters 2 to 4, summarized below, are presented in a fashion to allow for an independent reading. Finally, conclusions are drawn in Chapter 5.

Chapter 2) Nitsche's method for diffusion and Signorini problems In this chapter, we present two primal methods to weakly discretize (linear) Dirichlet and (nonlinear) Signorini boundary conditions in elliptic model problems. Both methods support polyhedral meshes with nonmatching interfaces and are based on a combination of the Hybrid High-Order (HHO) method and Nitsche's method. We extend the ideas of Chouly & Hild [41] for conforming finite elements to hybrid discretization methods and we derive optimal H^1-error estimates of order h^{k+1}, if face polynomials of order $k \geq 0$ are used together with cell polynomials of order $(k+1)$ (recall that the cell unknowns are eliminated locally by static condensation). As a preliminary step in our analysis, we estimate the HHO error in the case of linear Dirichlet boundary conditions that are weakly enforced by means of Nitsche's method. This is also a novel result in the analysis of HHO methods. The main difficulties associated with the mathematical analysis are i) the non-conformity of the HHO approximation, (ii) the bound on the consistency error, and (iii) the appropriate design of Nitsche's contact terms from face/cell unknowns in order to preserve optimal convergence properties. Since HHO methods involve both cell unknowns and face unknowns, this leads to different formulations of Nitsche's consistency and penalty

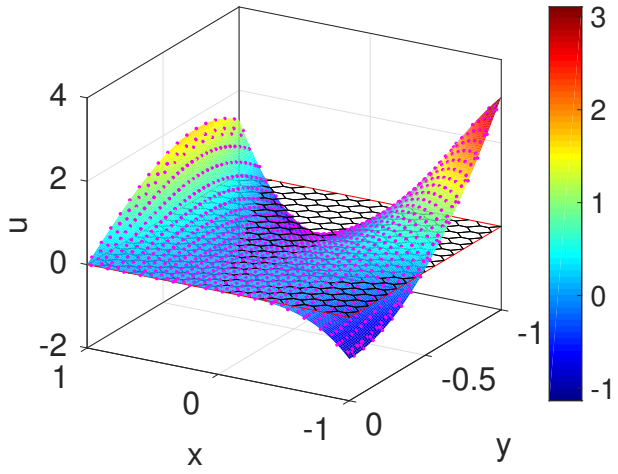

Figure 1.8: Signorini's exact solution for our numerical results from Chapter 2. The magenta dots represent the values of the numerical solution at the faces and cells barycenters of an hexagonal mesh (depicted in black). The contact boundary corresponds to the side $\{y = 0\}$.

terms, either using the trace of the cell unknowns (cell-based trace version) or using directly the face unknowns (face-based trace version). The face-based trace version uses equal order polynomials for cell and face unknowns, whereas the cell-based trace version uses cell unknowns of one order higher than face unknowns. The latter choice turns out to be the only one leading to theoretical optimal error estimates for Signorini's problem. For Dirichlet conditions, optimal error estimates are established for both versions. The key idea in the analysis, which is inspired from Burman & Ern [24] is to devise a local reconstruction operator without Dirichlet/contact faces contribution. Numerical results are presented for a test case with analytical solution to verify the theoretical predictions. The exact solution is depicted in Figure 2.6. Finally, although we do not exploit here the capability of hybrid discretization methods to support polyhedral meshes, we observe that the idea of using polyhedral meshes for contact problems has been advocated for instance by Wriggers et al. [131], where the authors use a Virtual Element method combined with either Lagrange multipliers or penalized formulations for contact problems. The work developed in this chapter has been submitted as the paper [36].

Chapter 3) Lowest-order adaptive method for antiplanar Bingham flows In Bingham pipe flow simulations (i.e., the antiplanar configuration where the velocity field is unidirectional), the velocity field is usually discretized using conforming Lagrange finite elements, see for instance the work by Saramito & Roquet [118, 117]. In contrast, we devise a hybrid lowest-order method for Bingham pipe flows, where the velocity is discretized by means of one unknown per mesh face and one unknown per mesh cell. The cell unknowns can be eliminated locally by static condensation. We consider the augmented Lagrangian method recalled in Section 1.2.2 to solve iteratively the variational inequalities resulting from the discrete Bingham problem. We use piecewise constant vector-valued fields for the auxiliary variable and the associated Lagrange multiplier. The advantage of considering hybrid discretization methods is twofold. First, these methods lead to local conservation properties at the cell level, whereas this conservation property is somewhat less local using nodal-based finite elements (typically, one needs to consider cell patches around mesh vertices, see, e.g., the work by Ern & Vohralík [67]). Second, and more importantly in the present context, hybrid discretization methods support polygonal/polyhedral meshes including cells with hanging nodes. The use of such meshes is exploited here when performing local mesh adaptation, including local refinement near the yield surface and possibly agglomeration-based coarsening in unyielded regions. For earlier works on agglomeration-based coarsening, we refer, e.g., to the work by Bassi et al. [11, 10] and

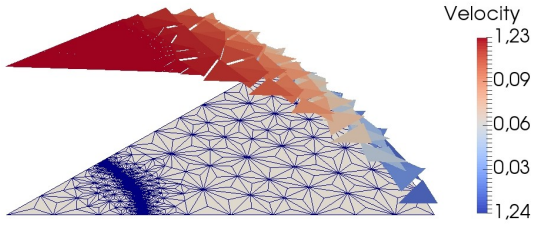

Figure 1.9: Discrete velocity and adapted mesh for the circular cross-section test case from Chapter 3.

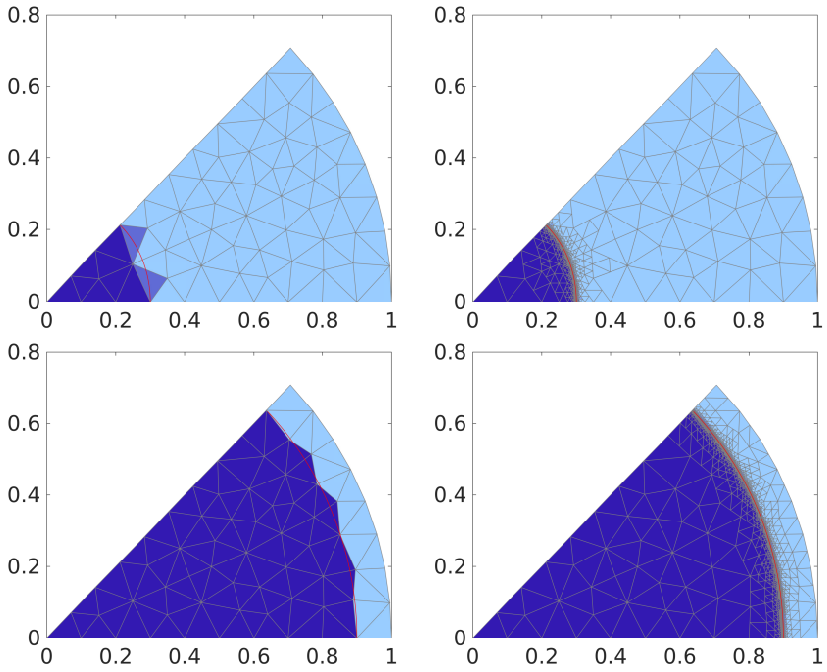

Figure 1.10: Uniform (left) and 5th adaptive mesh (right) for the circular cross-section test case from Chapter 3: the Bingham numbers are $Bi = 0.3$ (top) and $Bi = 0.9$ (bottom).

the references therein. We present numerical results in pipes with a circular cross-section, see Figures 1.9 and 1.10, and with an eccentric annulus cross-section, see Figure 1.11, for different Bingham numbers. The work developed in this chapter has been pusblished in the paper [35].

Chapter 4) Extension to Bingham vector flows In the general case of Bingham vector flows with an incompressibility constraint on the velocity field, one usually employs either inf-sup stable mixed finite elements as in the work of Saramito & Roquet [117] or stabilized equal-order finite element pairs as in the work of Latché & Vola [100]. The novelty in this chapter is that we devise a hybrid discetization method for Bingham vector flows, where the velocity is discretized by means of cell and face unknowns, which are polynomials of degree $k \geq 0$. We consider the lowest-order method with $k = 0$, where the face unknowns are constant polynomials but the cell unknowns are linear polynomials (so as to control the rigid-body motions). We also consider a higher-order method with $k = 1$, where the face and the cell unknowns are both linear polynomials. One difficulty with the higher-order method is the need to introduce quadrature rules in the formulation, mainly for the tensor variables. Another novelty is that we now need to account for the divergence-free constraint on the velocity, which

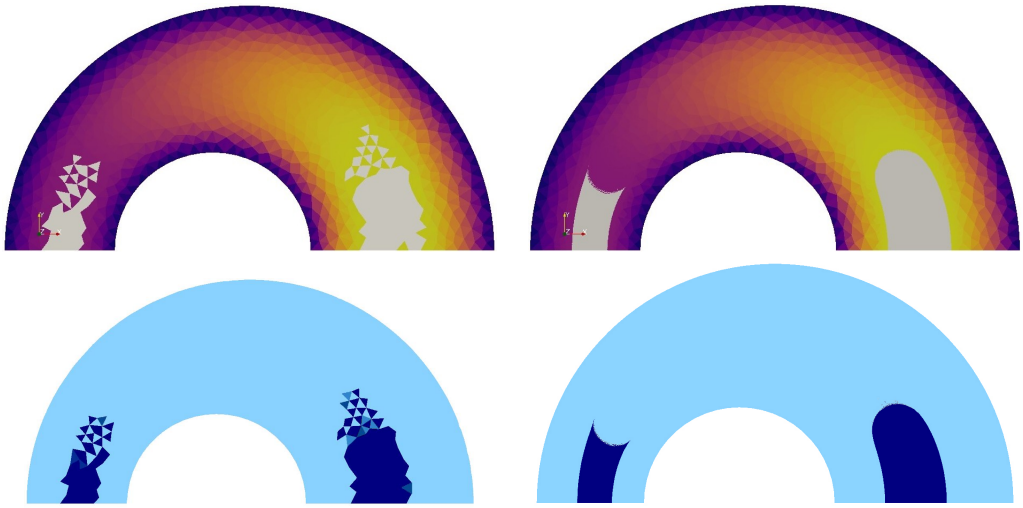

Figure 1.11: Initial (left) and 6th adaptive (right) meshes for the eccentric annulus cross-section test case from Chapter 3: discrete velocity (top) and stress colormap in the vicinity of the yield stress (bottom).

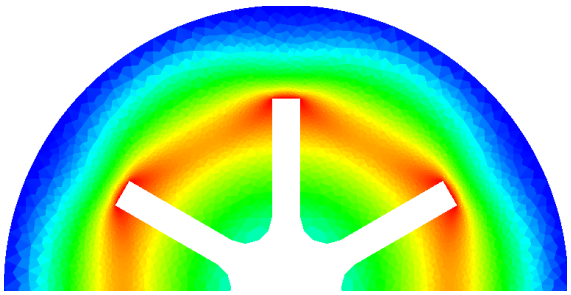

Figure 1.12: Velocity magnitude for the vane-in cup geometry test case from Chapter 4.

we do by introducing a discrete pressure. We consider the augmented Lagrangian method from Section 1.2.2 to solve the variational inequalities resulting from the discrete Bingham vector problem. The resulting linear Stokes-like system in the ADMM is solved, after static condensation, with discrete face-based velocities and cell-wise constant pressures. Additional variables as the auxiliary variable and the associated stress are discretized only with cell unknowns. Numerical results are presented for two test cases. The first one considers a confined flow in the well-known lid-driven cavity problem. Various results in this test case are available in the literature. The second test case is a confined flow in, this time in a Couette geometry with a vane tool. We are interested in this problem since there exist relatively recent experimental results challenging the assumption of a cylindrical thin layer of the material flowing around the vane tool at low velocity, see the work by Ovarlez et al. [113] for a further discussion on this topic. From our numerical simulations, we observe close agreement with the results from the above reference. The work developed in this chapter is intended under preparation for the paper [34].

Chapter 2

Nitsche's method for Dirichlet conditions and Signorini contact

Contents

In this chapter, we devise optimally convergent Hybrid High-Order (HHO) methods combined with Nitsche's method to impose boundary conditions in a natural fashion by means of a boundary penalty technique. We apply these methods to the Poisson model problem with linear Dirichlet boundary conditions and also to the nonlinear contact boundary conditions of Signorini's problem. Using Nitsche's technique, the contact conditions are treated in a weak sense without introducing Lagrange multipliers.

Before considering contact, and to exemplify the main ideas in the devising and analysis of Nitsche-HHO, we first deal with the linear case of Dirichlet boundary conditions. For both Dirichlet and Signorini conditions, the formulation of Nitsche's terms in combination with HHO methods leads to different schemes according to the choice of the unknown to be used in the writing of the boundary terms, namely: (i) the face unknown, for which we design an equal-order method, where the face and cell unknowns are of the same order; (ii) the trace

of the cell unknown, for which we need a mixed-order method, where the cell unknowns are of one order higher than the face unknowns. In what follows, we refer to these variants as the face-based and the cell-based trace versions of Nitsche-HHO, respectively. The devising of the cell version elaborates on the idea of modifying the local reconstruction operator, as proposed in [25] in the different context of geometrically unfitted methods.The difference with the usual HHO reconstruction operator is to drop the contribution of those boundary faces located on the part of the boundary treated by Nitsche's method. A third variant is to employ the trace of the reconstruction, but it will not be considered since it does not appear to bring further advantages. Our main results are on the one hand Theorem 2.12 and Theorem 2.17 which establish the optimal convergence of Nitsche-HHO for Dirichlet conditions, using face and cell versions, respectively, and on the other hand Theorem 2.21 which establishes the optimal convergence of the cell version of Nitsche-HHO for Signorini conditions. As for Nitsche-FEM, our proofs are valid in two and three dimensions and any polynomial degree $k \geq 0$, and do not require any extra assumption apart from suitable Sobolev regularity of the exact solution. To our knowledge, this is the first optimal error estimate of such generality for Signorini conditions using polyhedral methods. The face version can also be extended to Signorini conditions and indeed delivers optimally convergent results according to our simulations.

This chapter is organized as follows. We briefly recall the model problems in Section 2.1 as well as their conforming Nitsche-FEM discretization. We introduce the discrete setting in Section 2.2, and we also recall some useful analysis tools. Then, we present the Nitsche-HHO methods for Dirichlet conditions in Section 2.3 and in Section 2.4, where we use the face-based trace version and the cell-based trace version, respectively. In Section 2.5, we extend the cell-based trace discretization of Nitsche-HHO to Signorini conditions. For each section, we present numerical results of test cases with analytical solutions.

2.1 Model problems

The goal of this section is to briefly present the two model problems to be discretized by means of the Nitsche-HHO method. Let Ω be a polygon/polyhedron in $\mathbb{R}^d$, $d \in \{2, 3\}$, with boundary $\partial\Omega$ and unit outward normal vector $\boldsymbol{n}$. The scalar product in the Lebesgue space $L^2(\Omega)$ is denoted by $(\cdot,\cdot)_\Omega$. We denote by $H^s(\Omega)$, $s > 0$, the Sobolev spaces with scalar product (resp. norm) denoted by $(\cdot,\cdot)_{s,\Omega}$ (resp. $\|\cdot\|_{s,\Omega}$). Let $f : \Omega \to \mathbb{R}$ be a source term; we assume that $f \in L^2(\Omega)$. For a smooth enough function $v \in H^s(\Omega)$, $s > \frac{3}{2}$, we use in the entire chapter the following notation:

$$\sigma_n(v) = \boldsymbol{n}\cdot\nabla v \qquad \text{on } \partial\Omega. \tag{2.1}$$

2.1.1 Dirichlet conditions

We consider a partition of the boundary $\partial\Omega$ into two mutually disjoint subsets:

$$\partial\Omega = \overline{\Gamma_D} \cup \overline{\Gamma_N}, \tag{2.2}$$

where the boundary condition is respectively a Dirichlet and a Neumann condition. We assume that Γ_D has nonempty relative interior. Let us consider Dirichlet data $g_D \in H^{\frac{1}{2}}(\partial\Omega)$ restricted to Γ_D and Neumann data $g_N \in L^2(\Gamma_N)$. The Poisson model problem with mixed Dirichlet–Neumann conditions reads as follows:

$$\begin{aligned} \Delta u + f &= 0 && \text{in } \Omega, \\ u &= g_D && \text{on } \Gamma_D, \\ \sigma_n(u) &= g_N && \text{on } \Gamma_N. \end{aligned} \tag{2.3}$$

It is well-known that this problem is well-posed.

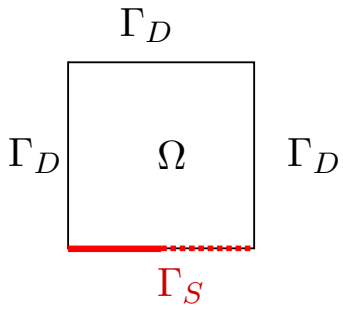

Figure 2.1: Boundary setting for Signorini's unilateral contact problem. The contact boundary is represented by a straight red line where contact is happening ($u = 0, \sigma_n(u) \leq 0$) and by a dashed red line otherwise ($u < 0, \sigma_n(u) = 0$).

The conforming Nitsche-FEM discretization of the model problem (2.3) is as follows:

$$\begin{cases} \text{Find } u_h \in V_h \text{ such that} \\ a_{\gamma\theta,h}(u_h, w_h) = \ell_{\gamma\theta,h}(w_h) \qquad \forall w_h \in V_h, \end{cases} \tag{2.4}$$

where $V_h := \{v_h \in C^0(\overline{\Omega}; \mathbb{R}) \mid v_{h|T} \in \mathbb{P}^k(T; \mathbb{R}); \forall T \in \mathcal{T}_h\}$, $k \geq 1$ is the polynomial degree, $\mathcal{T}_h$ is a member of a shape-regular sequence of meshes of Ω, and the bilinear and linear forms are defined as follows:

$$a_{\gamma\theta,h}(v_h, w_h) = (\nabla v_h, \nabla w_h)_\Omega - \int_{\Gamma_D} (\sigma_n(v_h) w_h + \theta v_h \sigma_n(w_h)) + \int_{\Gamma_D} \gamma v_h w_h, \tag{2.5a}$$

$$\ell_{\gamma\theta,h}(w_h) = (f, w_h)_\Omega - \int_{\Gamma_D} g_D \left(\theta \sigma_n(w_h) - \gamma w_h\right) + \int_{\Gamma_N} g_N w_h. \tag{2.5b}$$

Here, the user-dependent parameters are the symmetry parameter $\theta \in \{-1, 0, 1\}$ and the penalty parameter γ, that scales as $\gamma = \gamma_0 h^{-1}$ with γ_0 taken large enough to ensure coercivity (the minimum value depends on a discrete trace inequality and therefore on the shape-regularity of the mesh sequence and the polynomial degree k, see, e.g., [110, 123, 84]).

Remark 2.1. *The Nitsche-based FEM* (2.4) *encompasses symmetric and nonsymmetric variants depending upon the parameter θ. The symmetric case of [110] is recovered when $\theta = 1$. For the skew-symmetric variant $\theta = -1$, the well-posedness of the discrete formulation and the optimal convergence are preserved irrespectively of the value of the penalty parameter γ, that can even be taken as* 0 *(penalty-free Nitsche's method, see, e.g., [18, 23]). In the context of discontinuous Galerkin methods, such nonsymmetric variants are well-known as well (see, e.g., [58, Section 5.3.1]).*

2.1.2 Signorini's unilateral contact conditions

Let us now consider a partition of the boundary $\partial\Omega$ into three mutually disjoint subsets:

$$\Omega = \overline{\Gamma_D} \cup \overline{\Gamma_N} \cup \overline{\Gamma_S}, \tag{2.6}$$

where the boundary condition is respectively a Dirichlet, a Neumann, and Signorini's unilateral contact condition, see Figure 2.1. We assume that Γ_D has nonempty relative interior, and for simplicity, we consider a homogeneous Dirichlet boundary condition on Γ_D. The model problem reads as follows:

$$\Delta u + f = 0 \quad \text{in } \Omega, \tag{2.7a}$$
$$u = 0 \quad \text{on } \Gamma_D, \tag{2.7b}$$
$$\sigma_n(u) = g_N \quad \text{on } \Gamma_N, \tag{2.7c}$$

and the unilateral contact boundary conditions on Γ_S as follows:

$$u \le 0 \quad \text{on } \Gamma_S, \tag{2.8a}$$
$$\sigma_n(u) \le 0 \quad \text{on } \Gamma_S, \tag{2.8b}$$
$$u\sigma_n(u) = 0 \quad \text{on } \Gamma_S, \tag{2.8c}$$

It is well-known that the model problem (2.7)-(2.8) is well-posed (see, e.g., [80]).

The key idea to devise the Nitsche-FEM discretization of (2.7)-(2.8) is to reformulate Signorini conditions (2.8) as a single nonlinear equation on the normal flux $\sigma_n(u)$. For any real number x, let $[x]_{\mathbb{R}^-} := \min(x, 0)$ denotes its projection onto the closed convex subset $\mathbb{R}^- = (-\infty, 0]$. Let us recall from Lemma 1.3 (see also [54] and [37, Prop. 2.4]) that Signorini's unilateral contact conditions (2.8) are equivalent to

$$\sigma_n(u) = [\phi_\gamma(u)]_{\mathbb{R}^-}, \tag{2.9}$$

with the notation

$$\phi_\gamma(v) := \sigma_n(v) - \gamma v, \tag{2.10}$$

for any smooth function $v : \Omega \to \mathbb{R}$. This leads to the following conforming Nitsche-FEM discretization of the model problem (2.7)-(2.8) (see [38]):

$$\begin{cases} \text{Find } u_h \in V_{h,D} \text{ such that} \\ a_{\gamma\theta,h}(u_h; w_h) = \ell_{\gamma\theta,h}(w_h) \qquad \forall w_h \in V_{h,D}, \end{cases} \tag{2.11}$$

where $V_{h,D} := \{v_h \in V_h \mid v_{h|\Gamma_D} = 0\}$, V_h being defined above, and the semilinear and linear forms are defined as follows:

$$a_{\gamma\theta,h}(v_h; w_h) = (\nabla v_h, \nabla w_h)_\Omega - \int_{\Gamma_S} \frac{\theta}{\gamma}\sigma_n(v_h)\sigma_n(w_h) + \int_{\Gamma_S} \frac{1}{\gamma}\,[\phi_\gamma(v_h)]_{\mathbb{R}^-}\,\phi_{\theta\gamma}(w_h), \tag{2.12a}$$
$$\ell_{\gamma\theta,h}(w_h) = (f, w_h)_\Omega + \int_{\Gamma_N} g_N w_h, \tag{2.12b}$$

with $\phi_{\theta\gamma}(v) := \theta\sigma_n(v) - \gamma v$ (so that $\phi_{1\gamma} = \phi_\gamma$). Note that $a_{\gamma\theta,h}$ is nonlinear in its first argument owing to the weak enforcement of Signorini's condition. The user-dependent parameters θ and γ play the same role as in Section 2.1.1.

2.2 Discrete setting

In this section, we recall the basic notions concerning meshes and we restate some important functional inequalities to be used in the stability and error analysis of the various Nitsche-HHO methods.

2.2.1 Meshes

Let $(\mathcal{T}_h)_{h>0}$ be a mesh sequence, where for all $h > 0$, the mesh $\mathcal{T}_h$ is composed of nonempty disjoint cells such that $\overline{\Omega} = \bigcup_{T\in\mathcal{T}_h} \overline{T}$. The mesh cells are conventionally open subsets in $\mathbb{R}^d$, they can have a polygonal/polyhedral shape with straight edges (if $d = 2$) or planar faces (if $d = 3$). The mesh sequence $(\mathcal{T}_h)_{h>0}$ is assumed to be shape-regular in the sense of [59]. In a nutshell, each mesh $\mathcal{T}_h$ admits a matching simplicial submesh $\mathfrak{S}_h$ having locally equivalent length scales to those of $\mathcal{T}_h$, and the mesh sequence $(\mathfrak{S}_h)_{h>0}$ is shape-regular in the usual sense

of Ciarlet [49]. The meshsize is denoted $h = \max_{T\in\mathcal{T}_h} h_T$, with h_T the diameter of the cell T. A closed subset F of $\overline{\Omega}$ is called a mesh face if it is a subset with nonempty relative interior of some affine hyperplane H_F and if (i) either there are two distinct mesh cells $T_1(F), T_2(F) \in \mathcal{T}_h$ so that $F = \partial T_1(F) \cap \partial T_2(F) \cap H_F$ (and F is called an interface) (ii) or there is one mesh cell $T(F) \in \mathcal{T}_h$ so that $F = \partial T(F) \cap \Gamma \cap H_F$ (and F is called a boundary face). The mesh faces are collected in the set $\mathcal{F}_h$ which is further partitioned into the subset of interfaces $\mathcal{F}_h^i$ and the subset of boundary faces $\mathcal{F}_h^b$. For all $T \in \mathcal{T}_h$, $\mathcal{F}_{\partial T}$ is the collection of the mesh faces that are subsets of ∂T and $\boldsymbol{n}_T$ is the unit outward normal to T.

We use the symbol C to denote a generic constant whose value can change at each occurrence as long as it is uniform with respect to the mesh size; the value, which can change at each occurrence, depend on the mesh regularity and the underlying polynomial degree. We abbreviate as $a \lesssim b$ the inequality $a \le Cb$ with positive real numbers a, b and a constant $C > 0$, as above.

2.2.2 Analysis tools

Let us briefly state without proof four important technical results to be used in what follows: a discrete trace inequality on polynomials, a multiplicative trace inequality on H^1-functions, the Poincaré inequality on H^1-functions having zero mean-value and approximation properties of the L^2-orthogonal projection onto polynomials. The trace inequalities and the polynomial approximation error estimates are classical on meshes generated from a reference cell, whereas the Poincaré inequality is classical if the mesh cells are convex sets. On more general polyhedral meshes, we refer the reader to [58] and [68] for the proofs of the trace inequalities and the Poincaré inequality, respectively.

Lemma 2.2 (Discrete trace inequality)**.** *Let $k \ge 0$ be the polynomial degree. The following holds true:*

$$\|v_h\|_{\partial T} \le C_{\mathrm{dt}} h_T^{-\frac{1}{2}} \|v_h\|_T, \tag{2.13}$$

for all $T \in \mathcal{T}_h$ and all $v_h \in \mathbb{P}^k(T;\mathbb{R})$.

Lemma 2.3 (Multiplicative trace inequality)**.** *The following holds true:*

$$\|v\|_{\partial T} \le C_{\mathrm{mt}} \Big(h_T^{-\frac{1}{2}} \|v\|_T + h_T^{\frac{1}{2}} \|\nabla v\|_T \Big), \tag{2.14}$$

for all $T \in \mathcal{T}_h$ and all $v \in H^1(T)$.

Lemma 2.4 (Poincaré inequality)**.** *The following holds true:*

$$\|v\|_T \le C_{\mathrm{P}} h_T \|\nabla v\|_T, \tag{2.15}$$

for all $T \in \mathcal{T}_h$ and all $v \in H^1(T)$ such that $(v,1)_T = 0$.

Lemma 2.5 (Polynomial approximation)**.** *Let $k \ge 0$ be the polynomial degree. Let π_T^{k+1} denote the L^2-orthogonal projection onto $\mathbb{P}^{k+1}(T;\mathbb{R})$. Let $s > \frac{1}{2}$ and set $t := \min(k+1, s)$. The following holds true:*

$$\begin{aligned}\|v - \pi_T^{k+1}(v)\|_T + h_T^{\frac{1}{2}} \|v - \pi_T^{k+1}(v)\|_{\partial T} + h_T \|\nabla(v - \pi_T^{k+1}(v))\|_T \\ + h_T^{\frac{3}{2}} \|\nabla(v - \pi_T^{k+1}(v))\|_{\partial T} \le C_{\mathrm{app}}\, h_T^{1+t} |v|_{H^{1+t}(T)},\end{aligned} \tag{2.16}$$

for all $T \in \mathcal{T}_h$ and all $v \in H^{1+s}(T)$. The estimate (2.16) is optimal for $t = s = k+1$, in which case the right-hand side scales as $O(h_T^{k+2}|v|_{H^{k+2}(T)})$.

2.3 Dirichlet conditions with face-based traces

In this section, we devise and analyze the face-based trace version of the Nitsche-HHO method to approximate Dirichlet boundary conditions. We consider the face-based trace version with an equal order for the face and the cell unknowns. We assume that the meshes are compatible with the boundary partition $\partial\Omega = \overline{\Gamma_D} \cup \overline{\Gamma_N}$ from (2.2), which leads to the partition of boundary faces as $\mathcal{F}_h^b = \mathcal{F}_h^{b,D} \cup \mathcal{F}_h^{b,N}$ (with obvious notation). We first present the local reconstruction and stability operators which will be used for this method, then we define the corresponding discrete Nitsche-HHO formulation and prove its well-posedness. Finally we prove its optimal convergence.

2.3.1 Local reconstruction and stability operators

Let $k \geq 0$ be the polynomial degree. For all $T \in \mathcal{T}_h$, the local discrete space is

$$\hat{U}_T^k := \mathbb{P}^k(T;\mathbb{R}) \times \mathbb{P}^k(\mathcal{F}_{\partial T};\mathbb{R}), \tag{2.17}$$

where $\mathbb{P}^k(T;\mathbb{R})$ and $\mathbb{P}^k(\mathcal{F}_{\partial T};\mathbb{R})$ are the spaces spanned by the restrictions to T and $\mathcal{F}_{\partial T}$, respectively, of d-variate and piecewise $(d-1)$-variate polynomials of total degree $\leq k$. A generic element $\hat{v}_T \in \hat{U}_T^k$ is a pair $\hat{v}_T = (v_T, v_{\partial T})$ with $v_T \in \mathbb{P}^k(T;\mathbb{R})$ and $v_{\partial T} \in \mathbb{P}^k(\mathcal{F}_{\partial T};\mathbb{R})$.

For all $T \in \mathcal{T}_h$, we define the local reconstruction operator $R_T^{k+1} : \hat{U}_T^k \to \mathbb{P}^{k+1}(T;\mathbb{R})$ such that, for all $\hat{v}_T = (v_T, v_{\partial T}) \in \hat{U}_T^k$,

$$(\nabla R_T^{k+1}(\hat{v}_T), \nabla w)_T = (\nabla v_T, \nabla w)_T + (v_{\partial T} - v_T, \boldsymbol{n}_T \cdot \nabla w)_{\partial T} \quad \forall w \in \mathbb{P}^{k+1}(T;\mathbb{R}), \tag{2.18}$$

$$(R_T^{k+1}(\hat{v}_T), 1)_T = (v_T, 1)_T, \tag{2.19}$$

which leads to a local well-posed Neumann problem that is solved by inverting the local stiffness matrix in $\mathbb{P}^{k+1}(T;\mathbb{R})$. The local stabilization operator $S_{\partial T}^k : \hat{U}_T^k \to \mathbb{P}^k(\mathcal{F}_{\partial T};\mathbb{R})$ is used to penalize the difference between the face unknown $v_{\partial T}$ and the trace of the cell unknown $v_{T|\partial T}$ in a least-squares sense. The operator $S_{\partial T}^k$ is defined such that, for all $\hat{v}_T = (v_T, v_{\partial T}) \in \hat{U}_T^k$,

$$S_{\partial T}^k(\hat{v}_T) := \pi_{\partial T}^k(v_{\partial T} - R_T^{k+1}(\hat{v}_T)_{|\partial T}) - \pi_T^k(v_T - R_T^{k+1}(\hat{v}_T))_{|\partial T}, \tag{2.20}$$

where π_T^k and $\pi_{\partial T}^k$ denote the L^2-orthogonal projectors onto $\mathbb{P}^k(T;\mathbb{R})$ and $\mathbb{P}^k(\mathcal{F}_{\partial T};\mathbb{R})$, respectively. One readily verifies that $S_{\partial T}^k(\hat{v}_T) = 0$ whenever $v_{\partial T} = v_{T|\partial T}$ since $R_T^{k+1}(v_T, v_{T|\partial T}) = v_T$.

We use the two above operators to formulate the following local bilinear form $\hat{a}_T$ on $\hat{U}_T^k \times \hat{U}_T^k$ that mimics locally the exact local bilinear form $(\nabla v, \nabla w)_T$:

$$\hat{a}_T(\hat{v}_T, \hat{w}_T) := (\nabla R_T^{k+1}(\hat{v}_T), \nabla R_T^{k+1}(\hat{w}_T))_T + (\eta_{\partial T} S_{\partial T}^k(\hat{v}_T), S_{\partial T}^k(\hat{w}_T))_{\partial T}, \tag{2.21}$$

where $\eta_{\partial T}$ is the piecewise constant function on ∂T such that $\eta_{\partial T|F} = h_F^{-1}$, for all $F \in \mathcal{F}_{\partial T}$.

We equip the discrete space $\hat{U}_T^k$ with the following H^1-like seminorm:

$$|\hat{v}_T|_{\hat{U}_T^k}^2 := \|\nabla v_T\|_T^2 + \|\eta_{\partial T}^{\frac{1}{2}}(v_{\partial T} - v_{T|\partial T})\|_{\partial T}^2 \qquad \forall \hat{v}_T = (v_T, v_{\partial T}) \in \hat{U}_T^k, \tag{2.22}$$

so that $|\hat{v}_T|_{\hat{U}_T^k} = 0$ implies that $v_T = v_{\partial T} = cte$. Let us briefly outline the stability, boundedness, and polynomial invariance properties that motivate the design of the local operators R_T^{k+1} and $S_{\partial T}^k$. For the proofs, we refer the reader to [60].

Lemma 2.6 (Stability and boundedness)**.** *There is a real number $\rho > 0$, independent of h, such that, for all $T \in \mathcal{T}_h$ and all $\hat{v}_T \in \hat{U}_T^k$,*

$$\rho^{-1}|\hat{v}_T|_{\hat{U}_T^k}^2 \leq ||\nabla R_T^{k+1}(\hat{v}_T)||_T^2 + \|\eta_{\partial T}^{\frac{1}{2}} S_{\partial T}^k(\hat{v}_T)\|_{\partial T}^2 \leq \rho|\hat{v}_T|_{\hat{U}_T^k}^2. \tag{2.23}$$

The parameter ρ only depends on the mesh regularity and the polynomial degree. The first inequality in (2.23) *implies the coercivity of the bilinear form $\hat{a}_T$ on the one-dimensional subspace $\{\hat{v}_T \in \hat{U}_T^k;\ v_T = v_{\partial T} = c\}$.*

Proof. See [60, Lemma 4]. □

Lemma 2.7 (Polynomial invariance)**.** *Let $\hat{I}_T^k : H^1(T) \to \hat{U}_T^k$ be the local reduction operator such that $\hat{I}_T^k(v) = (\pi_T^k(v), \pi_{\partial T}^k(v_{|\partial T})) \in \hat{U}_T^k$, for all $v \in H^1(T)$ and all $T \in \mathcal{T}_h$. Then we have*

$$R_T^{k+1}(\hat{I}_T^k(v)) = E_T^{k+1}(v) \qquad \forall v \in H^1(T), \tag{2.24}$$

where $E_T^{k+1} : H^1(T) \to \mathbb{P}^{k+1}(T;\mathbb{R})$ is the standard local elliptic projector such that, for all $v \in H^1(T)$,

$$(\nabla(E_T^{k+1}(v) - v), \nabla w)_T = 0, \ \forall w \in \mathbb{P}^{k+1}(T;\mathbb{R}), \qquad (E_T^{k+1}(v) - v, 1)_T = 0. \tag{2.25}$$

Moreover the following holds true for the local stabilization operator:

$$S_{\partial T}^k(\hat{I}_T^k(p)) = 0 \qquad \forall p \in \mathbb{P}^{k+1}(T;\mathbb{R}). \tag{2.26}$$

Proof. See [60] or the sketch of the proof in Section 1.3.2. □

We will also need the following approximation result for the local elliptic projector and for the stabilization operator.

Lemma 2.8 (Approximation)**.** *Let $s > \frac{1}{2}$ and set $t := \min(k+1, s)$. There is a uniform constant C such that the following holds true for all $T \in \mathcal{T}_h$ and all $v \in H^{1+s}(T)$:*

$$\begin{aligned}\|v - E_T^{k+1}(v)\|_T + h_T^{\frac{1}{2}}\|v - E_T^{k+1}(v)\|_{\partial T} + h_T\|\nabla(v - E_T^{k+1}(v))\|_T \\ + h_T^{\frac{3}{2}}\|\nabla(v - E_T^{k+1}(v))\|_{\partial T} \le C\, h_T^{1+t}|v|_{H^{1+t}(T)}.\end{aligned} \tag{2.27}$$

Moreover, for all $T \in \mathcal{T}_h$ and all $v \in H^1(T)$, we have

$$\|\eta_{\partial T}^{\frac{1}{2}} S_{\partial T}^k(\hat{I}_T^k(v))\|_{\partial T} \le C\|\nabla(v - E_T^{k+1}(v))\|_T. \tag{2.28}$$

Proof. See [60, Lemma 3] for (2.27) (the proof uses the approximation result from Lemma 2.5). Concerning (2.28), we proceed as in [60, Eq. (45)]. Owing to the definition of $S_{\partial T}^k$ and since $E_T^{k+1} = R_T^{k+1} \circ \hat{I}_T^k$ (see (2.24)), we have

$$S_{\partial T}^k(\hat{I}_T^k(v)) = \pi_{\partial T}^k(v - E_T^{k+1}(v)_{|\partial T}) - \pi_T^k(v - E_T^{k+1}(v))_{|\partial T}.$$

We then use the triangle inequality, the stability of the L^2-projectors, that $\eta_{\partial T}$ is piecewise constant, the regularity of the mesh sequence, and the discrete trace inequality from Lemma 2.2 to infer that (the value of C can change at each occurrence)

$$\begin{aligned}\|\eta_{\partial T}^{\frac{1}{2}} S_{\partial T}^k(\hat{I}_T^k(v))\|_{\partial T} &\le \|\eta_{\partial T}^{\frac{1}{2}}\pi_{\partial T}^k(v - E_T^{k+1}(v))\|_{\partial T} + \|\eta_{\partial T}^{\frac{1}{2}}\pi_T^k(v - E_T^{k+1}(v))\|_{\partial T} \\ &\le \|\eta_{\partial T}^{\frac{1}{2}}(v - E_T^{k+1}(v))\|_{\partial T} + Ch_T^{-1}\|\pi_T^k(v - E_T^{k+1}(v))\|_T \\ &\le Ch_T^{-1}\left(h_T^{\frac{1}{2}}\|v - E_T^{k+1}(v)\|_{\partial T} + \|v - E_T^{k+1}(v)\|_T\right).\end{aligned}$$

To conclude, we invoke the multiplicative trace inequality from Lemma 2.3 and the local Poincaré inequality from Lemma 2.4 (since the function $v - E_T^{k+1}(v)$ has, by construction, zero mean-value in T). □

2.3.2 Discrete problem, stability and well-posedness

The global discrete space for the face-based trace version of the Nitsche-HHO method is defined to be

$$\hat{U}_h^k := \mathbb{P}^k(\mathcal{T}_h;\mathbb{R}) \times \mathbb{P}^k(\mathcal{F}_h;\mathbb{R}), \tag{2.29}$$

with the notation $\hat{v}_h = ((v_T)_{T\in\mathcal{T}_h}, (v_F)_{F\in\mathcal{F}_h})$ for a generic element $\hat{v}_h \in \hat{U}_h^k$. For all $T \in \mathcal{T}_h$, we denote by $\hat{v}_T = (v_T, v_{\partial T}) \in \hat{U}_T^k$ the components of $\hat{v}_h$ attached to the mesh cell T and the faces composing its boundary.

As in the conforming Nitsche-FEM (2.4), we consider a symmetry parameter $\theta \in \{-1, 0, 1\}$ and a penalty parameter $\gamma > 0$ that will be taken of the form $\gamma_{|F} = \gamma_0 h_F^{-1}$, for all $F \in \mathcal{F}_h^{b,D}$, with γ_0 large enough (depending on the constant $C_{\rm dt}$ from Lemma 2.2). The discrete Nitsche-HHO problem is as follows:

$$\begin{cases} \text{Find } \hat{u}_h \in \hat{U}_h^k \text{ such that} \\ \hat{a}_{\gamma\theta,h}(\hat{u}_h, \hat{w}_h) = \hat{\ell}_{\gamma\theta,h}(\hat{w}_h) \qquad \forall \hat{w}_h \in \hat{U}_h^k. \end{cases} \tag{2.30}$$

with the global discrete bilinear form $\hat{a}_{\gamma\theta,h}$ defined on $\hat{U}_h^k \times \hat{U}_h^k$ and the global discrete linear form $\hat{\ell}_{\gamma\theta,h}$ defined on $\hat{U}_h^k$ such that (compare with (2.5))

$$\begin{aligned} \hat{a}_{\gamma\theta,h}(\hat{v}_h, \hat{w}_h) := & \sum_{T\in\mathcal{T}_h} \hat{a}_T(\hat{v}_T, \hat{w}_T) - \sum_{F\in\mathcal{F}_h^{b,D}} \Big(\sigma_n(R_{T(F)}^{k+1}(\hat{v}_{T(F)})), w_F\Big)_F \\ & - \sum_{F\in\mathcal{F}_h^{b,D}} \theta\Big(v_F, \sigma_n(R_{T(F)}^{k+1}(\hat{w}_{T(F)}))\Big)_F + \sum_{F\in\mathcal{F}_h^{b,D}} \gamma(v_F, w_F)_F, \end{aligned} \tag{2.31a}$$

$$\begin{aligned} \hat{\ell}_{\gamma\theta,h}(\hat{w}_h) := & \sum_{T\in\mathcal{T}_h} (f, w_T)_T + \sum_{F\in\mathcal{F}_h^{b,N}} (g_N, w_F)_F \\ & - \sum_{F\in\mathcal{F}_h^{b,D}} \theta\Big(g_D, \sigma_n(R_{T(F)}^{k+1}(\hat{w}_{T(F)}))\Big)_F + \sum_{F\in\mathcal{F}_h^{b,D}} \gamma(g_D, w_F)_F, \end{aligned} \tag{2.31b}$$

where, for all $F \in \mathcal{F}_h^b$, we recall that $T(F)$ is the single mesh cell of which F is a boundary face. We equip the space $\hat{U}_h^k$ with the norm

$$\|\hat{v}_h\|_{\hat{U}_h^k}^2 := \sum_{T\in\mathcal{T}_h} |\hat{v}_T|_{\hat{U}_T^k}^2 + \sum_{F\in\mathcal{F}_h^{b,D}} h_F^{-1}\|v_F\|_F^2, \qquad \forall \hat{v}_h \in \hat{U}_h^k, \tag{2.32}$$

with the local seminorms $|\cdot|_{\hat{U}_T^k}$ defined in (2.22). Let us briefly outline why $\|\cdot\|_{\hat{U}_h^k}$ defines a norm on $\hat{U}_h^k$. The only non-trivial property is the definiteness. Let $\hat{v}_h \in \hat{U}_h^k$ be such that $\|\hat{v}_h\|_{\hat{U}_h^k} = 0$, then $v_T = v_{\partial T} = c_T$ for all $T \in \mathcal{T}_h$ (a constant depending on the mesh cell T). Since face unknowns are single-valued, this implies that $v_T = v_{\partial T} = c$ (a global constant). Finally, since $v_F = 0$ for all $F \in \mathcal{F}_h^{b,D}$, which is a non-empty set since the Dirichlet boundary has a nonempty relative interior, we conclude that $v_T = v_{\partial T} = 0$.

Let us now address the well-posedness of the discrete problem (2.30). To avoid the proliferation of proofs, we only present the proof for the choice $\theta = 1$ of the symmetry parameter. Well-posedness also holds true for $\theta = 0$ (with a less stringent lower bound on γ_0) and for $\theta = -1$ (with the simple requirement that $\gamma_0 > 0$). Let $n^{\rm b,D}$ be the maximum number of faces in $\mathcal{F}_h^{b,D}$ that a mesh cell can have ($n^{\rm b,D} \le d$ on simplicial meshes).

Lemma 2.9 (Coercivity and well-posedness)**.** *Assume that $\theta = 1$ and that $\gamma_0 > 2n^{\rm b,D}C_{\rm dt}^2$, where $C_{\rm dt}$ results from the discrete trace inequality of Lemma 2.2. Let us set the penalty parameter to $\gamma_{|F} := \gamma_0 h_F^{-1}$, for all $F \in \mathcal{F}_h^{b,D}$. Then the discrete bilinear form $\hat{a}_{\gamma\theta,h}$ is coercive, and the discrete problem* (2.30) *is well-posed.*

Proof. It suffices to prove coercivity since well-posedness then follows from the Lax–Milgram Lemma. Let $\hat{v}_h \in \hat{U}_h^k$. Using the discrete trace inequality from Lemma 2.2, we have

$$\begin{aligned}\sum_{F\in\mathcal{F}_h^{b,D}} 2\Big(\sigma_n(R_{T(F)}^{k+1}(\hat{v}_{T(F)})), v_F\Big)_F &\geq -\sum_{F\in\mathcal{F}_h^{b,D}} (n^{\mathrm{b,D}})^{-\frac{1}{2}} C_{\mathrm{dt}}^{-1} h_F^{\frac{1}{2}} \|\nabla R_{T(F)}^{k+1}(\hat{v}_{T(F)})\|_F \times 2(n^{\mathrm{b,D}})^{\frac{1}{2}} C_{\mathrm{dt}} h_F^{-\frac{1}{2}} \|v_F\|_F \\ &\geq -\sum_{T\in\mathcal{T}_h^{\mathrm{b,D}}} \frac{1}{2}\|\nabla R_T^{k+1}(\hat{v}_T)\|_T^2 - \sum_{F\in\mathcal{F}_h^{b,D}} 2n^{\mathrm{b,D}} C_{\mathrm{dt}}^2 h_F^{-1}\|v_F\|_F^2,\end{aligned}$$

where we used the discrete trace inequality from Lemma 2.2 and $\mathcal{T}_h^{\mathrm{b,D}}$ is the collection of the mesh cells having a boundary face in $\mathcal{F}_h^{b,D}$. Bounding the first summation by the summation over all the mesh cells and using the definition of $\hat{a}_{\gamma\theta,h}$, we infer that

$$\begin{aligned}\hat{a}_{\gamma\theta,h}(\hat{v}_h,\hat{v}_h) &\geq \sum_{T\in\mathcal{T}_h} \frac{1}{2}\|\nabla R_T^{k+1}(\hat{v}_T)\|_T^2 + \sum_{T\in\mathcal{T}_h} \|\eta_{\partial T}^{\frac{1}{2}} S_{\partial T}^k(\hat{v}_T)\|_{\partial T}^2 + (\gamma_0 - 2n^{\mathrm{b,D}}C_{\mathrm{dt}}^2)\sum_{F\in\mathcal{F}_h^{b,D}} h_F^{-1}\|v_F\|_F^2 \\ &\geq \min\big(\frac{1}{2}\rho^{-1}, \gamma_0 - 2n^{\mathrm{b,D}}C_{\mathrm{dt}}^2\big)\|\hat{v}_h\|_{\hat{U}_h^k}^2.\end{aligned}$$

This concludes the proof. □

Remark 2.10 (Choosing the symmetry parameter θ)**.** (i) *For $\theta = 1$, one obtains a discrete problem with variational structure, that is, the discrete problem takes the form of the Euler equations characterizing the minimizer of a convex energy functional, see the functional $\tilde{J}_{\gamma,h}$ defined by* (1.16)*.* (ii) *For $\theta = 0$, one recovers a simpler method since some terms in the formulation vanish, and the lower bound on γ_0 becomes $\gamma_0 > \frac{1}{2}n^{\mathrm{b,D}}C_{\mathrm{dt}}^2$.* (iii) *For $\theta = -1$, the stability properties of the method are stronger since it suffices to take $\gamma > 0$.*

2.3.3 Error analysis

The first important step in the error analysis is to bound the consistency error which is defined as follows:

$$\mathcal{E}_h(\hat{w}_h) := \hat{\ell}_{\gamma\theta,h}(\hat{w}_h) - \hat{a}_{\gamma\theta,h}(\hat{I}_h^k(u),\hat{w}_h), \qquad \forall \hat{w}_h \in \hat{U}_h^k, \tag{2.33}$$

where the global reduction operator $\hat{I}_h^k : H^1(\Omega) \to \hat{U}_h^k$ is defined such that the local components of $\hat{I}_h^k(v)$, for all $v \in H^1(\Omega)$, attached to a mesh cell $T \in \mathcal{T}_h$, are $\hat{I}_T^k(v_{|T})$ (this definition is meaningful since a function in $H^1(\Omega)$ is single-valued at all the mesh interfaces). As above, we only give proofs for $\theta = 1$; the proofs for the other values $\theta \in \{-1, 0\}$ follow by minor adaptations of the arguments for $\theta = 1$.

Lemma 2.11 (Consistency)**.** *Assume that $\theta = 1$ and that $u \in H^{1+s}(\Omega)$ with $s > \frac{1}{2}$. The following holds true:*

$$|\mathcal{E}_h(\hat{w}_h)| \lesssim \left(\sum_{T\in\mathcal{T}_h} \|u - E_T^{k+1}(u)\|_{\sharp,T}^2\right)^{\frac{1}{2}} \|\hat{w}_h\|_{\hat{U}_h^k}, \qquad \forall \hat{w}_h \in \hat{U}_h^k, \tag{2.34}$$

with $\|v\|_{\sharp,T}^2 := \|\nabla v\|_T^2 + h_T\|\boldsymbol{n}_T\cdot\nabla v\|_{\partial T}^2$ for any function $v \in H^{1+s}(T)$, $s > \frac{1}{2}$, and all $T \in \mathcal{T}_h$.

Proof. Let $\hat{w}_h \in \hat{U}_h^k$. Let us introduce the shorthand notation

$$\eta_{\gamma\theta}(\hat{w}_{T(F)}) := -\theta\sigma_n(R_{T(F)}^{k+1}(\hat{w}_{T(F)})) + \gamma w_F.$$

Using the definitions (2.31a)-(2.31b) of $\hat{a}_{\gamma\theta,h}$, $\hat{\ell}_{\gamma\theta,h}$, the PDE and the boundary conditions satisfied by the exact solution u, and since $R_T^{k+1} \circ \hat{I}_T^k = E_T^{k+1}$ (see (2.24)), we have

$$\begin{aligned}\mathcal{E}_h(\hat{w}_h) = &\sum_{T\in\mathcal{T}_h}(-\Delta u, w_T)_T + \sum_{F\in\mathcal{F}_h^{b,N}}(\sigma_n(u), w_F)_F + \sum_{F\in\mathcal{F}_h^{b,D}}\Big(u, \eta_{\gamma\theta}(\hat{w}_{T(F)})\Big)_F\\ &- \sum_{T\in\mathcal{T}_h}(\nabla E_T^{k+1}(u), \nabla R_T^{k+1}(\hat{w}_T))_T - \sum_{T\in\mathcal{T}_h}(\eta_{\partial T} S_{\partial T}^k(\hat{I}_T^k(u)), S_{\partial T}^k(\hat{w}_T))_{\partial T}\\ &+ \sum_{F\in\mathcal{F}_h^{b,D}}\Big(\sigma_n(E_{T(F)}^{k+1}(u)), w_F\Big)_F - \Big(\pi_F^k(u), \eta_{\gamma\theta}(\hat{w}_{T(F)})\Big)_F.\end{aligned}$$

Since $\eta_{\gamma\theta}(\hat{w}_{T(F)})$ is a polynomial of degree at most k on each boundary face in $\mathcal{F}_h^{b,D}$, we infer that $\Big(u, \eta_{\gamma\theta}(\hat{w}_{T(F)})\Big)_F = \Big(\pi_F^k(u), \eta_{\gamma\theta}(\hat{w}_{T(F)})\Big)_F$. Re-arranging terms leads to

$$\mathcal{E}_h(\hat{w}_h) = \mathcal{T}_1 - \mathcal{T}_2 - \mathcal{T}_3,$$

where

$$\begin{aligned}\mathcal{T}_1 &= \sum_{T\in\mathcal{T}_h}(-\Delta u, w_T)_T + \sum_{F\in\mathcal{F}_h^{b,N}}(\sigma_n(u), w_F)_F,\\ \mathcal{T}_2 &= \sum_{T\in\mathcal{T}_h}(\nabla E_T^{k+1}(u), \nabla R_T^{k+1}(\hat{w}_T))_T - \sum_{F\in\mathcal{F}_h^{b,D}}\Big(\sigma_n(E_{T(F)}^{k+1}(u)), w_F\Big)_F,\\ \mathcal{T}_3 &= \sum_{T\in\mathcal{T}_h}(\eta_{\partial T} S_{\partial T}^k(\hat{I}_T^k(u)), S_{\partial T}^k(\hat{w}_T))_{\partial T}.\end{aligned}$$

Integrating by parts in each mesh cell and using that $\sigma_n(u)$ is single-valued across all the mesh interfaces (and well-defined since $s > \frac{1}{2}$), we obtain

$$\begin{aligned}\mathcal{T}_1 &= \sum_{T\in\mathcal{T}_h}(\nabla u, \nabla w_T)_T - \sum_{T\in\mathcal{T}_h}(\sigma_n(u), w_T)_{\partial T} + \sum_{F\in\mathcal{F}_h^{b,N}}(\sigma_n(u), w_F)_F\\ &= \sum_{T\in\mathcal{T}_h}(\nabla u, \nabla w_T)_T - \sum_{T\in\mathcal{T}_h}(\sigma_n(u), w_T - w_{\partial T})_{\partial T} - \sum_{F\in\mathcal{F}_h^{b,D}}(\sigma_n(u), w_F)_F.\end{aligned}$$

Using the definition of $R_T^{k+1}(\hat{w}_T)$, we infer that

$$\mathcal{T}_2 = \sum_{T\in\mathcal{T}_h}(\nabla E_T^{k+1}(u), \nabla w_T)_T - \sum_{T\in\mathcal{T}_h}(\sigma_n(E_T^{k+1}(u)), w_T - w_{\partial T})_{\partial T} - \sum_{F\in\mathcal{F}_h^{b,D}}(\sigma_n(E_{T(F)}^{k+1}(u)), w_F)_F.$$

Consequently, if we define for all $T \in \mathcal{T}_h$ the function $\delta_T := u_{|T} - E_T^{k+1}(u_{|T})$, we obtain

$$\begin{aligned}\mathcal{T}_1 - \mathcal{T}_2 &= \sum_{T\in\mathcal{T}_h}(\nabla\delta_T, \nabla w_T)_T - \sum_{T\in\mathcal{T}_h}(\sigma_n(\delta_T), w_T - w_{\partial T})_{\partial T} - \sum_{F\in\mathcal{F}_h^{b,D}}(\sigma_n(\delta_{T(F)}), w_F)_F\\ &= -\sum_{T\in\mathcal{T}_h}(\sigma_n(\delta_T), w_T - w_{\partial T})_{\partial T} - \sum_{F\in\mathcal{F}_h^{b,D}}(\sigma_n(\delta_{T(F)}), w_F)_F,\end{aligned}$$

where we used that $(\nabla\delta_T, \nabla w_T)_T = 0$ since w_T is a polynomial of order at most k in T. Invoking the Cauchy–Schwarz inequality and recalling the definition of the norm $\|\hat{w}_h\|_{\hat{U}_h^k}$, we infer that

$$|\mathcal{T}_1 - \mathcal{T}_2| \lesssim \left(\sum_{T\in\mathcal{T}_h}\|\delta_T\|_{\sharp,T}^2\right)^{\frac{1}{2}}\|\hat{w}_h\|_{\hat{U}_h^k}.$$

Finally, the Cauchy–Schwarz inequality, the bound (2.28) and the upper bound in (2.23) imply that

$$|\mathcal{T}_3| \le \left(\sum_{T\in\mathcal{T}_h} \|\eta_{\partial T}^{\frac12} S_{\partial T}^k(\hat I_T^k(u))\|_{\partial T}^2\right)^{\frac12} \left(\sum_{T\in\mathcal{T}_h} \|\eta_{\partial T}^{\frac12} S_{\partial T}^k(\hat w_T)\|_{\partial T}^2\right)^{\frac12}$$
$$\lesssim \left(\sum_{T\in\mathcal{T}_h} \|\delta_T\|_{\sharp,T}^2\right)^{\frac12} \|\hat w_h\|_{\hat U_h^k}.$$

This concludes the proof. □

We now prove the optimal convergence of the method (2.30).

Theorem 2.12 (H^1-error estimate)**.** *Assume that $u \in H^{1+s}(\Omega)$ with $s > \frac12$. The following holds true:*

$$\sum_{T\in\mathcal{T}_h} \|\nabla(u - R_T^{k+1}(\hat u_T))\|_T^2 \lesssim \sum_{T\in\mathcal{T}_h} \|u - E_T^{k+1}(u)\|_{\sharp,T}^2. \tag{2.35}$$

Consequently, letting $t := \min(k+1, s)$, we have

$$\sum_{T\in\mathcal{T}_h} \|\nabla(u - R_T^{k+1}(\hat u_T))\|_T^2 \sum_{T\in\mathcal{T}_h} h_T^{2t} |u|_{H^{t+1}(T)}^2. \tag{2.36}$$

Proof. Let us set $\hat w_h := \hat u_h - \hat I_h^k(u) \in \hat U_h^k$. The coercivity of $\hat a_{\gamma\theta,h}$ from Lemma 2.9 and the bound on the consistency error from Lemma 2.11 imply that

$$\|\hat w_h\|_{\hat U_h^k} \lesssim \frac{\hat a_{\gamma\theta,h}(\hat w_h, \hat w_h)}{\|\hat w_h\|_{\hat U_h^k}} = \frac{\mathcal{E}_h(\hat w_h)}{\|\hat w_h\|_{\hat U_h^k}} \lesssim \left(\sum_{T\in\mathcal{T}_h} \|u - E_T^{k+1}(u)\|_{\sharp,T}^2\right)^{\frac12}.$$

Using the upper bound from Lemma 2.6, we infer that

$$\left(\sum_{T\in\mathcal{T}_h} \|\nabla(R_T^{k+1}(\hat u_T) - E_T^{k+1}(u))\|_T^2\right)^{\frac12} = \left(\sum_{T\in\mathcal{T}_h} \|\nabla R_T^{k+1}(\hat w_T)\|_T^2\right)^{\frac12}$$
$$\lesssim \|\hat w_h\|_{\hat U_h^k} \lesssim \left(\sum_{T\in\mathcal{T}_h} \|u - E_T^{k+1}(u)\|_{\sharp,T}^2\right)^{\frac12},$$

The estimate (2.35) results from this bound, the triangle inequality, and the definition of $\|\cdot\|_{\sharp,T}$. Finally, the estimate (2.36) is a consequence of (2.35) and Lemma 2.8. □

2.4 Dirichlet conditions with cell-based traces

The goal of this section is to extend our analysis to the cell-based trace version of the Nitsche-HHO method. In short, the cell unknowns are of one order higher than the face unknowns and are used in the formulation of Nitsche's consistency and penalty terms. We consider the linear model problem (2.3), as in the previous section, and we assume that the meshes are compatible with the boundary partition $\partial\Omega = \overline{\Gamma_D} \cup \overline{\Gamma_N}$ from (2.2), which leads again to the partition of boundary faces as $\mathcal{F}_h^b = \mathcal{F}_h^{b,D} \cup \mathcal{F}_h^{b,N}$.

From the analysis viewpoint, the main novelty is that we need to change the definition of the reconstruction operator. The reason for this change is somewhat subtle and will appear when bounding the consistency error; this change will be crucial to derive optimal energy-error estimates.

2.4.1 Local reconstruction and stability operators

In what follows, it is important to identify, for any mesh cell $T \in \mathcal{T}_h$, the (possibly empty) part of its boundary that is not located on the subset Γ_D (where Nitsche's method is employed). Thus, we set

$$\partial T^{\backslash} := \partial T \cap (\overline{\Omega} \setminus \Gamma_D). \tag{2.37}$$

Let $\mathcal{F}_{\partial T^{\backslash}}$ collect the faces of T located on $\partial T^{\backslash}$. Let $k \geq 0$ be the polynomial degree. For all $T \in \mathcal{T}_h$, the local discrete space is (we keep the same notation as in the previous section although the local space is now different concerning the degree of the cell unknowns and the support of the face unknowns):

$$\hat{U}_{T^{\backslash}}^k := \mathbb{P}^{k+1}(T;\mathbb{R}) \times \mathbb{P}^k(\mathcal{F}_{\partial T^{\backslash}};\mathbb{R}), \tag{2.38}$$

that is, the local face unknowns are only attached to those faces of T that are not located in Γ_D (this is why we introduce the subscript $T^{\backslash}$ rather than T for the local space). A generic element in $\hat{U}_{T^{\backslash}}^k$ is denoted $\hat{v}_T = (v_T, v_{\partial T^{\backslash}})$ with $v_T \in \mathbb{P}^{k+1}(T;\mathbb{R})$ and $v_{\partial T^{\backslash}} \in \mathbb{P}^k(\mathcal{F}_{\partial T^{\backslash}};\mathbb{R})$.

For all $T \in \mathcal{T}_h$, we define the local reconstruction operator $R_{T^{\backslash}}^{k+1} : \hat{U}_{T^{\backslash}}^k \to \mathbb{P}^{k+1}(T;\mathbb{R})$ such that, for all $\hat{v}_T = (v_T, v_{\partial T^{\backslash}}) \in \hat{U}_{T^{\backslash}}^k$,

$$(\nabla R_{T^{\backslash}}^{k+1}(\hat{v}_T), \nabla w)_T = (\nabla v_T, \nabla w)_T + (v_{\partial T^{\backslash}} - v_T, \boldsymbol{n}_T \cdot \nabla w)_{\partial T^{\backslash}} \quad \forall w \in \mathbb{P}^{k+1}(T;\mathbb{R}), \tag{2.39}$$

$$(R_{T^{\backslash}}^{k+1}(\hat{v}_T), 1)_T = (v_T, 1)_T, \tag{2.40}$$

which leads, as usual, to a local well-posed Neumann problem that is solved by inverting the local stiffness matrix in $\mathbb{P}^{k+1}(T;\mathbb{R})$. The local stabilization operator $S_{\partial T^{\backslash}}^k : \hat{U}_{T^{\backslash}}^k \to \mathbb{P}^k(\mathcal{F}_{\partial T^{\backslash}};\mathbb{R})$ is defined such that, for all $\hat{v}_T = (v_T, v_{\partial T^{\backslash}}) \in \hat{U}_{T^{\backslash}}^k$,

$$S_{\partial T^{\backslash}}^k(\hat{v}_T) := \pi_{\partial T^{\backslash}}^k(v_{\partial T^{\backslash}} - v_{T|\partial T^{\backslash}}) = v_{\partial T^{\backslash}} - \pi_{\partial T^{\backslash}}^k(v_{T|\partial T^{\backslash}}). \tag{2.41}$$

Observe that the above form of the stabilization operator is similar (up to the restriction to $\partial T^{\backslash}$) to the Lehrenfeld–Schöberl stabilization in the context of mixed-order HDG methods [102].

The local bilinear form $\hat{a}_{T^{\backslash}}$ on $\hat{U}_{T^{\backslash}}^k \times \hat{U}_{T^{\backslash}}^k$ is

$$\hat{a}_{T^{\backslash}}(\hat{v}_T, \hat{w}_T) := (\nabla R_{T^{\backslash}}^{k+1}(\hat{v}_T), \nabla R_{T^{\backslash}}^{k+1}(\hat{w}_T))_T + (\eta_{\partial T} S_{\partial T^{\backslash}}^k(\hat{v}_T), S_{\partial T^{\backslash}}^k(\hat{w}_T))_{\partial T^{\backslash}}, \tag{2.42}$$

where $\eta_{\partial T}$ is still the piecewise constant function on ∂T (which is only needed on $\partial T^{\backslash}$ now) given by $\eta_{\partial T|F} = h_F^{-1}$ for all $F \in \mathcal{F}_{\partial T^{\backslash}}$. We equip the discrete space $\hat{U}_{T^{\backslash}}^k$ with the following H^1-like seminorm: for all $\hat{v}_T = (v_T, v_{\partial T^{\backslash}}) \in \hat{U}_{T^{\backslash}}^k$,

$$|\hat{v}_T|_{\hat{U}_{T^{\backslash}}^k}^2 := \|\nabla v_T\|_T^2 + \|\eta_{\partial T}^{\frac{1}{2}}(v_{\partial T^{\backslash}} - v_{T|\partial T^{\backslash}})\|_{\partial T^{\backslash}}^2, \tag{2.43}$$

so that $|\hat{v}_T|_{\hat{U}_{T^{\backslash}}^k} = 0$ implies that $v_T = v_{\partial T^{\backslash}} = cte$. One can verify that the stability and boundedness properties from Lemma 2.6 still hold true for the discrete bilinear form $\hat{a}_{T^{\backslash}}$.

For all $T \in \mathcal{T}_h$, we define the local reduction operator $\hat{I}_{T^{\backslash}}^k : H^1(T) \to \hat{U}_{T^{\backslash}}^k$ such that, for all $v \in H^1(T)$,

$$\hat{I}_{T^{\backslash}}^k(v) := (\pi_T^{k+1}(v), \pi_{\partial T^{\backslash}}^k(v)) \in \hat{U}_{T^{\backslash}}^k. \tag{2.44}$$

There are two differences with the usual HHO reduction operator $\hat{I}_T^k$ considered in Lemma 2.7: for the cell component, we use a higher-order L^2-orthogonal projector onto $\mathbb{P}^{k+1}(T;\mathbb{R})$, and for the face component, we only project on those faces in $\mathcal{F}_{\partial T^{\backslash}}$. Then,

$$E_{T^{\backslash}}^{k+1} := R_{T^{\backslash}}^{k+1} \circ \hat{I}_{T^{\backslash}}^k : H^1(T) \to \mathbb{P}^{k+1}(T;\mathbb{R}) \tag{2.45}$$

still acts as an approximation operator, but it is no longer the elliptic projector, at least on those mesh cells having a boundary face in $\mathcal{F}_h^{b,D}$. It is therefore crucial at this stage to assert that $E_{T^\backslash}^{k+1}$ still enjoys optimal approximation properties. Let us recall the norm $\|v\|_{\sharp,T}^2 := \|\nabla v\|_T^2 + h_T\|\boldsymbol{n}_T\cdot\nabla v\|_{\partial T}^2$, for all $v \in H^{1+s}(T)$, $s > \frac{1}{2}$, and all $T \in \mathcal{T}_h$.

Lemma 2.13 (Approximation)**.** *There exists a uniform constant such that the following holds true:*

$$\|v - E_{T^\backslash}^{k+1}(v)\|_{\sharp,T} \le C\|v - \pi_T^{k+1}(v)\|_{\sharp,T}. \tag{2.46}$$

for all $v \in H^{1+s}(T)$, $s > \frac{1}{2}$, and all $T \in \mathcal{T}_h$. Moreover, for all $T \in \mathcal{T}_h$ and all $v \in H^1(T)$, we have

$$\|\eta_{\partial T}^{\frac{1}{2}} S_{\partial T^\backslash}^k(\hat{I}_{T^\backslash}^k(v))\|_{\partial T^\backslash} \le C\|\nabla(v - \pi_T^{k+1}(v))\|_T. \tag{2.47}$$

Proof. To prove (2.46), let us start by bounding $\|\nabla(v - E_{T^\backslash}^{k+1}(v))\|_T$. We have

$$\begin{aligned}
\|\nabla(E_{T^\backslash}^{k+1}(v) - \pi_T^{k+1}(v))\|_T &= \sup_{\substack{q\in\mathbb{P}^{k+1}(T;\mathbb{R})\\ \|\nabla q\|_T=1}} (\nabla(E_{T^\backslash}^{k+1}(v) - \pi_T^{k+1}(v)), \nabla q)_T \\
&= \sup_{\substack{q\in\mathbb{P}^{k+1}(T;\mathbb{R})\\ \|\nabla q\|_T=1}} (\nabla R_{T^\backslash}^{k+1}(\hat{I}_{T^\backslash}^k(v)) - \pi_T^{k+1}(v)), \nabla q)_T \\
&= \sup_{\substack{q\in\mathbb{P}^{k+1}(T;\mathbb{R})\\ \|\nabla q\|_T=1}} (\pi_{\partial T^\backslash}^k(v) - \pi_T^{k+1}(v), \boldsymbol{n}_T\cdot\nabla q)_{\partial T^\backslash} \\
&= \sup_{\substack{q\in\mathbb{P}^{k+1}(T;\mathbb{R})\\ \|\nabla q\|_T=1}} (v - \pi_T^{k+1}(v), \boldsymbol{n}_T\cdot\nabla q)_{\partial T^\backslash},
\end{aligned}$$

where we used that $E_{T^\backslash}^{k+1}(v) - \pi_T^{k+1}(v) \in \mathbb{P}^{k+1}(T;\mathbb{R})$ in the first line, the definition of $E_{T^\backslash}^{k+1}$ in the second line, the definition of $R_{T^\backslash}^{k+1}$ in the third line, and the fact that $\boldsymbol{n}_T\cdot\nabla q_{|\partial T^\backslash} \in \mathbb{P}^k(\mathcal{F}_{\partial T^\backslash};\mathbb{R})$ in the fourth line. Using the Cauchy–Schwarz inequality followed by the discrete trace inequality from Lemma 2.2 to bound $\|\boldsymbol{n}_T\cdot\nabla q\|_{\partial T^\backslash}$ and since $\|\nabla q\|_T = 1$, we conclude that

$$\|\nabla(E_{T^\backslash}^{k+1}(v) - \pi_T^{k+1}(v))\|_T \le Ch_T^{-\frac{1}{2}}\|v - \pi_T^{k+1}(v)\|_{\partial T^\backslash}.$$

The multiplicative trace inequality from Lemma 2.3 followed by the Poincaré inequality from Lemma 2.4 then lead to

$$\|\nabla(E_{T^\backslash}^{k+1}(v) - \pi_T^{k+1}(v))\|_T \le C\|\nabla(v - \pi_T^{k+1}(v))\|_T. \tag{2.48}$$

Let us now estimate $h_T^{\frac{1}{2}}\|\boldsymbol{n}_T\cdot\nabla(E_{T^\backslash}^{k+1}(v) - \pi_T^{k+1}(v))\|_{\partial T}$. The discrete trace inequality from Lemma 2.2, estimating the normal derivative by the norm of the full gradient, and the above bound (2.48) lead to

$$h_T^{\frac{1}{2}}\|\boldsymbol{n}_T\cdot\nabla(E_{T^\backslash}^{k+1}(v) - \pi_T^{k+1}(v))\|_{\partial T} \le C\|\nabla(E_{T^\backslash}^{k+1}(v) - \pi_T^{k+1}(v))\|_T \le C\|\nabla(v - \pi_T^{k+1}(v))\|_T.$$

We complete the proof of (2.46) by using the triangle inequality. We now turn to the proof of (2.47). Since $\pi_{\partial T^\backslash}^k \circ \pi_{\partial T^\backslash}^k = \pi_{\partial T^\backslash}^k$, we have

$$\|\eta_{\partial T}^{\frac{1}{2}} S_{\partial T^\backslash}^k(\hat{I}_{T^\backslash}^k(v))\|_{\partial T^\backslash} = \|\eta_{\partial T}^{\frac{1}{2}}\pi_{\partial T^\backslash}^k(v - \pi_T^{k+1}(v))\|_{\partial T^\backslash} \le Ch_T^{-\frac{1}{2}}\|v - \pi_T^{k+1}(v)\|_{\partial T},$$

where we used the L^2-stability of $\pi_{\partial T^\backslash}^k$, that $\eta_{\partial T}$ is piecewise constant, and that $\partial T^\backslash \subseteq \partial T$. We conclude by invoking the multiplicative trace inequality from Lemma 2.3 followed by the Poincaré inequality from Lemma 2.4. □

Remark 2.14 (Other estimates)**.** *The bound* (2.48) *together with a triangle inequality implies that* $\|\nabla(v - E_{T\backslash}^{k+1}(v))\|_T \le C\|\nabla(v - \pi_T^{k+1}(v))\|_T$*. Invoking the multiplicative trace inequality from Lemma 2.3 followed by the Poincaré inequality from Lemma 2.4, we conclude that*

$$\|v - E_{T\backslash}^{k+1}(v)\|_T + h_T^{\frac{1}{2}}\|v - E_{T\backslash}^{k+1}(v)\|_{\partial T} + h_T\|\nabla(v - E_{T\backslash}^{k+1}(v))\|_T \le Ch_T\|\nabla(v - \pi_T^{k+1}(v))\|_T$$

Optimal convergence rates on $(v - E_{T\backslash}^{k+1}(v))$ *for smooth functions* $v \in H^{1+s}(T)$*,* $s > \frac{1}{2}$*, can then be inferred from Lemma 2.5.*

2.4.2 Discrete problem, stability and well-posedness

The definition of the global discrete space is slightly modified (we keep the same notation for simplicity) since, in the cell-based trace version, there are no face unknowns attached to those faces in $\mathcal{F}_h^{b,D}$:

$$\hat{U}_h^k := \mathbb{P}^{k+1}(\mathcal{T}_h;\mathbb{R}) \times \mathbb{P}^k(\mathcal{F}_h^i \cup \mathcal{F}_h^{b,N};\mathbb{R}). \tag{2.49}$$

A generic element in $\hat{U}_h^k$ is denoted $\hat{w}_h = ((w_T)_{T\in\mathcal{T}_h}, (w_F)_{F\in\mathcal{F}_h^i\cup\mathcal{F}_h^{b,N}})$, and for all $T \in \mathcal{T}_h$, we denote by

$$\hat{w}_T = \Big(w_T, (w_F)_{F\in\mathcal{F}_{\partial T\backslash}}\Big) \in \hat{U}_{T\backslash}^k \tag{2.50}$$

the components of $\hat{w}_h$ attached to the mesh cell T and its faces composing $\partial T^{\backslash}$. We consider the following discrete Nitsche-HHO problem:

$$\begin{cases}\text{Find } \hat{u}_h \in \hat{U}_h^k \text{ such that}\\ \hat{a}_{\gamma\theta,h}(\hat{u}_h,\hat{w}_h) = \hat{\ell}_{\gamma\theta,h}(\hat{w}_h) \qquad \forall \hat{w}_h \in \hat{U}_h^k.\end{cases} \tag{2.51}$$

For all $\hat{v}_h, \hat{w}_h \in \hat{U}_h^k$, the global discrete bilinear form $\hat{a}_{\gamma\theta,h}$ and the global discrete linear form $\hat{\ell}_{\gamma\theta,h}$ are defined respectively by (compare with (**??**))

$$\begin{aligned}\hat{a}_{\gamma\theta,h}(\hat{v}_h,\hat{w}_h) :=& \sum_{T\in\mathcal{T}_h}\hat{a}_T(\hat{v}_T,\hat{w}_T) - \sum_{F\in\mathcal{F}_h^{b,D}}\Big(\sigma_n(R_{T(F)\backslash}^{k+1}(\hat{v}_{T(F)})), w_{T(F)}\Big)_F\\ &- \sum_{F\in\mathcal{F}_h^{b,D}}\theta\Big(v_{T(F)}, \sigma_n(R_{T(F)\backslash}^{k+1}(\hat{w}_{T(F)}))\Big)_F + \sum_{F\in\mathcal{F}_h^{b,D}}\gamma(v_{T(F)}, w_{T(F)})_F, \qquad (2.52a)\\ \hat{\ell}_{\gamma\theta,h}(\hat{w}_h) :=& \sum_{T\in\mathcal{T}_h}(f,w_T)_T + \sum_{F\in\mathcal{F}_h^{b,N}}(g_N,w_F)_F\\ &- \sum_{F\in\mathcal{F}_h^{b,D}}\theta\Big(g_D, \sigma_n(R_{T(F)\backslash}^{k+1}(\hat{w}_{T(F)}))\Big)_F + \sum_{F\in\mathcal{F}_h^{b,D}}\gamma(g_D, w_{T(F)})_F. \qquad (2.52b)\end{aligned}$$

Comparing (2.31a) with (2.52a), we see that $v_{T(F)}$ and $w_{T(F)}$ are now used in place of v_F and w_F in the three terms on $\mathcal{F}_h^{b,D}$ defining $\hat{a}_{\gamma\theta,h}$, and comparing (2.31b) with (2.52b), we see that $w_{T(F)}$ is now used in place of w_F in the penalty term on $\mathcal{F}_h^{b,D}$ defining $\hat{\ell}_{\gamma\theta,h}$; notice, however, that the enforcement of the Neumann condition in $\hat{\ell}_{\gamma\theta,h}$ still involves the face component w_F of the test function $\hat{w}_h$.

We equip the space $\hat{U}_h^k$ with the norm

$$\|\hat{v}_h\|_{\hat{U}_h^k}^2 := \sum_{T\in\mathcal{T}_h}|\hat{v}_T|_{\hat{U}_{T\backslash}^k}^2 + \sum_{F\in\mathcal{F}_h^{b,D}}h_F^{-1}\|v_{T(F)}\|_F^2, \qquad \forall \hat{v}_h \in \hat{U}_h^k, \tag{2.53}$$

with the local seminorms $|\cdot|_{\hat{U}_{T\backslash}^k}$ defined in (2.43). That $\|\cdot\|_{\hat{U}_h^k}$ defines a norm on $\hat{U}_h^k$ follows from similar arguments to those considered for the face-based trace scheme in the previous section. Let us now address the well-posedness of the discrete problem (2.51). As above, we only consider $\theta = 1$. Well-posedness also holds true for $\theta = 0$ (with a less stringent lower bound on γ_0) and for $\theta = -1$ (with the simple requirement that $\gamma_0 > 0$).

Lemma 2.15 (Coercivity and well-posedness)**.** *Assume that $\theta = 1$ and that $\gamma_0 > 2n^{\mathrm{b,D}}C_{\mathrm{dt}}^2$, where C_{dt} results from the discrete trace inequality of Lemma 2.2. Let us set the penalty parameter to $\gamma_{|F} := \gamma_0 h_F^{-1}$, for all $F \in \mathcal{F}_h^{b,D}$. Then the discrete bilinear form $\hat{a}_{\gamma\theta,h}$ is coercive, and the discrete problem* (2.51) *is well-posed.*

Proof. Identical to the proof of Lemma 2.9. □

2.4.3 Error analysis

We carry out the error analysis for $\theta = 1$; the proofs for the other values $\theta \in \{-1, 0\}$ follow by minor adaptations of the arguments for $\theta = 1$. As above, the first important step in the error analysis is to bound the consistency error; we recall that this error is defined such that

$$\mathcal{E}_h(\hat{w}_h) := \hat{\ell}_{\gamma\theta,h}(\hat{w}_h) - \hat{a}_{\gamma\theta,h}(\hat{I}_h^k(u), \hat{w}_h), \qquad \forall \hat{w}_h \in \hat{U}_h^k, \tag{2.54}$$

where the global reduction operator $\hat{I}_h^k : H^1(\Omega) \to \hat{U}_h^k$ is now such that the local components of $\hat{I}_h^k(v)$, for all $v \in H^1(\Omega)$, attached to a mesh cell $T \in \mathcal{T}_h$, are $\hat{I}_{T^\backslash}^k(v_{|T})$.

Lemma 2.16 (Consistency)**.** *Assume that $\theta = 1$ and $u \in H^{1+s}(\Omega)$ with $s > \frac{1}{2}$. The following holds true:*

$$|\mathcal{E}_h(\hat{w}_h)| \lesssim \left(\sum_{T\in\mathcal{T}_h} \|u - \pi_T^{k+1}(u)\|_{\sharp,T}^2 \right)^{\frac{1}{2}} \|\hat{w}_h\|_{\hat{U}_h^k}, \qquad \forall \hat{w}_h \in \hat{U}_h^k. \tag{2.55}$$

Proof. Let $\hat{w}_h \in \hat{U}_h^k$. Let us introduce the shorthand notation $\eta_\gamma(\hat{w}_{T(F)}) := -\sigma_n(R_{T(F)^\backslash}^{k+1}(\hat{w}_{T(F)})) + \gamma w_{T(F)}$. Using the definitions (2.52a)-(2.52b) of $\hat{a}_{\gamma\theta,h}$, $\hat{\ell}_{\gamma\theta,h}$, the PDE and the boundary conditions satisfied by the exact solution u, and since $R_{T^\backslash}^{k+1} \circ \hat{I}_{T^\backslash}^k = E_{T^\backslash}^{k+1}$, we have

$$\begin{aligned}
\mathcal{E}_h(\hat{w}_h) = &\sum_{T\in\mathcal{T}_h} (-\Delta u, w_T)_T + \sum_{F\in\mathcal{F}_h^{b,N}} (\sigma_n(u), w_F)_F + \sum_{F\in\mathcal{F}_h^{b,D}} \Big(u, \eta_\gamma(\hat{w}_{T(F)})\Big)_F \\
&- \sum_{T\in\mathcal{T}_h} (\nabla E_{T^\backslash}^{k+1}(u), \nabla R_{T^\backslash}^{k+1}(\hat{w}_T))_T - \sum_{T\in\mathcal{T}_h} (\eta_{\partial T} S_{\partial T^\backslash}^k(\hat{I}_{T^\backslash}^k(u)), S_{\partial T^\backslash}^k(\hat{w}_T))_{\partial T^\backslash} \\
&+ \sum_{F\in\mathcal{F}_h^{b,D}} \Big(\sigma_n(E_{T(F)^\backslash}^{k+1}(u)), w_{T(F)}\Big)_F - \Big(\pi_{T(F)}^{k+1}(u), \eta_\gamma(\hat{w}_{T(F)})\Big)_F.
\end{aligned}$$

Re-arranging terms leads to

$$\mathcal{E}_h(\hat{w}_h) = \mathcal{T}_1 - \mathcal{T}_2 - \mathcal{T}_3 + \mathcal{T}_4,$$

where

$$\begin{aligned}
\mathcal{T}_1 &= \sum_{T\in\mathcal{T}_h} (-\Delta u, w_T)_T + \sum_{F\in\mathcal{F}_h^{b,N}} (\sigma_n(u), w_F)_F, \\
\mathcal{T}_2 &= \sum_{T\in\mathcal{T}_h} (\nabla E_{T^\backslash}^{k+1}(u), \nabla R_{T^\backslash}^{k+1}(\hat{w}_T))_T - \sum_{F\in\mathcal{F}_h^{b,D}} \Big(\sigma_n(E_{T(F)^\backslash}^{k+1}(u)), w_{T(F)}\Big)_F, \\
\mathcal{T}_3 &= \sum_{T\in\mathcal{T}_h} (\eta_{\partial T} S_{\partial T^\backslash}^k(\hat{I}_{T^\backslash}^k(u)), S_{\partial T^\backslash}^k(\hat{w}_T))_{\partial T^\backslash}, \\
\mathcal{T}_4 &= \sum_{F\in\mathcal{F}_h^{b,D}} \Big(u - \pi_{T(F)}^{k+1}(u), \eta_\gamma(\hat{w}_{T(F)})\Big)_F.
\end{aligned}$$

Note that a term of the form $\mathcal{T}_4$ is not present in the consistency error of the face version of Nitsche-HHO. Integrating by parts in each mesh cell and using that $\sigma_n(u)$ is single-valued

across all the mesh interfaces (and well-defined since $s > \frac{1}{2}$), we obtain

$$\begin{aligned}\mathcal{T}_1 &= \sum_{T\in\mathcal{T}_h}(\nabla u,\nabla w_T)_T - \sum_{T\in\mathcal{T}_h}(\sigma_n(u),w_T)_{\partial T} + \sum_{F\in\mathcal{F}_h^{b,N}}(\sigma_n(u),w_F)_F\\ &= \sum_{T\in\mathcal{T}_h}(\nabla u,\nabla w_T)_T - \sum_{T\in\mathcal{T}_h}(\sigma_n(u),w_T - w_{\partial T^\backslash})_{\partial T^\backslash} - \sum_{F\in\mathcal{F}_h^{b,D}}(\sigma_n(u),w_{T(F)})_F.\end{aligned}$$

Comparing with the term $\mathcal{T}_1$ from the consistency proof of the face-based trace scheme, we see that on the right-hand side, the second term is now restricted to $\partial T^\backslash$ and that the third term is thus evaluated using $w_{T(F)}$ instead of w_F. Moreover, using the definition of $R_{T^\backslash}^{k+1}(\hat{w}_T)$, we infer that

$$\begin{aligned}\mathcal{T}_2 = \sum_{T\in\mathcal{T}_h}(\nabla E_{T^\backslash}^{k+1}(u),\nabla w_T)_T - \sum_{T\in\mathcal{T}_h}(\sigma_n(E_{T^\backslash}^{k+1}(u)),w_T - w_{\partial T^\backslash})_{\partial T^\backslash}\\ - \sum_{F\in\mathcal{F}_h^{b,D}}(\sigma_n(E_{T(F)^\backslash}^{k+1}(u)),w_{T(F)})_F.\end{aligned}$$

Consequently, if we define for all $T\in\mathcal{T}_h$ the function $\delta_T := u_{|T} - E_{T^\backslash}^{k+1}(u_{|T})$, we obtain

$$\mathcal{T}_1 - \mathcal{T}_2 = \sum_{T\in\mathcal{T}_h}(\nabla\delta_T,\nabla w_T)_T - \sum_{T\in\mathcal{T}_h}(\sigma_n(\delta_T),w_T - w_{\partial T^\backslash})_{\partial T^\backslash} - \sum_{F\in\mathcal{F}_h^{b,D}}(\sigma_n(\delta_{T(F)}),w_{T(F)})_F.$$

We can now bound $\mathcal{T}_1 - \mathcal{T}_2$ by proceeding as in the analysis of the face version, invoking the Cauchy–Schwarz inequality and recalling the definition of the norm $\|\hat{w}_h\|_{\hat{U}_h^k}$, we infer that

$$|\mathcal{T}_1 - \mathcal{T}_2| \lesssim \left(\sum_{T\in\mathcal{T}_h}\|\delta_T\|_{\sharp,T}^2\right)^{\frac{1}{2}}\|\hat{w}_h\|_{\hat{U}_h^k} \lesssim \left(\sum_{T\in\mathcal{T}_h}\|v-\pi_T^{k+1}(v)\|_{\sharp,T}^2\right)^{\frac{1}{2}}\|\hat{w}_h\|_{\hat{U}_h^k}.$$

where the last bound follows from the approximation result (2.46). Finally, the bound (2.47) on the stabilization operator composed with the reduction operator and the boundedness of $\hat{a}_{T^\backslash}$ imply that

$$\begin{aligned}|\mathcal{T}_3| &\le \left(\sum_{T\in\mathcal{T}_h}\|\eta_{\partial T}^{\frac{1}{2}}S_{\partial T^\backslash}^k(\hat{I}_{T^\backslash}^k(u))\|_{\partial T^\backslash}^2\right)^{\frac{1}{2}}\left(\sum_{T\in\mathcal{T}_h}\|\eta_{\partial T}^{\frac{1}{2}}S_{\partial T^\backslash}^k(\hat{w}_T)\|_{\partial T^\backslash}^2\right)^{\frac{1}{2}}\\ &\lesssim \left(\sum_{T\in\mathcal{T}_h}\|v-\pi_T^{k+1}(v)\|_{\sharp,T}^2\right)^{\frac{1}{2}}\|\hat{w}_h\|_{\hat{U}_h^k}.\end{aligned}$$

Finally, we bound $\mathcal{T}_4$ by means of the Cauchy–Schwarz inequality and observing that $h_{T(F)}^{-\frac{1}{2}}\|u-\pi_{T(F)}^{k+1}(u)\|_F \lesssim \|\nabla(u-\pi_{T(F)}^{k+1}(u))\|_{T(F)}$, as already argued in the proof of Lemma 2.13, and that

$$\begin{aligned}h_{T(F)}^{\frac{1}{2}}\|\eta_\gamma(\hat{w}_{T(F)})\|_F &\le h_{T(F)}^{\frac{1}{2}}\|\sigma_n(R_{T(F)^\backslash}^{k+1}(\hat{w}_{T(F)}))\|_F + \gamma_0 h_{T(F)}^{-\frac{1}{2}}\|w_{T(F)}\|_F\\ &\lesssim \|R_{T(F)^\backslash}^{k+1}(\hat{w}_{T(F)})\|_{T(F)} + h_{T(F)}^{-\frac{1}{2}}\|w_{T(F)}\|_F \lesssim |\hat{w}_T|_{\hat{U}_{T^\backslash}^k} + h_{T(F)}^{-\frac{1}{2}}\|w_{T(F)}\|_F,\end{aligned}$$

owing to the triangle inequality, the discrete trace inequality from Lemma 2.2, and the boundedness of the local bilinear form $\hat{a}_T$ defined in (2.42). This concludes the proof. □

Theorem 2.17 (H^1-error estimate)**.** *Assume that $u\in H^{1+s}(\Omega)$ with $s>\frac{1}{2}$. The following holds true:*

$$\sum_{T\in\mathcal{T}_h}\|\nabla(u-R_{T^\backslash}^{k+1}(\hat{u}_T))\|_T^2 \lesssim \sum_{T\in\mathcal{T}_h}\|u-\pi_T^{k+1}(u)\|_{\sharp,T}^2. \tag{2.56}$$

Consequently, letting $t := \min(k+1, s)$*, we have*

$$\sum_{T\in\mathcal{T}_h} \|\nabla(u - R_{T\setminus}^{k+1}(\hat{u}_T))\|_T^2 \lesssim \sum_{T\in\mathcal{T}_h} h_T^{2t}|u|_{H^{1+t}(T)}^2. \tag{2.57}$$

Proof. The proof of (2.56) uses Lemma 2.16 and proceeds as that of (2.35) for the face-based trace scheme. Finally, the estimate (2.57) is a consequence of (2.56) and Lemma 2.5. □

2.4.4 Numerical results

We consider the Poisson model problem (2.3). The domain Ω is the unit square. The numerical results are compared to the closed-form solution $u(x,y) = \cos(\pi x)\cos(\pi y)$ corresponding to the right-hand side $f(x,y) = 2\pi^2\cos(\pi x)\cos(\pi y)$ and satisfying a homogeneous Dirichlet condition over the whole boundary, i.e. we set $\Gamma_D = \partial\Omega$. We consider uniformly refined sequences of triangular meshes and of hexagonal meshes to illustrate the polyhedral capabilities of Nitsche-HHO.

The errors in the H^1-norm and the convergence rates are reported in Table 2.2 using the face version of Nitsche-HHO. We observe convergence rates that match those predicted by the theory (Theorem 2.12).

Table 2.2: H^1-error and convergence rates for Dirichlet conditions. Face version with $\theta = 1$, $\gamma_0 = 5$ and $k \in \{0,1,2,3\}$.

Triangles								
	$k=0$		$k=1$		$k=2$		$k=3$	
h	error	rate	error	rate	error	rate	error	rate
0.230	7.183e-01		9.291e-02		9.617e-03		5.278e-04	
0.115	3.418e-01	1.071	2.399e-02	1.953	1.241e-03	2.955	3.457e-05	3.932
0.057	1.665e-01	1.037	6.081e-03	1.980	1.569e-04	2.983	2.205e-06	3.971
0.029	8.217e-02	1.019	1.530e-03	1.991	1.971e-05	2.993	1.391e-07	3.986
Hexagons								
	$k=0$		$k=1$		$k=2$		$k=3$	
h	error	rate	error	rate	error	rate	error	rate
0.176	5.385e-01		5.005e-02		3.244e-03		1.438e-04	
0.091	2.633e-01	1.078	1.277e-02	2.059	4.183e-04	3.088	9.295e-06	4.129
0.046	1.299e-01	1.044	3.216e-03	2.038	5.303e-05	3.052	5.898e-07	4.075
0.023	6.446e-02	1.023	8.065e-04	2.021	6.674e-06	3.028	3.713e-08	4.040

We now consider the symmetric and nonsymmetric variants of the cell version of Nitsche-HHO. The errors in the H^1-norm and the convergence rates for the symmetric variant $\theta = 1$ and $\gamma_0 = 5$ are reported in Table 2.3. These results confirm the predictions from Theorem 2.17. The numerical results for the nonsymmetric variants are reported in Table 2.4 ($\theta = 0$ and $\gamma_0 = 1$) and Table 2.5 ($\theta = -1$ and $\gamma_0 = 0$). Notice that for the skew-symmetric method ($\theta = -1$), we consider the penalty-free variant ($\gamma_0 = 0$) and we still observe optimal rates. Though the analysis presented in this paper does not cover this case, our results are in agreement with the analysis presented in [23] for Lagrange and Crouzeix–Raviart finite elements. Moreover, we also performed convergence tests for in the equal-order case ($l = k$), and suboptimal convergence rates were observed (as expected). We do not present these results for the sake of brevity.

2.5 Signorini's conditions with cell-based traces

In this section, we devise and analyze a Nitsche-HHO method to approximate the model problem (2.7) with Signorini's unilateral contact conditions as specified in (2.8). We consider the

Table 2.3: H^1-error and convergence rates for Dirichlet conditions. Cell version with $\theta = 1$, $\gamma_0 = 5$ and $k \in \{0, 1, 2, 3\}$.

Triangles								
	$k=0$		$k=1$		$k=2$		$k=3$	
h	error	rate	error	rate	error	rate	error	rate
0.230	6.179e-01		9.071e-02		9.739e-03		5.222e-04	
0.115	3.188e-01	0.954	2.442e-02	1.893	1.322e-03	2.882	3.570e-05	3.87166
0.057	1.615e-01	0.982	6.323e-03	1.950	1.708e-04	2.952	2.330e-06	3.93836
0.029	8.118e-02	0.992	1.608e-03	1.976	2.167e-05	2.978	1.487e-07	3.97069
Hexagons								
	$k=0$		$k=1$		$k=2$		$k=3$	
h	error	rate	error	rate	error	rate	error	rate
0.176	4.895e-01		4.723e-02		3.150e-03		1.402e-04	
0.091	2.514e-01	1.004	1.239e-02	2.017	4.129e-04	3.063	9.184e-06	4.108
0.046	1.270e-01	1.010	3.168e-03	2.015	5.271e-05	3.042	5.864e-07	4.066
0.023	6.375e-02	1.007	8.005e-04	2.010	6.654e-06	3.024	3.702e-08	4.036

Table 2.4: H^1-error and convergence rates for Dirichlet conditions. Cell version with $\theta = 0$, $\gamma_0 = 1$ and $k \in \{0, 1, 2, 3\}$.

Triangles								
	$k=0$		$k=1$		$k=2$		$k=3$	
h	error	rate	error	rate	error	rate	error	rate
0.230	7.312e-01		9.482e-02		1.128e-02		6.219e-04	
0.115	3.453e-01	1.083	2.486e-02	1.931	1.409e-03	3.001	3.942e-05	3.979
0.057	1.678e-01	1.041	6.375e-03	1.963	1.760e-04	3.001	2.456e-06	4.004
0.029	8.271e-02	1.020	1.614e-03	1.982	2.199e-05	3.001	1.528e-07	4.007
Hexagons								
	$k=0$		$k=1$		$k=2$		$k=3$	
h	error	rate	error	rate	error	rate	error	rate
0.176	5.184e-01		5.140e-02		3.269e-03		1.448e-04	
0.091	2.582e-01	1.050	1.291e-02	2.083	4.196e-04	3.094	9.321e-06	4.134
0.046	1.286e-01	1.030	3.232e-03	2.047	5.311e-05	3.055	5.906e-07	4.077
0.023	6.414e-02	1.016	8.086e-04	2.025	6.678e-06	3.029	3.715e-08	4.041

cell-based trace scheme with a mixed-order, where the cell unknowns are of one order higher than the face unknowns. We assume that the meshes are compatible with the boundary partition $\partial\Omega = \overline{\Gamma_D} \cup \overline{\Gamma_N} \cup \overline{\Gamma_S}$ from (2.6), which leads to the partition of boundary faces as $\mathcal{F}_h^b = \mathcal{F}_h^{b,D} \cup \mathcal{F}_h^{b,N} \cup \mathcal{F}_h^{b,S}$ (with obvious notation). For simplicity, we employ the Nitsche technique only on the subset Γ_S where the nonlinear Signorini conditions are enforced, whereas we resort to a strong enforcement of the homogeneous Dirichlet condition on the subset Γ_D.

2.5.1 Local reconstruction and stability operators

For simplicity, we keep the same notation as in the previous section, although we keep in mind that we are now concerned with the subset Γ_S rather than Γ_D. For all $T \in \mathcal{T}_h$, we identify the (possibly empty) part of its boundary that is not located on the subset Γ_S (where Nitsche's method is employed):

$$\partial T^{\setminus} := \partial T \cap (\overline{\Omega} \setminus \Gamma_S), \tag{2.58}$$

Table 2.5: H^1-error and convergence rates for Dirichlet conditions. Cell version with $\theta = -1$, $\gamma_0 = 0$ and $k \in \{0, 1, 2, 3\}$.

Triangles								
	$k=0$		$k=1$		$k=2$		$k=3$	
h	error	rate	error	rate	error	rate	error	rate
0.230	6.767e-01		9.044e-02		1.019e-02		5.403e-04	
0.115	3.322e-01	1.026	2.426e-02	1.898	1.346e-03	2.920	3.635e-05	3.893
0.057	1.646e-01	1.013	6.298e-03	1.946	1.722e-04	2.967	2.352e-06	3.950
0.029	8.193e-02	1.006	1.604e-03	1.973	2.176e-05	2.985	1.494e-07	3.977
Hexagons								
	$k=0$		$k=1$		$k=2$		$k=3$	
h	error	rate	error	rate	error	rate	error	rate
0.176	5.069e-01		5.029e-02		3.213e-03		1.416e-04	
0.091	2.553e-01	1.034	1.278e-02	2.065	4.165e-04	3.079	9.227e-06	4.117
0.046	1.279e-01	1.022	3.216e-03	2.039	5.293e-05	3.049	5.877e-07	4.069
0.023	6.397e-02	1.012	8.065e-04	2.021	6.668e-06	3.027	3.706e-08	4.038

and we let, as before, $\mathcal{F}_{\partial T^\setminus}$ collect the faces of T located on $\partial T^\setminus$. Let $k \geq 0$ be the polynomial degree. For all $T \in \mathcal{T}_h$, the local discrete space is (we keep the same notation as in the previous section although the support of the face unknowns has changed):

$$\hat{U}_{T^\setminus}^k := \mathbb{P}^{k+1}(T;\mathbb{R}) \times \mathbb{P}^k(\mathcal{F}_{\partial T^\setminus};\mathbb{R}), \tag{2.59}$$

that is, the local face unknowns are only attached to those faces of T that are not located in Γ_S. A generic element in $\hat{U}_{T^\setminus}^k$ is denoted $\hat{v}_T = (v_T, v_{\partial T^\setminus})$ with $v_T \in \mathbb{P}^{k+1}(T;\mathbb{R})$ and $v_{\partial T^\setminus} \in \mathbb{P}^k(\mathcal{F}_{\partial T^\setminus};\mathbb{R})$.

For all $T \in \mathcal{T}_h$, the local reconstruction operator $R_{T^\setminus}^{k+1} : \hat{U}_{T^\setminus}^k \to \mathbb{P}^{k+1}(T;\mathbb{R})$ is still defined by (2.39), and the local stabilization operator $S_{\partial T^\setminus}^k : \hat{U}_{T^\setminus}^k \to \mathbb{P}^k(\mathcal{F}_{\partial T^\setminus};\mathbb{R})$ is still defined by (2.41). The local bilinear form $\hat{a}_{T^\setminus}$ on $\hat{U}_{T^\setminus}^k \times \hat{U}_{T^\setminus}^k$ is still defined by (2.42). We equip the discrete space $\hat{U}_{T^\setminus}^k$ with the H^1-like seminorm $|\cdot|_{\hat{U}_{T^\setminus}^k}$ defined by (2.43), and we recall that the discrete bilinear form $\hat{a}_{T^\setminus}$ satisfies the stability and boundedness properties from Lemma 2.6. We let the local reduction operator $\hat{I}_{T^\setminus}^k : H^1(T) \to \hat{U}_{T^\setminus}^k$ be defined by (2.44), and, as before, we let $E_{T^\setminus}^{k+1} := R_{T^\setminus}^{k+1} \circ \hat{I}_{T^\setminus}^k : H^1(T) \to \mathbb{P}^{k+1}(T;\mathbb{R})$. The approximation properties of $E_{T^\setminus}^{k+1}$ and of $S_{\partial T^\setminus}^k \circ \hat{I}_{T^\setminus}^k$ are those stated in Lemma 2.13.

2.5.2 Discrete problem and well-posedness

The global discrete space is

$$\hat{U}_h^k := \mathbb{P}^{k+1}(\mathcal{T}_h;\mathbb{R}) \times \mathbb{P}^k(\mathcal{F}_h^i \cup \mathcal{F}_h^{b,D} \cup \mathcal{F}_h^{b,N};\mathbb{R}). \tag{2.60}$$

A generic element in $\hat{U}_h^k$ is denoted $\hat{w}_h = ((w_T)_{T\in\mathcal{T}_h}, (w_F)_{F\in\mathcal{F}_h^i\cup\mathcal{F}_h^{b,D}\cup\mathcal{F}_h^{b,N}})$, and for all $T \in \mathcal{T}_h$, we denote by $\hat{w}_T = (w_T, (w_F)_{F\in\mathcal{F}_{\partial T^\setminus}}) \in \hat{U}_{T^\setminus}^k$ the components of $\hat{w}_h$ attached to the mesh cell T and its faces composing $\partial T^\setminus$. We enforce strongly the homogeneous Dirichlet condition on Γ_D by considering the subspace

$$\hat{U}_{h,0}^k := \{\hat{w}_h \in \hat{U}_h^k \mid w_F = 0 \quad \forall F \in \mathcal{F}_h^{b,D}\}.$$

We consider the following discrete Nitsche-HHO problem:

$$\begin{cases} \text{Find } \hat{u}_h \in \hat{U}_{h,0}^k \text{ such that} \\ \hat{a}_{\gamma\theta,h}(\hat{u}_h;\hat{w}_h) = \hat{\ell}_{\gamma\theta,h}(\hat{w}_h) \qquad \forall \hat{w}_h \in \hat{U}_{h,0}^k. \end{cases} \tag{2.61}$$

For all $\hat{v}_h, \hat{w}_h \in \hat{U}_{h,0}^k$, the global discrete semilinear form $\hat{a}_{\gamma\theta,h}$ and the global discrete linear form $\hat{\ell}_{\gamma\theta,h}$ are defined respectively by (compare with (2.12))

$$\hat{a}_{\gamma\theta,h}(\hat{v}_h;\hat{w}_h) := \sum_{T\in\mathcal{T}_h} \hat{a}_T(\hat{v}_T,\hat{w}_T) - \sum_{F\in\mathcal{F}_h^{b,S}} \frac{\theta}{\gamma}\Big(\sigma_n(R_{T(F)^\backslash}^{k+1}(\hat{v}_{T(F)})),\sigma_n(R_{T(F)^\backslash}^{k+1}(\hat{w}_{T(F)}))\Big)_F$$
$$+ \sum_{F\in\mathcal{F}_h^{b,S}} \frac{1}{\gamma}\Big(\Big[\hat{\phi}_\gamma(\hat{v}_{T(F)})\Big]_{\mathbb{R}^-},\hat{\phi}_{\gamma\theta}(\hat{w}_{T(F)})\Big)_F, \tag{2.62a}$$

$$\hat{\ell}_{\gamma\theta,h}(\hat{w}_h) := \sum_{T\in\mathcal{T}_h}(f,w_T)_T + \sum_{F\in\mathcal{F}_h^{b,N}}(g_N,w_F)_F, \tag{2.62b}$$

where

$$\hat{\phi}_{\gamma\theta}(\hat{w}_{T(F)}) := \theta\sigma_n(R_{T(F)^\backslash}^{k+1}(\hat{w}_{T(F)})) - \gamma w_{T(F)}, \tag{2.63a}$$

$$\hat{\phi}_\gamma(\hat{w}_{T(F)}) := \hat{\phi}_{\gamma 1}(\hat{w}_{T(F)}) = \sigma_n(R_{T(F)^\backslash}^{k+1}(\hat{w}_{T(F)})) - \gamma w_{T(F)}. \tag{2.63b}$$

Note that we are employing the trace of the cell unknown in the definition of $\hat{\phi}_{\gamma\theta}$ and $\hat{\phi}_\gamma$.

We equip the space $\hat{U}_{h,0}^k$ with the norm

$$\|\hat{v}_h\|_{\hat{U}_{h,0}^k}^2 := \sum_{T\in\mathcal{T}_h} |\hat{v}_T|_{\hat{U}_{T^\backslash}^k}^2, \qquad \forall \hat{v}_h \in \hat{U}_{h,0}^k, \tag{2.64}$$

with the local seminorms $|\cdot|_{\hat{U}_{T^\backslash}^k}$ defined in (2.43). That $\|\cdot\|_{\hat{U}_{h,0}^k}$ defines a norm on $\hat{U}_{h,0}^k$ follows from the usual arguments, keeping in mind that the subset $\mathcal{F}_h^{b,D}$, where the face unknowns are set to zero, is non-empty. Let us now address the well-posedness of the discrete problem (2.61). As above, we only consider $\theta = 1$. Well-posedness also holds true for $\theta = 0$ (with a less stringent lower bound on γ_0) and for $\theta = -1$ (with the simple requirement that $\gamma_0 > 0$). Let $n^{\mathrm{b,S}}$ be the maximum number of faces in $\mathcal{F}_h^{b,S}$ that a mesh cell can have ($n^{\mathrm{b,S}} \le d$ on simplicial meshes). In what follows, we use the fact that

$$([x]_{\mathbb{R}^-} - [y]_{\mathbb{R}^-})(x-y) \ge ([x]_{\mathbb{R}^-} - [y]_{\mathbb{R}^-})^2 \ge 0, \qquad \forall x,y\in\mathbb{R}. \tag{2.65}$$

Lemma 2.18 (Well-posedness)**.** *Assume that $\theta = 1$ and that $\gamma_0 \ge 2n^{\mathrm{b,S}}C_{\mathrm{dt}}^2$, where C_{dt} results from the discrete trace inequality of Lemma 2.2. Let us set the penalty parameter to $\gamma_{|F} := \gamma_0 h_F^{-1}$, for all $F \in \mathcal{F}_h^{b,S}$. Then the discrete problem* (2.61) *is well-posed.*

Proof. Let us first prove the following monotonicity property: for $\gamma_0 \ge 2n^{\mathrm{b,S}}C_{\mathrm{dt}}^2$, there is $\alpha > 0$, uniform with respect to h, such that, for all $\hat{v}_h, \hat{w}_h \in \hat{U}_{h,0}^k$,

$$\hat{a}_{\gamma 1,h}(\hat{v}_h;\hat{v}_h-\hat{w}_h) - \hat{a}_{\gamma 1,h}(\hat{w}_h;\hat{v}_h-\hat{w}_h) \ge \alpha\|\hat{v}_h-\hat{w}_h\|_{\hat{U}_{h,0}^k}^2 + \Delta\hat{\phi}_\gamma(\hat{v}_h,\hat{w}_h), \tag{2.66}$$

with the shorthand notation

$$\Delta\hat{\phi}_\gamma(\hat{v}_h,\hat{w}_h) := \sum_{F\in\mathcal{F}_h^{b,S}} \frac{1}{\gamma}\Big(\Big[\hat{\phi}_\gamma(\hat{v}_{T(F)})\Big]_{\mathbb{R}^-} - \Big[\hat{\phi}_\gamma(\hat{w}_{T(F)})\Big]_{\mathbb{R}^-}, \hat{\phi}_\gamma(\hat{v}_{T(F)}) - \hat{\phi}_\gamma(\hat{w}_{T(F)})\Big)_F. \tag{2.67}$$

Note that the identity (2.65) implies that $\Delta\hat{\phi}_\gamma(\hat{v}_h,\hat{w}_h) \ge 0$. Moreover, we have

$$\hat{a}_{\gamma 1,h}(\hat{v}_h;\hat{v}_h-\hat{w}_h) - \hat{a}_{\gamma 1,h}(\hat{w}_h;\hat{v}_h-\hat{w}_h)$$
$$= \sum_{T\in\mathcal{T}_h} \hat{a}_{T^\backslash}(\hat{v}_T-\hat{w}_T,\hat{v}_T-\hat{w}_T) - \sum_{F\in\mathcal{F}_h^{b,S}} \frac{h_F}{\gamma_0}\|\sigma_n(R_{T^\backslash}^{k+1}(\hat{v}_{T(F)}-\hat{w}_{T(F)}))\|_F^2 + \Delta\hat{\phi}_\gamma(\hat{v}_h,\hat{w}_h). \tag{2.68}$$

Let us denote by $\mathcal{T}_1$ and $\mathcal{T}_2$ the first two terms on the above right-hand side. We use the lower bound on γ_0 and the discrete trace inequality from Lemma 2.2 to infer that

$$\mathcal{T}_1 + \mathcal{T}_2 \geq \frac{1}{2} \sum_{T \in \mathcal{T}_h} \hat{a}_{T\setminus}(\hat{v}_T - \hat{w}_T, \hat{v}_T - \hat{w}_T),$$

and the stability property of $\hat{a}_{T\setminus}$ in the seminorm $|\cdot|_{\hat{U}^k_{T\setminus}}$ then implies that $\mathcal{T}_1 + \mathcal{T}_2 \geq \alpha \|\hat{v}_h - \hat{w}_h\|^2_{\hat{U}^k_{h,0}}$ for some uniform positive constant α. This proves the monotonicity property (2.66). To infer well-posedness from this property, we use the argument from [21, Corollary 15, p. 126]. Let $(\cdot,\cdot)_{\hat{U}^k_{h,0}}$ denote the inner product associated with the norm $\|\cdot\|_{\hat{U}^k_{h,0}}$. We define the nonlinear operator $B_h : \hat{U}^k_{h,0} \to \hat{U}^k_{h,0}$ so that $(B_h(\hat{v}_h), \hat{w}_h)_{\hat{U}^k_{h,0}} = \hat{a}_{\gamma 1,h}(\hat{v}_h; \hat{w}_h)$, for all $\hat{v}_h, \hat{w}_h \in \hat{U}^k_{h,0}$. We prove as in [40] that B_h is hemicontinuous and, invoking (2.66), we conclude that B_h is a one-to-one operator. □

Remark 2.19. *For $\theta = 1$, the Nitsche-HHO formulation* (2.61) *can be recovered as the first-order optimality condition of the functional*

$$\begin{aligned}\mathcal{J}^S_{h,\gamma}(\hat{v}_h) := \frac{1}{2} \sum_{T \in \mathcal{T}_h} \hat{a}_T(\hat{v}_T, \hat{v}_T) - \sum_{F \in \mathcal{F}^{b,S}_h} \frac{1}{2\gamma} ||\sigma_n(R^{k+1}_{T(F)\setminus}(\hat{v}_{T(F)}))||^2_F \\ + \sum_{F \in \mathcal{F}^{b,S}_h} \frac{1}{2\gamma} || \left[\hat{\phi}_\gamma(\hat{v}_{T(F)})\right]^2_{\mathbb{R}^-} ||^2_F - \sum_{T \in \mathcal{T}_h} (f, w_T)_T - \sum_{F \in \mathcal{F}^{b,N}_h} (g_N, w_F)_F,\end{aligned}$$

for all $\hat{v}_h \in \hat{U}^k_{h,0}$. Lemma 2.18 implies that for γ_0 large enough, $\mathcal{J}^S_{h,\gamma}$ is strongly convex.

2.5.3 Error analysis

The consistency error is defined by

$$\mathcal{E}_h(\hat{w}_h) := \hat{\ell}_{\gamma\theta,h}(\hat{w}_h) - \hat{a}_{\gamma\theta,h}(\hat{I}^k_h(u); \hat{w}_h), \qquad \forall \hat{w}_h \in \hat{U}^k_{h,0}, \tag{2.70}$$

with the global reduction operator $\hat{I}^k_h : H^1_D(\Omega) := \{v \in H^1(\Omega) \mid \gamma_{\partial\Omega}(v)_{|\Gamma_D} = 0\} \to \hat{U}^k_{h,0}$ such that the local components of $\hat{I}^k_h(v)$, for all $v \in H^1_D(\Omega)$, attached to a mesh cell $T \in \mathcal{T}_h$, are $\hat{I}^k_{T\setminus}(v_{|T})$. Owing to the nonlinearity of $\hat{a}_{\gamma\theta,h}$ in its first argument, we will not proceed with the same level of generality as in the linear case by bounding the consistency error acting on an arbitrary test function $\hat{w}_h \in \hat{U}^k_{h,0}$. We will consider more specifically the test function

$$\hat{z}_h := \hat{u}_h - \hat{I}^k_h(u) \in \hat{U}^k_{h,0}. \tag{2.71}$$

We only give proofs for $\theta = 1$; the proofs for the other values $\theta \in \{-1, 0\}$ follow by minor adaptations of the arguments for $\theta = 1$. Recall that $\|v\|^2_{\sharp,T} := \|\nabla v\|^2_T + h_T \|\boldsymbol{n}_T \cdot \nabla v\|^2_{\partial T}$ for any function $v \in H^{1+s}(T)$, $s > \frac{1}{2}$.

Lemma 2.20 (Consistency)**.** *Assume that $u \in H^{1+s}(\Omega)$ with $s > \frac{1}{2}$. Let $\hat{z}_h := \hat{u}_h - \hat{I}^k_h(u)$. There is a uniform constant C such that the following holds true:*

$$\begin{aligned}&\mathcal{E}_h(\hat{z}_h) + \sum_{F \in \mathcal{F}^{b,S}_h} \frac{1}{2\gamma} \left\| [\phi_\gamma(u)]_{\mathbb{R}^-} - \left[\hat{\phi}_\gamma(\hat{u}_{T(F)})\right]_{\mathbb{R}^-} \right\|^2_F \\ &\lesssim \left(\sum_{T \in \mathcal{T}_h} \|u - \pi^{k+1}_T(u)\|^2_{\sharp,T} \right)^{\frac{1}{2}} \|\hat{z}_h\|_{\hat{U}^k_{h,0}} + \sum_{T \in \mathcal{T}_h} \|u - \pi^{k+1}_T(u)\|^2_{\sharp,T} + \Delta\hat{\phi}_\gamma(\hat{u}_h, \hat{I}^k_h(u)),\end{aligned} \tag{2.72}$$

with the notation $\Delta\hat{\phi}_\gamma(\hat{v}_h, \hat{w}_h)$ defined in (2.67)*.*

Proof. Using the PDE and the Neumann boundary condition satisfied by the exact solution u, and since $R_{T^\setminus}^{k+1} \circ \hat{I}_{T^\setminus}^{k} = E_{T^\setminus}^{k+1}$ for all $T \in \mathcal{T}_h$, we have

$$\begin{aligned}\mathcal{E}_h(\hat{z}_h) = &\sum_{T\in\mathcal{T}_h} (-\Delta u, z_T)_T + \sum_{F\in\mathcal{F}_h^{b,N}} (\sigma_n(u), z_F)_F - \sum_{T\in\mathcal{T}_h} \hat{a}_T(\hat{I}_{T^\setminus}^k(u), \hat{z}_T)\\ &+ \sum_{F\in\mathcal{F}_h^{b,S}} \frac{1}{\gamma}\Big(\sigma_n(E_{T(F)^\setminus}^{k+1}(u)), \sigma_n(R_{T(F)^\setminus}^{k+1}(\hat{z}_{T(F)}))\Big)_F\\ &- \sum_{F\in\mathcal{F}_h^{b,S}} \frac{1}{\gamma}\Big(\Big[\hat{\phi}_\gamma(\hat{I}_{T(F)^\setminus}^k(u))\Big]_{\mathbb{R}^-}, \hat{\phi}_\gamma(\hat{z}_{T(F)})\Big)_F.\end{aligned}$$

Adding and subtracting $\sum_{F\in\mathcal{F}_h^{b,S}}(\sigma_n(u), z_{T(F)})_F$, we infer that

$$\mathcal{E}_h(\hat{z}_h) = \mathcal{T}_1 + \mathcal{T}_2,$$

where

$$\mathcal{T}_1 := \sum_{T\in\mathcal{T}_h} (-\Delta u, z_T)_T + \sum_{F\in\mathcal{F}_h^{b,D}\cup\mathcal{F}_h^{b,N}} (\sigma_n(u), z_F)_F + \sum_{F\in\mathcal{F}_h^{b,S}} (\sigma_n(u), z_{T(F)})_F \tag{2.73}$$

$$- \sum_{T\in\mathcal{T}_h} \hat{a}_T(\hat{I}_{T^\setminus}^k(u), \hat{z}_T), \tag{2.74}$$

$$\mathcal{T}_2 := \sum_{F\in\mathcal{F}_h^{b,S}} \frac{1}{\gamma}\Big(\sigma_n(E_{T(F)^\setminus}^{k+1}(u)), \sigma_n(R_{T(F)^\setminus}^{k+1}(\hat{z}_{T(F)}))\Big)_F \tag{2.75}$$

$$- \sum_{F\in\mathcal{F}_h^{b,S}} \frac{1}{\gamma}\Big(\Big[\hat{\phi}_\gamma(\hat{I}_{T(F)^\setminus}^k(u))\Big]_{\mathbb{R}^-}, \hat{\phi}_\gamma(\hat{z}_{T(F)})\Big)_F - \sum_{F\in\mathcal{F}_h^{b,S}} (\sigma_n(u), z_{T(F)})_F, \tag{2.76}$$

where we used in $\mathcal{T}_1$ that z_F is zero for all $F \in \mathcal{F}_h^{b,D}$. We then observe that the term $\mathcal{T}_1$ can be estimated as in the proof of Lemma 2.16 (by letting $\mathcal{F}_h^{b,S}$ play the former role of $\mathcal{F}_h^{b,D}$ and $\mathcal{F}_h^{b,D} \cup \mathcal{F}_h^{b,N}$ play the former role of $\mathcal{F}_h^{b,N}$). This leads to

$$\mathcal{T}_1 = \sum_{T\in\mathcal{T}_h} (\nabla(u - E_{T^\setminus}^{k+1}(u)), \nabla z_T)_T - \sum_{T\in\mathcal{T}_h} (\sigma_n(u - E_{T^\setminus}^{k+1}(u)), z_T - z_{\partial T^\setminus})_{\partial T^\setminus} \tag{2.77}$$

$$- \sum_{T\in\mathcal{T}_h} (\eta_{\partial T} S_{\partial T^\setminus}^k(\hat{I}_{T^\setminus}^k(u)), S_{\partial T^\setminus}^k(\hat{z}_T))_{\partial T^\setminus}. \tag{2.78}$$

so that, owing to the approximation result (2.46)-(2.47), we have

$$|\mathcal{T}_1| \lesssim \left(\sum_{T\in\mathcal{T}_h} \|u - \pi_T^{k+1}(u)\|_{\sharp,T}^2\right)^{\frac{1}{2}} \|\hat{z}_h\|_{\hat{U}_{h,0}^k}.$$

Concerning $\mathcal{T}_2$, we use that $\sigma_n(u) = [\phi_\gamma(u)]_{\mathbb{R}^-}$, and re-arranging terms, we infer that $\mathcal{T}_2 = -\mathcal{T}_{2,1} + \mathcal{T}_{2,2}$, where

$$\mathcal{T}_{2,1} := \sum_{F\in\mathcal{F}_h^{b,S}} \frac{1}{\gamma}\Big(\sigma_n(u - E_{T(F)^\setminus}^{k+1}(u)), \sigma_n(R_{T(F)^\setminus}^{k+1}(\hat{z}_{T(F)}))\Big)_F, \tag{2.79}$$

$$\mathcal{T}_{2,2} := \sum_{F\in\mathcal{F}_h^{b,S}} \frac{1}{\gamma}\Big([\phi_\gamma(u)]_{\mathbb{R}^-} - \Big[\hat{\phi}_\gamma(\hat{I}_{T(F)^\setminus}^k(u))\Big]_{\mathbb{R}^-}, \hat{\phi}_\gamma(\hat{z}_{T(F)})\Big)_F. \tag{2.80}$$

Recalling that $\gamma_{|F} = \gamma_0 h_F^{-1}$, we can bound $\mathcal{T}_{2,1}$ using the approximation result (2.46) together with the discrete trace inequality from Lemma 2.2 as follows:

$$|\mathcal{T}_{2,1}| \lesssim \left(\sum_{T\in\mathcal{T}_h} \|u - \pi_T^{k+1}(u)\|_{\sharp,T}^2\right)^{\frac{1}{2}} \|\hat{z}_h\|_{\hat{U}_{h,0}^k}.$$

Moreover, concerning $\mathcal{T}_{2,2}$, we have $\mathcal{T}_{2,2} = \mathcal{T}_{2,2,1} + \mathcal{T}_{2,2,2} + \mathcal{T}_{2,2,3}$, where

$$\mathcal{T}_{2,2,1} := \sum_{F\in\mathcal{F}_h^{b,S}} \frac{1}{\gamma}\Big(\Big[\hat\phi_\gamma(\hat u_{T(F)})\Big]_{\mathbb{R}^-} - \Big[\hat\phi_\gamma(\hat I^k_{T(F)^\backslash}(u))\Big]_{\mathbb{R}^-}, \hat\phi_\gamma(\hat z_{T(F)})\Big)_F, \tag{2.81}$$

$$\mathcal{T}_{2,2,2} := \sum_{F\in\mathcal{F}_h^{b,S}} \frac{1}{\gamma}\Big([\phi_\gamma(u)]_{\mathbb{R}^-} - \Big[\hat\phi_\gamma(\hat u_{T(F)})\Big]_{\mathbb{R}^-}, \hat\phi_\gamma(\hat u_{T(F)}) - \phi_\gamma(u)\Big)_F, \tag{2.82}$$

$$\mathcal{T}_{2,2,3} := \sum_{F\in\mathcal{F}_h^{b,S}} \frac{1}{\gamma}\Big([\phi_\gamma(u)]_{\mathbb{R}^-} - \Big[\hat\phi_\gamma(\hat u_{T(F)})\Big]_{\mathbb{R}^-}, \phi_\gamma(u) - \hat\phi_\gamma(\hat I^k_{T(F)^\backslash}(u))\Big)_F. \tag{2.83}$$

We have $\mathcal{T}_{2,2,1} = \Delta\hat\phi_\gamma(\hat u_h, \hat I^k_h(u))$ and

$$\mathcal{T}_{2,2,2} \le -\sum_{F\in\mathcal{F}_h^{b,S}} \frac{1}{\gamma}\Big\| [\phi_\gamma(u)]_{\mathbb{R}^-} - \Big[\hat\phi_\gamma(\hat u_{T(F)})\Big]_{\mathbb{R}^-}\Big\|_F^2,$$

where we used the identity (2.65). Moreover, using Young's inequality, we infer that

$$\mathcal{T}_{2,2,3} \le \sum_{F\in\mathcal{F}_h^{b,S}} \frac{1}{2\gamma}\Big\| [\phi_\gamma(u)]_{\mathbb{R}^-} - \Big[\hat\phi_\gamma(\hat u_{T(F)})\Big]_{\mathbb{R}^-}\Big\|_F^2 + \sum_{F\in\mathcal{F}_h^{b,S}} \frac{2}{\gamma}\Big\|\phi_\gamma(u) - \hat\phi_\gamma(\hat I^k_{T(F)^\backslash}(u))\Big\|_F^2, \tag{2.84}$$

and recalling the definitions of ϕ_γ, $\hat\phi_\gamma$, and γ, we have

$$\frac{2}{\gamma}\Big\|\phi_\gamma(u) - \hat\phi_\gamma(\hat I^k_{T(F)^\backslash}(u))\Big\|_F^2 \lesssim h_F\|\boldsymbol{n}_{T(F)}\cdot\nabla(u - E^{k+1}_{T^\backslash}(u))\|_F^2 + h_F^{-1}\|u - \pi^{k+1}_{T(F)}(u)\|_F^2 \tag{2.85}$$

$$\lesssim \|u - \pi^{k+1}_{T(F)}(u)\|^2_{\sharp,T(F)}, \tag{2.86}$$

where we used the approximation result (2.46) to bound the first term on the right-hand side and the arguments in the proof of Lemma 2.13 to bound the second term (implying that $h_F^{-1}\|u - \pi^{k+1}_{T(F)}(u)\|_F^2 \lesssim \|\nabla(u - \pi^{k+1}_{T(F)}(u))\|^2_{T(F)} \lesssim \|u - \pi^{k+1}_{T(F)}(u)\|^2_{\sharp,T(F)}$). Therefore, we obtain

$$\mathcal{T}_{2,2,2} + \mathcal{T}_{2,2,3} \le -\sum_{F\in\mathcal{F}_h^{b,S}} \frac{1}{2\gamma}\Big\| [\phi_\gamma(u)]_{\mathbb{R}^-} - \Big[\hat\phi_\gamma(\hat u_{T(F)})\Big]_{\mathbb{R}^-}\Big\|_F^2 + C\sum_{T\in\mathcal{T}_h}\|u - \pi^{k+1}_T(u)\|^2_{\sharp,T}. \tag{2.87}$$

Putting everything together, we obtain the expected estimate. □

Theorem 2.21 (H^1-error estimate)**.** *Assume that $u \in H^{1+s}(\Omega)$ with $s > \frac{1}{2}$. The following holds true:*

$$\sum_{T\in\mathcal{T}_h}\|\nabla(u - R^{k+1}_{T^\backslash}(\hat u_T))\|_T^2 + \sum_{F\in\mathcal{F}_h^{b,S}} h_{T(F)}\Big\| [\phi_\gamma(u)]_{\mathbb{R}^-} - \Big[\hat\phi_\gamma(\hat u_{T(F)})\Big]_{\mathbb{R}^-}\Big\|_F^2 \lesssim \sum_{T\in\mathcal{T}_h}\|u - \pi^{k+1}_T(u)\|^2_{\sharp,T}. \tag{2.88}$$

Consequently, letting $t := \min(k+1, s)$, we have,

$$\sum_{T\in\mathcal{T}_h}\|\nabla(u - R^{k+1}_{T^\backslash}(\hat u_T))\|_T^2 + \sum_{F\in\mathcal{F}_h^{b,S}} h_{T(F)}\Big\| [\phi_\gamma(u)]_{\mathbb{R}^-} - \Big[\hat\phi_\gamma(\hat u_{T(F)})\Big]_{\mathbb{R}^-}\Big\|_F^2 \lesssim \sum_{T\in\mathcal{T}_h} h_T^{2t}|u|^2_{H^{t+1}(T)}. \tag{2.89}$$

Proof. Recall that $\hat{z}_h = \hat{u}_h - \hat{I}_h^k(u)$. Owing to the monotonicity property (2.66), the definition of the consistency error, and the bound from Lemma 2.20, we infer that

$$\alpha\|\hat{z}_h\|_{\hat{U}_{h,0}^k}^2 + \Delta\hat{\phi}_\gamma(\hat{u}_h, \hat{I}_h^k(u)) + \sum_{F\in\mathcal{F}_h^{b,S}} \frac{1}{2\gamma}\Big\| \left[\phi_\gamma(u)\right]_{\mathbb{R}^-} - \left[\hat{\phi}_\gamma(\hat{u}_{T(F)})\right]_{\mathbb{R}^-} \Big\|_F^2 \tag{2.90}$$

$$\leq \mathcal{E}_h(\hat{z}_h) + \sum_{F\in\mathcal{F}_h^{b,S}} \frac{1}{2\gamma}\Big\| \left[\phi_\gamma(u)\right]_{\mathbb{R}^-} - \left[\hat{\phi}_\gamma(\hat{u}_{T(F)})\right]_{\mathbb{R}^-} \Big\|_F^2 \tag{2.91}$$

$$\leq \left(\sum_{T\in\mathcal{T}_h} \|u - \pi_T^{k+1}(u)\|_{\sharp,T}^2\right)^{\frac{1}{2}} \|\hat{z}_h\|_{\hat{U}_h^k} + \Delta\hat{\phi}_\gamma(\hat{u}_h, \hat{I}_h^k(u)). \tag{2.92}$$

Hence, clearing the term $\Delta\hat{\phi}_\gamma(\hat{u}_h, \hat{I}_h^k(u))$ and invoking Young's inequality leads to the expected bound (2.88). Finally, (2.89) follows from (2.88) and Lemma 2.5. □

Remark 2.22 (Face-based trace version)**.** *The main bottleneck when considering the face-based trace version of the Nitsche-HHO method is to bound the term* $h_F\|\phi_\gamma(u) - \hat{\phi}_\gamma(\hat{I}_{T(F)^\backslash}^k(u))\|_F^2$ *when estimating* $\mathcal{T}_{2,2,3}$*. Indeed, in this case, we end up with a term of the form* $h_F^{-1}\|u - \pi_F^k(u)\|_F^2$*, which is of order* $\mathcal{O}(h^{2k})$*, instead of* $h_F^{-1}\|u - \pi_{T(F)}^{k+1}(u)\|_F^2$*, which is of order* $\mathcal{O}(h^{2(k+1)})$*. Thus, the above analysis for the face version leads to a suboptimal* H^1*-error estimate of order* $\mathcal{O}(h^k)$*. Our numerical experiments, yet, indicate that one can still hope for the optimal rate* $\mathcal{O}(h^{k+1})$*.*

2.5.4 Numerical results

We present here two test cases for Signorini conditions. We consider the model problem (2.7)-(2.8) in two dimensions. To deal with the nonlinearity, we use a semi-smooth Newton solver [3, 97, 116] (see Algorithm 1.

Test case 1: manufactured solution

We build an exact solution using polar coordinates for the model problem (2.7)–(2.8), defined in $\Omega = [-1, 1] \times [-1, 0]$. The closed form solution $u : \Omega \to \mathbb{R}^2$ in polar coordinates is

$$u(r, \theta) = -r^{\frac{11}{2}} \sin\left(\frac{11}{2}\theta\right), \tag{2.93}$$

with a source term $f = 0$. The Signorini boundary is located at the top of the domain $\Gamma_S = [-1, 1] \times \{0\}$, and the transition between contact ($u = 0$) and non-contact ($u < 0$) happens at $(0, 0)$. Appropriate Dirichlet conditions are applied on the remaining boundaries. The exact solution is depicted in Figure 2.6 along with the numerical solution at each barycenter of faces and cells of an hexagonal mesh.

We present in Table 2.7 and Table 2.8 the errors in the H^1-norm and convergence rates using the symmetric variant of Nitsche-HHO ($\theta = 1$) and polynomial degrees up to 3, for the face and the cell versions, respectively. Notice that the analytical solution (2.93) enjoys the needed regularity to expect optimal convergence rates for these polynomial orders. We report the numerical results for the nonsymmetric variants of the cell version in Table 2.9 ($\theta = 0$) and Table 2.10 ($\theta = -1$). In order to match the theoretical lower bound on the penalty parameter, we use $\gamma_0 = (k + 1)(k + 2)$ for $\theta = 1$ and $\gamma_0 = \frac{1}{4}(k + 1)(k + 2)$ for $\theta = 0$. In all cases, the numerical results are in good agreement with the expected asymptotic convergence rates, even for the face version.

We display in Figure 2.11 and Figure 2.12 the H^1-error (left) and the number of iterations (right) as a function of the penalty parameter γ_0 with $k \in \{0, 3\}$ and $\theta \in \{-1, 1\}$. We present the relative errors, using the term $\sum_{T\in\mathcal{T}_h} ||\nabla(R_{T^\backslash}^{k+1} \circ \hat{I}_{T^\backslash}^k(u))||_T$ for normalization. We set a residual convergence threshold of 10^{-9} for the semi-smooth Newton solver. We run our test

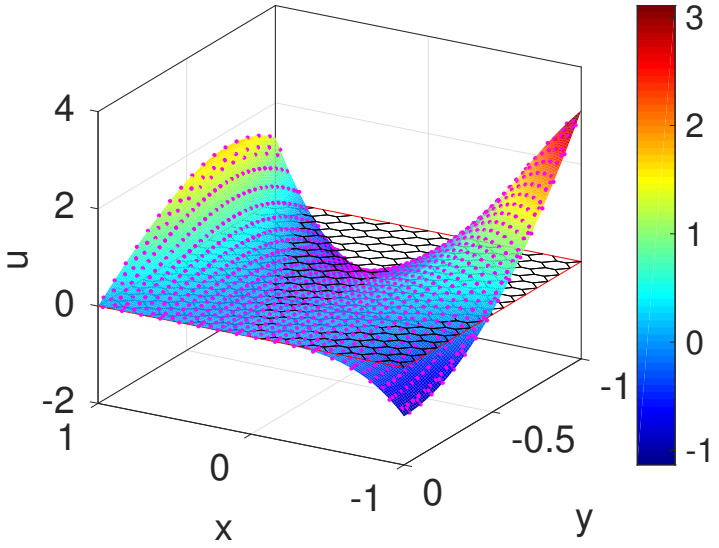

Figure 2.6: Exact solution for Signorini conditions and test case 1. The magenta dots represent the values of the numerical solution at the faces and cells barycenters of an hexagonal mesh (depicted in black). The contact boundary corresponds to the side $\{y = 0\}$.

Table 2.7: Test case 1 for Signorini conditions. H^1-error and convergence rates for the face version with $\theta = 1$, $\gamma_0 = (k+1)(k+2)$ and $k \in \{0, 1, 2, 3\}$.

Triangles								
	$k=0$		$k=1$		$k=2$		$k=3$	
h	error	rate	error	rate	error	rate	error	rate
0.168	1.311e+00		1.727e-01		1.68e-02		2.606e-04	
0.084	7.144e-01	0.876	4.588e-02	1.912	1.403e-03	3.058	1.667e-05	3.966
0.042	3.741e-01	0.933	1.186e-02	1.951	1.654e-04	3.084	1.054e-06	3.984
Hexagons								
	$k=0$		$k=1$		$k=2$		$k=3$	
h	error	rate	error	rate	error	rate	error	rate
0.622	3.621e+00		1.576e+00		2.262e-01		2.517e-02	
0.338	2.564e+00	0.566	4.494e-01	2.058	3.973e-02	3.327	1.809e-03	4.342
0.177	1.508e+00	0.824	1.190e-01	2.063	3.814e-03	3.188	1.214e-04	4.203
0.091	8.179e-01	0.918	3.057e-02	2.039	4.835e-04	3.100	7.856e-06	4.112

over a coarse uniform triangulation with meshsize $h = 0.168$ and a coarse hexagonal mesh with meshsize $h = 0.622$. For the value $\theta = 0$, and the lowest values of γ_0, we observed a severe degradation on the semi-smooth Newton convergence, and therefore the corresponding results are not reported. For triangular meshes, and for a wide range of values, the parameter γ_0 has almost no influence on the H^1-error. Also, the number of Newton iterations is almost independent of θ, and, as expected, depends mostly of the order k and the value of γ_0. Remark that for $k = 3$, the number of iterations increases notably when γ_0 is increased. For hexagonal meshes, γ_0 has a stronger influence, especially in the case $\theta = 1$. For instance, when $k = 3$, the semi-smooth Newton solver does not provide a good approximation if $\gamma_0 = 10^{-1}$ and does not even converge if γ_0 is taken smaller and below a threshold of approximatively 10^{-2}. This emphasizes the role of the shape of the cells on the constant C_{dt} involved in Lemma 2.18 (well-posedness).

Table 2.8: Test case 1 for Signorini conditions. H^1-error and convergence rates for the cell version with $\theta = 1$, $\gamma_0 = (k+1)(k+2)$ and $k \in \{0,1,2,3\}$.

Triangles								
	$k=0$		$k=1$		$k=2$		$k=3$	
h	error	rate	error	rate	error	rate	error	rate
0.168	1.338e+00		1.948e-01		1.377e-02		2.937e-04	
0.084	7.268e-01	0.880	5.210e-02	1.903	1.789e-03	2.944	1.917e-05	3.938
0.042	3.802e-01	0.935	1.356e-02	1.942	2.220e-04	3.010	1.220e-06	3.973
Hexagons								
	$k=0$		$k=1$		$k=2$		$k=3$	
h	error	rate	error	rate	error	rate	error	rate
0.622	3.708e+00		1.719e+00		2.2488e-01		2.582e-02	
0.338	2.613e+00	0.574	4.775e-01	2.100	3.142e-02	3.393	1.828e-03	4.342
0.177	1.525e+00	0.837	1.233e-01	2.101	3.927e-03	3.229	1.219e-04	4.203
0.091	8.226e-01	0.926	3.117e-02	2.064	4.907e-04	3.121	7.872e-06	4.112

Table 2.9: Test case 1 for Signorini conditions. H^1-error and convergence rates for the cell version with $\theta = 0$, $\gamma_0 = \frac{1}{4}(k+1)(k+2)$ and $k \in \{0,1,2,3\}$.

Triangles								
	$k=0$		$k=1$		$k=2$		$k=3$	
h	error	rate	error	rate	error	rate	error	rate
0.168	1.338e+00		1.944e-01		9.741e-03		2.880e-04	
0.084	7.271e-01	0.880	5.206e-02	1.901	1.265e-03	2.945	1.896e-05	3.925
0.042	3.803e-01	0.935	1.355e-02	1.942	1.609e-04	2.975	1.214e-06	3.964
Hexagons								
	$k=0$		$k=1$		$k=2$		$k=3$	
h	error	rate	error	rate	error	rate	error	rate
0.622	3.663e+00		1.719e+00		2.478e-01		2.526e-02	
0.338	2.604e+00	0.560	4.773e-01	2.101	3.129e-02	3.393	1.815e-03	4.317
0.177	1.522e+00	0.834	1.233e-01	2.101	3.918e-03	3.226	1.216e-04	4.197
0.091	8.218e-01	0.924	3.117e-02	2.064	4.901e-04	3.119	7.864e-06	4.109

A second test–case

We now consider a test case described in [13] (see also [29]) on the unit square $\Omega = (0,1)^2$. The contact boundary is located at the bottom of the domain $\Gamma_S = [0,1] \times \{0\}$, whereas an homogeneous Dirichlet condition is applied at the top boundary $\Gamma_D = [0,1] \times \{1\}$. On the remaining parts of the boundary, homogeneous Neumann boundary conditions are applied, i.e. $\Gamma_N = (\{0\} \times [0,1]) \cup (\{1\} \times [0,1])$. The expression for the source term is $f = 2\pi \sin(2\pi x)$.

There is no closed-form solution to this problem up to our knowledge, so that the reference solution is computed using a very fine triangulation with mesh size $h = 0.005$ and with quadratic and cubic polynomials on the faces and in the cells, respectively. A transition between contact ($u = 0$) and non-contact ($u < 0$) on Γ_S has been reported numerically in [13, 29], as well as optimal convergence rates in L^2- and H^1-norms for piecewise linear finite elements. We depict in Figure 2.13 our numerical solution, which matches (qualitatively) the one presented in [29]. We present H^1-errors and convergence rates in Table 2.14 with polynomials of order $k \in \{0,1,2\}$. Remark that for $k \in \{1,2\}$ the convergence rates are below the optimal value of $k+1$, due to the limited regularity of the exact solution, which is expected to be $H^{\frac{5}{2}-\varepsilon}, \varepsilon > 0$, in the neighborhood of Γ_S (see, e.g., [109]).

Table 2.10: Test case 1 for Signorini conditions. H^1-error and convergence rates for the cell version with $\theta = -1$, $\gamma_0 = 0.005$ and $k \in \{0, 1, 2, 3\}$.

Triangles								
	$k=0$		$k=1$		$k=2$		$k=3$	
h	error	rate	error	rate	error	rate	error	rate
0.168	1.311e+00		1.733e-01		8.645e-03		1.801e-04	
0.084	7.144e-01	0.876	4.601e-02	1.931	1.105e-03	2.968	1.149e-05	3.970
0.042	3.741e-01	0.933	1.189e-02	1.953	1.391e-04	2.989	7.231e-07	3.990
Hexagons								
	$k=0$		$k=1$		$k=2$		$k=3$	
h	error	rate	error	rate	error	rate	error	rate
0.622	3.640e+00		1.721e+00		2.487e-01		2.538e-02	
0.338	2.599e+00	0.552	4.780e-01	2.100	3.151e-02	3.387	1.824e-03	4.317
0.177	1.522e+00	0.831	1.235e-01	2.101	3.943e-03	3.227	1.219e-04	4.200
0.091	8.221e-01	0.924	3.121e-02	2.065	4.920e-04	3.123	7.875e-06	4.111

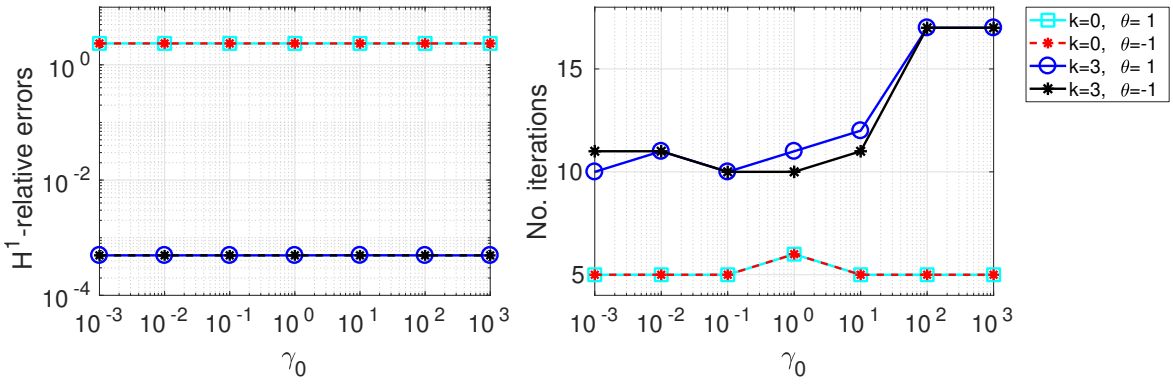

Figure 2.11: Influence of the penalty parameter γ_0 on the H^1-relative errors (left) and the number of semi-smooth Newton iterations (right). Triangular mesh with size $h = 0.168$, $\theta \in \{-1, 1\}$ and $k \in \{0, 3\}$.

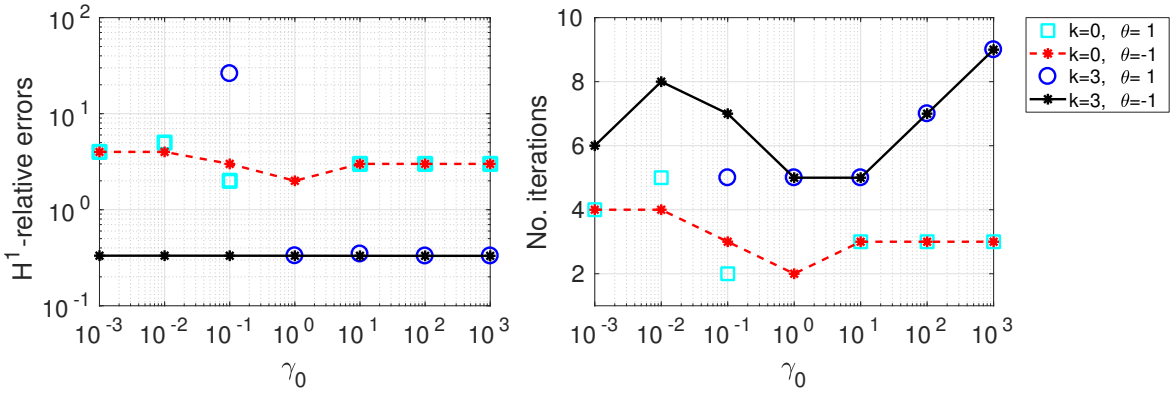

Figure 2.12: Influence of the penalty parameter γ_0 on the H^1-relative errors (left) and the number of semi-smooth Newton iterations (right). Hexagonal mesh with mesh-size $h = 0.622$, $\theta \in \{-1, 1\}$ and $k \in \{0, 3\}$.

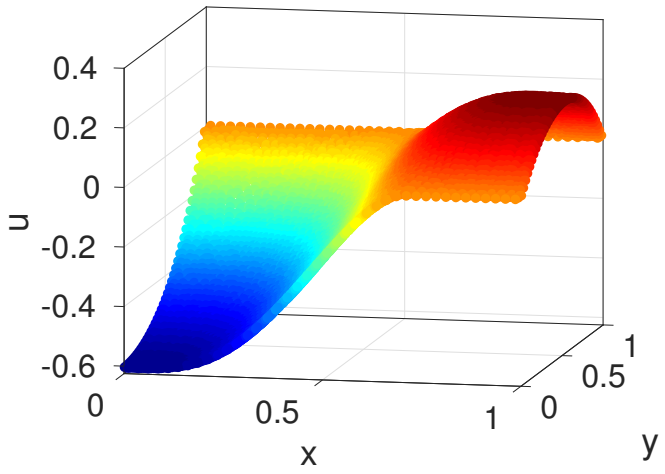

Figure 2.13: Computed numerical solution for Signorini conditions and test case 2.

Table 2.14: Test case 2 for Signorini conditions. H^1-errors and convergence rates. Cell version with $\theta = 1$ and $\gamma_0 = 10$.

	$k=0$		$k=1$		$k=2$	
h	error	rate	error	rate	error	rate
0.168	2.492e-01		3.734e-02		9.746e-03	
0.084	1.275e-01	0.967	9.794e-03	1.931	2.938e-03	1.730
0.042	6.445e-02	0.984	2.666e-03	1.877	1.143e-03	1.361
0.021	3.240e-02	0.992	7.754e-04	1.781	3.409e-04	1.746

Chapter 3

A lowest-order adaptive method for Bingham antiplanar flows

Contents

We devise a hybrid lowest-order discretization method for Bingham antiplanar flows, where the velocity is discretized by means of one unknown per mesh face and one unknown per mesh cell. The cell unknowns can be eliminated locally by static condensation. The main advantages of this hybrid discretization method are local conservativity and the possibility to use polygonal/polyhedral meshes. We exploit this feature in the context of adaptive mesh refinement to capture the yield surface by means of local mesh refinement and possible coarsening by agglomeration in the unyielded region. We consider the augmented Lagrangian method to solve iteratively the variational inequalities, using piecewise constant vector fields for the auxiliary variable and the associated Lagrange multiplier. Numerical results are presented in pipes with circular and eccentric annulus cross-section for different Bingham numbers. Analytical solutions are available for the first test case, whereas for the second test case, we compare our results to those in [124, 127].

This chapter is organized as follows. In Section 3.1, we present the model problem and we recall the Augmented Lagrangian setting. In Section 3.2, we describe the discrete formulation and the discrete augmented Lagrangian method. In Section 3.3, we outline the adaptive algorithm for the detection of the yield surface. Finally, in Section 3.4 we present our numerical results on Bingham antiplanar flows.

3.1 Introduction

The goal of the present chapter is to devise a hybrid discretization method of the velocity field to accurately track the yield surface using adaptive mesh refinement. Hybrid discretization

methods are formulated in terms of discrete unknowns attached to mesh faces. Cell-based unknowns are also introduced, but they are eliminated locally by a Schur complement technique known as static condensation. Salient examples of hybrid discretization methods include in the lowest-order case are Hybrid Finite Volumes (HFV) [70] and Mimetic Finite Differences (MFD) [22] (a unifying viewpoint between these two methods within the broad family of Hybrid-Mixed-Mimetic methods is developed in [64]), and in the higher-order case, Hybridizable Discontinuous Galerkin (HDG) methods [52] and Hybrid High-Order (HHO) methods [62, 59]. HHO and HDG methods have been bridged in [51], whereas in the lowest-order case, HHO methods are closely related to HFV methods, up to an equivalent choice of stabilization (see [62, Section 2.5] for further insight).

In this chapter, we consider a hybrid lowest-order discretization method. The present method can be recovered by setting the polynomial degree $k = 0$ in the HHO method. Specifically, the velocity unknown is approximated by a pair of discrete unknowns, consisting of a collection of values attached to the mesh faces and a collection of values attached to the mesh cells. In addition, we consider piecewise constant vector fields for the proxy of the strain rate vector and the associated Lagrange multiplier. We do not consider higher-order approximations in this chapter; such approximations (for $k = 1$) are considered in Chapter 4. The resulting discrete variational inequalities are solved using the Alternating Direction Method of Multipliers (ADMM) [79, 75].

Let us briefly outline the simplified version of the Bingham flow model for a viscoplastic fluid in pipes and the corresponding Augmented Lagrangian formulation. Let $\Omega \subset \mathbb{R}^2$ denote the cross-section of the pipe; Ω is an open, bounded, connected subset of $\mathbb{R}^2$ with a Lipschitz boundary. Given an external uni-directional force field $f : \Omega \to \mathbb{R}$ aligned with the transverse direction to the cross-section, and considering, for simplicity, homogeneous Dirichlet boundary conditions, the Bingham antiplanar flow model consists of looking for the stress vector field $\boldsymbol{\sigma} : \Omega \to \mathbb{R}^2$ and the uni-directional velocity field $u : \Omega \to \mathbb{R}$ such that

$$\begin{aligned} \nabla{\cdot}\boldsymbol{\sigma} + f &= 0 \qquad \text{in } \Omega, \\ u &= 0 \qquad \text{on } \partial\Omega, \end{aligned} \tag{3.1}$$

with the constitutive equation

$$\begin{cases} \boldsymbol{\sigma} = \mu\nabla u + \sigma_0 \dfrac{\nabla u}{|\nabla u|_{\ell^2}} & \text{for } |\boldsymbol{\sigma}|_{\ell^2} > \sigma_0, \\ \nabla u = \mathbf{0} & \text{for } |\boldsymbol{\sigma}|_{\ell^2} \le \sigma_0, \end{cases} \tag{3.2}$$

with $\mu > 0$ and $\sigma_0 > 0$ denoting, respectively, the shear viscosity and the shear yield stress and $|\boldsymbol{\tau}|_{\ell^2}$ denoting the Euclidean norm of any vector $\boldsymbol{\tau} \in \mathbb{R}^2$. The region where $|\boldsymbol{\sigma}|_{\ell^2} > \sigma_0$ is called the yielded zone and corresponds to liquid behavior, whereas the region where $|\boldsymbol{\sigma}|_{\ell^2} \le \sigma_0$ is called the unyielded zone and corresponds to solid behavior. The yield surface where $|\boldsymbol{\sigma}|_{\ell^2} = \sigma_0$ separates the two regions. The yield surface is not known a priori, and its prediction is an important aspect of viscoplastic flow simulation.

Remark 3.1 (Derivation from the full Bingham flow model)**.** *We recall from Chapter 1 that the Bingham flow model consists of looking for the total symmetric stress tensor field* $\boldsymbol{\sigma}_{\mathrm{tot}} : \Omega \to \mathbb{R}^{d\times d}_{\mathrm{s}}$ *(with* $d = 3$*) and the velocity field* $\boldsymbol{u} : \Omega \to \mathbb{R}^d$ *such that*

$$\begin{aligned} \nabla{\cdot}\boldsymbol{\sigma}_{\mathrm{tot}} + \boldsymbol{f} &= \mathbf{0} \qquad \textit{in } \Omega, \\ \nabla{\cdot}\boldsymbol{u} &= 0 \qquad \textit{in } \Omega, \\ \boldsymbol{u} &= \mathbf{0} \qquad \textit{on } \partial\Omega. \end{aligned} \tag{3.3}$$

The constitutive equation involves a von Mises criterion, i.e., a threshold on the norm of the deviatoric part of the stress tensor $\boldsymbol{\sigma} = \boldsymbol{\sigma}_{\mathrm{tot}} - \frac{1}{d}\mathtt{tr}(\boldsymbol{\sigma}_{\mathrm{tot}})\boldsymbol{I}_d$ *with* $\boldsymbol{I}_d$ *the identity tensor of* $\mathbb{R}^{d\times d}$*.*

Specifically, $\boldsymbol{\sigma}$ is related to the symmetric velocity gradient $\nabla_{\mathrm{s}}\boldsymbol{u} = \frac{1}{2}(\nabla\boldsymbol{u} + \nabla\boldsymbol{u}^{\mathrm{T}})$ as follows:

$$\begin{cases} \boldsymbol{\sigma} = 2\mu\nabla_{\mathrm{s}}\boldsymbol{u} + \sqrt{2}\sigma_0\dfrac{\nabla_{\mathrm{s}}\boldsymbol{u}}{|\nabla_{\mathrm{s}}\boldsymbol{u}|_{\ell^2}} & \text{for } |\boldsymbol{\sigma}|_{\ell^2} > \sqrt{2}\sigma_0, \\ \nabla_{\mathrm{s}}\boldsymbol{u} = \boldsymbol{0} & \text{for } |\boldsymbol{\sigma}|_{\ell^2} \le \sqrt{2}\sigma_0, \end{cases} \tag{3.4}$$

with $|\boldsymbol{\tau}|_{\ell^2} = \sqrt{\boldsymbol{\tau} : \boldsymbol{\tau}}$ now denoting the Frobenius norm for any tensor $\boldsymbol{\tau} \in \mathbb{R}^{d\times d}$. In the specific situation of pipe flows, the model problem can be simplified by assuming that the velocity field is a divariate uni-directional field, that is, $\Omega \subset \mathbb{R}^2$ now denotes the cross-section of the pipe, and letting $\boldsymbol{x} = (x, y)$ be the position vector in Ω, we have

$$\boldsymbol{u}(\boldsymbol{x}) = (0, 0, u(\boldsymbol{x}))^{\mathrm{T}}, \qquad 2\nabla_{\mathrm{s}}\boldsymbol{u} = \left[\begin{array}{c:c} \boldsymbol{0} & \nabla u \\ \hdashline \nabla u^{\mathrm{T}} & 0 \end{array}\right]. \tag{3.5}$$

Let us denote with $\boldsymbol{\sigma}_{(3.4)} \in \mathbb{R}^{3\times 3}_s$ the symmetric stress tensor satisfying (3.4) and by $\boldsymbol{\sigma}_{(3.2)} \in \mathbb{R}^2$ the stress vector satisfying (3.2). Then, we readily verify that

$$\boldsymbol{\sigma}_{(3.4)} = \left[\begin{array}{c:c} \boldsymbol{0} & \boldsymbol{\sigma}_{(3.2)} \\ \hdashline \boldsymbol{\sigma}_{(3.2)}^{\mathrm{T}} & 0 \end{array}\right], \tag{3.6}$$

so that $(0, 0, \nabla\cdot\boldsymbol{\sigma}_{(3.2)})^{\mathrm{T}} = \nabla\cdot\boldsymbol{\sigma}_{(3.4)} = -\boldsymbol{f} = -(0, 0, f)^{\mathrm{T}}$.

Let $L^2(\Omega)$ denote the space of square-integrable functions over Ω and let us set $\boldsymbol{L}^2(\Omega) := L^2(\Omega;\mathbb{R}^2)$. The inner product in both spaces is denoted $(\cdot,\cdot)_\Omega$ and the associated norm $\|\cdot\|_\Omega$. Let $H^1_0(\Omega)$ denote the space of functions from the Sobolev space $H^1(\Omega)$ (that is, functions from $L^2(\Omega)$ whose weak gradient is in $\boldsymbol{L}^2(\Omega)$) with null trace on $\partial\Omega$. Assuming $f \in L^2(\Omega)$, it is well-known that the velocity field solving (3.1)-(3.2) is the unique minimizer in $H^1_0(\Omega)$ of the following energy functional:

$$u = \underset{v\in H^1_0(\Omega)}{\arg\min}\,\{(H(\nabla v), 1)_\Omega - (f, v)_\Omega\}, \tag{3.7}$$

with the dissipation potential $H : \mathbb{R}^2 \to \mathbb{R}$ such that

$$H(\boldsymbol{g}) = \frac{\mu}{2}|\boldsymbol{g}|^2_{\ell^2} + \sigma_0|\boldsymbol{g}|_{\ell^2}, \qquad \forall \boldsymbol{g} \in \mathbb{R}^2. \tag{3.8}$$

The first term in the right-hand side of (3.8) evaluated with $\boldsymbol{g} = \nabla v$ represents the viscous dissipation potential and the second term the plastic dissipation potential. The weak form of (3.1) together with (3.2) is

$$(\boldsymbol{\sigma}, \nabla v)_\Omega = (f, v)_\Omega \quad \forall v \in H^1_0(\Omega), \tag{3.9}$$

where the stress vector $\boldsymbol{\sigma}$ is in the sub-differential

$$\partial H(\nabla u) = \{\boldsymbol{\tau} \in \mathbb{R}^2 \mid H(\boldsymbol{j}) - H(\nabla u) \ge \boldsymbol{\tau}\cdot(\boldsymbol{j} - \nabla u), \quad \forall \boldsymbol{j} \in \mathbb{R}^2\}. \tag{3.10}$$

Note that u is uniquely defined, whereas $\boldsymbol{\sigma}$ is uniquely defined only in the fluid regions where $|\boldsymbol{\sigma}|_{\ell^2} > \sigma_0$.

The minimization problem (3.7) can be tackled by decomposition-coordination methods. To decouple the nonlinearity from the velocity field, one introduces an auxiliary field $\boldsymbol{\gamma} \in \boldsymbol{L}^2(\Omega)$, and one enforces that $\boldsymbol{\gamma} = \nabla u$ by means of the Lagrange multiplier $\boldsymbol{\sigma} \in \boldsymbol{L}^2(\Omega)$ (which turns out to be indeed the stress vector) together with a least-squares penalty term. Let us set

$$X(\Omega) := H^1_0(\Omega) \times \boldsymbol{L}^2(\Omega) \times \boldsymbol{L}^2(\Omega). \tag{3.11}$$

The augmented Lagrangian is defined as $\mathcal{L} : X(\Omega) \to \mathbb{R}$ such that

$$\mathcal{L}(u, \boldsymbol{\gamma}, \boldsymbol{\sigma}) := (H(\boldsymbol{\gamma}), 1)_\Omega + (\boldsymbol{\sigma}, \nabla u - \boldsymbol{\gamma})_\Omega + \frac{\alpha}{2}\|\nabla u - \boldsymbol{\gamma}\|_\Omega^2 - (f, u)_\Omega, \tag{3.12}$$

where $\alpha > 0$ is the augmentation parameter. The triplet $(u, \boldsymbol{\gamma}, \boldsymbol{\sigma}) \in X(\Omega)$ is a saddle-point of the Lagrangian $\mathcal{L}$, that is to say, $\mathcal{L}(u, \boldsymbol{\gamma}, \boldsymbol{\tau}) \leq \mathcal{L}(u, \boldsymbol{\gamma}, \boldsymbol{\sigma}) \leq \mathcal{L}(v, \boldsymbol{\delta}, \boldsymbol{\sigma})$ for all $(v, \boldsymbol{\delta}, \boldsymbol{\tau}) \in X(\Omega)$, if and only if $\boldsymbol{\gamma} = \nabla u$ and the pair $(\boldsymbol{\sigma}, u)$ solves (3.1) and (3.2).

The ALG2 iterative method [77] minimizes first the augmented Lagrangian $\mathcal{L}$ jointly with respect to the pair $(u, \boldsymbol{\gamma})$ and then updates at each iteration the Lagrange multiplier $\boldsymbol{\sigma}$. The idea in the ADMM is that the joint minimization is replaced by a successive minimization with respect to $\boldsymbol{\gamma}$ and then to u. Let the superscript $n \geq 0$ denote the iteration index in the ADMM. Given the initial values $u^0 \in H_0^1(\Omega)$ and $\boldsymbol{\sigma}^0 \in \boldsymbol{L}^2(\Omega)$, we perform, for all $n \geq 0$, the three steps in Algorithm 3.

Algorithm 3 Antiplanar Bingham flows: ADMM in continuous form

1: Choose $(u^0, \boldsymbol{\sigma}^0) \in H_0^1(\Omega) \times \boldsymbol{L}^2(\Omega)$
2: Choose $\epsilon > 0$, set $R^0 = \infty$ and $n = 0$
3: **while** $R^n > \epsilon$ **do**
4: ***Step 1:*** Given $u^n \in H_0^1(\Omega)$ and $\boldsymbol{\sigma}^n \in \boldsymbol{L}^2(\Omega)$, we define the field $\boldsymbol{\gamma}^{n+1} \in \boldsymbol{L}^2(\Omega)$ pointwise (a.e.) in Ω as follows:

$$\boldsymbol{\gamma}^{n+1} := \begin{cases} \dfrac{1}{(\alpha+\mu)}\left(|\boldsymbol{\theta}^n|_{\ell^2} - \sigma_0\right)\dfrac{\boldsymbol{\theta}^n}{|\boldsymbol{\theta}^n|_{\ell^2}} & \text{if } |\boldsymbol{\theta}^n|_{\ell^2} > \sigma_0, \\ \mathbf{0} & \text{if } |\boldsymbol{\theta}^n|_{\ell^2} \leq \sigma_0, \end{cases} \tag{3.13}$$

where $\boldsymbol{\theta}^n := \boldsymbol{\sigma}^n + \alpha\nabla u^n$. A straightforward computation shows that we are actually enforcing $\partial_{\boldsymbol{\gamma}}\mathcal{L}(u^n, \boldsymbol{\gamma}^{n+1}, \boldsymbol{\sigma}^n) = 0$.
5: ***Step 2:*** We seek $u^{n+1} \in H_0^1(\Omega)$ solving the following variational problem where the stress terms are treated as explicit force terms:

$$\alpha(\nabla u^{n+1}, \nabla v)_\Omega = (f, v)_\Omega - (\boldsymbol{\sigma}^n - \alpha\boldsymbol{\gamma}^{n+1}, \nabla v)_\Omega, \quad \forall v \in H_0^1(\Omega), \tag{3.14}$$

which amounts to enforcing $\partial_u\mathcal{L}(u^{n+1}, \boldsymbol{\gamma}^{n+1}, \boldsymbol{\sigma}^n) = 0$.
6: ***Step 3:*** Finally, we update the Lagrange multiplier $\boldsymbol{\sigma}^{n+1} \in \boldsymbol{L}^2(\Omega)$ by setting

$$\boldsymbol{\sigma}^{n+1} := \boldsymbol{\sigma}^n + \alpha(\nabla u^{n+1} - \boldsymbol{\gamma}^{n+1}). \tag{3.15}$$

As the ADMM approaches convergence, we have $(\nabla u^{n+1} - \boldsymbol{\gamma}^{n+1}) \to \mathbf{0}$ so that $\partial_{\boldsymbol{\sigma}}\mathcal{L}(u^{n+1}, \boldsymbol{\gamma}^{n+1}, \boldsymbol{\sigma}^{n+1}) \to 0$.
7: We evaluate

$$R^{n+1} := \left(\|\boldsymbol{\sigma}^{n+1} - \boldsymbol{\sigma}^n\|_\Omega^2 + \alpha^2\|\nabla u^{n+1} - \nabla u^n\|_\Omega^2\right)^{\frac{1}{2}}. \tag{3.16}$$

8: $n = n + 1$
9: **end while**

3.2 Hybrid lowest-order discretization

In this section, we describe the hybrid lowest-order discretization method for our model problem, together with the resulting discrete augmented Lagrangian and the ADMM.

3.2.1 Discrete minimization problem on the velocity

We employ a hybrid lowest-order discretization method [62, 70, 64], with scalar velocity u approximated by a pair of discrete unknowns, consisting of a collection of scalar unknowns attached to the mesh faces and a collection of scalar unknowns attached to the mesh cells. The auxiliary variable $\boldsymbol{\gamma}$ and the Lagrange multiplier (or stress) $\boldsymbol{\sigma}$ are both discretized by a collection of vector unknowns attached to the mesh cells. One key advantage of considering a hybrid lowest-order discretization method is that all the discrete vector fields are piecewise constant on the mesh, which substantially facilitates the enforcement at the discrete level of Step 1 in Algorithm 4.

We consider a mesh sequence $(\mathcal{T}_\ell)_{\ell\in\mathbb{N}}$ where, for all $\ell \in \mathbb{N}$, $\mathcal{T}_\ell$ is a finite collection of nonempty, disjoint, open cells whose closures either cover Ω exactly or cover a close approximation thereof $\overline{\Omega}_\ell = \cup_{T\in\mathcal{T}_\ell}\overline{T}$ if Ω has curved boundaries. The subscript ℓ typically refers to a step in an adaptive mesh procedure which can involve local mesh refinement (and possibly coarsening). A generic mesh cell is denoted T, its boundary ∂T, its diameter h_T, and its unit outward normal $\boldsymbol{n}_T$. The mesh cells can have a polygonal shape, and the meshes can possess hanging nodes. We set $h_\ell := \min_{T\in\mathcal{T}_\ell} h_T$ (we consider the minimum value instead of the more usual maximum value since the meshes are locally refined). The mesh sequence is assumed to be shape-regular in the sense, e.g., of [59], meaning that every mesh $\mathcal{T}_\ell$ admits a simplicial matching refinement belonging to a shape-regular mesh sequence in the sense of Ciarlet. This assumption can be relaxed to allow for polygonal meshes with some face degeneration as in [32]; this is useful for instance when considering agglomeration-based mesh coarsening procedures. We say that the one-dimensional subset $F \subset \overline{\Omega}$ is a mesh interface (resp., mesh boundary face) if there are two distinct mesh cells $T_{F,1}, T_{F,2} \in \mathcal{T}_\ell$ and an affine hyperplane H_F so that $F = \partial T_{F,1} \cap \partial T_{F,2} \cap H_F$ (resp., there is a mesh cell $T_F \in \mathcal{T}_\ell$ and an affine hyperplane H_F so that $F = \partial T_F \cap \partial\Omega_\ell \cap H_F$, where $\Omega_\ell := \mathrm{int}(\bigcup_{T\in\mathcal{T}_\ell}\overline{T})$). Mesh interfaces are collected in the set $\mathcal{F}_\ell^i$, mesh boundary faces in $\mathcal{F}_\ell^b$, and we let $\mathcal{F}_\ell := \mathcal{F}_\ell^i \cup \mathcal{F}_\ell^b$ be the collection of the mesh faces. The diameter of a mesh face $F \in \mathcal{F}_\ell$ is denoted by h_F. For all $T \in \mathcal{T}_\ell$, we let $\mathcal{F}_{\partial T} := \{F \in \mathcal{F}_\ell \,|\, F \subset \partial T\}$ be the collection of the mesh faces composing ∂T. For all $F \in \mathcal{F}_{\partial T}$, $\boldsymbol{n}_{T,F}$ is defined as the unit normal to F pointing outward T; notice that, by definition, $\boldsymbol{n}_{T,F}$ is a constant vector over F. Let $A \subset \overline{\Omega}_\ell$ be a mesh cell, its boundary, or one of its faces; the inner product in $L^2(A)$ and in $\boldsymbol{L}^2(A) := L^2(A;\mathbb{R}^2)$ is denoted $(\cdot,\cdot)_A$ and the associated norm $\|\cdot\|_A$. For a finite set S, $|S|$ denotes its cardinal number.

Let $T \in \mathcal{T}_\ell$ be a mesh cell. Recall from [59, 62] that HHO methods are devised from a local reconstruction operator and a local stabilization operator. In the present lowest-order setting where $k = 0$, both operators can be written explicitly, see also [70, 64]. The local space of discrete velocity unknowns is defined as

$$\hat{U}_T := \mathbb{P}^0(T;\mathbb{R}) \times \mathbb{P}^0(\mathcal{F}_{\partial T};\mathbb{R}) \equiv \mathbb{R} \times \mathbb{R}^{|\mathcal{F}_{\partial T}|} \qquad \forall T \in \mathcal{T}_\ell, \tag{3.17}$$

where the first component of the pair is related to the cell and the second component to the faces composing its boundary. Moreover, $\mathbb{P}^0(\mathcal{F}_{\partial T})$ denotes the space composed of piecewise constant functions over ∂T. We use the notation $\hat{v}_T = (v_T, (v_F)_{F\in\mathcal{F}_{\partial T}})$ for a generic element in $\hat{U}_T$. Let $\mathbb{P}^0(T;\mathbb{R}^d)$ be composed of constant $\mathbb{R}^d$-valued functions in T. The local gradient reconstruction operator $\boldsymbol{G}_T : \hat{U}_T \to \mathbb{P}^0(T;\mathbb{R}^d)$ is such that, for all $\hat{v}_T \in \hat{U}_T$,

$$\boldsymbol{G}_T(\hat{v}_T) = \sum_{F\in\mathcal{F}_{\partial T}} \frac{|F|_{d-1}}{|T|_d}(v_F - v_T)\boldsymbol{n}_{T,F}, \tag{3.18}$$

where $|F|_{d-1}$ is the measure of the face F and $|T|_d$ that of the cell T. The stabilization operator $S_T : \hat{U}_T \to \mathbb{P}^0(\mathcal{F}_{\partial\mathcal{T}})$ is such that, for all $\hat{v}_T \in \hat{U}_T$, its restriction to a face $F \in \mathcal{F}_{\partial T}$ is defined as

$$S_{\partial T}(\hat{v}_T)|_F := v_F - v_T + \boldsymbol{G}_T(\hat{v}_T)\cdot(\boldsymbol{x}_F - \boldsymbol{x}_T), \tag{3.19}$$

where $\boldsymbol{x}_F$ and $\boldsymbol{x}_T$ are, respectively, the barycenter of F and of T. The above local gradient reconstruction and stabilization operators are to be used jointly to discretize the viscous energy. The main motivation is the following stability property (see, e.g., [62, Lemma 4]): letting $\eta_{\partial T}$ be the piecewise constant function on ∂T such that $\eta_{\partial T}|_F = h_F^{-1}$, there is a real number $\rho > 0$, independent of ℓ, such that, for all $\hat{v}_T \in \hat{U}_T$ and all $T \in \mathcal{T}_\ell$,

$$\rho|\hat{v}_T|_T^2 \le \|\boldsymbol{G}_T(\hat{v}_T)\|_T^2 + \|\eta_{\partial T}^{\frac{1}{2}} S_{\partial T}(\hat{v}_T)\|_{\partial T}^2 \le \rho^{-1}|\hat{v}_T|_T^2, \tag{3.20}$$

with the local H^1-like seminorm on $\hat{U}_T$ such that

$$|\hat{v}_T|_T^2 := \sum_{F\in\mathcal{F}_{\partial T}} h_F^{-1}\|v_F - v_T\|_F^2. \tag{3.21}$$

This result shows that the gradient reconstruction operator together with the stabilization operator are able to act as an H^1-like seminorm on $\hat{U}_T$.

We can now assemble the convex nonlinear minimization problem solved by the discrete velocity. Let us set

$$\hat{U}_\ell := \mathbb{P}^0(\mathcal{T}_\ell) \times \mathbb{P}^0(F_\ell) \equiv \mathbb{R}^{|\mathcal{T}_\ell|} \times \mathbb{R}^{|\mathcal{F}_\ell|}, \tag{3.22}$$

where the first component of the pair is related to the mesh cells and the second component to the mesh faces. We use the notation $\hat{v}_\ell = ((v_T)_{T\in\mathcal{T}_\ell}, (v_F)_{F\in\mathcal{F}_\ell})$ for a generic element in $\hat{U}_\ell$, and for any mesh cell $T \in \mathcal{T}_\ell$ and any $\hat{v}_\ell \in \hat{U}_\ell$, we let $\hat{v}_T \in \hat{U}_T$ be composed of the components of $\hat{v}_\ell$ attached to the cell T and its faces. We enforce the homogeneous Dirichlet condition on the discrete velocity explicitly by introducing the subspace

$$\hat{U}_{\ell,0} := \{\hat{v}_\ell \in \hat{U}_\ell \mid v_F = 0,\ \forall F \in \mathcal{F}_\ell^b\}. \tag{3.23}$$

The discrete counterpart of (3.7) is to seek the unique discrete velocity field $\hat{u}_\ell = (u_{\mathcal{T}_\ell}, u_{\mathcal{F}_\ell}) \in \hat{U}_{\ell,0}$ such that

$$\hat{u}_\ell = \operatorname*{arg\,min}_{\hat{v}_\ell\in\hat{U}_{\ell,0}} \sum_{T\in\mathcal{T}_\ell} \Big\{(H(\boldsymbol{G}_T(\hat{v}_T)),1)_T + \frac{\alpha}{2}\|\eta_{\partial T}^{\frac{1}{2}} S_{\partial T}(\hat{v}_T)\|_{\partial T}^2 - (f, v_T)_T\Big\}, \tag{3.24}$$

with the dissipation potential $H : \mathbb{R}^2 \to \mathbb{R}$ defined in (3.8) and where α is the augmentation parameter of the Lagrangian. The stabilization term is needed to ensure stability in the discrete system of Step 2 of Algorithm 4, see below. Our numerical experiments in Section 3.4.1 show that this term does not have an influence on the velocity error if the parameter α is not too small (e.g., of the order of the shear viscosity or larger).

3.2.2 Discrete augmented Lagrangian and ADMM

The derivation of the discrete augmented Lagrangian is identical to the continuous setting in that we introduce, for all $T \in \mathcal{T}_\ell$, the auxiliary field $\boldsymbol{\gamma}_T \in \mathbb{R}^2$, and we enforce that $\boldsymbol{\gamma}_T = \boldsymbol{G}_T(\hat{u}_T)$ by means of the Lagrange multiplier $\boldsymbol{\sigma}_T \in \mathbb{R}^2$. Then, setting

$$X(\mathcal{T}_\ell) := \hat{U}_{\ell,0} \times \mathbb{R}^{2|\mathcal{T}_\ell|} \times \mathbb{R}^{2|\mathcal{T}_\ell|} \qquad \mathbb{R}^{2|\mathcal{T}_\ell|} := \mathbb{R}^{2|\mathcal{T}_\ell|}, \tag{3.25}$$

the discrete augmented Lagrangian is defined as $\mathcal{L}_\ell : X(\mathcal{T}_\ell) \to \mathbb{R}$ such that

$$\begin{aligned}\mathcal{L}_\ell(\hat{u}_\ell, \boldsymbol{\gamma}_\ell, \boldsymbol{\sigma}_\ell) := \sum_{T\in\mathcal{T}_\ell} \Big\{&(H(\boldsymbol{\gamma}_T),1)_T + \frac{\alpha}{2}\|\eta_{\partial T}^{\frac{1}{2}} S_{\partial T}(\hat{u}_T)\|_{\partial T}^2 - (f, u_T)_T \\ &+ (\boldsymbol{\sigma}_T, \boldsymbol{G}_T(\hat{u}_T) - \boldsymbol{\gamma}_T)_T + \frac{\alpha}{2}\|\boldsymbol{G}_T(\hat{u}_T) - \boldsymbol{\gamma}_T\|_T^2\Big\},\end{aligned} \tag{3.26}$$

where we used the notation $\boldsymbol{\gamma}_\ell = (\boldsymbol{\gamma}_T)_{T\in\mathcal{T}_\ell}$ and $\boldsymbol{\sigma}_\ell = (\boldsymbol{\sigma}_T)_{T\in\mathcal{T}_\ell}$ for all $\boldsymbol{\gamma}_\ell, \boldsymbol{\sigma}_\ell \in \mathbb{R}^{2|\mathcal{T}_\ell|}$. If $(\hat{u}_\ell, \boldsymbol{\gamma}_\ell, \boldsymbol{\sigma}_\ell)$ is a saddle-point of the discrete Lagrangian $\mathcal{L}_\ell$, then $\boldsymbol{G}_T(\hat{u}_T) = \boldsymbol{\gamma}_T$ for all $T \in \mathcal{T}_\ell$ and $\hat{u}_\ell$ is the unique minimizer of (3.24).

The ADMM applied to the discrete augmented Lagrangian reads as follows: Given the initial values $\hat{u}_\ell^0 \in \hat{U}_{\ell,0}$ and $\boldsymbol{\sigma}_\ell^0 \in \mathbb{R}^{2|\mathcal{T}_\ell|}$, we perform, for all $n \geq 0$, the three steps in Algorithm 4. Notice in Step 2 that, as it is customary with hybrid discretization methods, the cell unknowns can be locally eliminated in each mesh cell by static condensation. After this elimination is performed, (3.28) reduces to a linear system in terms of the face unknowns whose stencil couples neighboring faces sharing a mesh cell. As shown, e.g., in [51], this linear system can be interpreted as a global transmission problem expressing the balance of appropriately defined local fluxes in each mesh cell. We refer the reader to [50] for further aspects of the implementation of HHO methods.

Algorithm 4 Antiplanar Bingham flows: ADMM in discrete form

1: Choose $(\hat{u}_\ell^0, \boldsymbol{\sigma}_\ell^0) \in \hat{U}_{\ell,0} \times \mathbb{R}^{2|\mathcal{T}_\ell|}$
2: Choose $\epsilon > 0$, set $R^0 = \infty$ and $n = 0$
3: **while** $R^n > \epsilon$ **do**
4: ***Step 1:*** Given $\hat{u}_\ell^n \in \hat{U}_{\ell,0}$ and $\boldsymbol{\sigma}_\ell^n \in \mathbb{R}^{2|\mathcal{T}_\ell|}$, we define the field $\boldsymbol{\gamma}_\ell^{n+1} \in \mathbb{R}^{2|\mathcal{T}_\ell|}$ such that, for all $T \in \mathcal{T}_\ell$,

$$\boldsymbol{\gamma}_T^{n+1} := \begin{cases} \dfrac{1}{(\alpha+\mu)}\left(|\boldsymbol{\theta}_T^n|_{\ell^2} - \sigma_0\right)\dfrac{\boldsymbol{\theta}_T^n}{|\boldsymbol{\theta}_T^n|_{\ell^2}} & \text{if } |\boldsymbol{\theta}_T^n|_{\ell^2} > \sigma_0, \\ \mathbf{0} & \text{if } |\boldsymbol{\theta}_T^n|_{\ell^2} \leq \sigma_0, \end{cases} \tag{3.27}$$

where $\boldsymbol{\theta}_T^n := \boldsymbol{\sigma}_T^n + \alpha \boldsymbol{G}_T(\hat{u}_T^n)$.
5: ***Step 2:*** We seek $\hat{u}_\ell^{n+1} \in \hat{U}_{\ell,0}$ solving the following discrete variational problem where the stress terms are treated as explicit force terms: For all $\hat{v}_\ell \in \hat{U}_{\ell,0}$,

$$\sum_{T\in\mathcal{T}_\ell}\left\{\alpha(\boldsymbol{G}_T(\hat{u}_T^{n+1}), \boldsymbol{G}_T(\hat{v}_T))_T + \alpha(\eta_{\partial T} S_{\partial T}(\hat{u}_T^{n+1}), S_{\partial T}(\hat{v}_T))_{\partial T}\right\}$$
$$= \sum_{T\in\mathcal{T}_\ell}\left\{(f, v_T)_T - (\boldsymbol{\sigma}_T^n - \alpha\boldsymbol{\gamma}_T^{n+1}, \boldsymbol{G}_T(\hat{v}_T))_T\right\}. \tag{3.28}$$

6: ***Step 3:*** Finally, we update the Lagrange multiplier $\boldsymbol{\sigma}_\ell^{n+1} \in \mathbb{R}^{2|\mathcal{T}_\ell|}$ by setting, for all $T \in \mathcal{T}_\ell$,

$$\boldsymbol{\sigma}_T^{n+1} := \boldsymbol{\sigma}_T^n + \alpha(\boldsymbol{G}_T(\hat{u}_T^{n+1}) - \boldsymbol{\gamma}_T^{n+1}). \tag{3.29}$$

7: We evaluate the residual:

$$R_\ell^{n+1} := \left(\sum_{T\in\mathcal{T}_\ell} \|\boldsymbol{\sigma}_T^{n+1} - \boldsymbol{\sigma}_T^n\|_T^2 + \alpha^2 \sum_{T\in\mathcal{T}_\ell} \|\boldsymbol{G}_T(\hat{u}_T^{n+1}) - \boldsymbol{G}_T(\hat{u}_T^n)\|_T^2\right)^{\frac{1}{2}}.$$

8: $n = n + 1$
9: **end while**

Remark 3.2 (Jump-based plastic energy)**.** *In each mesh cell $T \in \mathcal{T}_\ell$, the stabilization operator $S_{\partial T}$ defined in* (3.19) *essentially depends on the difference between the face unknowns and the trace of cell unknown, i.e., it represents a jump term. We notice that in* (3.24) *and in* (3.26) *this jump term only contributes to the viscous potential. This is rather natural since the jump term tends to zero as the mesh is refined (see, e.g., [62, Eq. (45)]). One can consider an additional jump-based contribution to the plastic energy. This presents, however, the drawback of introducing additional face-based auxiliary variables and Lagrange multipliers, thus significantly*

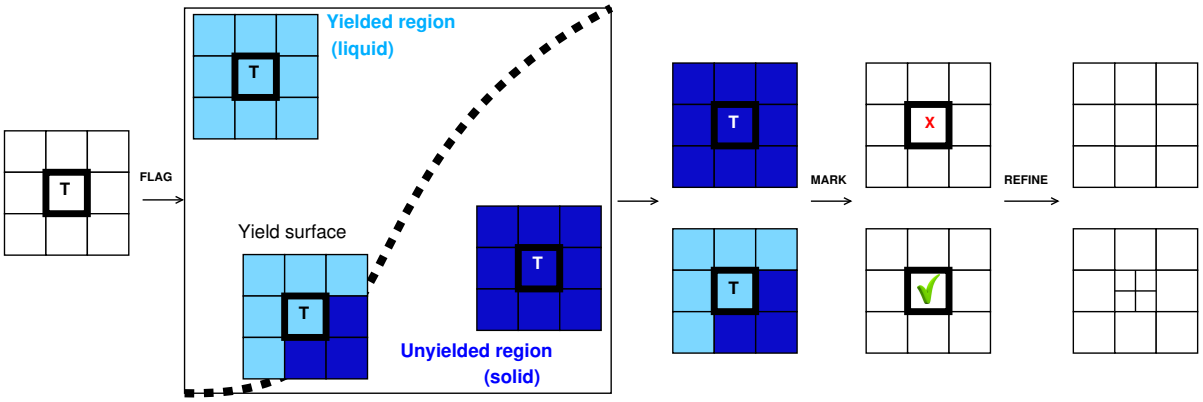

Figure 3.1: Schematic of the marking procedure for refinement.

increasing the computational costs. Moreover, we have observed in our numerical experiments that these additional auxiliary variables and Lagrange multipliers do not improve the accuracy of the simulations, even on relatively coarse meshes.

3.3 Mesh adaptation

The mesh sequence $(\mathcal{T}_\ell)_{\ell\in\mathbb{N}}$ is generated iteratively by means of an adaptive procedure. The step $\ell \geq 0$ of this procedure consists of solving the discrete minimization problem (3.24) on $\mathcal{T}_\ell$ by means of Algorithm 4, marking some cells of $\mathcal{T}_\ell$ for refinement or coarsening, and producing the new mesh $\mathcal{T}_{\ell+1}$. To describe our adaptive procedure, we introduce, for any mesh cell $T \in \mathcal{T}_\ell$, the subset $\mathcal{N}_T^{\mathrm{v}} := \{T' \in \mathcal{T}_\ell \mid \partial T' \cap \partial T \neq \emptyset\}$ which collects all the mesh cells (including T itself) sharing at least a vertex with T, and the subset $\mathcal{N}_T^{\mathrm{f}} := \{T' \in \mathcal{T}_\ell \mid \partial T' \cap \partial T \in \mathcal{F}_\ell\}$ which collects all the mesh cells sharing a face with T. Furthermore, during the adaptive procedure, any mesh cell is assigned a level $\iota(T) \in \mathbb{N}$ which is equal to the number of refinements that were necessary to obtain the cell T from its ancestor in the original mesh $\mathcal{T}_0$ (and all the mesh cells in $\mathcal{T}_0$ are assigned the level 0); thus, if $T \in \mathcal{T}_\ell$, then $\iota(T) \in \{0, \ldots, \ell\}$.

3.3.1 Cell marking for refinement

The marking of the cells in $\mathcal{T}_\ell$ for refinement involves two steps. First, all the cells in $\mathcal{T}_\ell$ are flagged according to the value of the quantities $\{|\boldsymbol{\theta}_T^n|_{\ell^2}\}_{T\in\mathcal{T}_\ell}$ once the ADMM has reached convergence, that is, the cell flag is set to $\texttt{flag}(T) = \texttt{SOLID}$ if $|\boldsymbol{\theta}_T^n|_{\ell^2} < \sigma_0$ and to $\texttt{flag}(T) = \texttt{LIQUID}$ otherwise. Then, the first marking step increases by one the level of all the mesh cells such that the set $\mathcal{M}_T^{\mathrm{v}} := \{\texttt{flag}(T') \mid T' \in \mathcal{N}_T^{\mathrm{v}}\}$ contains both LIQUID and SOLID flags. The aim of the second marking step is to control the level of hanging nodes produced by the first step. Although the present hybrid discretization method can support more than one hanging node per edge, we actually limit the number of hanging nodes per edge to one at most so as to ensure a smoother transition of the mesh near the yield surface. To achieve this goal, we perform a second marking of the cells to ensure that in any subset $\mathcal{N}_T^{\mathrm{f}}$, the difference of cell levels is one at most. The whole marking procedure is summarized in Algorithm 5 and Figure 3.1. Finally, the mesh refinement step consists in performing a subdivision of the marked cells in 4 congruent subcells (known in the literature as red refinement [126]).

Remark 3.3 (Comparison)**.** *Other criteria for flagging the cells near the yield surface can be considered. For instance, in [128, 132], the contrast in the norm of the strain rate tensor in vertex-based cell patches is used. We also notice that the present local mesh refinement procedure is more local than those considered in the context of conforming finite elements which need to build a mesh without hanging nodes. Here, there is still some non-locality because we limit the*

Algorithm 5 Marking procedure

Require: collection of cell flags $\{\texttt{flag}(T)\}_{T\in\mathcal{T}_\ell}$
for $T \in \mathcal{T}_\ell$ **do**
    Build the subsets of neighbors $\mathcal{N}_T^{\mathrm{v}}$ and their labels $\mathcal{M}_T^{\mathrm{v}}$
    if $\mathcal{M}_T^{\mathrm{v}} = \{\texttt{LIQUID},\texttt{SOLID}\}$ **then**
        Mark T and increase level $\iota(T) = \iota(T) + 1$
    end if
end for
for $T \in \mathcal{T}_\ell$ **do**
    Build the subset of neighbors $\mathcal{N}_T^{\mathrm{f}}$
    for $T' \in \mathcal{N}_T^{\mathrm{f}}$ **do**
        if $|\iota(T') - \iota(T)| > 1$ **then**
            Mark and increase level of cell with lower level
        end if
    end for
end for

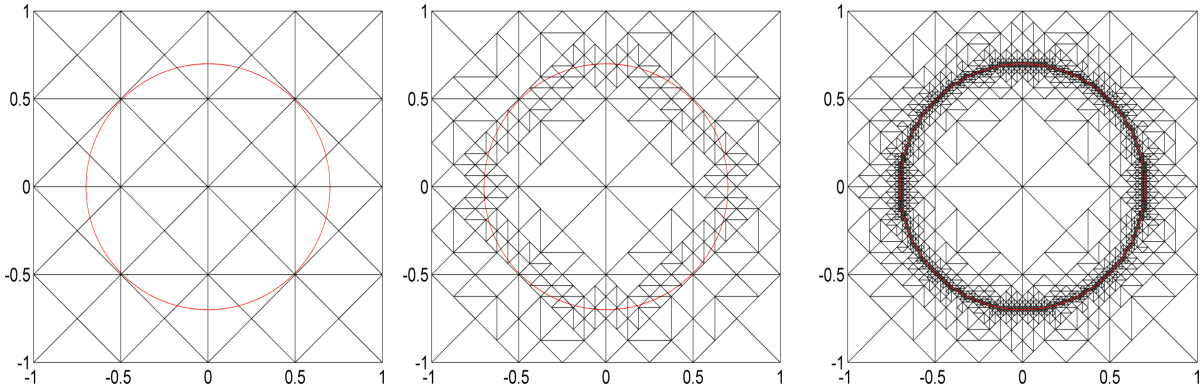

Figure 3.2: Adaptive meshes: (a) Initial mesh, (b) 2nd adapted mesh, (c) 5th adapted mesh

number of hanging nodes to one, but we can also consider a larger value for the number of hanging nodes.

In order to test the adaptive procedure with control on the number of hanging nodes, we perform an adaptation test in $\Omega = [-1, 1]^2$ by considering that the interface is a circle of radius 0.7 and marking the cells for refinement whenever the circle cuts them. Figure 3.2 shows the resulting meshes with hanging nodes. The circle is depicted in red. The final figure confirms the expected behavior of the algorithm.

3.3.2 Agglomeration-based coarsening

The agglomeration strategy is devoted to eliminate possible unnecessary degrees of freedom. This can be exploited in antiplanar viscoplastic flows where the velocity is constant in the unyielded region. The main idea is to agglomerate a collection of neighboring cells with `SOLID` flags, denoted here as the agglomerate $\mathcal{A}$. We additionally impose a restriction over each cell T to be included in $\mathcal{A}$, which reads such that $\mathcal{M}_T^{\mathrm{v}} = \{\texttt{SOLID}\}$ and assures T is surrounded by cells in solid state. This strategy searches to take only cells inside the unyielded region and to limit the coarsening procedure close enough to the yield surface. In this fashion, we allow a transition between unyielded and yielded regions, which in turns leaves a strip to drive the adaptation refinement (keeping the search of the yield surface) and to prevent the partition of the agglomerates.

Notice that there can be different agglomerates through the domain, which allows to handle problems with different unyielded regions as in the annulus cross-section problem (shown in below). The set $\mathcal{A}$ is composed minimun by one cell.

We introduce two additional subsets $\mathcal{N}_{T^\backslash}^{\mathrm{v}} := \mathcal{N}_T^{\mathrm{v}} \setminus \{T\}$ to denote the neighbors of a mesh cell T (without including T itself), and $\mathcal{M}_{T^\backslash}^{\mathrm{v}} := \{\texttt{flag}(T') \mid T' \in \mathcal{N}_T^{\mathrm{v}}\}$ to denote the subset of flags for the neighbors of T. See Algorithm 7.

Algorithm 6 Recursive Function `findPatch`

```
findPatch(T, A)
Build the subsets of neighbors N^v_{T\} and their labels M^v_{T\}
if M^v_{T\} = {SOLID} then
    A = {T} ∪ A
    for T' ∈ N^v_{T\} \A do
        findPatch(T', A)
    end for
end if
```

Algorithm 7 Module AGGLOMERATE

```
for T ∈ T_ℓ do
    Build the subset of neighbors N^v_T
    if flag = SOLID then
        A = φ
        findPatch (T, A)
        Agglomerate cells in A
    end if
end for
```

3.4 Numerical results

In this section, we present our numerical results for Bingham flow problems. We consider flows in pipes with a circular cross-section and an eccentric annular cross-section. The first setting leads to one of the few Bingham pipe flow problems with known exact solution, whereas the second setting is well-documented in the literature (see, among others, [124, 127, 16]). In all cases, the external force f, which represents the transverse pressure gradient forcing the flow, is constant over the cross-section. The (non-dimensional) Bingham number is defined as

$$\texttt{Bi} = \frac{\sigma_0 R}{\mu V}, \tag{3.30}$$

where R is a reference length (the radius of the outer boundary) and the reference velocity V is computed as $V = \frac{fR^2}{2\mu}$, so that we have

$$\texttt{Bi} = \frac{2\sigma_0}{fR}. \tag{3.31}$$

In our numerical experiments, we set the convergence threshold in the ADMM to $\epsilon = 10^{-8}$. The augmentation parameter is set to $\alpha = 10$ and the pipe radius to $R = 1$. The external force is set to $f = 1$ and then the yield stress is equal to the half of the Bingham number.

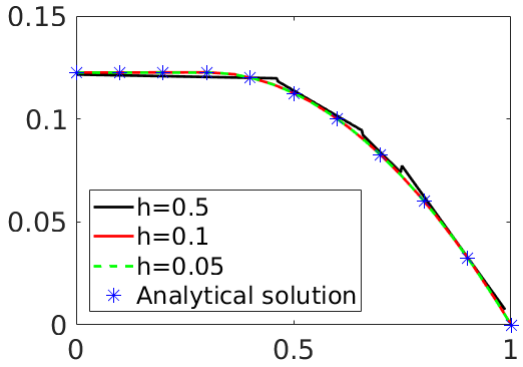

Figure 3.3: Velocity profiles along the line with azimuthal angle $\frac{\pi}{6}$ for uniform triangulations with mesh-sizes $h \in \{0.5, 0.1, 0.05\}$.

3.4.1 Circular cross-section

The cross-section Ω is a disk centered at the origin and of radius R. The exact velocity only depends on the radial coordinate r and is given by

$$\frac{u(r)}{V} = \begin{cases} \frac{1}{2}\left(1 - \frac{r^2}{R^2}\right) - \mathtt{Bi}\left(1 - \frac{r}{R}\right) & \text{if } \frac{r}{R} \geq \mathtt{Bi}, \\ \frac{1}{2}\left(1 - \mathtt{Bi}\right)^2 & \text{if } \frac{r}{R} \leq \mathtt{Bi}. \end{cases} \tag{3.32}$$

The flow consists of a central solid region of radius $\mathtt{Bi} \times R$ moving at a uniform velocity and a liquid region connecting the central rigid plug to the pipe walls. In particular, no flow occurs ($u = 0$) if the Bingham number is larger than 1 whereas the case $\mathtt{Bi} = 0$ (no solid region) corresponds to the classical Newtonian Poiseuille flow, i.e. either we consider the stress yield is zero or the pressure gradient (represented here as f) goes to infinity.

We use the hybrid discretization method from Section 3.2.1 together with the augmented Lagrangian and ADMM from Section 3.2.2. We actually discretize only one eighth of the unit disk and enforce symmetry conditions on the sides of the resulting angular sector. In Figure 3.3, we display the velocity profile along a line of azimuthal angle $\frac{\pi}{6}$ for uniform triangulations with mesh-sizes $h \in \{0.5, 0.1, 0.05\}$. In each mesh cell, the velocity is reconstructed as an affine function using the cell-value to assign its mean-value and the gradient reconstruction operator to evaluate its gradient. We observe very close profiles between $h = 0.1$ and $h = 0.05$.

We show in Figure 3.4 the velocity error $\|u - u_h\|_{L^2(\mathcal{T}_\ell)}$ vs. the mesh-size for the values of the augmentation parameter $\alpha = 10^k$ with $k \in \{-2, -1, 0, 1, 2\}$. We first observe for $\alpha \geq 1$, the velocity error is essentially independent of this parameter (and converging with first-order in the mesh-size). For lower values of α, we see a degradation of the velocity error, which is more pronounced for coarser meshes. Additionally, we found that the number of iterations to reach a residual threshold of 10^{-5} for the above values of α is $\{5, 4, 14, 93, 913\}$. The choice $\alpha = 10$ made above appears as a reasonable compromise between (velocity) accuracy and computational efficiency.

The approximation of the curved boundary with the mesh triangulation introduces an error on the boundary conditions. To address this issue, we compute the energy of the discrete solution using sequences of meshes producing circumscribed and inscribed polygons to the exact circular domain. By placing the mesh nodes on the unit circle, we form an inscribed polygon, whereas by placing them on a circle with radius $1/\cos(\theta/2J)$, where $J = 2^j$ is the number of boundary segments and $j \in \{3, 4, 5, 6\}$, we form a circumscribed polygon. In Table 3.5, we report the energy difference for the discrete solutions produced by the circumscribed and inscribed triangulations. We observe that this difference converges to zero with essentially second-order in the mesh-size.

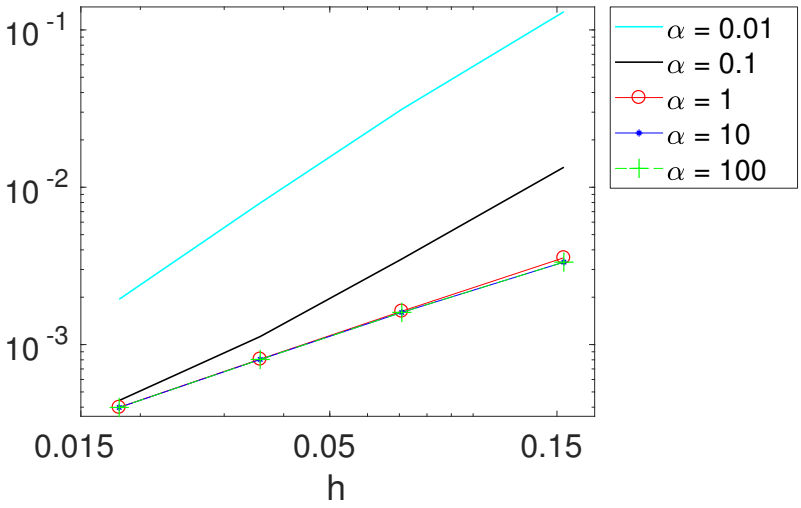

Figure 3.4: Velocity error $||u - u_h||_{L^2(\mathcal{T}_\ell)}$ vs. the mesh-size for $\mathtt{Bi} = 0.3$ and various values of the augmentation parameter α. The curves calculated with $\alpha \in \{1, 10, 100\}$ overlap.

Table 3.5: Energy difference between circumscribed and inscribed uniform triangulations with radial boundary divided by $J = 2^j$ segments and h_J the maximum mesh-size of the circumscribed mesh-triangulation.

j	h_J	$\mathtt{Bi} = 0.3$	$\mathtt{Bi} = 0.9$
3	1.55E-1	4.323e-4	9.667e-5
4	7.08E-2	1.076e-4	2.159e-5
5	3.57E-2	2.699e-5	5.753e-6
6	1.81E-2	9.237e-6	2.131e-6

We perform local mesh adaptation to detect the yield surface as described in Section 3.3 starting from an initial triangulation $\mathcal{T}_0$ with uniform mesh-size $h_0 = 0.1$. We run the adaptive loop five times, thereby producing the locally refined triangulations $\mathcal{T}_\ell$, $\ell \in \{1, \dots, 5\}$. Figure 3.6 shows the discrete residual R_ℓ as a function of the iteration number in the ADMM for a fine uniform triangulation with mesh-size $h = 0.0075$ and for the adaptation levels $\ell \in \{1, 3, 5\}$ and for $\mathtt{Bi} = 0.3$ and $\mathtt{Bi} = 0.9$. We observe a similar convergence behavior for all meshes and for both Bingham numbers. Notice that we do not initialize the ADMM at some level $\ell \geq 1$ with the interpolated solution from level $(\ell - 1)$, but simply by zero; we indeed observed that after a few tens of iterations, the behavior of the ADMM is similar for both choices of the initialization. Moreover, we observe in this specific example that in all cases, the ADMM first reaches a convergence rate of order $O(1/n)$, but then switches to a faster rate as the discrete residual approaches zero.

In Figures 3.7 and 3.8, we show for $\mathtt{Bi} = 0.3$ and $\mathtt{Bi} = 0.9$, respectively, the locally refined meshes and the stress norm $|\boldsymbol{\sigma}|_{\ell^2}$ for the adaptation levels $\ell \in \{0, 1, 3, 5\}$. The exact yield surface is depicted in red. We observe the progressive capture of the yield surface as the adaptation loop progresses. Note that the locally refined meshes have a mesh-size near the yield surface that is about the same as that of the uniform triangulation ($h = 0.0075$), but they lead to reduction factors in the number of DOFs of 15 for $\mathtt{Bi} = 0.3$ and of 6 for $\mathtt{Bi} = 0.9$. To provide a more quantitative measure of accuracy in the detection of the yield surface, we report in Tables 3.9 and 3.10, for $\mathtt{Bi} = 0.3$ and $\mathtt{Bi} = 0.9$, respectively, the error on the mean-value and variance for the distribution of the normalized radial coordinate of the mesh nodes attached to edges separating a cell marked as belonging to the unyielded region with a cell marked as

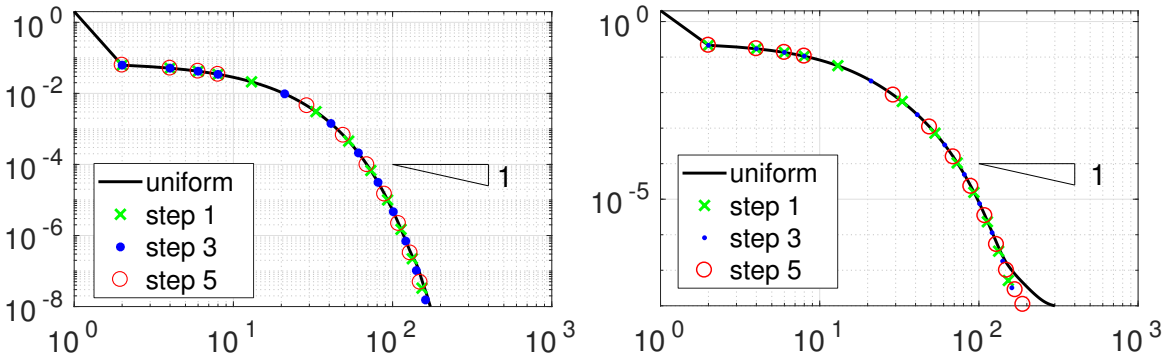

Figure 3.6: Discrete residual vs. ADMM iteration number for $\mathtt{Bi} = 0.3$ (left) and $\mathtt{Bi} = 0.9$ (right) for a fine uniform triangulation with $h = 0.0075$ and for locally refined meshes at adaptation levels $\ell \in \{1, 3, 5\}$.

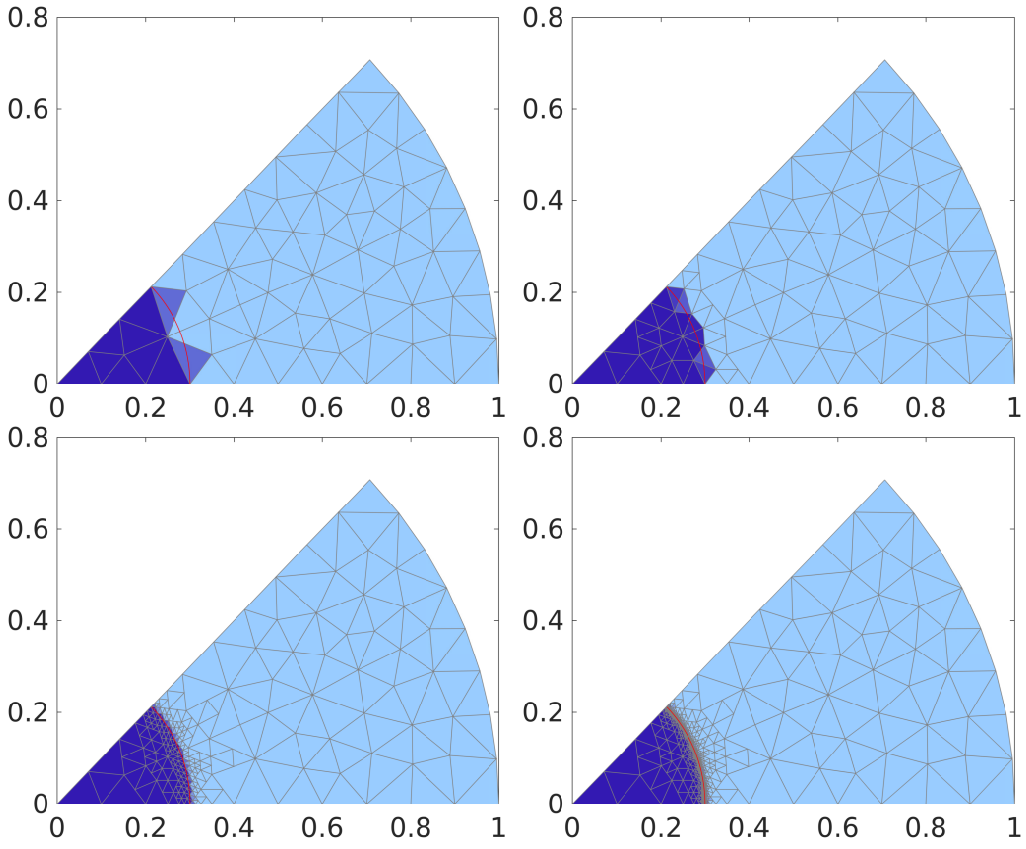

Figure 3.7: Stress norm $|\boldsymbol{\sigma}|_{\ell^2}$ for $\mathtt{Bi} = 0.3$ and, from top to bottom and from left to right, for adaptation levels $\ell \in \{0, 1, 3, 5\}$. The colormap (from dark blue to light blue) corresponds to the interval $[\sigma_0, \sigma_0 + \delta]$ with $\sigma_0 = 0.15$ and $\delta = 0.005$.

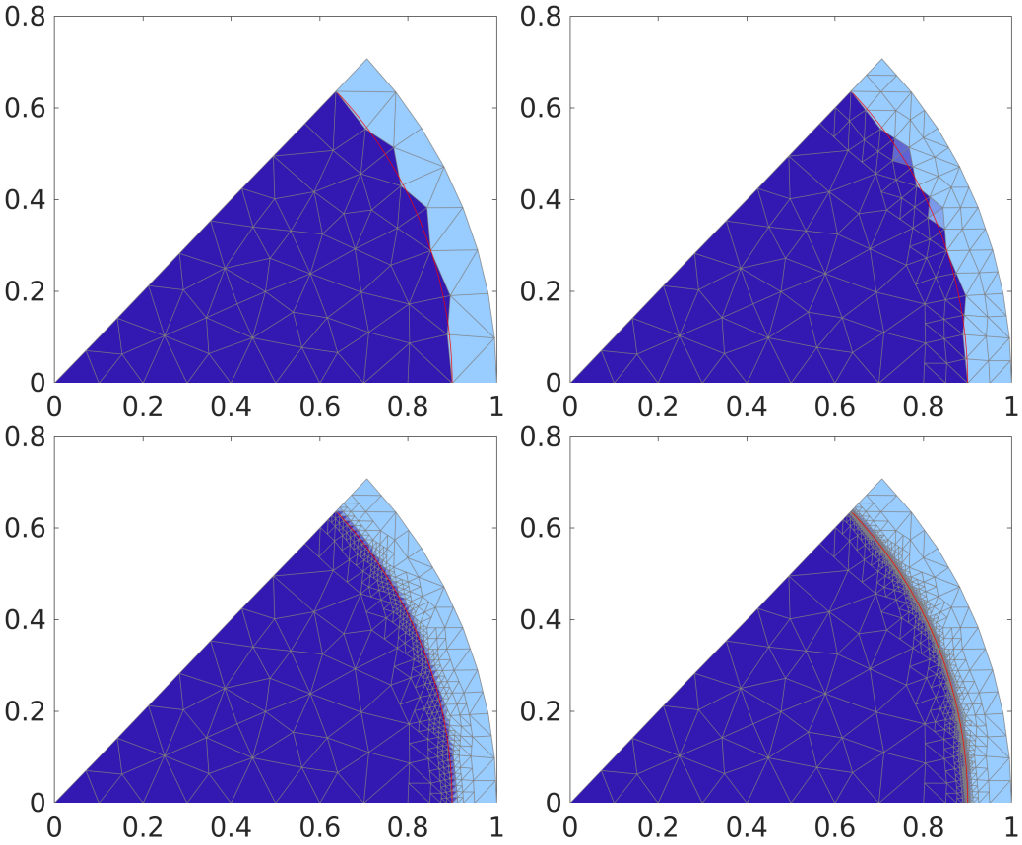

Figure 3.8: Stress norm $|\boldsymbol{\sigma}|_{\ell^2}$ for $\mathtt{Bi} = 0.9$ and, from top to bottom and from left to right, for adaptation levels $\ell \in \{0, 1, 3, 5\}$. The colormap (from dark blue to light blue) corresponds to the interval $[\sigma_0, \sigma_0 + \delta]$ with $\sigma_0 = 0.45$ and $\delta = 0.005$.

Table 3.9: Error on the mean-value and variance for the distribution of the radial coordinate at the vertices of the discrete yield surface for $\mathtt{Bi} = 0.3$.

ℓ	h_ℓ	DOFs	mean err.	var.
0	8.10E-2	167	3.55E-2	1.78E-2
1	5.00E-2	217	2.51E-2	1.67E-2
2	2.50E-2	343	8.93E-3	7.79E-3
3	1.25E-2	563	3.39E-3	3.80E-3
4	6.25E-3	1011	1.26E-3	1.73E-3
5	3.12E-3	1864	7.20E-4	9.07E-4

belonging to the yielded region (we can view the collection of such edges as the discrete yield surface). The radial coordinate is normalized by the exact radius of the yield surface which is equal to $\mathtt{Bi}$. In Tables 3.9 and 3.10, the column DOFs reports the total number of face-based velocity unknowns. We observe from these tables that the error on the mean-value and the variance converge to zero, essentially with first-order in h_ℓ. It is also interesting to notice that the variance ranges between one-third and one-fourth of h_ℓ.

Finally, we study the possibility of agglomeration-based mesh coarsening in the unyielded region. We consider here just a simple illustration where we perform the coarsening on the locally refined mesh $\mathcal{T}_3$. We agglomerate all the cells in $\mathcal{T}_3$ that are in the unyielded region and such that all their neighbors in the sense of faces are also in the unyielded region. We call the

Table 3.10: Error on the mean-value and variance for the distribution of the radial coordinate at the vertices of the discrete yield surface for $\texttt{Bi} = 0.9$.

ℓ	h_ℓ	DOFs	mean err.	var.
0	8.10E-2	167	6.29e-3	1.27E-2
1	4.62E-2	321	4.03e-4	9.70E-3
2	2.31E-2	632	2.00e-3	5.71E-3
3	1.15E-2	1256	1.49e-3	3.04E-3
4	5.77E-3	2499	7.22e-4	1.99E-3
5	2.88E-3	5058	4.24e-4	8.66E-4

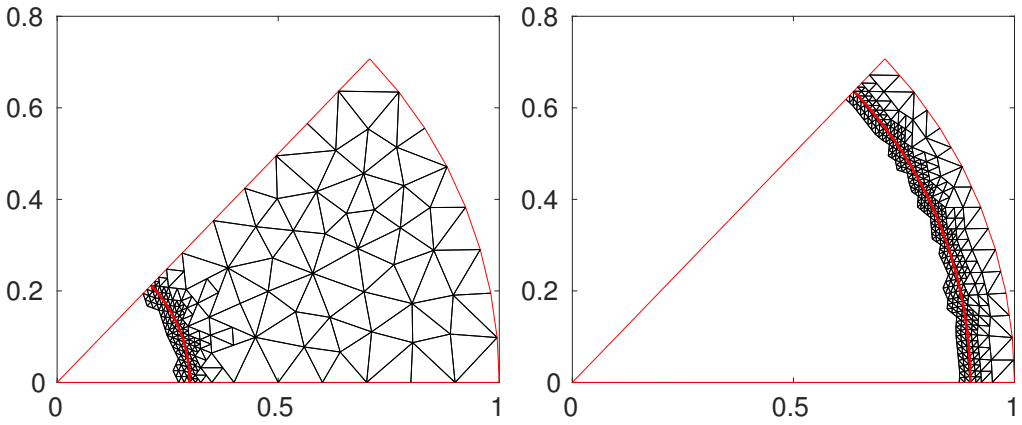

Figure 3.11: Locally refined meshes with agglomeration-based coarsening in the unyielded region for $\texttt{Bi} = 0.3$ (left) and $\texttt{Bi} = 0.9$ (right).

resulting mesh $\mathcal{T}_3^*$. These meshes are shown in Figure 3.11 for $\texttt{Bi} = 0.3$ and $\texttt{Bi} = 0.9$. They lead, respectively, to 511 and 1027 DOFs (face-based velocity unknowns), which represents a relative savings of 9.2% and 58.9% with respect to the corresponding mesh without agglomeration. Computing a new discrete solution on $\mathcal{T}_3^*$, we observe that the H^1-error on the velocity is 1.5×10^{-3} whereas it is 1.1×10^{-3} when computed on the mesh $\mathcal{T}_3$. Thus, performing an agglomeration-based mesh coarsening does not really hamper accuracy while at the same time reducing the computational costs, especially for $\texttt{Bi} = 0.9$ where the unyielded region is quite large.

3.4.2 Eccentric annular cross-section

The geometric setting for the eccentric annular cross-section is illustrated in Figure 3.12. The parameters are $R_e = 1$ for the external radius, $R_i = 0.4$ for the inner radius, and $e = -0.15$ for the eccentricity of the inner hole. We take advantage of the symmetry by discretizing only one half of the cross-section. The Bingham number is set to $\texttt{Bi} = 0.2$.

Figure 3.13 shows the discrete residual R_ℓ as a function of the iteration number in the ADMM for a fine uniform triangulation with mesh-size $h = 0.0075$ and for the adaptation levels $\ell \in \{2, 4, 6\}$ with initial mesh-size $h = 0.05$. As before, we observe a similar convergence behavior for all meshes (with a few irregularities). However, in contrast with the previous test case, the convergence rate is $O(1/n)$ when the discrete residual goes below 10^{-6}, whereas this rate is higher when the residual is in the range $[10^{-6}, 10^{-2}]$. The locally refined meshes at the adaptation levels $\ell \in \{2, 6\}$ are presented in Figure 3.14.

The left panel of Figure 3.15 shows the spatial distribution of the velocity field and of the

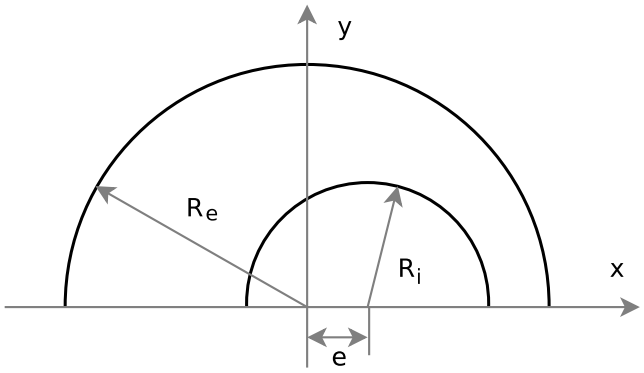

Figure 3.12: Geometric setting for the eccentric annular cross-section.

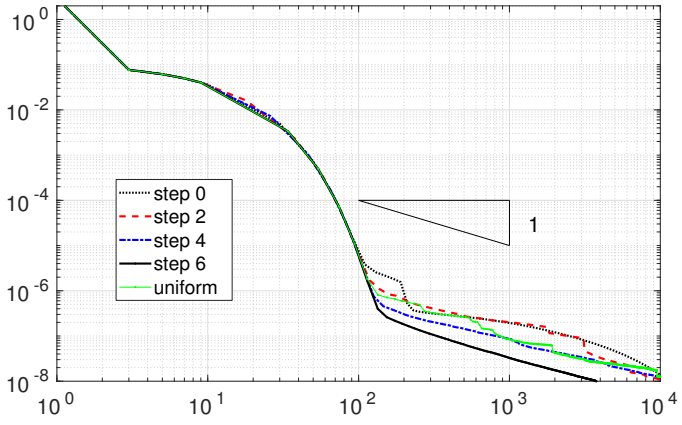

Figure 3.13: Discrete residual vs. ADMM iteration number for adaptation levels $\ell \in \{0, 2, 4, 6\}$.

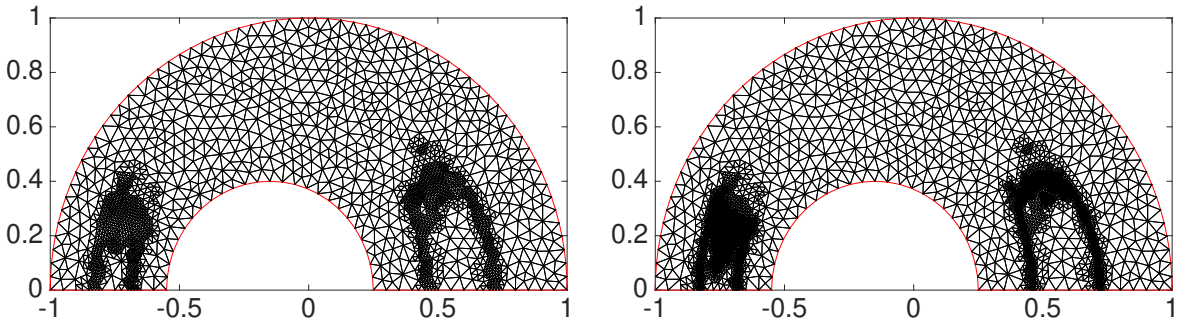

Figure 3.14: Locally refined meshes for $\ell = 2$ (left) and $\ell = 6$ (right).

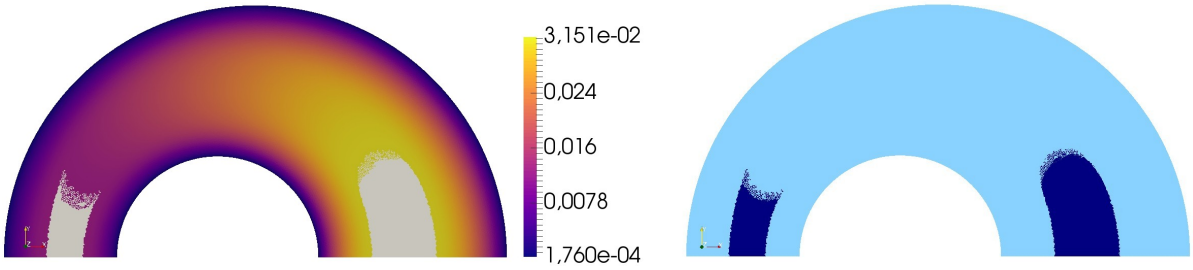

Figure 3.15: Computations on a uniform triangulation with mesh-size $h = 0.0075$. Left: velocity field and unyielded region (gray); Right: stress norm with colormap (from dark gray to light gray) corresponding to the interval $[\sigma_0, \sigma_0 + \delta]$ with $\sigma_0 = 0.1$ and $\delta = 0.005$.

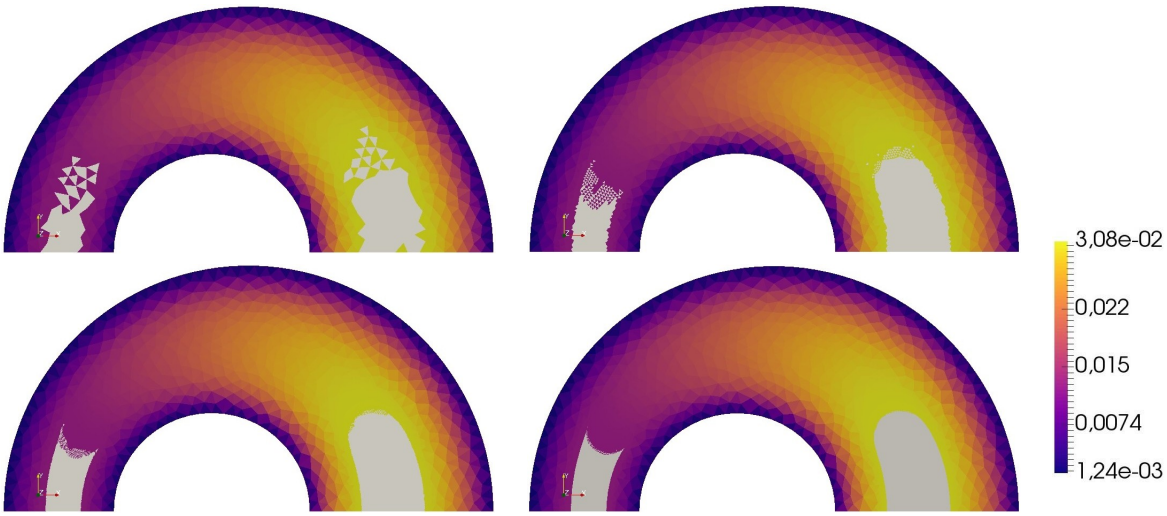

Table 3.16: Velocity field and unyielded region (gray). From top to bottom and left to right: adaptation levels $\ell \in \{0, 2, 4, 6\}$.

unyielded region (notice that this region is composed of two connected components having a different shape). The right panel of Figure 3.15 shows the spatial distribution of the stress norm $|\boldsymbol{\sigma}|_{\ell^2}$. These results are obtained using a fine uniform triangulation with mesh-size $h = 0.0075$, and can be compared with the results presented in Figure 3.16 (velocity field and unyielded region) and in Figure 3.17 (stress norm) which are obtained using locally refined meshes. We can observe the progressive capture of the yield surface and that the predictions on the sixth locally refined mesh match well with those on the fine uniform triangulation. We notice that the locally refined mesh $\mathcal{T}_6$ leads to about 10^5 DOFs as the uniform triangulation with $h = 0.0075$, but the local mesh-size in $\mathcal{T}_6$ near the yield surface is about 10 times smaller. This leads to a much sharper resolution as shown in Figure 3.18, where we provide a zoom of two regions around the yield surface for the stress norm distribution.

The above results on the velocity field and the localization of the yield surface also match well with the predictions reported in [16]. To provide a more quantitative comparison, we present in Table 3.19 the value of the flux $Q = (u_h, 1)_{\Omega_\ell}$ across the cross-section as predicted using the methodology from [16] (recall that it is based on a conforming finite element discretization, and the numerical solver uses either the ADMM or second-order cone programming) and the present one. We consider uniformly refined meshes as the conforming finite

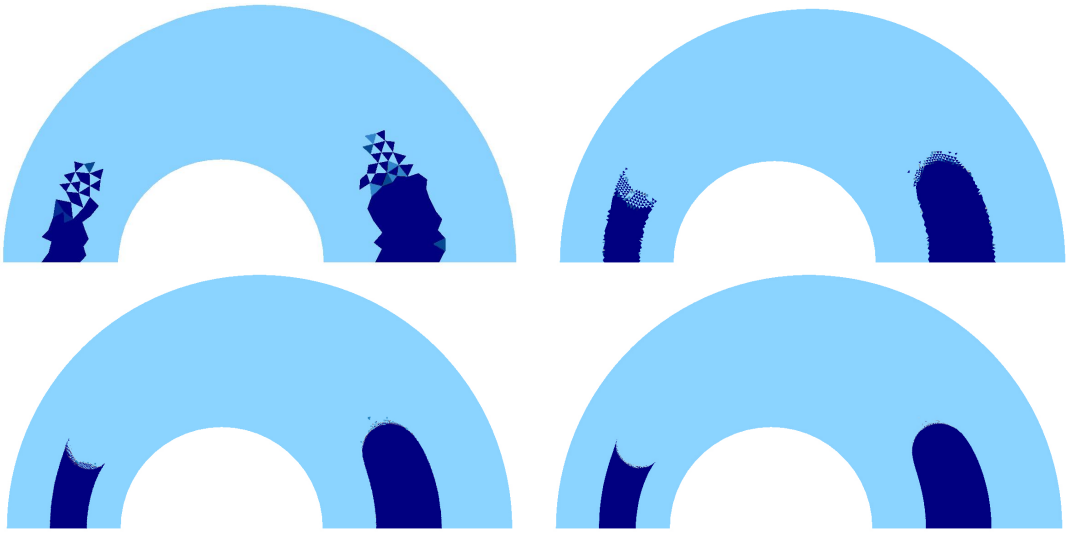

Figure 3.17: Stress norm with colormap (from dark gray to light gray) corresponding to the interval $[\sigma_0, \sigma_0 + \delta]$ with $\sigma_0 = 0.1$ and $\delta = 0.005$. From top to bottom and left to right: adaptation levels $\ell \in \{0, 2, 4, 6\}$.

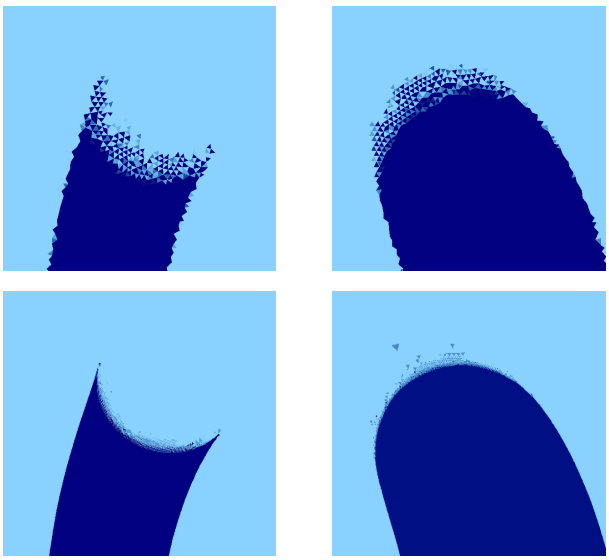

Figure 3.18: Zoom of two regions around the yield surface. Top row: calculation using the uniform triangulation with $h = 0.0075$; bottom row: calculations using the locally refined mesh $\mathcal{T}_6$. Both meshes lead to approximately the same number of DOFs.

Table 3.19: Fluxes Q for $\sigma_0 = 0.1$ and different values of f computed with the finite element method and the present hybrid lowest-order method.

	f			
h	0.5	1	1.5	2
	Finite element method			
0.100	3.55e-3	2.38e-2	4.57e-2	6.77e-2
0.050	3.40e-3	2.34e-2	4.49e-2	6.67e-2
0.025	3.36e-3	2.33e-2	4.48e-2	6.64e-2
	Hybrid lowest-order method			
0.100	3.55e-3	2.37e-2	4.57e-2	6.77e-2
0.050	3.40e-3	2.34e-2	4.49e-2	6.67e-2
0.025	3.36e-3	2.32e-2	4.47e-2	6.63e-2

element solver does not support locally refined meshes with hanging nodes. We consider mesh-sizes $h \in \{0.1, 0.05, 0.025\}$. We observe that the results obtained with both methods match quite closely.

Chapter 4

Lowest- and higher-order methods for Bingham vector flows

Contents

The goal of this chapter is to devise hybrid discretization methods for Bingham vector flows. Contrary to the previous chapter, the velocity is now vector-valued. Another novelty is that both a lowest-order method with piecewise constant face velocities and a higher-order method with piecewise affine face velocities are considered. In both cases piecewise affine cell velocities are considered. The difficulty with the latter method is the need to introduce quadrature rules. The third novelty is that we now need to account for the divergence-free constraint on the velocity, which we do by introducing a pressure.

This chapter is organized as follows. In Section 4.1, we recall the model problem and the Augmented Lagrangian setting. In Section 4.2, we describe the hybrid lowest-order discretization method and the discrete ADMM algorithm. In Section 4.3, we extend our discretization to higher-order using quadrature rules. Finally in Section 4.4, we present numerical results on the lid-driven cavity problem and on a problem involving a rotating vane-in-cup geometry.

4.1 Continuous setting

Let us briefly recall the viscoplastic flow model described in Chapter 1. Let $\Omega \subset \mathbb{R}^d$, $d \geq 2$, denote an open, bounded, connected subset of $\mathbb{R}^d$ with a Lipschitz boundary. Let $\boldsymbol{f} : \Omega \to \mathbb{R}^d$ be the external force field and let us consider non-homogeneous Dirichlet boundary conditions, where the Dirichlet datum $\boldsymbol{g} : \partial\Omega \to \mathbb{R}^d$ satisfies the compatibility condition $\int_{\partial\Omega} \boldsymbol{g}\cdot\boldsymbol{n} = 0$ and $\boldsymbol{n}$ is the unit outward normal to $\partial\Omega$. The model problem consists of finding the total symmetric

stress tensor field $\boldsymbol{\sigma}_{\rm tot} : \Omega \to \mathbb{R}^{d\times d}_{\rm s}$ and the velocity field $\boldsymbol{u} : \Omega \to \mathbb{R}^d$ solving the following boundary-value problem:

$$\begin{aligned} \nabla\cdot\boldsymbol{\sigma}_{\rm tot} + \boldsymbol{f} &= \boldsymbol{0} \qquad && \text{in } \Omega, \\ \nabla\cdot\boldsymbol{u} &= 0 && \text{in } \Omega, \\ \boldsymbol{u} &= \boldsymbol{g} && \text{on } \partial\Omega, \end{aligned} \tag{4.1}$$

with the constitutive relation

$$\begin{cases} \boldsymbol{\sigma} = 2\mu\nabla_{\rm s}\boldsymbol{u} + \sqrt{2}\sigma_0\dfrac{\nabla_{\rm s}\boldsymbol{u}}{|\nabla_{\rm s}\boldsymbol{u}|_{\ell^2}} & \text{for } |\boldsymbol{\sigma}|_{\ell^2} > \sqrt{2}\sigma_0, \\ \nabla_{\rm s}\boldsymbol{u} = \boldsymbol{0} & \text{for } |\boldsymbol{\sigma}|_{\ell^2} \le \sqrt{2}\sigma_0, \end{cases} \tag{4.2}$$

where the deviatoric part $\boldsymbol{\sigma}$ of the total stress tensor $\boldsymbol{\sigma}_{\rm tot}$ and the symmetric velocity gradient $\nabla_{\rm s}\boldsymbol{u}$ are defined as follows:

$$\boldsymbol{\sigma} = \boldsymbol{\sigma}_{\rm tot} - \frac{1}{d}\mathtt{tr}(\boldsymbol{\sigma}_{\rm tot})\boldsymbol{I}_d, \qquad \nabla_{\rm s}\boldsymbol{u} = \frac{1}{2}(\nabla\boldsymbol{u} + \nabla\boldsymbol{u}^{\rm T}), \tag{4.3}$$

and $\boldsymbol{I}_d$ is the identity tensor of $\mathbb{R}^{d\times d}$. Moreover, $\mu > 0$ and $\sigma_0 > 0$ denote, respectively, the shear viscosity and the shear yield stress, and the Frobenius norm is defined as follows:

$$|\boldsymbol{\tau}|_{\ell^2} := (\boldsymbol{\tau} : \boldsymbol{\tau})^{\frac{1}{2}} = \left(\sum_{i,j=1}^{d} \tau_{ij}^2\right)^{\frac{1}{2}} \qquad \forall \boldsymbol{\tau} \in \mathbb{R}^{d\times d}. \tag{4.4}$$

The yield surface corresponds to $|\boldsymbol{\sigma}|_{\ell^2} = \sqrt{2}\sigma_0$ and separates the solid and liquid regions. To obtain the yielded zone, corresponding to liquid behavior, the criterion $|\boldsymbol{\sigma}|_{\ell^2} > \sqrt{2}\sigma_0$ must be satisfied. Otherwise, the region is called the unyielded zone and corresponds to solid behavior.

Let $L^2(\Omega)$ denote the space of square-integrable functions over Ω and let us set $\boldsymbol{L}^2(\Omega) := L^2(\Omega;\mathbb{R}^d)$. We also consider the space $L^2(\Omega;\mathbb{R}^{d\times d}_s)$ composed of square-integrable tensor-valued functions taking symmetric values. The inner product in the three spaces is denoted $(\cdot,\cdot)_\Omega$ and the associated norm $\|\cdot\|_\Omega$. Let $\boldsymbol{H}^1(\Omega) := H^1(\Omega;\mathbb{R}^d)$, $\boldsymbol{H}^{\frac{1}{2}}(\partial\Omega) := H^{\frac{1}{2}}(\partial\Omega;\mathbb{R}^d)$, and let $\gamma_{\partial\Omega} : \boldsymbol{H}^1(\Omega) \to \boldsymbol{H}^{\frac{1}{2}}(\partial\Omega)$ be the classical trace map acting componentwise. Let the following affine subspace specifying the velocity trace on the boundary of the domain:

$$\boldsymbol{H}^1_{\boldsymbol{g}}(\Omega) := \{\boldsymbol{v} \in \boldsymbol{H}^1(\Omega) \mid \gamma_{\partial\Omega}(\boldsymbol{v}) = \boldsymbol{g}\}, \tag{4.5}$$

and the affine subspace of velocities with zero divergence:

$$\boldsymbol{V}_{\boldsymbol{g}}(\Omega) := \{\boldsymbol{v} \in \boldsymbol{H}^1_{\boldsymbol{g}}(\Omega) \mid \nabla\cdot\boldsymbol{v} = 0\}. \tag{4.6}$$

The tangent space to $\boldsymbol{V}_{\boldsymbol{g}}(\Omega)$ is the linear subspace

$$\boldsymbol{V}_0(\Omega) := \{\boldsymbol{v} \in \boldsymbol{H}^1_0(\Omega) \mid \nabla\cdot\boldsymbol{v} = 0\}, \tag{4.7}$$

where we recall that

$$\boldsymbol{H}^1_0(\Omega) := \{\boldsymbol{v} \in \boldsymbol{H}^1(\Omega) \mid \gamma_{\partial\Omega}(\boldsymbol{v}) = \boldsymbol{0}\}. \tag{4.8}$$

Let us now introduce the dissipation potential $H : \mathbb{R}^{d\times d}_s \to \mathbb{R}$ such that

$$H(\boldsymbol{d}) = \mu|\boldsymbol{d}|^2_{\ell^2} + \sqrt{2}\sigma_0|\boldsymbol{d}|_{\ell^2}, \qquad \forall \boldsymbol{d} \in \mathbb{R}^{d\times d}_s. \tag{4.9}$$

The first term in the right-hand side of (4.9) evaluated with $\boldsymbol{d} = \nabla_{\rm s}\boldsymbol{u}$ represents the viscous dissipation potential and the second term the plastic dissipation potential. Note that due to the latter term, the classical derivative of H is not well-defined when $\boldsymbol{d} = \boldsymbol{0}$, and we need to

consider a generalized concept of differentiation for convex functions, named the sub-differential

$$\partial H(\boldsymbol{d}) = \left\{ \boldsymbol{\tau} \in \mathbb{R}^{d\times d}_s \mid H(\boldsymbol{e}) - H(\boldsymbol{d}) \geq \boldsymbol{\tau} : (\boldsymbol{e}-\boldsymbol{d}) \quad \forall \boldsymbol{e} \in \mathbb{R}^{d\times d}_s \right\}. \tag{4.10}$$

Let us now consider the weak formulation for (4.1) and let us assume $\boldsymbol{f} \in \boldsymbol{L}^2(\Omega)$ and $\boldsymbol{g} \in \boldsymbol{H}^{\frac{1}{2}}(\partial\Omega)$. Since we have $(\mathtt{tr}(\boldsymbol{\sigma}_{\rm tot})\boldsymbol{I}_d, \nabla_{\rm s}\boldsymbol{v})_\Omega = 0$ for all $\boldsymbol{v} \in \boldsymbol{V}_0(\Omega)$, since $\nabla\cdot\boldsymbol{v} = 0$, we infer that $(\boldsymbol{\sigma}_{\rm tot}, \nabla_{\rm s}\boldsymbol{v})_\Omega = (\boldsymbol{\sigma}, \nabla_{\rm s}\boldsymbol{v})_\Omega$ for all $\boldsymbol{v} \in \boldsymbol{V}_0(\Omega)$ (to recover the trace of the total stress, we have to consider de Rham's theorem and search $\boldsymbol{u} \in \boldsymbol{H}^1_{\boldsymbol{g}}(\Omega)$, see Remark 1.12). Hence, the weak form of (4.1)-(4.2) is: Find $\boldsymbol{u} \in \boldsymbol{V}_{\boldsymbol{g}}(\Omega)$ such that

$$\begin{cases} (\boldsymbol{\sigma}, \nabla_{\rm s}\boldsymbol{v})_\Omega = (\boldsymbol{f}, \boldsymbol{v})_\Omega \quad \forall \boldsymbol{v} \in \boldsymbol{V}_0(\Omega), \\ \boldsymbol{\sigma} \in \partial H(\nabla_{\rm s}\boldsymbol{u}). \end{cases} \tag{4.11}$$

It is well-known, see [76], that the velocity field solving (4.1)-(4.2) is the unique minimizer in $\boldsymbol{V}_{\boldsymbol{g}}(\Omega)$ of the following energy functional:

$$\boldsymbol{u} = \underset{\boldsymbol{v}\in\boldsymbol{V}_{\boldsymbol{g}}(\Omega)}{\arg\min} \left\{ (H(\nabla_s\boldsymbol{v}), 1)_\Omega - (\boldsymbol{f}, \boldsymbol{v})_\Omega \right\}, \tag{4.12}$$

Recall that $\boldsymbol{\sigma}$ is uniquely defined only in the unyielded region.

The minimization problem (4.12) can be tackled by decomposition-coordination methods. To decouple the nonlinearity from the velocity field, an auxiliary symmetric tensor field $\boldsymbol{\gamma} \in L^2(\Omega; \mathbb{R}^{d\times d}_s)$ is introduced and one enforces that $\boldsymbol{\gamma} = \nabla_{\rm s}\boldsymbol{u}$ by means of the Lagrange multiplier $\boldsymbol{\sigma} \in L^2(\Omega; \mathbb{R}^{d\times d}_s)$ (which turns out to be indeed the deviatoric stress tensor) together with a least-squares penalty term. Let us set

$$X(\Omega) := \boldsymbol{V}_{\boldsymbol{g}}(\Omega) \times L^2(\Omega; \mathbb{R}^{d\times d}_s) \times L^2(\Omega; \mathbb{R}^{d\times d}_s). \tag{4.13}$$

The augmented Lagrangian is defined as $\mathcal{L} : X(\Omega) \to \mathbb{R}$ such that

$$\mathcal{L}(\boldsymbol{u}, \boldsymbol{\gamma}, \boldsymbol{\sigma}) := (H(\boldsymbol{\gamma}), 1)_\Omega + (\boldsymbol{\sigma}, \nabla_s\boldsymbol{u} - \boldsymbol{\gamma})_\Omega + \alpha\|\nabla_s\boldsymbol{u} - \boldsymbol{\gamma}\|^2_\Omega - (\boldsymbol{f}, \boldsymbol{u})_\Omega, \tag{4.14}$$

where $\alpha > 0$ is the augmentation parameter. The triplet $(\boldsymbol{u}, \boldsymbol{\gamma}, \boldsymbol{\sigma}) \in X(\Omega)$ is a saddle-point of the Lagrangian $\mathcal{L}$, that is to say

$$\mathcal{L}(\boldsymbol{u}, \boldsymbol{\gamma}, \boldsymbol{\tau}) \leq \mathcal{L}(\boldsymbol{u}, \boldsymbol{\gamma}, \boldsymbol{\sigma}) \leq \mathcal{L}(\boldsymbol{v}, \boldsymbol{\delta}, \boldsymbol{\sigma}) \qquad \forall (\boldsymbol{v}, \boldsymbol{\delta}, \boldsymbol{\tau}) \in X(\Omega), \tag{4.15}$$

if and only if $\boldsymbol{\gamma} = \nabla_s\boldsymbol{u}$ and the pair $(\boldsymbol{u}, \boldsymbol{\sigma})$ solves (4.1)-(4.2). Note that $\nabla\cdot\boldsymbol{u} = 0$ in Ω and the boundary condition $\boldsymbol{u} = \boldsymbol{g}$ on $\partial\Omega$ are enforced directly from $\boldsymbol{u} \in \boldsymbol{V}_{\boldsymbol{g}}(\Omega)$.

The ALG2 method from [72, 77] is an iterative method that, at each step, minimizes the augmented Lagrangian $\mathcal{L}$ jointly with respect to the pair $(\boldsymbol{u}, \boldsymbol{\gamma})$ and then updates the Lagrange multiplier $\boldsymbol{\sigma}$. The idea in the Alternating Direction Method of Multipliers (ADMM) [79, 75] is that the joint minimization is replaced by a successive minimization with respect to $\boldsymbol{\gamma}$, and then with respect to $\boldsymbol{u}$. This method is presented in Algorithm 8, where in Step 2 we use $\boldsymbol{H}^1_{\boldsymbol{g}}(\Omega)$ as trial space and we enforce the divergence constraint $\nabla\cdot\boldsymbol{u}^{n+1} = 0$ weakly, which leads to a mixed formulation. The stopping criterion for the ADMM is $R^{n+1} \leq \epsilon$ with $\epsilon > 0$ a prescribed stopping tolerance, and the residual is defined in terms of discrete stress and discrete gradient residuals, see (4.19).

Remark 4.1 (Optimality conditions)**.** *It is readily seen that the optimality conditions are obtained by zeroing the following equations for all* $(\boldsymbol{v}, \boldsymbol{\delta}, \boldsymbol{\tau}) \in \boldsymbol{V}_0(\Omega) \times L^2(\Omega; \mathbb{R}^{d\times d}_s) \times L^2(\Omega; \mathbb{R}^{d\times d}_s)$*:*

$$\begin{aligned} &\partial_{\boldsymbol{\gamma}}\mathcal{L}(\boldsymbol{u}, \boldsymbol{\gamma}, \boldsymbol{\sigma})[\boldsymbol{\delta}] = 2(\mu+\alpha)(\boldsymbol{\gamma}, \boldsymbol{\delta})_\Omega + (\sqrt{2}\sigma_0\mathbf{sgn}(\boldsymbol{\gamma}), \boldsymbol{\delta})_\Omega - (\boldsymbol{\sigma} + 2\alpha\nabla_{\rm s}\boldsymbol{u}, \boldsymbol{\delta})_\Omega, \\ &\partial_{\boldsymbol{u}}\mathcal{L}(\boldsymbol{u}, \boldsymbol{\gamma}, \boldsymbol{\sigma})[\boldsymbol{v}] = (\boldsymbol{\sigma} - 2\alpha\boldsymbol{\gamma}, \nabla_{\rm s}\boldsymbol{v})_\Omega + 2\alpha(\nabla_{\rm s}\boldsymbol{u}, \nabla_{\rm s}\boldsymbol{v})_\Omega - (\boldsymbol{f}, \boldsymbol{v})_\Omega, \\ &\partial_{\boldsymbol{\sigma}}\mathcal{L}(\boldsymbol{u}, \boldsymbol{\gamma}, \boldsymbol{\sigma})[\boldsymbol{\tau}] = (\nabla_{\rm s}\boldsymbol{u} - \boldsymbol{\gamma}, \boldsymbol{\tau})_\Omega, \end{aligned}$$

Algorithm 8 Bingham vector flows: ADMM in continuous form

Choose $(\boldsymbol{u}^0, \boldsymbol{\sigma}^0) \in \boldsymbol{H}^1_{\boldsymbol{g}}(\Omega) \times L^2(\Omega; \mathbb{R}^{d\times d}_s)$
Choose $\epsilon > 0$, set $R^0 = \infty$ and $n = 0$
while $R^n > \epsilon$ **do**
Step 1: We define $\boldsymbol{\gamma}^{n+1} \in L^2(\Omega; \mathbb{R}^{d\times d}_s)$ such that:

$$\boldsymbol{\gamma}^{n+1} := \begin{cases} \dfrac{1}{2(\alpha+\mu)} \left(|\boldsymbol{\theta}^n|_{\ell^2} - \sqrt{2}\sigma_0 \right) \dfrac{\boldsymbol{\theta}^n}{|\boldsymbol{\theta}^n|_{\ell^2}} & \text{if } |\boldsymbol{\theta}^n|_{\ell^2} > \sqrt{2}\sigma_0, \\ \mathbf{0} & \text{if } |\boldsymbol{\theta}^n|_{\ell^2} \le \sqrt{2}\sigma_0, \end{cases} \tag{4.16}$$

with $\boldsymbol{\theta}^n := \boldsymbol{\sigma}^n + 2\alpha\nabla_s \boldsymbol{u}^n$.
Step 2: We seek $(\boldsymbol{u}^{n+1}, p^{n+1}) \in \boldsymbol{H}^1_{\boldsymbol{g}}(\Omega) \times L^2_0(\Omega)$ s.t. $\forall (\boldsymbol{v}, q) \in \boldsymbol{H}^1_0(\Omega) \times L^2_0(\Omega)$:

$$\begin{aligned} 2\alpha(\nabla_s \boldsymbol{u}^{n+1}, \nabla_s \boldsymbol{v})_\Omega - (p^{n+1}, \nabla\cdot\boldsymbol{v})_\Omega &= (\boldsymbol{f}, \boldsymbol{v})_\Omega - (\boldsymbol{\sigma}^n - 2\alpha\boldsymbol{\gamma}^{n+1}, \nabla_s \boldsymbol{v})_\Omega, \\ (q, \nabla\cdot\boldsymbol{u}^{n+1})_\Omega &= 0. \end{aligned} \tag{4.17}$$

Step 3: We update the Lagrange multiplier $\boldsymbol{\sigma}^{n+1} \in L^2(\Omega; \mathbb{R}^{d\times d}_s)$:

$$\boldsymbol{\sigma}^{n+1} := \boldsymbol{\sigma}^n + 2\alpha(\nabla_{\mathrm{s}} \boldsymbol{u}^{n+1} - \boldsymbol{\gamma}^{n+1}). \tag{4.18}$$

We evaluate the residual:

$$R^{n+1} := \left(\|\boldsymbol{\sigma}^{n+1} - \boldsymbol{\sigma}^n\|^2_\Omega + \alpha^2 \|\nabla_s(\boldsymbol{u}^{n+1} - \boldsymbol{u}^n)\|^2_\Omega \right)^{\frac{1}{2}}. \tag{4.19}$$

$n = n + 1$
end while

where $\mathbf{sgn}(\cdot)$ *is defined such that for all* $\boldsymbol{\delta} \in \mathbb{R}^{d\times d}_s$,

$$\mathbf{sgn}(\boldsymbol{\delta}) = \begin{cases} \{\boldsymbol{\varsigma} \in \mathbb{R}^{d\times d}_s \mid |\boldsymbol{\varsigma}|_{\ell^2} \le 1\} & \text{for } |\boldsymbol{\delta}|_{\ell^2} = 0, \\ \dfrac{\boldsymbol{\delta}}{|\boldsymbol{\delta}|_{\ell^2}} & \text{for } |\boldsymbol{\delta}|_{\ell^2} > 0. \end{cases} \tag{4.20}$$

A straightforward computation shows that we are actually enforcing $\partial_{\boldsymbol{\gamma}} \mathcal{L}(u^n, \boldsymbol{\gamma}^{n+1}, \boldsymbol{\sigma}^n) = \mathbf{0}$ *in Step 1, see* (4.16)*. Next in Step 2,* (4.17) *amounts to enforcing* $\partial_{\boldsymbol{u}} \mathcal{L}(\boldsymbol{u}^{n+1}, \boldsymbol{\gamma}^{n+1}, \boldsymbol{\sigma}^n) = 0$ *(first line) and* $\nabla\cdot\boldsymbol{u}^{n+1} = 0$ *(second line). Finally, as the ADMM approaches convergence, we have* $(\nabla_{\mathrm{s}} \boldsymbol{u}^{n+1} - \boldsymbol{\gamma}^{n+1}) \to \mathbf{0}$ *so that* $\partial_{\boldsymbol{\sigma}} \mathcal{L}(\boldsymbol{u}^{n+1}, \boldsymbol{\gamma}^{n+1}, \boldsymbol{\sigma}^{n+1}) \to 0$ *owing to Step 3, see* (4.18)*. In conclusion, the ADMM converge to a critical point of the augmented Lagrangian.*

4.2 Hybrid lowest-order (HLO) discretization

In this section, we devise a hybrid lowest-order discretization method for Bingham vector flows. HHO family. We also introduce some notation for the discrete setting, which will also be useful in the next section.

4.2.1 Discrete setting

We consider a mesh sequence $(\mathcal{T}_\ell)_{\ell\in\mathbb{N}}$ where, for all $\ell \in \mathbb{N}$, $\mathcal{T}_\ell$ is a finite collection of nonempty, disjoint, open cells whose closures either cover Ω exactly or cover a close approximation thereof if Ω has curved boundaries. In this case, we set $\Omega_\ell := \mathrm{int}(\bigcup_{T\in\mathcal{T}_\ell} \overline{T})$. The subscript ℓ typically refers to a step in an adaptive mesh procedure which can involve local mesh refinement (and possibly coarsening). A generic mesh cell is denoted T, its boundary ∂T, its diameter h_T, and its unit outward normal $\boldsymbol{n}_T$. The mesh cells can have a polygonal/polyhedral shape, and the

meshes can possess hanging nodes. We set $h_\ell := \min_{T\in\mathcal{T}_\ell} h_T$ (we consider the minimum value instead of the more usual maximum value since the meshes are locally refined). The mesh sequence is assumed to be shape-regular in the sense, e.g., of [59], meaning that every mesh $\mathcal{T}_\ell$ admits a simplicial matching refinement belonging to a shape-regular mesh sequence in the sense of Ciarlet. This $(d-1)$-assumption can be relaxed to allow for polygonal meshes with some face degeneration as in [32]; this is useful for instance when considering agglomeration-based mesh coarsening procedures. We say that the dimensional subset $F \subset \overline{\Omega}$ is a mesh interface (resp., mesh boundary face) if there are two distinct mesh cells $T_{F,1}, T_{F,2} \in \mathcal{T}_\ell$ and an affine hyperplane H_F so that $F = \partial T_{F,1} \cap \partial T_{F,2} \cap H_F$ (resp., there is a mesh cell $T_F \in \mathcal{T}_h$ and an affine hyperplane H_F so that $F = \partial T_F \cap \partial\Omega_\ell \cap H_F$. Mesh interfaces are collected in the set $\mathcal{F}_\ell^i$, mesh boundary faces in $\mathcal{F}_\ell^b$, and we let $\mathcal{F}_\ell := \mathcal{F}_\ell^i \cup \mathcal{F}_\ell^b$ be the collection of the mesh faces. The diameter of a mesh face $F \in \mathcal{F}_\ell$ is denoted by h_F. For all $T \in \mathcal{T}_\ell$, we let $\mathcal{F}_{\partial T} := \{F \in \mathcal{F}_\ell \,|\, F \subset \partial T\}$ be the collection of the mesh faces composing ∂T. For all $F \in \mathcal{F}_{\partial T}, \boldsymbol{n}_{T,F} := \boldsymbol{n}_{T|F}$ is the unit normal to F pointing outward T; notice that, by definition, $\boldsymbol{n}_{T,F}$ is a constant vector over F. Let $A \subset \overline{\Omega}_\ell$ be a mesh cell, ∂A its boundary, or one of its faces; the inner product in $L^2(A)$ and in $\boldsymbol{L}^2(A) := L^2(A;\mathbb{R}^d)$ is denoted $(\cdot,\cdot)_A$ and the associated norm $\|\cdot\|_A$. For a finite set S, $|S|$ denotes its cardinal number.

4.2.2 Discrete minimization problem on the velocity

Let $T \in \mathcal{T}_\ell$ be a mesh cell. Recall from [59, 62] that HHO methods are devised from a local reconstruction operator and a local stabilization operator. In the present lowest-order setting where $k = 0$, both operators can be written explicitly, see also [70, 64]. The local space of discrete velocity unknowns is defined as

$$\hat{\boldsymbol{U}}_T := \mathbb{P}^1(T;\mathbb{R}^d) \times \mathbb{P}^0(\mathcal{F}_{\partial T};\mathbb{R}^d) \qquad \forall T \in \mathcal{T}_\ell, \tag{4.21}$$

where the first component of the pair is related to the cell and the second component to the faces composing its boundary. Here, $\mathbb{P}^0(\mathcal{F}_{\partial T};\mathbb{R}^d)$ denotes the space composed of piecewise constant vector functions over ∂T. We use the notation $\hat{\boldsymbol{v}}_T = (\boldsymbol{v}_T, (\boldsymbol{v}_F)_{F\in\mathcal{F}_{\partial T}})$ for a generic element in $\hat{\boldsymbol{U}}_T$. This is the same discrete setting as in Chapter 3 for antiplanar flows, except that both cell- and the face-velocities are now vector-valued. The local symmetric gradient reconstruction operator $\boldsymbol{E}_T : \hat{\boldsymbol{U}}_T \to \mathbb{R}^{d\times d}_s$ is such that, for all $\hat{\boldsymbol{v}}_T \in \hat{\boldsymbol{U}}_T$,

$$\boldsymbol{E}_T(\hat{\boldsymbol{v}}_T) = \sum_{F\in\mathcal{F}_{\partial T}} \frac{|F|_{d-1}}{2|T|_d}(\boldsymbol{v}_F \otimes \boldsymbol{n}_{T,F} + \boldsymbol{n}_{T,F} \otimes \boldsymbol{v}_F), \tag{4.22}$$

where $|F|_{d-1}$ is the measure of the face F and $|T|_d$ the measure of the cell T. It is also convenient to define a local discrete divergence by setting

$$D_T(\hat{\boldsymbol{v}}_T) := \sum_{F\in\mathcal{F}_{\partial T}} \frac{|F|_{d-1}}{|T|_d} \boldsymbol{v}_F \cdot \boldsymbol{n}_{T,F}. \tag{4.23}$$

where we used that $\sum_{F\in\mathcal{F}_{\partial T}} |F|_{d-1}\boldsymbol{n}_{T,F} = 0$. Note that

$$D_T(\hat{\boldsymbol{v}}_T) = \mathtt{tr}(\boldsymbol{E}_T(\hat{\boldsymbol{v}}_T)). \tag{4.24}$$

The local symmetric gradient reconstruction is to be used to discretize the viscous and the plastic dissipation potential.

The local stabilization operator $\boldsymbol{S}_{\partial T} : \hat{\boldsymbol{U}}_T \to \mathbb{P}^0(\mathcal{F}_{\partial T};\mathbb{R}^d)$ is such that, for all $\hat{\boldsymbol{v}}_T \in \hat{\boldsymbol{U}}_T$, its restriction to a face $F \in \mathcal{F}_{\partial T}$ is defined as

$$\boldsymbol{S}_{\partial T}(\hat{\boldsymbol{v}}_T)|_F := \pi_F^0(\boldsymbol{v}_F - \boldsymbol{v}_T), \tag{4.25}$$

We can now assemble the convex nonlinear minimization problem solved by the discrete velocity. Let us set

$$\hat{\boldsymbol{U}}_\ell := \mathbb{P}^1(\mathcal{T}_\ell;\mathbb{R}^d) \times \mathbb{P}^0(\mathcal{F}_\ell;\mathbb{R}^d), \tag{4.26}$$

where the first component of the pair is related to the mesh cells and the second component to the mesh faces. We use the notation $\hat{\boldsymbol{u}}_\ell = ((\boldsymbol{v}_T)_{T\in\mathcal{T}_\ell}, (\boldsymbol{v}_F)_{F\in\mathcal{F}_\ell})$ for a generic element in $\hat{\boldsymbol{U}}_\ell$, and for any mesh cell $T \in \mathcal{T}_\ell$ and any $\hat{\boldsymbol{v}}_\ell \in \hat{\boldsymbol{U}}_\ell$, we let $\hat{\boldsymbol{v}}_T \in \hat{\boldsymbol{U}}_T$ be composed of the components of $\hat{\boldsymbol{v}}_\ell$ attached to the cell T and its faces. We enforce the Dirichlet condition on the discrete velocity explicitly by introducing the subspace

$$\hat{\boldsymbol{U}}_{\ell,\boldsymbol{g}} := \left\{\hat{\boldsymbol{v}}_\ell \in \hat{\boldsymbol{U}}_\ell \mid \boldsymbol{v}_F = \boldsymbol{\pi}_F^0(\boldsymbol{g}); \forall F \in \mathcal{F}_\ell^b\right\}, \tag{4.27}$$

where $\boldsymbol{\pi}_F^0$ denotes the $L^2(F;\mathbb{R}^d)$-orthogonal projection onto $\mathbb{P}^0(F;\mathbb{R}^d)$. Note that $\boldsymbol{v}_F = \boldsymbol{\pi}_F^0(\boldsymbol{g})$ is nothing but the mean-value of $\boldsymbol{g}$ over F. We also define the subspace with homogeneous discrete velocities on the boundary

$$\hat{\boldsymbol{U}}_{\ell,0} := \left\{\hat{\boldsymbol{v}}_\ell \in \hat{\boldsymbol{U}}_\ell \mid \boldsymbol{v}_F = \boldsymbol{0}; \forall F \in \mathcal{F}_\ell^b\right\}. \tag{4.28}$$

The incompressibility condition is enforced by defining the following subspaces:

$$\hat{\boldsymbol{V}}_{\ell,\boldsymbol{g}} := \left\{\hat{\boldsymbol{v}}_\ell \in \hat{\boldsymbol{U}}_{\ell,\boldsymbol{g}} \mid D_T(\hat{\boldsymbol{v}}_T) = 0; \forall T \in \mathcal{T}_\ell\right\}, \tag{4.29}$$

$$\hat{\boldsymbol{V}}_{\ell,0} := \left\{\hat{\boldsymbol{v}}_\ell \in \hat{\boldsymbol{U}}_{\ell,0} \mid D_T(\hat{\boldsymbol{v}}_T) = 0; \forall T \in \mathcal{T}_\ell\right\}. \tag{4.30}$$

The discrete counterpart of (4.12) is to seek the discrete velocity field $\hat{\boldsymbol{u}}_\ell \in \hat{\boldsymbol{V}}_{\ell,\boldsymbol{g}}$ such that

$$\hat{\boldsymbol{u}}_\ell = \underset{\hat{\boldsymbol{v}}_\ell\in\hat{\boldsymbol{V}}_{\ell,\boldsymbol{g}}}{\arg\min} \sum_{T\in\mathcal{T}_\ell} \left\{(H(\boldsymbol{E}_T(\hat{\boldsymbol{v}}_T)),1)_T + \beta\|\eta_{\partial T}^{\frac{1}{2}}\boldsymbol{S}_{\partial T}(\hat{\boldsymbol{v}}_T)\|_{\partial T}^2 - (\boldsymbol{f},\boldsymbol{v}_T)_T\right\}, \tag{4.31}$$

with the dissipation potential $H : \mathbb{R}_s^{d\times d} \to \mathbb{R}$ defined in (4.9), where $\beta > 0$ is a numerical parameter, and $\eta_{\partial T}$ is, as before, the piecewise constant function on ∂T such that $\eta_{\partial T}|_F = h_F^{-1}$, for all $F \in \mathcal{F}_{\partial T}$. The stabilization term is needed to ensure stability in the discrete system considered in Step 2 of Algorithm 9 below. We set in what follows the parameter $\beta = \mu$. We notice that as the mesh is refined, the stabilization term tends to zero, so that the influence of β on the minimizer becomes more and more marginal.

4.2.3 Discrete augmented Lagrangian

The derivation of the discrete augmented Lagrangian is identical to the continuous setting. We introduce, for all $T \in \mathcal{T}_\ell$, the space $\boldsymbol{\Sigma}_T := \mathbb{P}^0(T;\mathbb{R}_s^{d\times d}) \equiv \mathbb{R}_s^{d\times d}$ and the auxiliary field $\boldsymbol{\gamma}_T \in \boldsymbol{\Sigma}_T$ and we enforce $\boldsymbol{\gamma}_T = \boldsymbol{E}_T(\hat{\boldsymbol{u}}_T)$ by means of the Lagrange multiplier $\boldsymbol{\sigma}_T \in \boldsymbol{\Sigma}_T$. Then, setting

$$\boldsymbol{\Sigma}_\ell := \left(\mathbb{R}_s^{d\times d}\right)^{|\mathcal{T}_\ell|}, \qquad X(\mathcal{T}_\ell) := \hat{\boldsymbol{U}}_\ell \times \boldsymbol{\Sigma}_\ell \times \boldsymbol{\Sigma}_\ell, \tag{4.32}$$

the discrete augmented Lagrangian is defined as $\mathcal{L}_\ell : X(\mathcal{T}_\ell) \to \mathbb{R}$ such that

$$\begin{aligned}\mathcal{L}_\ell(\hat{\boldsymbol{u}}_\ell,\boldsymbol{\gamma}_\ell,\boldsymbol{\sigma}_\ell) := \sum_{T\in\mathcal{T}_\ell} \Big\{&(\boldsymbol{H}(\boldsymbol{\gamma}_T),1)_T + \mu\|\eta_{\partial T}^{\frac{1}{2}}\boldsymbol{S}_{\partial T}(\hat{\boldsymbol{v}}_T)\|_{\partial T}^2 - (\boldsymbol{f},\boldsymbol{u}_T)_T\\ &+ (\boldsymbol{\sigma}_T, \boldsymbol{E}_T(\hat{\boldsymbol{u}}_T) - \boldsymbol{\gamma}_T)_T + \alpha\|\boldsymbol{E}_T(\hat{\boldsymbol{u}}_T) - \boldsymbol{\gamma}_T\|_T^2\Big\},\end{aligned} \tag{4.33}$$

where we used the notation $\boldsymbol{\gamma}_\ell = (\boldsymbol{\gamma}_T)_{T\in\mathcal{T}_\ell}$ and $\boldsymbol{\sigma}_\ell = (\boldsymbol{\sigma}_T)_{T\in\mathcal{T}_\ell}$ for all $\boldsymbol{\gamma}_\ell, \boldsymbol{\sigma}_\ell \in \boldsymbol{\Sigma}_\ell$. Note that $(\hat{\boldsymbol{u}}_\ell,\boldsymbol{\gamma}_\ell,\boldsymbol{\sigma}_\ell)$ is a saddle-point of the discrete Lagrangian $\mathcal{L}_\ell$ if and only if $\boldsymbol{E}_T(\hat{\boldsymbol{u}}_T) = \boldsymbol{\gamma}_T$ for all $T \in \mathcal{T}_\ell$ and $\hat{\boldsymbol{u}}_\ell$ is the unique minimizer of (4.31).

The ADMM applied to the discrete augmented Lagrangian is described in Algorithm 9: Given the initial values $\hat{\boldsymbol{u}}_\ell^0 \in \hat{\boldsymbol{U}}_{\ell,\boldsymbol{g}}$ and $\boldsymbol{\sigma}_\ell^0 \in \boldsymbol{\Sigma}_\ell$, we perform, for all $n \geq 0$, the following three

Algorithm 9 Bingham vector flows: ADMM in discrete form for HLO

1: Choose $(\hat{\boldsymbol{u}}_\ell^0, \boldsymbol{\sigma}_\ell^0) \in \hat{\boldsymbol{U}}_{\ell,\boldsymbol{g}} \times \boldsymbol{\Sigma}_\ell$
2: Choose $\epsilon > 0$, set $R^0 = \infty$ and $n = 0$
3: **while** $R_\ell^n > \epsilon$ **do**
4: ***Step 1:*** We define $\boldsymbol{\gamma}_\ell^{n+1} \in \boldsymbol{\Sigma}_\ell$ such that, $\forall T \in \mathcal{T}_\ell$,

$$\boldsymbol{\gamma}_T^{n+1} := \begin{cases} \dfrac{1}{2(\alpha+\mu)} \left(|\boldsymbol{\theta}_T^n|_{\ell^2} - \sqrt{2}\sigma_0 \right) \dfrac{\boldsymbol{\theta}_T^n}{|\boldsymbol{\theta}_T^n|_{\ell^2}} & \text{if } |\boldsymbol{\theta}_T^n|_{\ell^2} > \sqrt{2}\sigma_0, \\ \boldsymbol{0} & \text{if } |\boldsymbol{\theta}_T^n|_{\ell^2} \leq \sqrt{2}\sigma_0, \end{cases} \tag{4.34}$$

with $\boldsymbol{\theta}_T^n := \boldsymbol{\sigma}_T^n + 2\alpha \boldsymbol{E}_T(\hat{\boldsymbol{u}}_T^n)$.
5: ***Step 2:*** We seek $(\hat{\boldsymbol{u}}_\ell^{n+1}, p_l^{n+1}) \in \hat{\boldsymbol{U}}_{\ell,\boldsymbol{g}} \times P_\ell$ s.t. $\forall (\hat{\boldsymbol{v}}_\ell, q_\ell) \in \hat{\boldsymbol{U}}_{\ell,0} \times P_\ell$:

$$\sum_{T\in\mathcal{T}_\ell} \left\{ 2\hat{a}_{T,\alpha\mu}(\hat{\boldsymbol{u}}_T^{n+1}, \hat{\boldsymbol{v}}_T) - |T|_d D_T(\hat{\boldsymbol{v}}_T) p_T^{n+1} \right\} = \sum_{T\in\mathcal{T}_\ell} \Big\{ (\boldsymbol{f}, \boldsymbol{v}_T)_T - (\boldsymbol{\sigma}_T^n - 2\alpha\boldsymbol{\gamma}_T^{n+1}, \boldsymbol{E}_T(\hat{\boldsymbol{v}}_T))_T \Big\}, \tag{4.35}$$

$$\sum_{T\in\mathcal{T}_\ell} |T|_d D_T(\hat{\boldsymbol{u}}_T^{n+1}) q_T = 0, \tag{4.36}$$

where $\hat{a}_{T,\alpha\mu} \in \hat{\boldsymbol{U}}_{\ell,\boldsymbol{g}} \times \hat{\boldsymbol{U}}_{\ell,0}$ is the local bilinear form defined as

$$\hat{a}_{T,\alpha\mu}(\hat{\boldsymbol{w}}_T, \hat{\boldsymbol{v}}_T) := \alpha(\boldsymbol{E}_T(\hat{\boldsymbol{w}}_T), \boldsymbol{E}_T(\hat{\boldsymbol{v}}_T))_T + \mu(\eta_{\partial T} \boldsymbol{S}_{\partial T}(\hat{\boldsymbol{w}}_T), \boldsymbol{S}_{\partial T}(\hat{\boldsymbol{v}}_T))_{\partial T}, \tag{4.37}$$

and where we recall that $D_T(\hat{\boldsymbol{v}}_T) = \mathtt{tr}(\boldsymbol{E}_T(\hat{\boldsymbol{v}}_T))$.
6: ***Step 3:*** We update the Lagrange multiplier $\boldsymbol{\sigma}_\ell^{n+1} \in \boldsymbol{\Sigma}_\ell$ for all $T \in \mathcal{T}_\ell$,

$$\boldsymbol{\sigma}_T^{n+1} := \boldsymbol{\sigma}_T^n + 2\alpha(\boldsymbol{E}_T(\hat{\boldsymbol{u}}_T^{n+1}) - \boldsymbol{\gamma}_T^{n+1}). \tag{4.38}$$

7: We evaluate the residual:

$$R_\ell^{n+1} := \Big(\sum_{T\in\mathcal{T}_\ell} \|\boldsymbol{\sigma}_T^{n+1} - \boldsymbol{\sigma}_T^n\|_T^2 + \alpha^2 \sum_{T\in\mathcal{T}_\ell} \|\boldsymbol{E}_T(\hat{\boldsymbol{u}}_T^{n+1}) - \boldsymbol{E}_T(\hat{\boldsymbol{u}}_T^n)\|_T^2 \Big)^{\frac{1}{2}}. \tag{4.39}$$

8: $n = n + 1$
9: **end while**

steps: We first define $\boldsymbol{\gamma}_\ell^{n+1} \in \boldsymbol{\Sigma}_\ell$. Given $\boldsymbol{\sigma}_\ell^n$ and $\boldsymbol{\gamma}_\ell^{n+1}$ in Step 2, letting $P_\ell := \mathbb{P}^0(\mathcal{T}_\ell;\mathbb{R}) \equiv \mathbb{R}^{|\mathcal{T}_\ell|}$ denote the space of piecewise constant pressures having zero mean-value in Ω, we seek $(\hat{\boldsymbol{u}}_\ell^{n+1}, p_l^{n+1}) \in \hat{\boldsymbol{U}}_{\ell,\boldsymbol{g}} \times P_\ell$ solving the Stokes-like discrete variational problem (4.35)-(4.36), where the stress terms are treated explicitly. Finally in Step 3, we update the Lagrange multiplier $\boldsymbol{\sigma}_\ell^{n+1} \in \boldsymbol{\Sigma}_\ell$.

4.3 Hybrid higher-order (HHO) discretization

In this section, we generalize the previous developments to the HHO method. Let $k \geq 1$ be the polynomial degree. For the sake of simplicity, we use a similar notation to that of the previous section, just by adding a superscript k to denote the obvious analogous higher-order version of the formerly defined spaces and variables.

4.3.1 Discrete minimization problem on the velocity

For all $T \in \mathcal{T}_\ell$, the local discrete space is

$$\hat{\boldsymbol{U}}_T^k := \mathbb{P}^k(T;\mathbb{R}^d) \times \mathbb{P}^k(\mathcal{F}_{\partial T};\mathbb{R}^d), \tag{4.40}$$

where $\mathbb{P}^k(T;\mathbb{R}^d)$ and $\mathbb{P}^k(\mathcal{F}_{\partial T};\mathbb{R}^d)$ are the spaces spanned by the restrictions to T and $\mathcal{F}_{\partial T}$, respectively, of $d-$ and piecewise $(d-1)-$variate vector-valued polynomials of total degree $\le k$. A generic element of $\hat{\boldsymbol{U}}_T^k$ is denoted by $\hat{\boldsymbol{v}}_T = (\boldsymbol{v}_T, \boldsymbol{v}_{\partial T})$. Following [20], we reconstruct a symmetric discrete gradient in the space $\mathbb{P}^k(T;\mathbb{R}_s^{d\times d})$, such that the local symmetric gradient operator $\boldsymbol{E}_T^k : \hat{\boldsymbol{U}}_T^k \to \mathbb{P}^k(T;\mathbb{R}_s^{d\times d})$ is obtained by solving the following problem: For all $\hat{\boldsymbol{v}}_T = (\boldsymbol{v}_T, \boldsymbol{v}_{\partial T}) \in \hat{\boldsymbol{U}}_T^k$,

$$(\boldsymbol{E}_T^k(\hat{\boldsymbol{v}}_T), \boldsymbol{w})_T = (\nabla_{\rm s}\boldsymbol{v}_T, \boldsymbol{w})_T + (\boldsymbol{v}_{\partial T} - \boldsymbol{v}_T, \boldsymbol{w}\boldsymbol{n}_T)_{\partial T} \quad \forall \boldsymbol{w} \in \mathbb{P}^k(T;\mathbb{R}_s^{d\times d}). \tag{4.41}$$

Computing $\boldsymbol{E}_T^k(\hat{\boldsymbol{v}}_T)$ entails inverting the mass matrix in $\mathbb{P}^k(T;\mathbb{R}_s^{d\times d})$. Actually, we only need to invert the mass matrix in $\mathbb{P}^k(T;\mathbb{R})$, and $\boldsymbol{E}_T^k(\hat{\boldsymbol{v}}_T)$ is then computed componentwise by solving a system similar to (4.41) for various right-hand sides. This results in significant computational savings. For the purpose of stabilization, we also define for all $T \in \mathcal{T}_\ell$ the local reconstruction operator $\boldsymbol{R}_T^{k+1} : \hat{\boldsymbol{U}}_T^k \to \mathbb{P}^{k+1}(T;\mathbb{R}^d)$ so that, for all $\hat{\boldsymbol{v}}_T = (\boldsymbol{v}_T, \boldsymbol{v}_{\partial T}) \in \hat{\boldsymbol{U}}_T^k$,

$$(\nabla_{\rm s}\boldsymbol{R}_T^{k+1}(\hat{\boldsymbol{v}}_T), \nabla_{\rm s}\boldsymbol{w})_T = (\nabla_{\rm s}\boldsymbol{v}_T, \nabla_{\rm s}\boldsymbol{w})_T + (\boldsymbol{v}_{\partial T} - \boldsymbol{v}_T, \nabla_{\rm s}\boldsymbol{w}\boldsymbol{n}_T)_{\partial T} \quad \forall \boldsymbol{w} \in \mathbb{P}^{k+1}(T;\mathbb{R}^d), \tag{4.42}$$

which entails inverting the local stiffness matrix in $\mathbb{P}^{k+1}(T;\mathbb{R}^d)$ with Neumann boundary conditions. The rigid-body motion of $R_T^{k+1}(\hat{v}_T)$ are prescribed by those of v_T; this actual value is irrelevant on what follows.

We define the local stabilization operator $\boldsymbol{S}_{\partial T}^k : \hat{\boldsymbol{U}}_T^k \to \mathbb{P}^k(\mathcal{F}_{\partial T};\mathbb{R}^d)$ to penalize the difference between $\boldsymbol{v}_{\partial T}$ and $\boldsymbol{v}_{T|\partial T}$ such that, for all $\hat{\boldsymbol{v}}_T = (\boldsymbol{v}_T, \boldsymbol{v}_{\partial T}) \in \hat{\boldsymbol{U}}_T^k$, we have

$$\boldsymbol{S}_{\partial T}^k(\hat{\boldsymbol{v}}_T) := \boldsymbol{\pi}_{\partial T}^k(\boldsymbol{v}_{\partial T} - \boldsymbol{R}_T^{k+1}(\hat{\boldsymbol{v}}_T)_{|\partial T}) - \boldsymbol{\pi}_T^k(\boldsymbol{v}_T - \boldsymbol{R}_T^{k+1}(\hat{\boldsymbol{v}}_T))_{|\partial T}. \tag{4.43}$$

where $\boldsymbol{\pi}_{\partial T}^k$ and $\boldsymbol{\pi}_T^k$ denote the $\boldsymbol{L}^2$-orthogonal projectors onto $\mathbb{P}^k(\mathcal{F}_{\partial T};\mathbb{R}^d)$ and $\mathbb{P}^k(T;\mathbb{R}^d)$, respectively. Finally, the local discrete divergence operator $D_T^k : \hat{\boldsymbol{U}}_T \to \mathbb{P}^k(T;\mathbb{R})$ acts as follows: For all $\hat{\boldsymbol{v}}_T \in \hat{\boldsymbol{U}}_T^k$,

$$\begin{aligned}(D_T^k(\hat{\boldsymbol{v}}_T), q) &:= (\nabla\cdot\boldsymbol{v}_T, q)_T + (\boldsymbol{v}_{\partial T} - \boldsymbol{v}_T, q\boldsymbol{n}_T)_{\partial T},\\ &= -(\boldsymbol{v}_T, \nabla q)_T + (\boldsymbol{v}_{\partial T}, q\boldsymbol{n}_T)_{\partial T} \qquad \forall q \in \mathbb{P}^k(T;\mathbb{R}).\end{aligned} \tag{4.44}$$

Taking $\omega = q\boldsymbol{I}_d$ in (4.41), it is readily seen that $D_T^k(\hat{\boldsymbol{v}}_T) = \mathtt{tr}(\boldsymbol{E}_T^k(\hat{\boldsymbol{v}}_T))$.

Turning now to the assembly of the convex nonlinear minimization problem solved by the discrete velocity, let us set

$$\hat{\boldsymbol{U}}_\ell^k := \mathbb{P}^k(\mathcal{T}_\ell;\mathbb{R}^d) \times \mathbb{P}^k(\mathcal{F}_\ell;\mathbb{R}^d). \tag{4.45}$$

We also define the spaces

$$\hat{\boldsymbol{U}}_{\ell,\boldsymbol{g}}^k = \{\hat{\boldsymbol{v}}_\ell \in \hat{\boldsymbol{U}}_\ell^k \mid \boldsymbol{v}_F = \pi_F^k(\boldsymbol{g}); \forall F \in F_\ell^b\}, \tag{4.46}$$

$$\hat{\boldsymbol{U}}_{\ell,0}^k = \{\hat{\boldsymbol{v}}_\ell \in \hat{\boldsymbol{U}}_\ell^k \mid \boldsymbol{v}_F = \boldsymbol{0}; \forall F \in F_\ell^b\}, \tag{4.47}$$

where π_F^k denote the L^2-orthogonal projection onto $\mathbb{P}^k(F;\mathbb{R}^d)$. The incompressibility constraint is enforced by defining the subspaces

$$\hat{\boldsymbol{V}}_{\ell,\boldsymbol{g}}^k = \{\hat{\boldsymbol{v}}_\ell \in \hat{\boldsymbol{U}}_{\ell,\boldsymbol{g}}^k \mid D_T^k(\hat{\boldsymbol{v}}_T) = 0; \forall T \in \mathcal{T}_\ell\}, \tag{4.48}$$

$$\hat{\boldsymbol{V}}_{\ell,0}^k = \{\hat{\boldsymbol{v}}_\ell \in \hat{\boldsymbol{U}}_{\ell,0}^k \mid D_T^k(\hat{\boldsymbol{v}}_T) = 0; \forall T \in \mathcal{T}_\ell\}. \tag{4.49}$$

The plastic term cannot be computed exactly for polynomials of degree $k \geq 1$, so that quadrature rules must be used. This occurs when the cells lie at the same time in the yielded and the unyielded regions (recall that we do not know *a priori* the location of the yield surface). Our first step is therefore to rewrite the minimization problem by means of quadrature rules. For all $T \in \mathcal{T}_\ell$, let $\boldsymbol{\chi}_T = (\boldsymbol{\chi}_{T,g})_{1\leq g\leq N_q}$ with $\boldsymbol{\chi}_{T,g} \in T$, for all $1 \leq g \leq N_q$, denote the set of quadrature points in T. We write more concisely $\boldsymbol{\chi}_T \in T^{N_q}$. Similarly, let $\boldsymbol{\omega}_T = (\omega_{T,g})_{1\leq g\leq N_q}$ with $\omega_{T,g} \in \mathbb{R}$, for all $1 \leq g \leq N_q$, denote the corresponding quadrature weights. We write more concisely $\boldsymbol{\omega}_T \in \mathbb{R}^{N_q}$. We assume that the quadrature is at least of order $2k$, so that

$$(s,1)_T = \sum_{g=1}^{N_q} \omega_{T,g} s(\boldsymbol{\chi}_{T,g}) \qquad \forall s \in \mathbb{P}^{2k}(T;\mathbb{R}). \tag{4.50}$$

Let us define for symmetric tensors $\boldsymbol{\rho}$ and $\boldsymbol{\tau}$:

$$(\boldsymbol{\rho},\boldsymbol{\tau})_{Q_T} := \sum_{g=1}^{N_q} \omega_{T,g} \boldsymbol{\rho}(\boldsymbol{\chi}_{T,g}) : \boldsymbol{\tau}(\boldsymbol{\chi}_{T,g}), \qquad |\boldsymbol{\rho}|_{Q_T} := (\boldsymbol{\rho},\boldsymbol{\rho})_{Q_T}^{\frac{1}{2}}. \tag{4.51}$$

Then, we introduce the local and global spaces of degrees of freedom for the auxiliary variables and Lagrange multipliers only defined at the quadrature points, such that

$$\check{\boldsymbol{\Sigma}}_T = \left(\mathbb{R}_s^{d\times d}\right)^{N_q}, \qquad \check{\boldsymbol{\Sigma}}_\ell = \left(\mathbb{R}_s^{d\times d}\right)^{N_q\times|\mathcal{T}_\ell|}. \tag{4.52}$$

The integration of the dissipation potential must take into account the quadrature rule. To this aim, we introduce a discrete integrated dissipation potential $h_{Q_T} : \check{\boldsymbol{\Sigma}}_T \to \mathbb{R}$ such that

$$h_{Q_T}(\boldsymbol{e}) = \mu|\boldsymbol{e}|_{Q_T}^2 + \sqrt{2}\sigma_0|\boldsymbol{e}|_{Q_T} \qquad \forall \boldsymbol{e} \in \check{\boldsymbol{\Sigma}}_T. \tag{4.53}$$

The discrete counterpart of (4.12) for the higher-order discretization is to seek the discrete velocity field $\hat{\boldsymbol{u}}_\ell \in \hat{\boldsymbol{V}}_{\ell,\boldsymbol{g}}^k$ such that

$$\hat{\boldsymbol{u}}_\ell = \operatorname*{arg\,min}_{\hat{\boldsymbol{v}}_\ell\in\hat{\boldsymbol{V}}_{\ell,\boldsymbol{g}}^k} \sum_{T\in\mathcal{T}_\ell} \left\{ h_{Q_T}(\check{\boldsymbol{E}}_T^k(\hat{\boldsymbol{v}}_T)) + \mu\|\eta_{\partial T}^{\frac{1}{2}}\boldsymbol{S}_{\partial T}^k(\hat{\boldsymbol{v}}_T)\|_{\partial T}^2 - (\boldsymbol{f},\boldsymbol{v}_T)_T \right\}, \tag{4.54}$$

where we introduced $\check{\boldsymbol{E}}_T^k(\hat{\boldsymbol{v}}_T) \in \check{\boldsymbol{\Sigma}}_T$ as the vector collecting the values of $\boldsymbol{E}_T^k(\hat{\boldsymbol{v}}_T)$ at all the quadratures points $(\boldsymbol{\chi}_{T,g})_{1\leq g\leq N_q}$. Note that we keep for the two rightmost terms in (4.54) the integral notation, since first, we can assume that $\boldsymbol{f}$ is a smooth enough function so that the integration of $(\boldsymbol{f},\boldsymbol{v}_T)_T$ in each cell is not an issue, and second, we can assume that the surface quadrature rule is exact for the stabilization term by using a surface quadrature of degree $2k$.

4.3.2 Discrete augmented Lagrangian

Owing to the inexactness of the numerical integral of the plastic term, the constraint $\boldsymbol{\gamma} = \nabla_{\mathrm{s}}\boldsymbol{u}$ can be ensured only at the quadrature points. We introduce a global auxiliary field $\check{\boldsymbol{\gamma}}_\ell := (\boldsymbol{\gamma}_T)_{T\in\mathcal{T}_\ell} \in \check{\boldsymbol{\Sigma}}_\ell$ and we enforce that $\check{\boldsymbol{\gamma}}_\ell := (\boldsymbol{\gamma}_T)_{T\in\mathcal{T}_\ell}$ satisfies $\boldsymbol{\gamma}_T = \check{\boldsymbol{E}}_T^k(\hat{\boldsymbol{u}}_T)$ for all $T \in \mathcal{T}_\ell$, by means of the Lagrangian multiplier $\check{\boldsymbol{\sigma}}_\ell := (\boldsymbol{\sigma}_T)_{T\in\mathcal{T}_\ell} \in \check{\boldsymbol{\Sigma}}_\ell$. Then, we define

$$X_\ell := \hat{\boldsymbol{U}}_{\ell,\boldsymbol{g}}^k \times \check{\boldsymbol{\Sigma}}_\ell \times \check{\boldsymbol{\Sigma}}_{\boldsymbol{\ell}}, \tag{4.55}$$

and additionally $P_\ell^k := L_0^2(\Omega) \cap \mathbb{P}^k(\mathcal{T}_\ell,\mathbb{R})$ for the discrete pressures with zero mean-value in the domain. We introduce the discrete augmented Lagrangian $\mathcal{L}_\ell : X_\ell \to \mathbb{R}$ such that

$$\begin{aligned}\mathcal{L}_\ell(\hat{\boldsymbol{u}}_\ell,\check{\boldsymbol{\gamma}}_\ell,\check{\boldsymbol{\sigma}}_\ell) := \sum_{T\in\mathcal{T}_\ell} \Big\{ & h_{Q_T}(\check{\boldsymbol{\gamma}}_T) + \mu\|\eta_{\partial T}^{\frac{1}{2}}\boldsymbol{S}_{\partial T}^k(\hat{\boldsymbol{u}}_T)\|_{\partial T} - (\boldsymbol{f},\boldsymbol{u}_T)_T \\ & + (\check{\boldsymbol{\sigma}}_T, \check{\boldsymbol{E}}_T^k(\hat{\boldsymbol{u}}_T) - \check{\boldsymbol{\gamma}}_T)_{Q_T} + \alpha\|\check{\boldsymbol{E}}_T^k(\hat{\boldsymbol{u}}_T) - \check{\boldsymbol{\gamma}}_T\|_{Q_T}^2 \Big\}.\end{aligned} \tag{4.56}$$

Algorithm 10 Bingham vector flows: ADMM in discrete form for HHO

Choose $(\hat{\boldsymbol{u}}_\ell^0, \check{\boldsymbol{\sigma}}_\ell^0) \in \hat{\boldsymbol{U}}_{\ell,\boldsymbol{g}} \times \check{\boldsymbol{\Sigma}}_\ell$
Choose $\epsilon > 0$, set $R^0 = \infty$ and $n = 0$
while $R_\ell^n > \epsilon$ **do**
Step 1: We define $\check{\boldsymbol{\gamma}}_\ell^{n+1} \in \check{\boldsymbol{\Sigma}}_\ell$, for all $T \in \mathcal{T}_\ell$ and all $1 \le g \le N_q$, such that

$$\check{\boldsymbol{\gamma}}_{T,g}^{n+1} = \begin{cases} \dfrac{1}{2(\alpha+\mu)} \Big(|\boldsymbol{\theta}_{T,g}^n| - \sqrt{2}\sigma_0 \Big) \dfrac{\boldsymbol{\theta}_{T,g}^n}{|\boldsymbol{\theta}_{T,g}^n|_{\ell^2}} & \text{for } |\boldsymbol{\theta}_{T,g}^n|_{\ell^2} > \sqrt{2}\sigma_0, \\ \mathbf{0} & \text{for } |\boldsymbol{\theta}_{T,g}^n|_{\ell^2} \le \sqrt{2}\sigma_0. \end{cases} \tag{4.57}$$

with $\boldsymbol{\theta}_{T,g}^n := \check{\boldsymbol{\sigma}}_{T,g}^n + 2\alpha \boldsymbol{E}_T^k(\hat{\boldsymbol{u}}_T^n)(\boldsymbol{\chi}_{T,g})$.
Step 2: We seek $(\hat{\boldsymbol{u}}_\ell^{n+1}, p_\ell^{n+1}) \in \hat{\boldsymbol{U}}_{\ell,\boldsymbol{g}}^k \times P_\ell^k$ s.t. $\forall (\hat{\boldsymbol{v}}_\ell, q_\ell) \in \hat{\boldsymbol{U}}_{\ell,0}^k \times P_\ell^k$:

$$\sum_{T\in\mathcal{T}_\ell} \Big\{ 2\hat{a}_{T,\alpha\mu}(\hat{\boldsymbol{u}}_T^{n+1}, \hat{\boldsymbol{v}}_T) + \hat{b}_T(p_T^{n+1}, \hat{\boldsymbol{v}}_T) \Big\} = \sum_{T\in\mathcal{T}_\ell} \Big\{ (\boldsymbol{f}, \boldsymbol{v}_T)_T - (\check{\boldsymbol{\sigma}}_T^n - 2\alpha\check{\boldsymbol{\gamma}}_T^{n+1}, \check{\boldsymbol{E}}_T^k(\hat{\boldsymbol{v}}_T))_{Q_T} \Big\}, \tag{4.58}$$

$$\sum_{T\in\mathcal{T}_\ell} \hat{b}_T(q_T, \hat{\boldsymbol{u}}_T^{n+1}) = 0, \tag{4.59}$$

where $\hat{a}_{T,\alpha\mu} \in \hat{\boldsymbol{U}}_T^k \times \hat{\boldsymbol{U}}_T^k$ and $\hat{b}_T \in \mathbb{P}^k(T;\mathbb{R}) \times \hat{\boldsymbol{U}}_T^k$ are the bilinear forms defined as

$$\hat{a}_{T,\alpha\mu}(\hat{\boldsymbol{w}}_T, \hat{\boldsymbol{v}}_T) := \alpha(\boldsymbol{E}_T^k(\hat{\boldsymbol{w}}_T), \boldsymbol{E}_T^k(\hat{\boldsymbol{v}}_T))_T + \mu(\eta_{\partial T}\boldsymbol{S}_{\partial T}^k(\hat{\boldsymbol{w}}_T), \boldsymbol{S}_{\partial T}^k(\hat{\boldsymbol{v}}_T))_{\partial T}, \tag{4.60}$$

$$\hat{b}_T(q_T, \hat{\boldsymbol{u}}_T) := -(q_T, D_T^k(\hat{\boldsymbol{v}}_T))_T. \tag{4.61}$$

Step 3: We update the Lagrange multiplier $\check{\boldsymbol{\sigma}}_\ell^{n+1} \in \check{\boldsymbol{\Sigma}}_\ell$ for all $T \in \mathcal{T}_\ell$ and all $1 \le g \le N_q$,

$$\check{\boldsymbol{\sigma}}_{T,g}^{n+1} := \check{\boldsymbol{\sigma}}_{T,g}^n + 2\alpha\Big(\boldsymbol{E}_T^k(\hat{\boldsymbol{u}}_T^{n+1})(\boldsymbol{\chi}_{T,g}) - \check{\boldsymbol{\gamma}}_{T,g}^{n+1}\Big). \tag{4.62}$$

We evaluate the residual

$$R_\ell^{n+1} := \left(\sum_{T\in\mathcal{T}_h} (|\check{\boldsymbol{\sigma}}_\ell^{n+1} - \check{\boldsymbol{\sigma}}_\ell^n|_{Q_T}^2 + \alpha^2 |\widetilde{\boldsymbol{E}}_T^k(\hat{\boldsymbol{u}}_T^{n+1} - \hat{\boldsymbol{u}}_T^n)|_{Q_T}^2) \right)^{\frac{1}{2}}. \tag{4.63}$$

Note that $|\check{\boldsymbol{E}}_T^k(\hat{\boldsymbol{v}}_T)|_{Q_T} = \|\boldsymbol{E}_T^k(\hat{\boldsymbol{v}}_T)\|_T$ for all $\hat{\boldsymbol{v}}_T \in \hat{\boldsymbol{U}}_T^k$.
$n = n + 1$
end while

The ADMM algorithm is devised as in the previous sections, see Algorithm 10. We perform the standard three steps. First, given $(\hat{\boldsymbol{u}}_\ell^n, \check{\boldsymbol{\sigma}}_\ell^n) \in \hat{\boldsymbol{U}}_{\ell,\boldsymbol{g}}^k \times \check{\boldsymbol{\Sigma}}_\ell$, the minimization of the Lagrangian with respect to $\check{\boldsymbol{\gamma}}_\ell$ leads to a point-wise definition of $\check{\boldsymbol{\gamma}}_\ell^{n+1}$ at all the Gauss quadrature points of all the mesh cells. Second, we seek $(\hat{\boldsymbol{u}}_\ell^{n+1}, p_\ell^{n+1}) \in \hat{\boldsymbol{U}}_{\ell,\boldsymbol{g}}^k \times P_\ell^k$ by solving the Stokes-like discrete variational problem (4.59), where the stress terms are treated as explicit force terms. Finally, we update the Lagrange multiplier in each mesh cell, at each quadrature point, see (4.62).

Remark 4.2 (Number of points)**.** *Note that $\check{\boldsymbol{\gamma}}_\ell^{n+1}$ and $\check{\boldsymbol{\sigma}}_\ell^{n+1}$ are computable at any point $\boldsymbol{x}$, where $\boldsymbol{E}_T(\hat{\boldsymbol{u}}_T^{n+1})(\boldsymbol{x})$ is known. Therefore, it is possible to have a more detailed knowledge of these fields by evaluating them at more points. However, this comes at the expense of an increase in the computational cost (storage and computations).*

4.4 Numerical results

In this section, we present our numerical results for Bingham vector flow problems. We use the hybrid lowest-order discretization with the ADMM from Section 4.2; results with the higher-order discretization from Section 4.3 and are under way. The first setting is the lid-driven cavity benchmark, which is well documented in the literature (see, among others, [16, 124, 127]). The second test case we consider is a confined flow in a Couette geometry (i.e. a hollow circular cylinder) with a vane tool. It is a commonly used geometry in the viscoplasticity community, especially to study the behavior of pasty materials that are difficult to pour in the annulus of one cylinder inside another (classical Couette geometry) or that are likely to slip along the inner cylinder wall. However, due to the complexity of the geometry, solving analytically the flow equations is not feasible in practice and therefore there is no explicit solution for nonlinear cases. However, there exist numerical and experimental results relying on the assumption of a cylindrical thin layer of the material flowing around the vane tool at low velocity. Nonetheless, this assumption was recently questioned in [113]. To our knowledge, there are no numerical simulations that replicate the recent experimental data.

4.4.1 Lid-driven cavity

We consider the standard Lid-driven cavity problem with unitary square domain, where the flow is driven by a lid moving with uniform horizontal velocity and the remaining walls are stationary. Despite the simplicity of the cavity setting, singular effects may occur at the top corners, since the velocity field is required to accomplish the non-homogeneous and the no-slip boundary conditions at the same time. The singularities at the corners weaken the expected regularity of the solution, so that $\boldsymbol{u} \in H^s(\Omega)$ with $s < 1$.

The adimensional Bingham number is defined as

$$\mathtt{Bi} = \frac{\sigma_0 L}{\mu V}, \tag{4.64}$$

where L is a reference length (the width of the square) and V the reference velocity (the lid velocity $V = 1$). We set the augmentation parameter to $\alpha = 10$ and the convergence threshold for the discrete residual defined in (4.39) is set to $\epsilon = 10^{-8}$.

Figure 4.1 shows the discrete residual R_ℓ as a function of the iteration number in the ADMM for quadrilateral meshes with $h = 1/32$ and $h = 1/128$ for $\mathtt{Bi} = 2$ and $\mathtt{Bi} = 50$. We also vary the α parameter of the ADMM algorithm. We observe similar convergence behavior for all the cases, where there are some perturbations before changing to a faster convergence. We also notice that these perturbations are more pronounced when increasing Bi. One possible explanation is that yield effects dominate the solution when increasing Bi, which is a well-known reason of numerical difficulties, caused by the non-smoothness of the yield term. We additionally observe that using finer meshes for both Bi numbers results in general in an increasing of the number

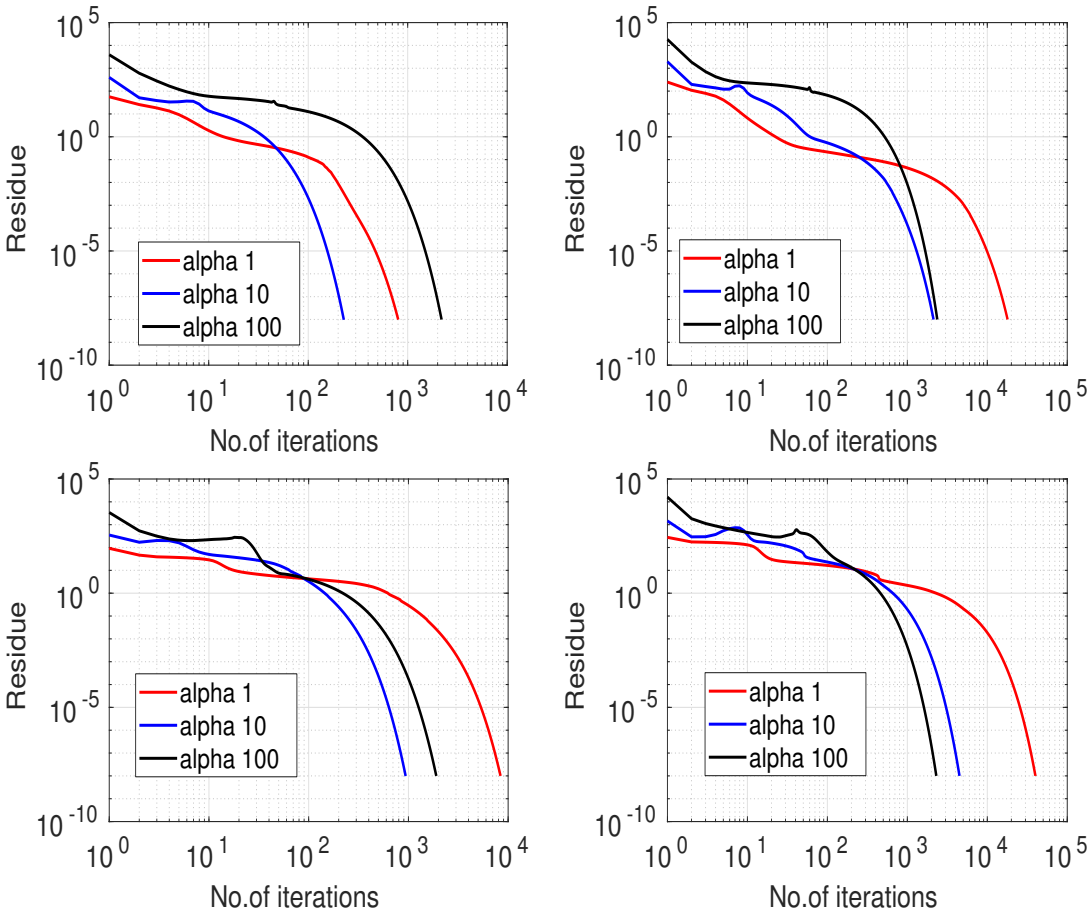

Figure 4.1: Discrete residual vs. ADMM iteration number for $\texttt{Bi} = 2$ (top) and $\texttt{Bi} = 50$ (bottom) for quadrilateral meshes with $h = 1/32$ (left) and $h = 1/128$ (right).

of iterations. However, we notice that when the augmentation parameter $\alpha = 100$, the ADMM algorithm is in general taking less number of iterations for the finer meshes. Thus, all the experiments shown in what follows are computed using this value for the α parameter.

In Figure 4.2, we display the velocity profile along the middle axis $x = 1/2$ for uniform quadrilateral meshes with mesh-size $h = 1/256$ and various Binhgam numbers $\texttt{Bi} = 2, 5, 20, 50$. We observe very close profiles (qualitatively) and a good agreement with the results found in [124]. In Figure 4.3, present color isocontours for the velocity magnitude. We also show the mesh cells so as to illustrate the presence of polygonal (hexagonal) cells in two cases.

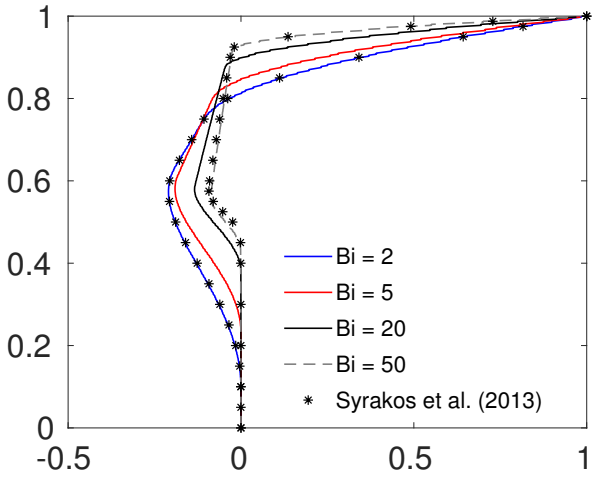

Figure 4.2: Horizontal velocity profile along the axis $x = 0.5$ for $\texttt{Bi} = 2, 5, 20, 50$ and $\alpha = 100$.

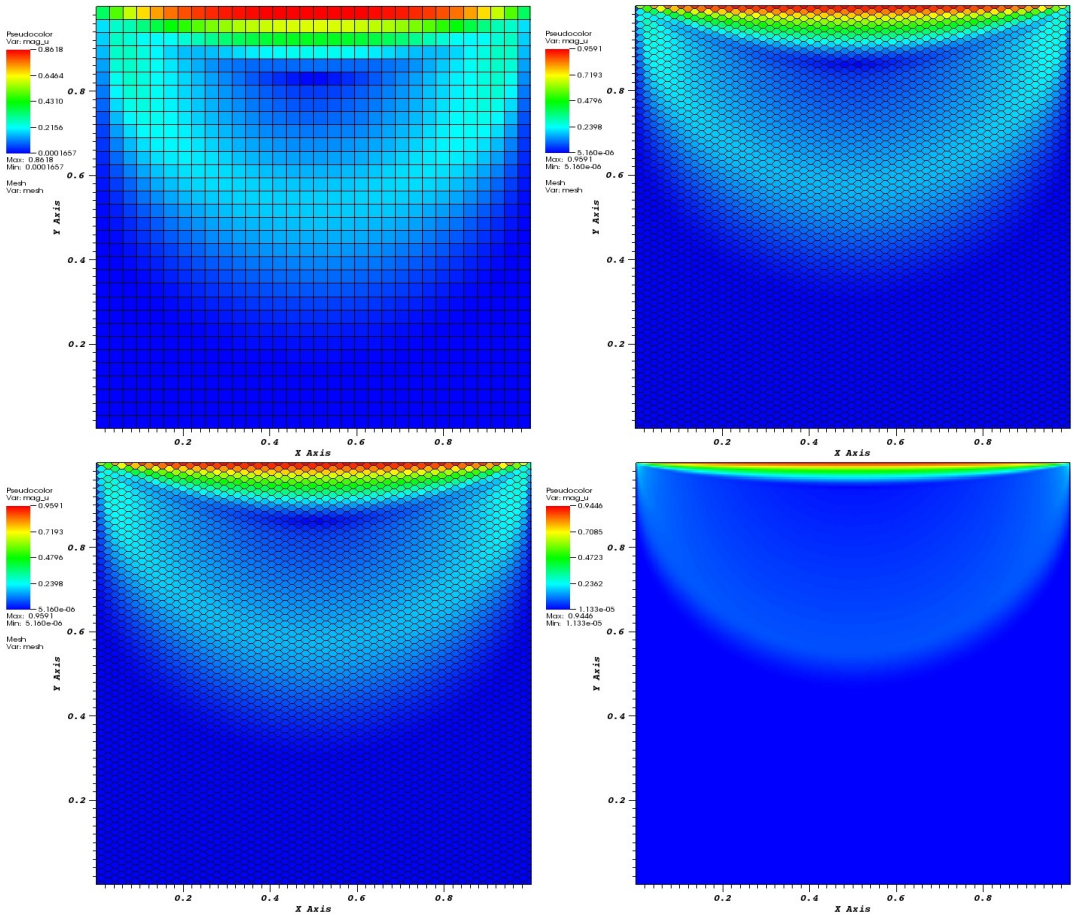

Figure 4.3: Velocity magnitude with $\alpha = 100$, varying the Bi number and different polygonal meshes: $\texttt{Bi} = 2$ (left-top) and $\texttt{Bi} = 50$ (right–bottom) with quadrilateral meshes, and $\texttt{Bi} = 5$ (right-top) and $\texttt{Bi} = 20$ (left-bottom) with hexagonal meshes.

We show the spatial distribution of the stress norm $|\boldsymbol{\sigma}|_{\ell^2}$ in Figure 4.4 for $\mathtt{Bi} = 2, 50$ and in Figure 4.5 for $\mathtt{Bi} = 5, 20$. We can observe in general two solid regions. The first solid region is placed in the lower part of the cavity, where the flow is slowed down due to the nonslip boundary conditions (considering also the lack of an external force). The second solid region is located in the middle upper part of the cavity, driven by the rotating motion and occurring around the central vortex (caused by the lid movement). As expected, we can see that both regions expand when Bi increases, which leads to a very tight unyielded zone closer and closer to the lid. In 4.4, we also notice two liquid diagonal strips from the lower corners of the cavity. We believe that this is in fact due to the lack of mesh resolution and we see that these strips tend to change to solid state with a higher mesh quality. Mesh requirements are stronger with the increase of the Bingham number, mainly due to the higher gradients occurring when the plastic terms dominate over viscous terms. The steepest gradients can also be observed with the horizontal-component velocity profiles in Figure 4.2.

4.4.2 The vane-in-cup geometry

Adapting the test case proposed by [113], we consider the computational domain depicted in Figure 4.6. No-slip conditions are applied on the external border and a velocity $\boldsymbol{u} = (-\omega y, \omega x)$ on the internal border due to the rotation of the vane, with ω the angular velocity. The (non-dimensional) Bingham number is defined as

$$\mathtt{Bi} = \frac{\sigma_0 R}{\mu V}, \tag{4.65}$$

where R is a reference length (the radius of the outer boundary) and the reference velocity V is computed as $V = \omega R_i$, so that we have $\mathtt{Bi} = \frac{\sigma_0}{\mu\omega}$. In our numerical experiments, we take $\omega = 1$, $R_e = 6$, $R_i = 4$ and the characteristic dimension $R = R_e - R_i$.

$$\mathtt{Bi} = \frac{\sigma_0 (R_e - R_i)}{\mu\omega R_i} = \frac{\sigma_0}{2}, \tag{4.66}$$

The augmentation parameter is set to $\alpha = 5$.

This example is slightly more difficult than the previous one. We used a quadrangular mesh refined near the vane tips, due to the reported high shear in the region around the tips. We see that this local refinement of the mesh is justified in Figure 4.8 for $\mathtt{Bi} = 1, 10$, where we observe the strong dependency of the velocity profile and the stress magnitude with respect to the angle θ for both Bingham numbers.

It is important to recall that we do not compare quantitatively our results, since in [113] the experiments were carried out for a Herschel-Buckley material. Therefore, we claim a fair agreement with [113] in the sense that we reproduce the concept of the non-cylindrical streamlines near the blades.

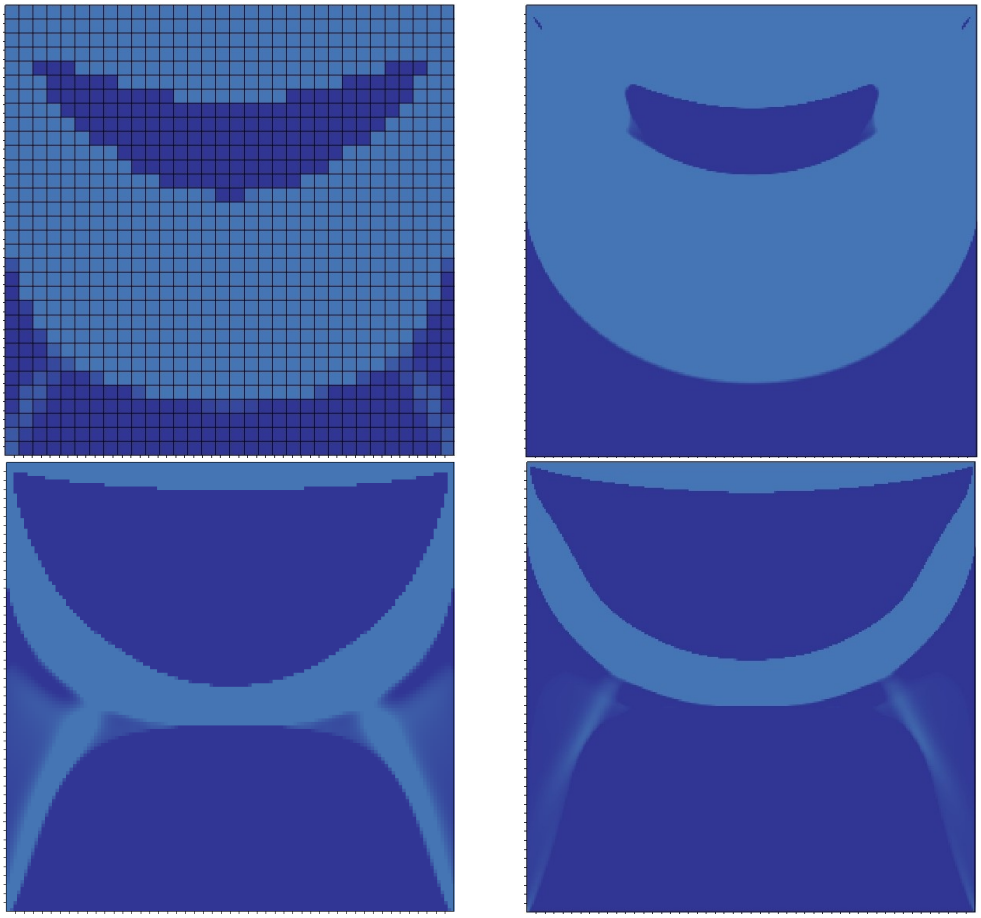

Figure 4.4: Stress colormap with $[\sigma_0; \sigma_0+\delta]$; $\delta = 0.05$ for $\texttt{Bi} = 2$ (top) and $\texttt{Bi} = 50$ (bottom) for uniform quadrangular meshes varying the mesh size and with $\alpha = 100$. For $\texttt{Bi} = 2$ (top), the coarser mesh (left-top) has a mesh size $h = 1/32$ and the finer mesh has a mesh size $h = 1/256$ (right-top). For $\texttt{Bi} = 50$, the coarser mesh (left-bottom) has a mesh size $h = 1/128$ and the finer mesh has a mesh size $h = 1/256$ (right-bottom).

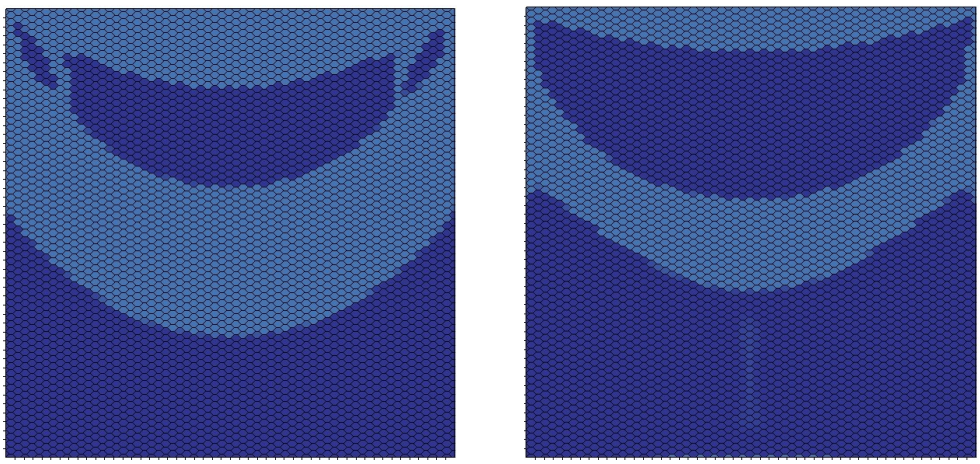

Figure 4.5: Colormap for $[\sigma_0; \sigma_0 + \delta]$; $\delta = 0.05$ for $\texttt{Bi} = 5$ (left) and $\texttt{Bi} = 20$ (right) for hexagonal meshes with $\alpha = 100$, with mesh size $h = 0.023$.

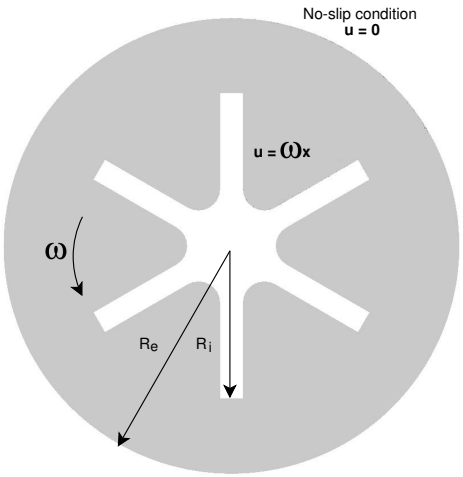

Figure 4.6: Sketch of the vane-in-cup geometry (light grey) and the computational domain (dark grey).

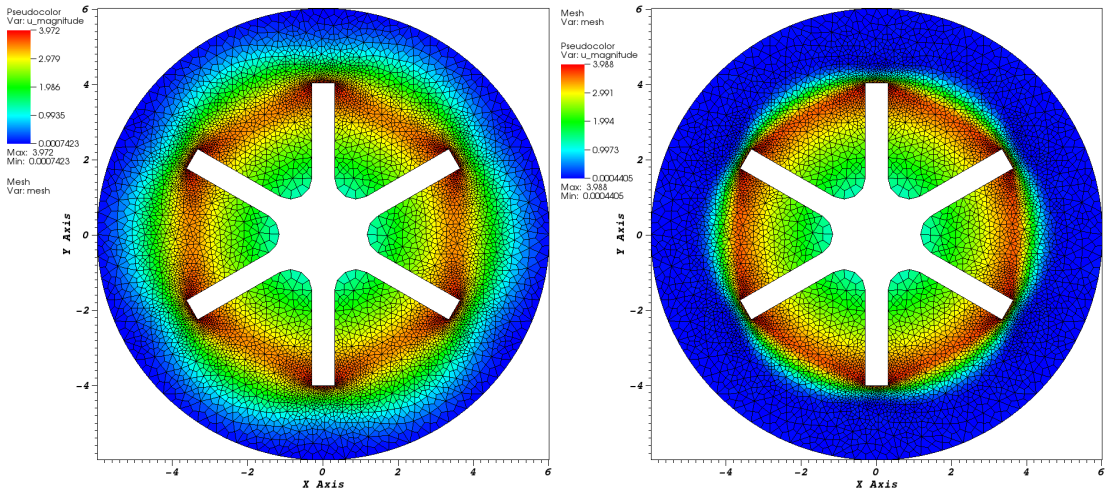

Figure 4.7: Velocity field for `Bi` $= 1$ (left) and `Bi` $= 10$ (right) for a quadrangular mesh with $h = h = 0.144$ and $\alpha = 0.1$. Colormap is $[\sigma_0; \sigma_0 + \delta]$; $\delta = 0 : 0.05$

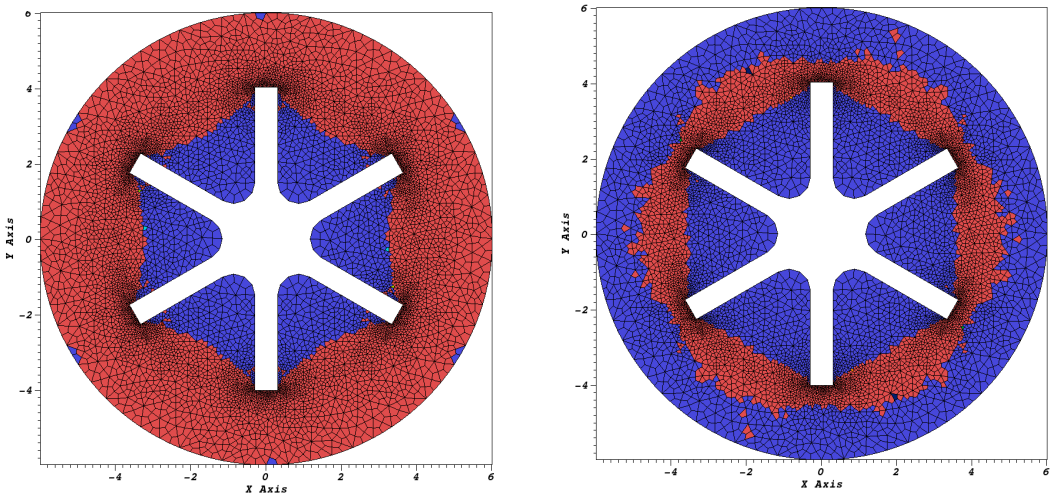

Figure 4.8: Stress colormap for `Bi` $= 1$ (left) and `Bi` $= 10$ (right) for a quadrangular mesh with $h = h = 0.144$ and $\alpha = 5.$. Colormap is $[\sigma_0; \sigma_0 + \delta]$; $\delta = 0 : 0.05$

Chapter 5

Conclusions and perspectives

The work carried out in this thesis made it possible to introduce a polyhedral method to approximate the solution of two nonlinear problems: Signorini's unilateral contact problem and Bingham's viscoplastic flows, commonly solved using conforming Finite Element methods. More precisely, we have brought the following contributions:

- We have devised a hybrid discretization method combined with Nitsche's method to handle Signorini's unilateral contact conditions in a weak fashion. We proved convergence estimates of order $(k+1)$ provided a mixed order is used with face polynomials of order $k \geq 0$ together with cell polynomials of order $(k+1)$. As a preliminary step, we have devised a novel analysis for the Poisson model problem with linear Dirichlet conditions, and afterwards, we have extended the analysis to the nonlinear case of Signorini's conditions.

  We have proposed two consistent formulations for the trace of the primal unknown resulting from this approach. The first formulation uses the degrees of freedom associated with the faces of the mesh. The second formulation uses instead the trace of the unknowns associated with the cells of the mesh. The latter approach was chosen since it preserves optimal convergence in the nonlinear case. The main idea in the analysis is to introduce a variant of the Hybrid High-Order (HHO) local operators that does not take into account the Dirichlet/contact boundary contribution.

  Concerning the error estimates, we have proved optimal convergence with both variants of the Nitsche-HHO formulation in the linear case and with the cell-based trace of the Nitsche-HHO formulation in the nonlinear case.

- Concerning viscoplastic flows, we have first presented a new discretization scheme for Bingham pipe flows by means of a hybrid lowest-order method combined with the Alternating Direction Method of Multipliers (ADMM). The velocity is discretized by means of one unknown per mesh face and one unknown per mesh cell (the cell unknowns can be locally eliminated by static condensation). We have also used piecewise constant vector-valued fields for the auxiliary variable and the associated Lagrange multiplier.

  We have exploited the possibility of using polygonal meshes including hanging nodes to perform local mesh adaptation around the yield surface. We have performed numerical tests in pipe geometries, where we have considered a circular cross-section test case with analytical solution, and an annulus cross-section. Our numerical experiments for the analytical test case have showed quantitatively the capture of the yield surface as the adaptation loop progressed. We have additionally observed a substantial reduction of degrees of freedom, when compared with a uniform mesh of equivalent meshsize around the yield surface). Exploiting the capabilities of polyhedral methods, we have also evaluated agglomeration-based mesh coarsening in the solid regions, where there are no stringent requirements on mesh resolution. The numerical results showed that the resulting decrease of degrees of freedom slightly decreases the accuracy of the approximation. On the

other hand, the results for the annulus-cross section have confirmed the usefulness of the local mesh adaptation, observed in the previous test case, when compared with a uniform mesh of equivalent meshsize. We have also provided more quantitative comparisons on the value of the flux across the cross-section and we have observed a good agreement with the results from the literature.

In a second step, we have extended our lowest-order discretization method to model Bingham vector flows with ADMM. We have first devised a lowest-order method with $k = 0$ for the face unknowns and $\ell = 1$ for the cell unknowns. We have also devised a higher-order method with $k = \ell = 1$ for the face and the cell unknowns and for which we have introduced quadrature rules in the formulation. We have presented numerical results on the lid-driven cavity benchmark and as second test case, we have considered a confined flow in a Couette geometry with a vane tool. For the first test case, we have observed a close agreement with previously published results on the velocity profiles, on the vertical axis $\{x = 0.5\}$ and for different Bingham numbers. We have additionally observed the matching of the yield surface in our experiments with simulations when compared with the previous references. The second test case has no explicit solution and additionally, the shape of the velocity field between the blades of the vane has been debated in the literature, with recent experiments [113] contradicting previously published simulation results. We have provided numerical simulations that are in good agreement with the recent experiments data in the previous reference.

- Finally, the methods devised in this thesis have been implemented in the Open Source Disk++ library, available at `https://github.com/wareHHOuse/diskpp`. Disk++ is a C++ template library for Discontinuous Skeletal methods like discontinuous Galerkin (dG) and Hybrid High-Order (HHO) methods. We have contributed with the modules concerning viscoplasticity, explicitly written for the bi-dimensional scalar and the bi-dimensional vector Bingham problem, with the additional corresponding tools for the augmented Lagrangian algorithm. We have also added the module for Signorini's unilateral contact using a Generalized Newton's method or the fixed steepest descent method to solve Nitsche's formulation. Additionally, we have added a module for mesh refinement using hanging nodes (triangles and squares) and coarsening tools for agglomeration of polygonal mesh cells.

Several further developments of mathematical and numerical nature can be identified as possible perspectives to this thesis.

In Chapter 2, we have developed a method for scalar Signorini's unilateral contact problem. An extension to vector deformations seems to be the obvious next step to be considered. Additionally, the physics of the model might be enriched by adding friction laws such as Tresca's friction or the much more challenging Coulomb friction. The latter law poses difficulties in the proof of existence and uniqueness, since the standard results of convex analysis do not apply.

In Chapter 3, we have highlighted in the scalar case the computational effectiveness of the adaptive mesh procedure to capture the yield surface. Nonetheless, the current numerical procedure can be enhanced by using *hp*-refinement techniques, and a posteriori error estimation in the yielded regions. Moreover, some of the acceleration techniques mentioned in the introduction for the ADMM [125, 9] can be considered, as well as second-order cone programming [16, 17].

The mathematical model could be also enriched by using a Herschel-Buckley constitutive law or by enhancing the state law with visco-elasto-plasticity models, see the review [73]. The first improvement intends to have a more accurate representation of physical effects, by adding a power law for the viscous term. The second approach includes elastic effects to have a more accurate characterization of different phenomena [53].

Regarding the extension of our developments to 3D in the Disk++ library, let us emphasize that this library is based upon dimension-independent and element-independent data struc-

tures. Therefore, it already supports 1D, 2D and 3D settings with polygonal / polyhedral shape meshes and hence, it is readily feasible to implement a 3D Bingham vector model.

Finally, an interesting perspective is the simulation of an air bubble immersed in a non-Newtonian fluid [33, 103, 96]. This problem is of considerable interest for many materials such as food foams, insulating building materials, among others. The modeling and the numerical treatment of these airy materials is very challenging due to the bubble-fluid interface, the bubble shape deformation, the forces exerted by the fluid, etc. An immersed boundary based method using the so-called Cut-FEM approach [28] can be considered. Note that some recent advances in the state-of-the-art have been achieved on the unfitted version of the HHO method (Cut-HHO) for interface problems [25]. These advances can be highly instrumental to extend the present work to the simulation of a suspension of air bubbles in a non-Newtonian fluid.

Bibliography

[1] M. Abbas, A. Ern, and N. Pignet. A Hybrid High-Order method for incremental associative plasticity with small deformations. Available at `http://hal.archives-ouvertes.fr/hal-01768411`, 2018.

[2] M. Abbas, A. Ern, and N. Pignet. Hybrid High-Order methods for finite deformations of hyperelastic materials. *Comput. Mech.*, 62(4):909–928, 2018.

[3] P. Alart. Méthode de Newton généralisée en mécanique du contact. *J. Math. Pures Appl. (9)*, 76(1):83–108, 1997.

[4] Yahya Alnashri and Jérôme Droniou. Gradient schemes for the signorini and the obstacle problems, and application to hybrid mimetic mixed methods. *Computers and Mathematics with Applications*, 72(11):2788 – 2807, 2016.

[5] John Andersson. Optimal regularity and free boundary regularity for the Signorini problem. *Algebra i Analiz*, 24(3):1–21, 2012.

[6] C. Annavarapu, R. R. Settgast, S. M. Johnson, P. Fu, and E. B. Herbold. A weighted Nitsche stabilized method for small-sliding contact on frictional surfaces. *Comput. Methods Appl. Mech. Engrg.*, 283:763–781, 2015.

[7] B. Ayuso de Dios, K. Lipnikov, and G. Manzini. The nonconforming virtual element method. *ESAIM: Math. Model. Numer. Anal. (M2AN)*, 50(3):879–904, 2016.

[8] N. J. Balmforth, I. A. Frignard, and G. Ovarlez. Yielding to stress: recent developments in viscoplastic fluid mechanics. *Annu. Rev. Fluid. Mech.*, 46:121–146, 2016.

[9] S. Bartels and M. Milicevic. Alternating direction method of multipliers with variable step sizes. Available online at `aam.uni-freiburg.de/agba/prof/preprints/BarMil17-pre.pdf`, 2017.

[10] F. Bassi, L. Botti, A. Colombo, D. A. Di Pietro, and P. Tesini. On the flexibility of agglomeration based physical space discontinuous Galerkin discretizations. *J. Comput. Phys.*, 231(1):45–65, 2012.

[11] F. Bassi, L. Botti, A. Colombo, and S. Rebay. Agglomeration based discontinuous Galerkin discretization of the Euler and Navier-Stokes equations. *Comput. & Fluids*, 61:77–85, 2012.

[12] Z. Belhachmi and F. Ben Belgacem. Quadratic finite element approximation of the Signorini problem. *Math. Comp.*, 72(241):83–104, 2003.

[13] F. Ben Belgacem and Y. Renard. Hybrid finite element methods for the Signorini problem. *Math. Comp.*, 72(243):1117–1145, 2003.

[14] M. Bercovier and M. Engelman. A finite element method for incompressible non-Newtonian flows. *J. Comput. Phys.*, 36(3):313–326, 1980.

[15] E. C. Bingham. *Fluidity and plasticity.* McGraw-Hill, New York, USA, 1922.

[16] J. Bleyer. Advances in the simulation of viscoplastic fluid flows using interior-point methods. *Comput. Methods Appl. Mech. Engrg.*, 330:368–394, 2018.

[17] J. Bleyer, M. Maillard, P. de Buhan, and P. Coussot. Efficient numerical computations of yield stress fluid flows using second-order cone programming. *Comput. Methods Appl. Mech. Engrg.*, 283:599–614, 2015.

[18] T. Boiveau and E. Burman. A penalty-free Nitsche method for the weak imposition of boundary conditions in compressible and incompressible elasticity. *IMA J. Numer. Anal.*, 36(2):770–795, 2016.

[19] J. Bonelle and A. Ern. Analysis of compatible discrete operator schemes for elliptic problems on polyhedral meshes. *ESAIM Math. Model. Numer. Anal.*, 48(2):553–581, 2014.

[20] M. Botti, D. Di Pietro, and P. Sochala. A Hybrid High-Order method for nonlinear elasticity. *SIAM J. Numer. Anal.*, 55(6):2687–2717, 2017.

[21] H. Brezis. Équations et inéquations non linéaires dans les espaces vectoriels en dualité. *Ann. Inst. Fourier (Grenoble)*, 18(fasc. 1):115–175, 1968.

[22] F. Brezzi, K. Lipnikov, and M. Shashkov. Convergence of the mimetic finite difference method for diffusion problems on polyhedral meshes. *SIAM J. Numer. Anal.*, 43(5):1872–1896, 2005.

[23] E. Burman. A penalty-free nonsymmetric Nitsche-type method for the weak imposition of boundary conditions. *SIAM J. Numer. Anal.*, 50(4):1959–1981, 2012.

[24] E. Burman and A. Ern. A nonlinear consistent penalty method weakly enforcing positivity in the finite element approximation of the transport equation. *Comput. Methods Appl. Mech. Engrg.*, 320:122–132, 2017.

[25] E. Burman and A. Ern. An unfitted Hybrid High-Order method for elliptic interface problems. *SIAM J. Numer. Anal.*, 56(3):1525–1546, 2018.

[26] E. Burman, M. A. Fernández, and S. Frei. A Nitsche-based formulation for fluid-structure interactions with contact. Research Report RR-9172, Inria, May 2018.

[27] E. Burman and P. Hansbo. Deriving robust unfitted finite element methods from augmented Lagrangian formulations. In *Geometrically unfitted finite element methods and applications*, volume 121 of *Lect. Notes Comput. Sci. Eng.*, pages 1–24. Springer, Cham, 2017.

[28] E. Burman, P. Hansbo, and M. G. Larson. A stabilized cut finite element method for partial differential equations on surfaces: the Laplace-Beltrami operator. *Comput. Methods Appl. Mech. Engrg.*, 285:188–207, 2015.

[29] E. Burman, P. Hansbo, and M. G. Larson. Augmented Lagrangian finite element methods for contact problems. *arXiv preprint arXiv:1609.03326*, September 2016.

[30] E. Burman, P. Hansbo, and M. G. Larson. The penalty-free Nitsche method and nonconforming finite elements for the Signorini problem. *SIAM J. Numer. Anal.*, 55(6):2523–2539, 2017.

[31] E. Burman, P. Hansbo, M. G. Larson, and R. Stenberg. Galerkin least squares finite element method for the obstacle problem. *Comput. Meth. Appl. Mech. Engrg.*, 313:362–374, September 2017.

[32] A. Cangiani, E. H. Georgoulis, and P. Houston. *hp*-version discontinuous Galerkin methods on polygonal and polyhedral meshes. *Math. Models Methods Appl. Sci.*, 24(10):2009–2041, 2014.

[33] I. Cantat, S. Cohen-Addad, F. Elias, F. Graner, R. Hohler, O. Pitois, F. Rouyer, A. Saint-Jalmes, R. Flatman, and S. Cox. *Foams: Structure and Dynamics*. Oxford University Press, 2013.

[34] K. L. Cascavita, J. Bleyer, X. Chateau, and A. Ern. Hybrid discretization methods for the simulation of Bingham fluid flows (in preparation).

[35] K. L. Cascavita, J. Bleyer, X. Chateau, and A. Ern. Hybrid Discretization Methods with Adaptive Yield Surface Detection for Bingham Pipe Flows. *J. Sci. Comput.*, 77(3):1424–1443, 2018.

[36] K. L. Cascavita, F. Chouly, and A. Ern. Hybrid high-order discretizations combined with Nitsche's method for contact dirichlet and signorini boundary conditions.

[37] F. Chouly. An adaptation of Nitsche's method to Tresca friction problem. *J. Math. Anal. Appl.*, 411(1):329–339, 2014.

[38] F. Chouly, M. Fabre, P. Hild, R. Mlika, R. Pousin, and Y. Renard. An overview of recent results on Nitsche's method for contact problems. In *Geometrically unfitted finite element methods and applications*, volume 121 of *Lect. Notes Comput. Sci. Eng.*, pages 93–141. Springer, Cham, 2017.

[39] F. Chouly, M. Fabre, P. Hild, R. Pousin, and Y. Renard. Residual-based *a posteriori* error estimation for contact problems approximated by Nitsche's method. *IMA J. Numer. Anal.*, 38(2):921–954, 2018.

[40] F. Chouly and P. Hild. A Nitsche-based method for unilateral contact problems: numerical analysis. *SIAM J. Numer. Anal.*, 51(2):1295–1307, 2013.

[41] F. Chouly and P. Hild. On convergence of the penalty method for unilateral contact problems. *Appl. Numer. Math.*, 65:27–40, 2013.

[42] F. Chouly, P. Hild, V. Lleras, and Y. Renard. Nitsche-based finite element method for contact with Coulomb friction. *Lecture Notes in Computational Science and Engineering*, 2017. To appear. Proceedings of the European Conference on Numerical Mathematics and Advanced Applications ENUMATH 2017.

[43] F. Chouly, P. Hild, and Y. Renard. A Nitsche finite element method for dynamic contact: 1. Space semi-discretization and time-marching schemes. *ESAIM Math. Model. Numer. Anal.*, 49(2):481–502, 2015.

[44] F. Chouly, P. Hild, and Y. Renard. A Nitsche finite element method for dynamic contact: 2. Stability of the schemes and numerical experiments. *ESAIM Math. Model. Numer. Anal.*, 49(2):503–528, 2015.

[45] F. Chouly, P. Hild, and Y. Renard. Symmetric and non-symmetric variants of Nitsche's method for contact problems in elasticity: theory and numerical experiments. *Math. Comp.*, 84(293):1089–1112, 2015.

[46] F. Chouly, R. Mlika, and Y. Renard. An unbiased Nitsche's approximation of the frictional contact between two elastic structures. *Numer. Math.*, 139(3):593–631, 2018.

[47] F. Chouly and Y. Renard. Explicit Verlet time–integration for a Nitsche–based approximation of elastodynamic contact problems. hal-01814774. Submitted.

[48] Franz Chouly, Mathieu Fabre, Patrick Hild, Rabii Mlika, Jérôme Pousin, and Yves Renard. An overview of recent results on nitsche's method for contact problems. In Stéphane P. A. Bordas, Erik Burman, Mats G. Larson, and Maxim A. Olshanskii, editors, *Geometrically Unfitted Finite Element Methods and Applications*, pages 93–141, Cham, 2017. Springer International Publishing.

[49] P.-G. Ciarlet. *The finite element method for elliptic problems*, volume II of *Handbook of Numerical Analysis (eds. P.G. Ciarlet and J.L. Lions)*. North-Holland Publishing Co., Amsterdam, 1991.

[50] M. Cicuttin, D. Di Pietro, and A. Ern. Implementation of Discontinuous Skeletal methods on arbitrary-dimensional, polytopal meshes using generic programming. *J. Comput. Appl. Math.*, 344:852–874, 2018.

[51] B. Cockburn, D. A. Di Pietro, and A. Ern. Bridging the hybrid high-order and hybridizable discontinuous Galerkin methods. *ESAIM Math. Model. Numer. Anal.*, 50(3):635–650, 2016.

[52] B. Cockburn, J. Gopalakrishnan, and R. Lazarov. Unified hybridization of discontinuous Galerkin, mixed, and continuous Galerkin methods for second order elliptic problems. *SIAM J. Numer. Anal.*, 47(2):1319–1365, 2009.

[53] P. Coussot. Bingham's heritage. *Rheol. Acta*, 6:163–176, 2016.

[54] A. Curnier and P. Alart. A generalized Newton method for contact problems with friction. *J. Méc. Théor. Appl.*, 7(suppl. 1):67–82, 1988.

[55] E. J. Dean, R. Glowinski, and G. Guidoboni. On the numerical simulation of Bingham visco-plastic flow: Old and new results. *J. Non-Newton. Fluid Mech.*, 142(1):36–62, 2007.

[56] D. Di Pietro and J. Droniou. A Hybrid High-Order method for Leray-Lions elliptic equations on general meshes. *Math. Comp.*, 86(307):2159–2191, 2017.

[57] D. Di Pietro, J. Droniou, and A. Ern. A discontinuous-skeletal method for advection-diffusion-reaction on general meshes. *SIAM J. Numer. Anal.*, 53(5):2135–2157, 2015.

[58] D. Di Pietro and A. Ern. *Mathematical aspects of discontinuous Galerkin methods*, volume 69 of *Mathématiques & Applications (Berlin) [Mathematics & Applications]*. Springer, Heidelberg, 2012.

[59] D. Di Pietro and A. Ern. A Hybrid High-Order locking-free method for linear elasticity on general meshes. *Comput. Methods Appl. Mech. Engrg.*, 283:1–21, 2015.

[60] D. Di Pietro, A. Ern, and S. Lemaire. An arbitrary-order and compact-stencil discretization of diffusion on general meshes based on local reconstruction operators. *Comput. Methods Appl. Math.*, 14(4):461–472, 2014.

[61] D. Di Pietro, A. Ern, A. Linke, and F. Schieweck. A discontinuous skeletal method for the viscosity-dependent Stokes problem. *Comput. Methods Appl. Mech. Engrg.*, 306:175–195, 2016.

[62] D. A. Di Pietro, A. Ern, and S. Lemaire. An arbitrary-order and compact-stencil discretization of diffusion on general meshes based on local reconstruction operators. *Comput. Methods Appl. Math.*, 14(4):461–472, 2014.

[63] D. A. Di Pietro and S. Krell. A Hybrid High-Order method for the steady incompressible Navier–Stokes problem. *J. Sci. Comput.*, 74(3):1677–1705, 2018.

[64] J. Droniou, R. Eymard, T. Gallouët, and R. Herbin. A unified approach to mimetic finite difference, hybrid finite volume and mixed finite volume methods. *Math. Models Methods Appl. Sci.*, 20(2):265–295, 2010.

[65] G. Drouet and P. Hild. Optimal convergence for discrete variational inequalities modelling Signorini contact in 2D and 3D without additional assumptions on the unknown contact set. *SIAM J. Numer. Anal.*, 53(3):1488–1507, 2015.

[66] G. Duvaut and J.-L. Lions. *Inequalities in mechanics and physics*. Springer-Verlag, Berlin-New York, 1976. Translated from the French by C. W. John, Grundlehren der Mathematischen Wissenschaften, 219.

[67] A. Ern and M. Vohralík. Polynomial-degree-robust a posteriori estimates in a unified setting for conforming, nonconforming, discontinuous Galerkin, and mixed discretizations. *SIAM J. Numer. Anal.*, 53(2):1058–1081, 2015.

[68] Alexandre Ern and Jean-Luc Guermond. Finite element quasi-interpolation and best approximation. *ESAIM Math. Model. Numer. Anal.*, 51(4):1367–1385, 2017.

[69] R. Eymard, T. Gallouët, and R. Herbin. Discretization of heterogeneous and anisotropic diffusion problems on general nonconforming meshes SUSHI: a scheme using stabilization and hybrid interfaces. *IMA J. Numer. Anal.*, 30(4):1009–1043, 2010.

[70] R. Eymard, T. Gallouët, and R. Herbin. Discretization of heterogeneous and anisotropic diffusion problems on general nonconforming meshes. SUSHI: a scheme using stabilization and hybrid interfaces. *IMA J. Numer. Anal.*, 30(4):1009–1043, 2010.

[71] M. Fabre, J. Pousin, and Y. Renard. A fictitious domain method for frictionless contact problems in elasticity using Nitsche's method. *SMAI J. Comput. Math.*, 2:19–50, 2016.

[72] M. Fortin and R. Glowinski. *Augmented Lagrangian methods*, volume 15 of *Studies in Mathematics and its Applications*. North-Holland Publishing Co., Amsterdam, 1983. Applications to the numerical solution of boundary value problems, Translated from the French by B. Hunt and D. C. Spicer.

[73] D. Fraggedakis, Y. Dimakopoulos, and J. Tsamopoulos. Yielding the yield stress analysis: a thorough comparison of recently proposed elasto-visco-plastic (EVP) fluid models. *J. Non-Newton. Fluid Mech.*, 236:104–122, 2016.

[74] M. Fuchs and G. Seregin. *Variational methods for problems from plasticity theory and for generalized Newtonian fluids*, volume 1749 of *Lecture Notes in Mathematics*. Springer-Verlag, Berlin, 2000.

[75] D. Gabay and B. Mercier. A dual algorithm for the solution of nonlinear variational problems via finite element approximations. *Comput. Math. Appl.*, 2:17–40, 1976.

[76] R. Glowinski. *Numerical methods for nonlinear variational problems*. Springer Series in Computational Physics. Springer-Verlag, New York, 1984.

[77] R. Glowinski and P. Le Tallec. *Augmented Lagrangian and operator-splitting methods in nonlinear mechanics*, volume 9 of *SIAM Studies in Applied Mathematics*. Society for Industrial and Applied Mathematics (SIAM), Philadelphia, PA, 1989.

[78] R. Glowinski, J.-L. Lions, and R. Trémolières. *Numerical analysis of variational inequalities*, volume 8 of *Studies in Mathematics and its Applications*. North-Holland Publishing Co., Amsterdam-New York, 1981. Translated from the French.

[79] R. Glowinski and A. Marrocco. Sur l'approximation, par éléments finis d'ordre un, et la résolution, par pénalisation-dualité, d'une classe de problèmes de Dirichlet non linéaires. *Rev. Française Automat. Informat. Recherche Opérationnelle Sér. Rouge Anal. Numér.*, 9(R-2):41–76, 1975.

[80] Roland Glowinski. *Numerical methods for nonlinear variational problems*. Scientific Computation. Springer-Verlag, Berlin, 2008. Reprint of the 1984 original.

[81] T. Gustafsson, R. Stenberg, and J. Videman. Nitsche's method for unilateral contact problems. *ArXiv e-prints*, May 2018.

[82] Weimin Han and Mircea Sofonea. *Quasistatic contact problems in viscoelasticity and viscoplasticity*, volume 30 of *AMS/IP Studies in Advanced Mathematics*. American Mathematical Society, Providence, RI, 2002.

[83] P. Hansbo, A. Rashid, and K. Salomonsson. Least-squares stabilized augmented Lagrangian multiplier method for elastic contact. *Finite Elem. Anal. Des.*, 116:32–37, 2016.

[84] Peter Hansbo. Nitsche's method for interface problems in computational mechanics. *GAMM-Mitt.*, 28(2):183–206, 2005.

[85] J. Haslinger. Finite element analysis for unilateral problems with obstacles on the boundary. *Apl. Mat.*, 22(3):180–188, 1977.

[86] J. Haslinger, I. Hlaváček, and J. Nečas. *Numerical methods for unilateral problems in solid mechanics*, volume IV of *Handbook of Numerical Analysis (eds. P.G. Ciarlet and J.L. Lions)*. North-Holland Publishing Co., Amsterdam, 1996.

[87] B. He and X. Yuan. On non-ergodic convergence rate of Douglas-Rachford alternating direction method of multipliers. *Numer. Math.*, 130(3):567–577, 2015.

[88] Raphaèle Herbin and Emmanuelle Marchand. Finite volume approximation of a class of variational inequalities. *IMA Journal of Numerical Analysis*, 21(2):553–585, 04 2001.

[89] M. R. Hestenes. Multiplier and gradient methods. *J. Optimization Theory Appl.*, 4:303–320, 1969.

[90] P. Hild. Numerical implementation of two nonconforming finite element methods for unilateral contact. *Comput. Methods Appl. Mech. Engrg.*, 184(1):99–123, 2000.

[91] P. Hild and Y. Renard. A stabilized Lagrange multiplier method for the finite element approximation of contact problems in elastostatics. *Numer. Math.*, 115(1):101–129, 2010.

[92] P. Hild and Y. Renard. An improved a priori error analysis for finite element approximations of Signorini's problem. *SIAM J. Numer. Anal.*, 50(5):2400–2419, 2012.

[93] S. Hüeber and B. I. Wohlmuth. An optimal a priori error estimate for nonlinear multibody contact problems. *SIAM J. Numer. Anal.*, 43(1):156–173, 2005.

[94] N. Kikuchi and J. T. Oden. *Contact problems in elasticity: a study of variational inequalities and finite element methods*, volume 8 of *SIAM Studies in Applied Mathematics*. Society for Industrial and Applied Mathematics (SIAM), Philadelphia, PA, 1988.

[95] David Kinderlehrer. Remarks about Signorini's problem in linear elasticity. *Ann. Scuola Norm. Sup. Pisa Cl. Sci. (4)*, 8(4):605–645, 1981.

[96] M. Kogan, L. Ducloué, J. Goyon, X. Chateau, O. Pitois, and G. Ovarlez. Mixtures of foam and paste: suspensions of bubbles in yield stress fluids. *Rheologica Acta*, pages doi: 10.1007/s00397–013–0677–7, 2013.

[97] K. Kunisch and G. Stadler. Generalized Newton methods for the 2D-Signorini contact problem with friction in function space. *M2AN Math. Model. Numer. Anal.*, 39(4):827–854, 2005.

[98] Y. Kuznetsov, K. Lipnikov, and M. Shashkov. The mimetic finite difference method on polygonal meshes for diffusion-type problems. *Comput. Geosci.*, 8(4):301–324 (2005), 2004.

[99] P. Laborde and Y. Renard. Fixed point strategies for elastostatic frictional contact problems. *Math. Methods Appl. Sci.*, 31(4):415–441, 2008.

[100] J.-C. Latché and D. Vola. Analysis of the Brezzi-Pitkäranta stabilized Galerkin scheme for creeping flows of Bingham fluids. *SIAM J. Numer. Anal.*, 42(3):1208–1225, 2004.

[101] Tod A. Laursen. *Computational contact and impact mechanics*. Springer-Verlag, Berlin, 2002.

[102] C. Lehrenfeld. *Hybrid Discontinuous Galerkin methods for solving incompressible flow problems*. PhD thesis, Rheinisch-Westfälische Technische Hochschule Aachen, 2010.

[103] J. Li and Y. Y. Renardy. Shear-induced rupturing of a viscous drop in a bingham liquid. *Journal of Non-Newtonian Fluid Mechanics*, 95(2):235 – 251, 2000.

[104] Jacques-Louis Lions and Stampacchia Guido. Variational inequalities. *Communications on Pure and Applied Mathematics*, 20(3):493–519, 1967.

[105] R. Mlika, Y. Renard, and F. Chouly. An unbiased Nitsche's formulation of large deformation frictional contact and self-contact. *Comput. Methods Appl. Mech. Engrg.*, 325:265–288, 2017.

[106] P. P. Mosolov and V. P. Miasnikov. Variational methods in the theory of the fluidity of a viscous-plastic medium. *J. Appl. Math. Mech.*, 29(3):545–577, 1965.

[107] P. P. Mosolov and V. P. Miasnikov. On stagnant flow regions of a viscous-plastic medium in pipes. *J. Appl. Math. Mech.*, 30(4):841–854, 1966.

[108] P. P. Mosolov and V. P. Miasnikov. On qualitative singularities of the flow of a viscoplastic medium in pipes. *J. Appl. Math. Mech.*, 31(3):609–613, 1967.

[109] Mohand Moussaoui and Khadidja Khodja. Régularité des solutions d'un problème mêlé Dirichlet-Signorini dans un domaine polygonal plan. *Comm. Partial Differential Equations*, 17(5-6):805–826, 1992.

[110] J. Nitsche. Über ein Variationsprinzip zur Lösung von Dirichlet-Problemen bei Verwendung von Teilräumen, die keinen Randbedingungen unterworfen sind. *Abh. Math. Sem. Univ. Hamburg*, 36:9–15, 1971. Collection of articles dedicated to Lothar Collatz on his sixtieth birthday.

[111] I. Oikawa. A hybridized discontinuous Galerkin method with reduced stabilization. *J. Sci. Comput.*, published online on December 2014.

[112] J. G. Oldroyd. A rational formulation of the equations of plastic flow for a Bingham solid. *Proc. Cambridge Philos. Soc.*, 43:100–105, 1947.

[113] G. Ovarlez, F. Mahaut, F. Bertrand, and X. Chateau. Flows and heterogeneities with a vane tool: Magnetic resonance imaging measurements. *Journal of rheology*, 55:197–223, 2011.

[114] T. C. Papanastasiou. Flows of materials with yield. *J. Rheol.*, 31(5):385–404, 1987.

[115] M. J. D. Powell. A method for nonlinear constraints in minimization problems. In *Optimization (Sympos., Univ. Keele, Keele, 1968)*, pages 283–298. Academic Press, London, 1969.

[116] Y. Renard. Generalized Newton's methods for the approximation and resolution of frictional contact problems in elasticity. *Comput. Methods Appl. Mech. Engrg.*, 256:38–55, 2012.

[117] N. Roquet and P. Saramito. An adaptive finite element method for Bingham fluid flows around a cylinder. *Comput. Methods Appl. Mech. Engrg.*, 192(31-32):3317–3341, 2003.

[118] P. Saramito and N. Roquet. An adaptive finite element method for viscoplastic fluid flows in pipes. *Comput. Methods Appl. Mech. Engrg.*, 190(40):5391–5412, 2001.

[119] P. Saramito and A. Wachs. Progress in numerical simulation of yield stress fluid flows. *Rheol. Acta*, 56"(3):211–230, 2017.

[120] F. Scarpini and M.-A. Vivaldi. Error estimates for the approximation of some unilateral problems. *RAIRO Anal. Numér.*, 11(2):197–208, 1977.

[121] A. Seitz, W. A. Wall, and A. Popp. Nitsche's method for finite deformation thermomechanical contact problems. *Computational Mechanics*, Sep 2018.

[122] A. Signorini. Sopra alcune questioni di elastostatica. *Atti della Societa per il Progresso della Scienza*, 1933.

[123] Rolf Stenberg. On some techniques for approximating boundary conditions in the finite element method. *J. Comput. Appl. Math.*, 63(1-3):139–148, 1995.

[124] P. Szabo and O. Hassager. Flow of viscoplastic fluids in eccentric annular geometries. *J. Non-Newton. Fluid Mech.*, 45:149–169, 1992.

[125] T. Treskatis, M. A. Moyers-González, and C. J. Price. An accelerated dual proximal gradient method for applications in viscoplasticity. *J. Non-Newton. Fluid Mech.*, 238:115–130, 2016.

[126] R. Verfürth. *A posteriori error estimation techniques for finite element methods*. Numerical Mathematics and Scientific Computation. Oxford University Press, Oxford, 2013.

[127] A. Wachs. Numerical simulaiton of steady Bingham flow through an eccentric annular cross-section by distributed Lagrange multiplier/fictitious domain and augmented Lagrangian methods. *J. Non-Newton. Fluid Mech.*, 142:183–198, 2007.

[128] Y. Wang. Tracking of the yield surfaces of laminar viscoplastic flows in noncircular ducts using an adaptive scheme. *Proc. Nat. Sci. Counc. ROC(A)*, 23(2):311–318, 1999.

[129] B. Wohlmuth. Variationally consistent discretization schemes and numerical algorithms for contact problems. *Acta Numer.*, 20:569–734, 2011.

[130] P. Wriggers. *Computational Contact Mechanics*. Wiley, 2002.

[131] P. Wriggers, W. T. Rust, and B. D. Reddy. A virtual element method for contact. *Comput. Mech.*, 58(6):1039–1050, 2016.

[132] J. Zhang. An augmented Lagrangian approach to simulating yield stress fluid flows around a spherical gas bubble. *Internat. J. Numer. Methods Fluids*, 69(3):731–746, 2012.

Résumé

Cette thèse s'intéresse à la conception et à l'analyse de méthodes de discrétisation hybrides pour les inégalités variationnelles non linéaires apparaissant en mécanique des fluides et des solides. Les principaux avantages de ces méthodes sont la conservation locale au niveau des mailles, la robustesse par rapport à différents régimes de paramètres et la possibilité d'utiliser des maillages polygonaux / polyédriques avec des nœuds non coïncidants, ce qui est très intéressant dans le contexte de l'adaptation de maillage. Les méthodes de discrétisation hybrides sont basées sur des inconnues discrètes attachées aux faces du maillage. Des inconnues discrètes attachées aux mailles sont également utilisées, mais elles peuvent être éliminées localement par condensation statique. Deux applications principales des discrétisations hybrides sont abordées dans cette thèse. La première est le traitement par la méthode de Nitsche du problème de contact de Signorini (dans le cas scalaire) avec une non-linéarité dans les conditions aux limites. Nous prouvons des estimations d'erreur optimales conduisant à des taux de convergence d'erreur d'énergie d'ordre $(k+1)$, si des polynômes de face de degré $k \geq 0$ sont utilisés. La deuxième application principale concerne les fluides à seuil viscoplastiques. Nous concevons une méthode de Lagrangien augmenté discrète appliquée à la discrétisation hybride. Nous exploitons la capacité des méthodes hybrides d'utiliser des maillages polygonaux avec des nœuds non coïncidants afin d'effectuer l'adaptation de maillage local et mieux capturer la surface limite. La précision et la performance des schémas sont évaluées sur des cas tests bidimensionnels, y compris par des comparaisons avec la littérature.

Mot-clés. *Méthodes de discrétisation hybrides, problème de contact de Signorini, méthode de Nitsche, viscoplasticité, fluides à seuil, adaptation du maillage.*

Abstract

This thesis is concerned with the devising and the analysis of hybrid discretization methods for nonlinear variational inequalities arising in computational mechanics. Salient advantages of such methods are local conservation at the cell level, robustness in different regimes and the possibility to use polygonal/polyhedral meshes with hanging nodes, which is very attractive in the context of mesh adaptation. Hybrid discretization methods are based on discrete unknowns attached to the mesh faces. Discrete unknowns attached to the mesh cells are also used, but they can be eliminated locally by static condensation. Two main applications of hybrid discretization methods are addressed in this thesis. The first one is the treatment using Nitsche's method of Signorini's contact problem (in the scalar-valued case) with a nonlinearity in the boundary conditions. We prove optimal error estimates leading to energy-error convergence rates of order $(k+1)$ if face polynomials of degree $k \geq 0$ are used. The second main application is on viscoplastic yield flows. We devise a discrete augmented Lagrangian method applied to the present hybrid discretization. We exploit the capability of hybrid methods to use polygonal meshes with hanging nodes to perform local mesh adaptation and better capture the yield surface. The accuracy and performance of the present schemes are assessed on bi-dimensional test cases including comparisons with the literature.

Keywords. *Hybrid discretization methods, Signorini's contact problem, Nitsche's method, viscoplasticity, yield fluids, adaptive mesh refinement.*